UNIVERSITÉ LIBRE DE BRUXELLES

ULB

Symmetry breaking in nuclear mean-field models

by

Wouter RYSSENS

Supervisors:
Prof. Dr. Ir. P. DESCOUVEMONT
Prof. Dr. Ir. P.-H. HEENEN

Dissertation presented in fulfillment of the requirements for the degree of Doctor in Physics

Academic year 2015-2016

Contents

Resumé de la thèse

Dans les années 1970, Vautherin et Brink [1] ont effectué les premiers calculs auto-consistents du problème à N-corps nucléaire en utilisant une interaction de Skyrme [2]. Aujourd'hui la méthode de la fonctionnelle de densité (EDF) ou la méthode champ-moyen est toujours utilisée à grande échelle pour étudier la structure nucléaire. Le premier point fort de cette méthode est sa simplicité computationnelle qui permet de l'appliquer dans l'entièreté de la charte nucléaire, des noyaux les plus légers aux éléments super lourds à plus que 250 nucléons [3]. Depuis le début des années 1980, les initiales 'BFH', représentant Paul Bonche, Hubert Flocard et Paul-Henri Heenen, ont signé un grand nombre des papiers depuis 1984 [4, 5]. Ces trois scientifiques sont les auteurs de trois codes numériques iconiques `ev8`, `cr8` et `ev4`. Des versions évoluées de ces codes sont toujours utilisées fréquemment aujourd'hui par des nombreux chercheurs. Au fil des années, deux désavantages de ces trois codes sont apparus. Le premier désavantage est lié à la physique: bien que `ev8`, `ev4`, et `cr8` offrent à l'utilisateur accès à une variété de combinaisons de symétries conservées et brisées, un grand nombre n'est pas accessible. De plus en plus souvent, les applications traitant des noyaux exotiques demandent des calculs champ-moyen qui sont moins limités par les symétries imposées. Le deuxième désavantage est d'une nature plus pratique: le maintien au même niveau d'une combinaison de trois codes qui ont des buts comparables est difficile.

Le projet de mon doctorat était de construire un code qui unifie et généralise les fonctionnalités de `ev8`, `cr8` et `ev4`. Aujourd'hui MOCCa, un acronyme de **M**odular **C**ranking **C**ode, est capable de reproduire toutes les fonctionnalités des codes BFH. De plus, il est maintenant possible d'effectuer des calculs champ-moyen pour un nombre des combinaisons de symétries conservées et brisées, offrant un domaine d'applications énorme. Quatre symétries ont été toujours imposées dans les codes BFH, et sont maintenant toutes soumises au choix de l'utilisateur, qui peut les conserver où les briser indépendamment. Ceci résulte en 16 modes d'opération différents du code, dont tous ont des intérêts physiques pour décrire des phénomènes nucléaires. La déformation octupolaire du ^{224}Ra [6] et les bandes chirales du ^{138}Nd [7] sont des exemples récents d'intérêt expérimental, dont la description théorique est maintenant abordable avec un seul outil. Cet outil fait preuve d'une grande complexité: sur le plan physique, des méthodes ont été développées pour résoudre les équations du champ-moyen en l'absence des symétries facilitant le problème, tandis que sur le plan pratique, le traitement d'un nombre de degrés de liberté non-physiques a eté amelioré. La dernière partie de la thèse, la plus importante probablement du point de vue des futurs collaborateurs, est pour cette raison constituée d'un manuel d'utilisateur. Deux applications de la méthode sont ainsi présentées: la description des transitions de forme dans les isotopes de Radium et une étude de l'évolution des rayons de charge dans la chaîne isotopique du mercure démontrent la viabilité de la méthode.

Acknowledgments

While there is only my own name on the front page of this dissertation, several people merit at least a mention for their role in bringing this work to fruition. For those who do not master either Dutch or French, please forgive me for using the languages of the persons in question[1].
To my jury members that do not figure on the rest of this page: prof. Michel Godefroid, prof. Pierre Descouvemont and prof. Stéphane Goriely from ULB, prof. Piet Van Duppen of KULeuven and prof. Thomas Duguet of the CEA/Saclay (but also partly from KULeuven): thank you for agreeing to read and evaluate this rather long and technical document.
Au centre du calcul de l'ULB (et du VUB) et et le CÉCI en géneral: j'ai pu profiter des vos CPU et vos disques durs (presque) sans problèmes pendant quatre années. Vous avez répondu rapidement et clairement à des nombreux questions de ma part, même les plus idiotes. Merci pour votre support!
To the BriX network, I hope you do not regret your investment. Thank you for taking care of the financial side of things.
To Michael, who does not want to teach, yet has a knack for explaining things very clearly and concisely. In addition, his door has always been open for answering the questions of a poor PhD student who is trying to make sense of things. Thank you for your patience and explanations.
Aan Veerle, die jarenlang naar mijn frustraties geluisterd heeft, zowel tijdens haar tijd aan de ULB als tijdens de laatste maanden van mijn doctoraat. Ik hoop dat ik ook goed geluisterd heb naar je frustraties over het moederschap. Dank je voor het luisteren.
Aan mama, die toch nog steeds de reden is dat ik fysicus en geen wiskundige ben geworden. Aan papa, die blijft luisteren en vragen stellen, ook al begrijpt hij er niets van. Dank je voor de steun van ondertussen bijna 26 jaar.
Aan Kaat, die me is gevolgd naar Brussel en binnenkort ook naar Lyon. Mij delen met fysica is niet makkelijk, en het spijt me van de eenzame uren die je hebt moeten doorstaan tijdens deze laatste maanden. Dank je voor je flauwe humor, je ogen, je begrip, je enthousiasme, je reislust, je haar, je geduld, je speelsheid en soms ook je niet-flauwe humor. Dank je om bij mij te willen zijn.
À Paul-Henri, qui à pris un étudiant perdu de Leuven sous ses ailes. J'ai fait ce que je pouvais pour assimiler tout ce que vous avez essayé de m'apprendre: j'en ai retiré un amour pour le champ-moyen, une connaissance approfondie du français mais aussi une vue plus réaliste (et parfois un peu cynique) du monde. Mais après quatre années, il est clair que je pourrai jamais atteindre la profondeur de votre connaissance de tout ce qui est physique nucléaire. Je m'excuse aussi pour mes moments d'entêtement, et pour le fait que je me suis peut-être trop centré sur l'aspect computationnel au lieu de la physique. Merci pour quatre années de confiance.
Finally, I want to thank you, the reader for making it already this far into this dissertation. I hope it will satisfy your curiosity and I apologize for the places where it might not. In fact, you are likely to discover several such places, as many things in this dissertation are still the subject of ongoing research and I do not pretend to have final answers for everything. This seems to be the eternal curse of research, but we should keep in mind what Richard Feynman once said:

I think it's much more interesting to live not knowing than to have answers which might be wrong.

[1] Except for German, sorry Michael!

Introduction

Mean-field theory with Skyrme functionals In the seventies, Vautherin and Brink [1] were the first to perform self-consistent calculations using an effective interaction from the hand of Skyrme [2] some 14 years earlier. Several decades later energy density functional (EDF) theory or mean-field theory is still a widely used method to study nuclear structure. While functionals have replaced effective interactions in the majority of cases, the spirit of the method remains very much intact: use the variational principle with a very simple ansatz to obtain an approximation to the energy of a nucleus [3].
The main appealing future of modeling nuclear structure in this way is the computational simplicity of the method. Single calculations of limited complexity can in principle be performed on smartphones and already quite involved calculations can be performed on personal computers. More complicated work like the one presented here is only feasible with access to a scientific computing center, but is certainly not among the more demanding applications typical in the academic world. This computational simplicity makes it possible to apply the model to any nucleus, regardless of mass, in stark contrast to other microscopic models that are often limited to light nuclei.
The greatest strength of density functional theory is also one of its weaknesses: the simplicity of the variational ansatz. Already one year after the first paper, Vautherin [8] published an extended calculation without the rotational symmetry that was assumed in his previous work. The breaking of symmetries in mean-field theory is a practical way of on one hand maintaining the simplicity of the variational ansatz, while on the other hand enlarging the variational space and greatly enhancing the power of the method. This dissertation is in that sense a direct continuation of this work: understanding the consequences of conserved symmetries and enlarging the grasp of mean-field models by lifting the restrictions they impose.

EV8, CR8 and EV4 Since the start of the eighties, my advisor prof. Heenen has been working on mean-field theory together with a variety of people in Brussels and abroad. In particular the famous 'BFH' initials, standing for Paul Bonche, Hubert Flocard and Heenen, have been signed on a great number of papers since 1984. They are the original authors of the original tools-of-the-trade computer codes named `ev8`, `cr8` and `ev4`[2]. Today, evolved versions of these three codes are still in frequent use.
Of these, `ev8` is the original template on which the other two codes are based. It represents the wavefunctions on a 3D coordinate mesh [9, 10] and solves the mean-field equations without any rotational symmetry assumption. Several point-symmetries, such as parity, however still are conserved, resulting in a code that is very modest in its CPU time requirements today, even though it was very demanding in 1984. `ev4` is based on the exact same principle as `ev8`, and differs solely in the assumption of parity: `ev8` assumes the solution to be invariant under parity, while `ev4` does not. `cr8` is another variation on the theme of `ev8`, this time `cr8` does not respect time-reversal invariance while `ev8` does. Breaking the symmetries of parity and time-reversal results in an extra layer of complexity for `ev4` and `cr8` compared to `ev8`, but consequently also a greater range of application.

MOCCa The combination of these three codes are at the base of a large body of work by many people, spanning several decades. Over the years two drawbacks of the triumvirate of codes have become apparent.
The first is rooted in the physics: while `ev8`, `cr8` and `ev4` offer the user access to various combinations of conserved and broken symmetries, the coverage is far from complete. More and more, applications to exotic nuclei demand mean-field wavefunctions that are less restricted by symmetry. A more general approach is thus needed in order to enlarge the reach of the methods (and the associated experience) encoded in the BFH mean-field codes. An option of course would have been to simply write an additional code for every interesting symmetry combination, but this is sheer madness given the amount of possibilities.
A second drawback is more rooted in the practical world: a set of three computer codes is needlessly hard to maintain. Any new development (say, a new term in the functional) would have been coded and debugged

[2]Other mean-field codes have also seen some use, but these three really are the 'flagships'.

(at least) three times, respecting for every code the quirks that had evolved over the years. Of course, in practice this meant that various features were implemented and tested in one code and afterwards did not (or only partially) find their way into the other codes.
The project for my dissertation was thus born: constructing a computer code that united and extended the possibilities of the flagship codes. Now, at the end of my PhD, it exists and is called MOCCa, for **M**odular **C**ranking **C**ode. The only function of the final **a** is to make the acronym memorable. In hindsight, the other parts of the acronym are not too indicative either: cranking is but one aspect of the code, while modular just indicates that I did my best to keep everything tidy, organized and extensible.
At this point in time, MOCCa is able to recreate any result of the flagship codes obtained before the start of my PhD[3]. On top of that, the code offers the user an unprecedented freedom with regards to symmetries imposed on the wavefunctions. While it turned out that there are relevant symmetry combinations that MOCCa cannot access, the application range of the current version is already staggering.
MOCCa consists at the moment of slightly more than 32000 lines of FORTRAN code. Arguably the most advanced flagship code, cr8, consisted of slightly less than 16000 lines in its version 1.6.9[4]. A software project of this size and complexity is difficult to keep track of and keep understandable to less involved users. For this reason I have opted to include in this dissertation rather complete discussions of many numerical aspects of the solving algorithms in the code. While a significant portion of these are only slightly adapted from the older codes, I feel that their inclusion here is quite valuable if only to gather and expand their documentation, so that the poor PhD student that one day employs the code needs to spend less time trying to understand arcane computational details.

Organisation This dissertation is composed of four parts. Part I aims to introduce the reader to self-consistent calculations in nuclear mean-field theory. Chapter 1 introduces Hartree-Fock calculations and the Skyrme energy density functional. Chapter 2 introduces the concept of self-consistent symmetries, the symmetry groups we are mainly interested in as well as the physical motivation for not respecting those symmetries. Chapter 3 introduces the HFB ansatz as way to introduce pairing into the many-body wavefunctions from chapter 1. Part II discusses the implementation of MOCCa. Chapter 4 discusses how we represent the nuclear wavefunctions and how we solve the mean-field equations. We outline how we generate and control symmetry breaking configurations in chapter 5. The following chapter in this part, chapter 6 details how the pairing equations from chapter 3 can be solved in practice. During this PhD, a lot of time was spent on ensuring MOCCa could reproduce the older codes and so in Chapter 7 some tests of MOCCa are presented. The final chapter in this part deals with the numerical accuracy of the suite of mean-field codes, ev8, ev4, cr8 and MOCCa. An extensive study was published and is attached. Part III deals with applications of the framework discussed in the previous parts. Chapter 9 shows the capabilities of MOCCa in a proof-of-concept study of a number of Radium isotopes. The second chapter of this part, chapter 10 details a series of calculations along the isotopic chain, focusing on the rms charge radii of these nuclei. The final part, part IV, consists of a single chapter: a manual for MOCCa. It is perhaps the most important chapter of all, as MOCCa is a complex code, that is unfortunately still hard to use.

[3]Some developments were made during my PhD that still have to find their way into MOCCa.

[4]V1.6.9 is a rather old version, and the latest version of cr8 consists of slightly more than 30000 lines of code. Nevertheless, I feel justified comparing to v1.6.9 since automated computer scripts wrote a large part of those roughly 14000 lines of difference

Part I

Skyrme energy density functional theory

Chapter 1

The Hartree-Fock approach

This first chapter will deal with the basics of everything that follows: the Hartree-Fock method applied to the nuclear many-body problem. The initial sections introduce the formal background of the variational calculations which `MOCCa` performs. These sections are heavily indebted to [11, 12] and the interested reader will have no trouble to find other excellent introductions to the subject both in nuclear structure and in other fields. After this introduction we will specify more precisely to the nuclear problem and the concept of Skyrme energy density functionals (EDFs).
Section 1.1 will introduce the problem and the concept of Slater determinants, while section 1.2 introduces formally the variational procedure that is at the heart of dissertation. The single-particle wavefunctions that are the fundamental variables of the Hartree-Fock method are further specified in section 1.3. The Skyrme energy density functional and its various constituents will be introduced in section 1.4. Some remarks on the strong and weak points of the method are collected in section 1.5, while configuration mixing as a beyond-mean-field procedure is introduced briefly in section 1.6.

1.1 The nuclear many-body problem: Slater determinants

Let us consider the nuclear many-body problem, with Hamiltonian $\hat{\mathcal{H}}$. We would like to solve the static Schrödinger equation exactly for the many-body wavefunction Ψ of a given nucleus with A nucleons, of which Z are protons and N are neutrons. Solving the many-body problem means then that we would like to find the eigenstates of the many-body Hamiltonian $|\Psi_i\rangle$ so that

$$\hat{\mathcal{H}}|\Psi_i\rangle = E_i|\Psi_i\rangle \qquad i = 1, 2, \dots . \tag{1.1}$$

Note that we use capital Greek letters for many-body wavefunctions and calligraphic letters for many-body operators. We will not specify the Hamiltonian $\hat{\mathcal{H}}$ for now, and neither will we specify any symmetries of either the Hamiltonian or the many-body wavefunctions, and we leave the indexing integer i undefined. This introduction aims to introduce the most general problem, that can later be amended by specifying a specific form for $\hat{\mathcal{H}}$, which might exhibit some particular many-body symmetries.
Consider a complete orthonormal basis of single-particle states $|\phi_\ell\rangle$, indexed by an integer ℓ. Note that we will always use lowercase Greek letters for single-particle wavefunctions. For each of these single-particle states we have a corresponding creation and annihilation operator $\hat{a}_l^\dagger, \hat{a}_l$. Since we are dealing with protons and neutrons, the $|\phi_l\rangle$ are two-component spinors representing spin $\frac{1}{2}$ fermions. The creation and annihilation operators consequently obey the following fermionic commutation relations

$$\begin{aligned} \left\{\hat{a}_i, \hat{a}_j\right\} &= 0\,, \\ \left\{\hat{a}_i^\dagger, \hat{a}_j^\dagger\right\} &= 0\,, \\ \left\{\hat{a}_i, \hat{a}_j^\dagger\right\} &= \delta_{ij}\,. \end{aligned} \tag{1.2}$$

Consider the vacuum $|0\rangle$. By simply acting on it with creation operators A times, we get an A-body state $|\Psi_{\text{Slater}}\rangle$

$$|\Psi_{\text{Slater}}\rangle = \prod_{l=1}^{A} \hat{a}_l^\dagger |0\rangle\,. \tag{1.3}$$

This kind of many-body wavefunction is called a Slater determinant. We call the single-particle states in the chosen basis occupied if they enter the product in Eq. (1.3) and unoccupied otherwise. It is important to notice that a Slater determinant is completely determined by the set of occupied levels. Note that we cannot allow an index l to be repeated in Eq. (1.3): this would correspond to occupying a given level twice and thus annihilating the resulting Slater determinant.

An important object is the density matrix $\hat{\rho}$ of a many-body state, which is a single-particle operator. The simplest way to define it is through its matrix elements in the basis of the single-particle states

$$\rho_{ij} = \langle \Psi | \hat{a}_j^\dagger \hat{a}_i | \Psi \rangle \,. \tag{1.4}$$

The density matrix takes on a rather specific form when dealing with Slater determinants

$$\hat{\rho} = \sum_{l=1}^{A} |\phi_l\rangle\langle\phi_l| \,, \tag{1.5}$$

where the $|\phi_l\rangle$ in the sum are the occupied levels of the Slater determinant. This means that $\hat{\rho}$ is a projector, so that

$$\hat{\rho}^2 = \hat{\rho} \,. \tag{1.6}$$

We can thus deduce from the density matrix the set of occupied levels of the Slater determinant: they are precisely the eigenstates of $\hat{\rho}$ with eigenvalue equal to 1.

1.2 Selecting the best Slater Determinant: Hartree-Fock equations

The Hilbert space of the quantum-mechanical many-body problem is mind-bogglingly big: some simplification is needed so that we even might start making a chance to solve it. This is the main interest of the Slater determinants introduced in the previous section: their simplicity. The space of all Slater determinants makes up only a very small part of the total Hilbert space[1] and we can simplify the nuclear many-body problem greatly by restricting ourselves to only the many-body states that are Slater determinants.
It is idle hope however that the eigenstates of the many-body Hamiltonian $\hat{\mathcal{H}}$ will be Slater determinants: the space of Slater determinants is too small to contain the exact solution $|\Psi_{\text{exact}}\rangle$. We can however look for an optimal Slater determinant that best approximates the ground-state of the system. We now define the Hartree-Fock energy of a Slater determinant $|\Psi_{\text{Slater}}\rangle$ as

$$E_{\text{HF}} = \langle \Psi_{\text{Slater}} | \hat{\mathcal{H}} | \Psi_{\text{Slater}} \rangle \,. \tag{1.7}$$

The variational principle now guarantees us that the lowest E_{HF} we can find is an upper bound for the energy of the true ground state of $\hat{\mathcal{H}}$. Using variational calculus, we can write this problem as

$$\delta E_{\text{HF}} = \delta \langle \Psi | \hat{\mathcal{H}} | \Psi \rangle = 0 \,, \tag{1.8}$$

where the variation is over all possible Slater determinants. It turns out that the condition that determines the Slater determinant [11] with the lowest Hartree-Fock energy is

$$\left[\hat{h}, \hat{\rho}\right] = 0 \,, \tag{1.9}$$

where we also define the single-particle Hamiltonian $\hat{h}$ as

$$h_{ij} = \frac{\partial E_{\text{HF}}(\rho)}{\partial \rho_{ji}} \,. \tag{1.10}$$

Eq. (1.9) has as major implication that $\hat{h}$ and $\hat{\rho}$ can be diagonalized simultaneously. The single-particle basis in which both are diagonal is called the Hartree-Fock basis[2]. In this basis Eq. (1.9) corresponds to an eigenvalue problem

$$h_{ij} = \epsilon_i \delta_{ij} \,. \tag{1.11}$$

Note that this equation determines the eigenstates of $\hat{h}$ and thus the entire Hartree-Fock basis. But it is still up to us to choose which of the single-particle states in the resulting basis to occupy, meaning that we can still build several Slater determinants out of all the basis vectors. Occupying the lowest-lying single-particle states will (in general) result in the ground state, and different choices of occupation will lead to excited states.
Unfortunately, the optimal $\hat{h}$ from Eq. (1.10) depends on the particular many-body state under consideration (through $\hat{\rho}$) and as such the problem posed by the combination of Eqs. (1.9) and (1.10) is very much nontrivial

[1] In fact, the Slater determinants form an infinite-dimensional basis of the complete Hilbert space.
[2] Strictly speaking the variation of Eq. (1.9) has as subsidiary condition that the single-particle states in the Slater determinants should be orthonormal.

```
Guess initial Slater Determinant |Ψ^(0)⟩
while [ĥ^(i), ρ̂^(k)] ≠ 0 do
    Compute density matrix ρ̂^(i)
    Compute single-particle Hamiltonian ĥ^(i) (ρ̂)
    Find levels φ_i^(i) by diagonalizing ĥ^(i)
    Choose A levels to occupy
    Construct new Slater Determinant |Ψ^(i)⟩
    i = i + 1
end
```

Algorithm 1: Schematic algorithm for the solution of the Hartree-Fock equations.

to solve. Problems like these are often called self-consistent equations and we can only hope to solve them through an iterative scheme. Schematically one proceeds as in algorithm 1: starting with an initial guess one proceeds at iteration (i) by diagonalizing $\hat{h}^{(i)}$ to get new single-particle wavefunctions $|\phi_i^{(i)}\rangle$. With a specific choice of occupation, they generate a Slater determinant $|\Psi^{(i)}\rangle$ which in turns gives rise to $\hat{h}^{(i+1)}$. When this process returns the same Slater determinant, that is to say $|\Psi^{(i)}\rangle \approx |\Psi^{(i+1)}\rangle$, one has reached self-consistency and we have solved the Hartree-Fock equations. In practice, however, Algorithm 1 is far from a practical manual to solve the Hartree-Fock equations. We will enter in great detail how `MOCCa` solves the equations in chapter 4.

1.3 Single-particle states

Some more comments are in order on the subject of the single-particle states $|\phi_l\rangle$. The above discussion can be applied to the general quantum-many-body system, but we will now specify somewhat to the nuclear problem. Important coordinates for the single-particle wavefunctions in this case are not only the spatial coordinate $\mathbf{r}$, but also the spin coordinate σ and the isospin coordinate q. The full dependency of the single-particle wavefunctions in coordinate space is thus

$$\phi_l\left(x, y, z, \sigma, q\right) \text{ with } \sigma = \pm 1\,, q = \pm 1. \tag{1.12}$$

Note that it is not a priori clear that the single-particle wavefunctions correspond to definite isospin: definite neutron or proton single-particle wavefunctions. The components of the $|\phi_l\rangle$ can thus simultaneously be non-zero for both $q = +1$ and $q = -1$. We will often drop the isospin index q to a subscript where practical to lighten the notation.

It is important to stress that the complete set of occupied orbitals $|\phi_l\rangle$ completely determine the density matrix $\hat{\rho}$ of a Slater determinant. The density matrix in turn completely specifies a given Slater determinant $|\Psi_{HF}\rangle$ up to an overall phase. This implies that it is in fact very natural (and practical) to consider them (and their values in coordinate-spin-isospin space) as the degrees of freedom of the variational problem Eq. (1.8). The actual implementation of `MOCCa` will greatly depend on this, see chapter 4.

A result that will be significant in chapter 2 is the following: Slater determinants are invariant under unitary transformations that do not mix occupied and unoccupied states. Indeed, suppose we transform the single particle states $|\phi_i\rangle$ with a unitary transform $\hat{U}$ into single-particle states $|\chi_j\rangle$ we get for the new density matrix ρ'

$$\hat{\rho} = \sum_{i=1}^{A} |\phi_i\rangle\langle\phi_i| = \sum_{i=1}^{A}\sum_{j=1}^{A}\sum_{k=1}^{A} U_{ji}|\chi_j\rangle\langle\chi_k|U^*_{ki} = \sum_{j=1}^{A} |\chi_j\rangle\langle\chi_j| = \hat{\rho}' \tag{1.13}$$

where we have used in the second equality that $\hat{U}$ is a unitary transformation by explicitly taking the sum over index i. Since this transformation leaves $\hat{\rho}$ invariant, it will also leave the Slater determinant $|\Psi\rangle$ invariant (up to a phase).

1.4 The Skyrme energy density functional

Let us now focus on the nuclear Hamiltonian $\hat{\mathcal{H}}$ that we left unspecified before. Since nucleons are composite particles made of quarks that interact by the strong interaction, we need to content ourselves with a model for $\hat{\mathcal{H}}$, an effective interaction $\hat{\mathcal{H}}_{\text{eff}}$. In fact, we don't even need that: notice that Eqs. (1.9) and (1.10) only directly reference its expectation value $\langle\hat{\mathcal{H}}_{\text{eff}}\rangle$. A formula that models E_{HF} (and its derivative, the single-particle Hamiltonian) is all we need to solve the Hartree-Fock equations. The Skyrme energy density functional is exactly such a model. We will split it into four different terms [10]

$$E_{\text{HF}} = E_{\text{Kin}} + E_{\text{Coul}} + E_{\text{Skyrme}} + E_{\text{Corr}}\,. \tag{1.14}$$

In this decomposition E_{Kin} is the kinetic energy and E_{Coul} is the energy due to the Coulomb repulsion of the protons in the nucleus. E_{Skyrme} is the Skyrme part of the functional, aiming to provide an effective way to capture the effect of the strong interaction in the nucleus. The term E_{Corr} is a collection of different possible corrections to the energy. We will come back in detail to every term in the following sections.
The three first terms of the Hartree-Fock energy can be written as integrals over energy densities, meaning that all of these three terms can be written as

$$E_i = \int d\mathbf{r}\,\mathcal{E}_{\text{i}}(\mathbf{r})\,. \tag{1.15}$$

The quantities $\mathcal{E}_i(\mathbf{r})$ are functions in position space, meaning that the terms E_i become functionals: thus the nomenclature of the energy density functional. Aside from the Coulomb contribution, the kinetic and Skyrme energy density are local functions, as they depend only on a single space-coordinate $\mathbf{r}$. This locality presents an enormous advantage for every practical calculation of E_{HF} as the numerical cost of evaluating Eq. (1.14) is quite modest[3]. The Coulomb term of course is not local, as the Coulomb interaction has infinite range and involves a double integral over coordinate space.
This locality of the Skyrme energy density is historically based on a zero-range effective interaction $\hat{v}_{\text{Skyrme}}$ that contributed to an effective many-body Hamiltonian $\hat{\mathcal{H}}_{\text{eff}}$. Many terms in Eq.(1.14) are directly inspired by contributions of this type of interaction to the expectation value of $\hat{\mathcal{H}}_{\text{eff}}$. However, the prescription we will present can no longer be related to an expectation value of a many-body Hamiltonian. Many widely used functionals that perform well on the mean-field level share this characteristic, even though it is very much a problem for beyond-mean-field calculations [14, 15, 16].
Although a detailed discussion of the Skyrme EDF is outside of the scope of this work, a note is in order on how particular functionals are constructed. People wishing to construct a new functional have two main things to do: first determine the terms in the functional they want to include and what parameters control them. The first step concerns many choices: which Skyrme terms to allow? Do we include pairing in the fit? If so, what kind? Should the functional be derived from a many-body Hamiltonian or not? After fixing all of these (and many more) choices, the coupling constants that govern the terms should be fitted to a suitable set of experimental data. Most of the time the experimental data in question are the binding energies and mean-square radii of (doubly-)magic nuclei [17] and properties of the interaction in infinite nuclear matter. Other observables can in principle be included but are more rare, such as fission barrier heights in [18].
A final remark is in order before specifying the terms in Eq. (1.14). The particular form of the Skyrme EDF that will be presented here does not in any way represent the simplest, nor the most general, nor the most widely accepted form of a Skyrme EDF. It simply corresponds to the type of functionals that `cr8` was able to handle in 2012 [19], which form is sufficient to treat many of the more widely used functionals in recent history, see Appendix A. Note that the more recent type of functionals respecting the connection with many-body Hamiltonians such as SLyMR0 [16] are not incorporated yet.

[3] Functionals using non-local energy densities (and consequently non-local mean-field densities) exist, for a recent example see [13].

1.4.1 Mean-field densities

Before we move on to specify the terms of the functional further, we will introduce the mean-field densities as functions in coordinate-isospin space that characterize a particular Slater determinant

$$\rho_q(\mathbf{r}) = \sum_{j,\sigma} \phi_j^*(\mathbf{r},\sigma,q)\phi_j(\mathbf{r},\sigma,q) \tag{1.16a}$$

$$\tau_q(\mathbf{r}) = \sum_{j,\sigma} \left[\boldsymbol{\nabla}\phi_j^*(\mathbf{r},\sigma,q)\right]\cdot\left[\boldsymbol{\nabla}\phi_j(\mathbf{r},\sigma,q)\right] , \tag{1.16b}$$

$$J_{\mu\nu,q}(\mathbf{r}) = \frac{1}{2i}\sum_{\sigma_1,\sigma_2}\sigma_{\nu,\sigma_1,\sigma_2}\sum_j \left[\phi_j^*(\mathbf{r},\sigma_1,q)\right]\left[\nabla_\mu\phi_j(\mathbf{r},\sigma_2,q)\right] - \left[\nabla_\mu\phi_j^*(\mathbf{r},\sigma_1,q)\right]\left[\phi_i(\mathbf{r},\sigma_2,q)\right] , \tag{1.16c}$$

$$s_{\mu,q}(\mathbf{r}) = \sum_{j,\sigma_1,\sigma_2}\sigma_{\mu,\sigma_1,\sigma_2}\phi_j^*(\mathbf{r},\sigma_1,q)\phi_j(\mathbf{r},\sigma_2,q) , \tag{1.16d}$$

$$j_{\mu,q}(\mathbf{r}) = \frac{1}{2i}\sum_{j,\sigma}\left[\phi_j^*(\mathbf{r},\sigma,q)\right]\left[\nabla_\mu\phi_j(\mathbf{r},\sigma,q)\right] - \left[\nabla_\mu\phi_j^*(\mathbf{r},\sigma,q)\right]\left[\phi_j(\mathbf{r},\sigma,q)\right] , \tag{1.16e}$$

$$T_{\mu,q}(\mathbf{r}) = \sum_{j,\sigma_1,\sigma_2}\sigma_{\mu,\sigma_1,\sigma_2}\left[\boldsymbol{\nabla}\phi_j^*(\mathbf{r},\sigma_1,q)\right]\cdot\left[\boldsymbol{\nabla}\phi_j(\mathbf{r},\sigma_2,q)\right] , \tag{1.16f}$$

$$F_{\mu,q}(\mathbf{r}) = \frac{1}{2}\sum_{\nu,\sigma_1,\sigma_2}\sigma_{\nu,\sigma_1,\sigma_2}\sum_j \left[\nabla_\mu\phi_j^*(\mathbf{r},\sigma_1,q)\right]\left[\nabla_\nu\phi_j(\mathbf{r},\sigma_2,q)\right] + \left[\nabla_\nu\phi_j^*(\mathbf{r},\sigma_1,q)\right]\left[\nabla_\mu\ \phi_j(\mathbf{r},\sigma_2,q)\right] . \tag{1.16g}$$

Where $q = n, p$ is an isospin index, the Greek indices μ, ν range over the Cartesian directions x, y, z and the $\sigma_{\mu,\sigma_1,\sigma_2}$ are the matrix elements of the Pauli matrices. The mean-field density ρ is simply called the density, while τ is the kinetic density and $J_{\mu\nu}$ is often called the spin-current density. The densities $\mathbf{s}, \mathbf{j}, \mathbf{T}$ and $\mathbf{F}$ are respectively called the spin density, current density, spin-kinetic density and tensor-kinetic density [20]. The only single-particle wavefunctions $|\phi_j\rangle$ that enter the sums in these definitions are the occupied orbitals in the Hartree-Fock basis.
The total density $\rho_t(\mathbf{r})$ as well as the isoscalar $\rho_0(\mathbf{r})$ and isovector density $\rho_1(\mathbf{r})$ will make frequent appearances:

$$\rho_t(\mathbf{r}) = \rho_0(\mathbf{r}) = \rho_n(\mathbf{r}) + \rho_p(\mathbf{r}) , \qquad \rho_1(\mathbf{r}) = \rho_n(\mathbf{r}) - \rho_p(\mathbf{r}) . \tag{1.17}$$

When no subscript is specified, it is the total density that is implied. Similar definitions of course hold for all of the mean-field densities above.
The following alternative notations for parts of the tensor density $J_{\mu\nu}$ that will be used throughout the text are

$$J^{(0)}(\mathbf{r}) = \sum_{\mu=x,y,z} J_{\mu\mu}(\mathbf{r}) , \tag{1.18a}$$

$$J^{(1)}_\kappa(\mathbf{r}) = \sum_{\mu,\nu=x,y,z}\epsilon_{\kappa\mu\nu}J_{\mu\nu}(\mathbf{r}) , \tag{1.18b}$$

$$J^{(2)}_{\mu\nu}(\mathbf{r}) = \frac{1}{2}\left[J_{\mu\nu}(\mathbf{r}) + J_{\nu\mu}(\mathbf{r})\right] - \frac{1}{3}\delta_{\mu\nu}J^{(0)}(\mathbf{r}) . \tag{1.18c}$$

Note that $J^{(0)}, J^{(1)}$ and $J^{(2)}$ correspond to the decomposition of the tensor $J_{\mu\nu}$ into a pseudoscalar, vector and symmetric traceless tensor [21].

1.4.2 The kinetic energy density $\mathcal{E}_{\mathsf{Kin}}$

The kinetic energy density is given by

$$\mathcal{E}_{\mathsf{Kin}}(\mathbf{r}) = \sum_{q=n,p}\frac{\hbar^2}{2m_q}\tau_q(\mathbf{r}) , \tag{1.19}$$

where m_q is the nucleon mass. Note that the majority of Skyrme parameterizations do not use the physical nucleon masses but rather set m_q to the average of the physical masses, rendering the kinetic energy an isoscalar.

1.4.3 The Skyrme contribution $\mathcal{E}_{\text{Skyrme}}$

The most general form of the Skyrme energy density $\mathcal{E}_{\text{Skyrme}}$ that can be used in MOCCa is [22, 21, 23, 19, 10]

$$\begin{aligned}
\mathcal{E}_{\text{Skyrme}} &= \mathcal{E}^t_{\text{Skyrme}} + \sum_{q=p,n} \mathcal{E}^q_{\text{Skyrme}}\,,\\
\mathcal{E}^t_{\text{Skyrme}}(\mathbf{r}) &= B_1\rho_t^2 + B_3\left(\rho_t\tau_t - \mathbf{j}_t^2\right) + B_5\rho_t\Delta\rho_t + B_{7a}\rho_t^{2+\alpha_a} + B_{7b}\rho_t^{2+\alpha_b} + B_9\left(\rho_t\nabla\cdot\mathbf{J}_t + \mathbf{j}_t\cdot\nabla\times\mathbf{s}_t\right)\\
&\quad + B_{10}\mathbf{s}_t^2 + B_{12a}\rho_t^{\alpha_a}\mathbf{s}_t^2 + B_{12b}\rho_t^{\alpha_b}\mathbf{s}_t^2 + B_{14}\left(\sum_{\mu,\nu=x,y,z} J_{t,\mu\nu}J_{t,\mu\nu} - \mathbf{s}_t\cdot\mathbf{T}_t\right)\\
&\quad + B_{16}\left[\left(\sum_{\mu=x,y,z} J_{t,\mu\mu}\right)^2 + \sum_{\mu,\nu} J_{t,\mu\nu}J_{t,\nu\mu} - 2\mathbf{s}_t\cdot\mathbf{F}_t\right] + B_{18}\mathbf{s}_t\cdot\Delta\mathbf{s}_t + B_{20}\left(\boldsymbol{\nabla}\cdot\mathbf{s}_t\right)^2\,,\\
\mathcal{E}^q_{\text{Skyrme}}(\mathbf{r}) &= B_2\rho_q^2 + B_4\left(\rho_q\tau_q - \mathbf{j}_q^2\right) + B_6\rho_q\Delta\rho_q + B_{8a}\rho_t^{\alpha_a}\rho_q^2 + B_{8b}\rho_t^{\alpha_b}\rho_q^2 + B_{9q}\left(\rho_q\nabla\cdot\mathbf{J}_q + \mathbf{j}_q\cdot\nabla\times\mathbf{s}_q\right)\\
&\quad + B_{11}\mathbf{s}_q^2 + B_{13a}\rho_t^{\alpha_a}\mathbf{s}_q^2 + B_{13b}\rho_t^{\alpha_b}\mathbf{s}_q^2 + B_{15}\left(\sum_{\mu,\nu=x,y,z} J_{q,\mu\nu}J_{q,\mu\nu} - \mathbf{s}_q\cdot\mathbf{T}_q\right)\\
&\quad + B_{17}\left[\left(\sum_{\mu=x,y,z} J_{q,\mu\mu}\right)^2 + \sum_{\mu,\nu} J_{q,\mu\nu}J_{q,\nu\mu} - 2\mathbf{s}_q\cdot\mathbf{F}_q\right] + B_{19}\mathbf{s}_q\cdot\Delta\mathbf{s}_q + B_{21}\left(\boldsymbol{\nabla}\cdot\mathbf{s}_q\right)^2\,.
\end{aligned} \tag{1.20}$$

The coupling constants B_1 through B_{21} and the density dependence parameters α_a and α_b are in principle free parameters of the functional.

1.4.4 The Coulomb energy density $\mathcal{E}_{\text{Coul}}$

The energy density associated with the Coulomb field can be split into two parts, the direct term and the exchange term, and is given by [10]

$$\mathcal{E}_{\text{Coul}}(\mathbf{r}) = \mathcal{E}^{\text{dir.}}_{\text{Coul}} + \mathcal{E}^{\text{exch.}}_{\text{Coul}}\,, \tag{1.21a}$$

$$\mathcal{E}^{\text{dir.}}_{\text{Coul}}(\mathbf{r}) = \frac{e^2}{2}\int d\mathbf{r}'\frac{\rho_p(\mathbf{r})\rho_p(\mathbf{r}')}{|\mathbf{r}-\mathbf{r}'|}\,, \tag{1.21b}$$

$$\mathcal{E}^{\text{exch.}}_{\text{Coul}}(\mathbf{r}) = -\frac{3e^2}{4}\left(\frac{3}{\pi}\right)^{1/3}\rho_p^{4/3}(\mathbf{r})\,, \tag{1.21c}$$

were e is the charge of the proton. The direct term is simply the classical electrostatic energy density of a charge density given by $\rho_p(\mathbf{r})$. The actual calculation of this contribution is not trivial. We will elaborate in part II on how to do it in practice.
The exchange term is the quantum-mechanical correction due to the antisymmetrization of the many-body wavefunction. The expression given here for the exchange term is in fact already an approximation usually called the Slater approximation, as the full formula would be extremely costly to evaluate numerically. The Slater approximation suffices for our purposes, and introduces an error on the order of few percent on the Coulomb exchange energy [3, 24].
Using the local proton density to generate the Coulomb field is not completely rigorous and a more complete calculation should take into account the finite charge radius of the proton. This is however not usually incorporated into mean-field theories but can in principle be done [3].

1.4.5 The correction term

Several authors impose extra phenomenological corrections to the functional in a term we will denote E_{Corr}. This term can encompass many different contributions that authors have wished to include. A rotational correction [13] is a typical example, as is the Wigner energy [25, 26]. In general this term aims to approximatively take into account the effect of restoring the symmetries broken in the calculation, see section 1.6.
The centre-of-mass correction [10] is one example that is very often incorporated and is implemented partially in MOCCa. Since any computational method necessarily locates the wavefunction of the nucleus in space, the

resulting breaking of the translational invariance implies some admixture of finite momenta to the nuclear ground state. To remove this effect one can add a term E_{cm} to the functional

$$E_{\mathsf{cm}} = -\sum_{q=n,p} \frac{1}{2M} \langle \hat{\mathcal{P}}_q^2 \rangle = E_{\mathsf{cm},1} + E_{\mathsf{cm},2}\,, \tag{1.22}$$

where $M = Zm_p + Nm_n$ is the total mass of all the nucleons and $\hat{\mathcal{P}}_q$ is the total momentum operator of particle species q. One typically separates this into two contributions, called respectively one-body and two-body centre-of-mass correction.

$$E_{\mathsf{cm},1} = \frac{\hbar^2}{2M} \sum_j \langle \phi_j | \boldsymbol{\nabla}^2 | \phi_j \rangle\,, \tag{1.23}$$

$$E_{\mathsf{cm},2} = \frac{\hbar^2}{2M} \sum_{j,k} |\langle \phi_k | \boldsymbol{\nabla} | \phi_j \rangle|^2\,, \tag{1.24}$$

where the sums are again over the occupied states in a Hartree-Fock basis. Various parameterizations use only $E_{\mathsf{cm},1}$, while others use the full E_{cm} (examples of both can be found in [17]), while still others prefer not to use it at all [18][4]. Note that `MOCCa` is currently equipped to deal with the one-body centre-of-mass term only. The inclusion of $E_{\mathsf{cm},2}$ is straightforward to implement, and was simply omitted due to time constraints.

1.5 Advantages and disadvantages of the density functional method

The mean-field scheme and in particular the Hartree-Fock scheme are not new: they have been established in a variety of fields with much success. The main interest of the approach is the numerical complexity or rather the absence of it: the variational space of Slater determinants is enormously smaller than the full Hilbert space of the many-body problem. It is not hard to see that Algorithm 1 is essentially linear in the number of particles A: for every particle we need to find an occupied single-particle level by diagonalizing $\hat{h}$.[5] The locality of the Skyrme functional further helps to keep the computational cost limited.

For the nuclear many-body problem this translates to a large range of applicability. One can solve the Hartree-Fock equations with reasonable computational effort from the lightest nuclei up to the super-heavy elements $A \approx 250$ and far beyond. This stands in strict contrast to other microscopic approaches. Among them are the shell model (nuclei not too far from magic numbers for large A, like ^{208}Pb and ^{210}Bi [28]), and various ab initio approaches such as in-medium similarity normalization group and coupled cluster theory (calculations up to $A \approx 132$[29, 30, 31]). Although all of them will enormously benefit from increases in computer power in the future and will be able to severely extend their reach, the size of their variational space grows extremely fast with increasing particle number and it will be a long time before they cover the entirety of the nuclear chart.

The price to pay for this computational tractability is simplicity of the variational ansatz: the Slater Determinant. It is very much the ultimate independent-particle wavefunction. Apart from the antisymmetrization inherent for fermions, one can imagine every individual nucleon to occupy a definite orbital level. It is clear that this is an enormous simplification of the picture, as this implies that Slater determinants cannot capture any kind of additional correlations between the nucleons. For many nuclei, correlations play an important role and it is clear that any Slater determinant will constitute a rather bad approximation to the exact nuclear many-body wavefunction. We will partly remedy this situation by enlarging the variational space in chapters 2 and 3, but this will remain a weak point of the EDF method.

[4] Note that parameterizations that have been fitted with differing schemes have very different properties, see [27]. It is most important when using a certain parameterization to use the corresponding correction.

[5] You might argue that the diagonalization of $\hat{h}$ is not linear in the number of particles, but it is still polynomial. Most other microscopic methods scale far worse than polynomial in the number of particles.

1.6 Beyond-mean-field: Configuration mixing with the generator coordinate method

A (formally) simple way of improving the mean-field wavefunctions obtained by solving the mean-field equations consists of allowing for superpositions of mean-field states [3]. Consider a collection of mean-field many-body states $|\Psi(\theta)\rangle$ that can be indexed by the variable θ, which is usually called the generator coordinate. θ can in principle be any kind of quantity and primarily serves to distinguish the different mean-field states.
One then proposes the ansatz

$$|\Psi_{\mathsf{GCM}}\rangle = \int d\theta f(\theta)|\Psi(\theta)\rangle\,. \tag{1.25}$$

Varying with respect to the weight function $f(\theta)$ then leads to the Hill-Wheeler equation

$$\int d\theta' \left[\mathcal{H}_{\mathsf{GCM}}(\theta',\theta) - E\,\mathcal{I}_{\mathsf{GCM}}(\theta',\theta)\right] f(\theta') = 0\,, \tag{1.26}$$

where $\mathcal{H}_{GCM}(\theta',\theta)$ and $\mathcal{I}_{GCM}(\theta',\theta)$ are called the Hamiltonian and norm matrix respectively and are given by

$$\mathcal{H}_{\mathsf{GCM}}(\theta',\theta) = \langle\Psi(\theta')|\hat{\mathcal{H}}|\Psi(\theta)\rangle\,, \tag{1.27a}$$
$$\mathcal{I}_{\mathsf{GCM}}(\theta',\theta) = \langle\Psi(\theta')|\Psi(\theta)\rangle\,. \tag{1.27b}$$

Even attempting to sketch how to solve these equations is far beyond the aim of this text. Suffice it to say that the $|\Psi_{GCM}\rangle$ resulting from this procedure is far richer than the ingredient wavefunctions $|\Psi(\theta)\rangle$: it contains many more correlations as a consequence of being a superposition of a large number of comparatively simple states.
There are no general restrictions on the choice of the generator coordinate q and the corresponding wavefunctions $|\Psi(\theta)\rangle$, other than that they should be motivated by the physics that one wishes to study. Popular choices for q include expectation values of multipole operators $\hat{\mathcal{Q}}_{\ell m}$ (especially the quadrupole moments $\ell = 2$ [32, 33]), as well as a Cartesian projection of the angular momentum $\langle\hat{\mathcal{J}}_\mu\rangle$ [34].
We will not make use of this framework in this dissertation and stay on the mean-field level, although it is useful to keep in mind the possible extensions of the theory explained. In particular, `MOCCa` does not implement any kind of beyond-mean-field procedure to enrich the many-body wavefunctions, but it might serve to generate the ingredient wavefunctions $|\Psi(\theta)\rangle$ that can be used for more complete studies.

Chapter 2

Symmetries: conservation and breaking

In the previous chapter we introduced the Hartree-Fock equations and the concept of a Skyrme energy density functional, carefully avoiding any elements that would render the formulation less general. This chapter concerns the possibilities that the conservation and breaking of symmetries of the Slater determinants afford us. We are in particular interested in two groups of point symmetries, respectively denoted by $\mathcal{D}_{2h}^{T}$ and $\mathcal{D}_{2h}^{TD}$, although rotational invariance will make frequent appearances. While this chapter is written solely for Slater determinants, it is worth emphasizing that the entire discussion is valid for the more general Hartree-Fock-Bogoliubov ansatz that will be introduced in chapter 3.
We will start by considering the consequences of conserved symmetries. Section 2.1 will introduce the general framework of symmetries of both EDF and Slater determinants. Afterwards, section 2.2 introduces the point symmetries we are interested in for single-particle wavefunctions, which will give rise to many-body symmetry groups in 2.3. Z-isospin symmetry, as a possible addition to the group structure will be discussed in section 2.4. The classification of the various subgroups of $\mathcal{D}_{2h}^{T}$ and $\mathcal{D}_{2h}^{TD}$ will be formulated in section 2.5, and their consequences for the possible sets of many-body symmetries that can simultaneously be conserved will be discussed in section 2.6. The consequences of conserved symmetries for single-particle wavefunctions and the mean-field densities and potentials will be introduced in sections 2.7 and 2.8. Afterwards, we will discuss the motivation, as well as the advantages and disadvantages of breaking self-consistent symmetries in 2.9, including a (non-exhaustive) list of physically relevant degrees of freedom that become accessible through this mechanism. Although the framework will not be employed in this dissertation, we discuss symmetry restoration and how it can improve the EDF formalism in section 2.10.

2.1 Many-body symmetry conservation

The many-body symmetry operators that interest us are all of the following form

$$\hat{\mathcal{U}} = \bigotimes_{j=1}^{A} \hat{U}_j \,, \tag{2.1}$$

where $\hat{U}$ is the corresponding single-particle operator. They can either be linear operators $\hat{\mathcal{U}}$, denoted with a hat or antilinear operators, $\check{\mathcal{U}}$, denoted by an inverted hat. All of the studied symmetry operators will be unitary but they can be either hermitian or antihermitian. In what follows, we will frequently distinguish between these four type of operators. Some results and clarification regarding this classification can be found in Appendix B.
A many-body interaction given by a many-body Hamiltonian $\hat{\mathcal{H}}$ is said to conserve a given symmetry if the many-body Hamiltonian commutes with the symmetry operator $\hat{\mathcal{U}}$.

$$\left[\hat{\mathcal{U}}, \hat{\mathcal{H}}\right] = 0 \,. \tag{2.2}$$

For linear operators, this means that $\hat{\mathcal{U}}$ and $\hat{\mathcal{H}}$ can be diagonalized simultaneously: the eigenstates of the many-body Hamiltonian have quantum numbers associated with the symmetry $\hat{\mathcal{U}}$. When there are several conserved symmetries $\hat{\mathcal{U}}_\mu$, the resulting quantum numbers can often be used to differentiate between the different states of the quantum system.
The hydrogen atom is a good example of this: the eigenstates of the Hamiltonian can be indexed by the well-known quantum numbers (n, l, m). A state $|\Psi_{nlm}\rangle$ can be chosen as an eigenstate of the Hamiltonian $\hat{\mathcal{H}}$, the $\mathbf{L}^2$ operator and the $\mathbf{J}_z$ operator at the same time. The underlying reason is of course that the Coulomb interaction is rotationally invariant. This is no different for the nuclear many-body problem: energy levels in nuclei can be assigned angular momentum and parity in order to classify and interpret them. The interactions

in a nuclear medium are rotation- as well as parity-invariant[1].
Consider a Slater determinant $|\Psi\rangle$ that is an eigenstate of a many-body symmetry $\hat{\mathcal{U}}$, that is to say

$$\hat{\mathcal{U}}|\Psi\rangle = u|\Psi\rangle\,, \tag{2.3}$$

Since the symmetry transformed Slater determinant is equal to the original $|\Psi\rangle$, up to a phase, the density matrix $\hat{\rho}_{\mathcal{U}}$ corresponding to it must be equal to the original density matrix $\hat{\rho}$. This leads us directly to the condition that

$$\hat{\rho}_{\mathcal{U}} = \hat{U}^\dagger \hat{\rho} \hat{U} = \hat{\rho}\,. \tag{2.4}$$

A Slater determinant is thus invariant if and only if its density matrix is invariant under the single-particle symmetry operator $\hat{U}$. One can prove [11] that if ρ is symmetrical under a symmetry of the Hamiltonian that the single-particle Hamiltonian is also symmetric, that is to say

$$\hat{U}^\dagger \hat{h}\left[\hat{\rho}\right]\hat{U} = \hat{h}\left[\hat{U}^\dagger \hat{\rho} \hat{U}\right]\,, \tag{2.5}$$

where the brackets mean to emphasize that $\hat{h}$ is a function of $\hat{\rho}$. This is a rather important result: consider again the solving of the Hartree-Fock equations in Algorithm 1. If the Slater determinant at iteration (i) $|\Psi^{(i)}\rangle$ is an eigenstate of $\hat{\mathcal{U}}$, then the single-particle Hamiltonian will be symmetric, and consequently the Slater determinant $|\Psi^{(i+1)}\rangle$ at the next iteration will still be an eigenstate of $\hat{\mathcal{U}}$, because of Eq. (2.5). Since symmetries get propagated in this way throughout the self-consistent scheme, one talks about self-consistent symmetries.
The Skyrme functional from last chapter is in general not related to a many-body Hamiltonian and one needs to slightly modify the concept of a conserved symmetry. An EDF E_{HF} is invariant with respect to a symmetry $\hat{\mathcal{U}}$ if its associated energy density $\mathcal{E}(\hat{\mathbf{r}})$ is symmetry covariant[20, 35], meaning that

$$\mathcal{E}(\hat{\mathcal{U}}^\dagger \hat{\mathbf{r}} \hat{\mathcal{U}}) = \hat{\mathcal{U}}^\dagger \mathcal{E}(\hat{\mathbf{r}}) \hat{\mathcal{U}}\,. \tag{2.6}$$

It is easy to see that if this is the case the integral over the energy density is then invariant under the symmetry transformation $\hat{\mathcal{U}}$. Eq. (2.6) is thus the correct generalization of symmetry conservation for a functional, and one can show that Eq. (2.5) still holds when the expectation value of a many-body Hamiltonian is replaced by a functional.
All of these considerations are independent of whether the symmetry operator $\hat{\mathcal{U}}$ is linear or antilinear. In the case of an antilinear and hermitian $\hat{\mathcal{U}}$ we only have to replace eigenstates by invariants in the discussion above. The only exception are antilinear, antihermitian operators that don't have eigenstates.
As a closing remark: we need to make a distinction between the symmetries of the functional E_{HF} and those of the corresponding single-particle Hamiltonian $\hat{h}$. While the considerations from the previous paragraph indicate that symmetries of $\hat{\mathcal{H}}$ can be kept throughout the self-consistent process, this does not have to be the case. The 'computational' symmetries kept throughout the self-consistent process can be any subset of the 'physical' symmetries of the functional E_{HF}. The Skyrme functional introduced in chapter 1 respects a great many symmetries (such as rotational invariance and parity), and the main objects of interest in this chapter are the computational symmetries of $\hat{h}$ and how they can help us describe nuclear structure.

2.2 The single-particle group D_{2h}^{TD}

The easiest introduction to the symmetry group of interest is by first introducing the single-particle symmetry operators, by defining their action on single-particle wavefunctions $\phi(x, y, z, \sigma, q)$[36]

$$\left[\hat{P}\phi\right](x,y,z,\sigma,q) = \quad \phi\ (-x,-y,-z,\quad \sigma,q)\,, \tag{2.7a}$$
$$\left[\check{T}\phi\right](x,y,z,\sigma,q) = \quad \sigma\phi^*(\ \ x,\quad y,\quad z,-\sigma,q)\,, \tag{2.7b}$$
$$\left[\hat{R}_x\phi\right](x,y,z,\sigma,q) = -i\ \ \phi\ (\ \ x,-y,-z,-\sigma,q)\,, \tag{2.7c}$$
$$\left[\hat{R}_y\phi\right](x,y,z,\sigma,q) = \quad \sigma\phi\ (-x,\quad y,-z,\quad \sigma,q)\,, \tag{2.7d}$$
$$\left[\hat{R}_z\phi\right](x,y,z,\sigma,q) = -i\sigma\phi\ (-x,-y,\quad z,\quad \sigma,q)\,. \tag{2.7e}$$

[1] Leaving aside the weak interaction.

The parity operator $\hat{P}$ is unitary and hermitian, while the signature operators $\hat{R}_\mu$ are linear and antihermitian and time reversal $\check{T}$ is antilinear and antihermitian. One can check that this definition of $\hat{R}_\mu$ is equivalent to

$$\hat{R}_\mu = \exp\left[-i\frac{\pi}{\hbar}\hat{J}_\mu\right] \tag{2.8}$$

where $\hat{J}_\mu$ is the single-particle angular momentum operator. It is interesting to note that the signature operators are elements of SO(3), as they represent the rotation of the system with 180° around their corresponding axis. They are special cases of the rotation operators of SO(3)

$$\hat{R}(\alpha,\beta,\gamma) = \exp\left[-i\frac{\alpha}{\hbar}\hat{J}_x\right]\exp\left[-i\frac{\beta}{\hbar}\hat{J}_y\right]\exp\left[-i\frac{\gamma}{\hbar}\hat{J}_z\right]. \tag{2.9}$$

The group thus only represents specific rotations as symmetries (180° around the Cartesian axes) and not general rotational invariance.
Starting from these operators, one can define the simplex operators $\hat{S}_\mu$, the time-simplex operators $\check{S}_\mu^T$ and the time-parity operator $\check{P}^T$ as

$$\check{P}^T = \hat{P}\check{T}\,, \qquad \hat{S}_\mu = \hat{P}\hat{R}_\mu\,, \qquad \check{S}_\mu^T = \hat{P}\check{T}\hat{R}_\mu\,. \tag{2.10}$$

$\check{P}^T$ is antihermitian and antilinear, the $\hat{S}_\mu$ operators are antihermitian and linear and the $\check{S}_\mu^T$ are hermitian and antilinear, see appendix B for definitions. The order of multiplications in these definitions do not matter, as we have the following commutation relations[2]

$$\left[\check{T},\hat{P}\right] = 0\,, \qquad \left[\hat{R}_\mu,\hat{P}\right] = 0\,, \qquad \left[\hat{R}_\mu,\check{T}\right] = 0\,. \tag{2.11}$$

The signature operators $\hat{R}_\mu$ don't commute among each other and one can check using the alternative definition in Eq. (2.8) that we have the following multiplication rules

$$\hat{R}_\mu\hat{R}_\nu = \epsilon_{\mu\nu\kappa}\hat{R}_\kappa - \delta_{\mu\nu}\,. \tag{2.12}$$

If we introduce the operators $\hat{\mathbb{1}}$ and $-\hat{\mathbb{1}}$ we recover a full group structure.[3] We denote this group as D_{2h}^{TD}

$$D_{2h}^{TD} = \left\{\hat{\mathbb{1}}, -\hat{\mathbb{1}}, \hat{P}, -\hat{P}, \check{T}, -\check{T}, \hat{R}_\mu, -\hat{R}_\mu, \hat{S}_\mu, -\hat{S}_\mu, \check{S}_\mu^T, -\check{S}_\mu^T\right\}, \tag{2.13}$$

where μ ranges over the three Cartesian axes x, y and z. This group is not Abelian, since the signature operators don't commute among each other. In order to complete the multiplication table, we can write down the following equations to identify the inverse elements

$$\hat{R}_\mu^\dagger\hat{R}_\mu = -\hat{R}_\mu\hat{R}_\mu = \hat{\mathbb{1}}\,, \qquad \check{T}^\dagger\check{T} = -\check{T}\check{T} = \hat{\mathbb{1}}\,, \tag{2.14a}$$

$$\check{S}_\mu^{T,\dagger}\check{S}_\mu^T = \check{S}_\mu^T\check{S}_\mu^T = \hat{\mathbb{1}}\,, \qquad \hat{P}^\dagger\hat{P} = \hat{P}\hat{P} = \hat{\mathbb{1}}\,. \tag{2.14b}$$

The group D_{2h}^{TD}can be interpreted starting from a subgroup called the classical point-group D_{2h}

$$D_{2h} = \left\{\hat{\mathbb{1}}, \hat{P}, \hat{R}_\mu, \hat{S}_\mu\right\}. \tag{2.15}$$

This is exactly the point group of interest, precisely because it contains the three plane symmetries denoted by the simplex operators $\hat{S}_\mu$. It is the largest subgroup of $SO(3)\times\{\hat{\mathbb{1}},\hat{P}\}$ that is consistent with the most general triaxial ellipsoid shapes[4]. As such, D_{2h} has all of the purely spatial symmetries we are interested in. We can form $D_{2h}^{TD}$by taking the direct product with another simple group

$$D_{2h}^{TD} = D_{2h}\times\left\{\hat{\mathbb{1}}, -\hat{\mathbb{1}}, \check{T}, -\check{T}\right\}. \tag{2.16}$$

While the group D_{2h} can be interpreted purely classically, the completion to D_{2h}^{TD}cannot due to the multiplication table of $\check{T}$. This is the direct consequence of the fact that fermions do not haves classical counterparts.

[2]Commutation relations in this context are a complete abuse of notation, as there is no addition operation in the group structure. Nevertheless it is compact and familiar notation.

[3]Note that we are severely abusing notation in this definition: multiplying by the number -1 is not a group element. The elements $\hat{\mathbb{1}}$ and $-\hat{\mathbb{1}}$ denote different group elements. This seemingly artificial construction is completely due to the problem of mapping classical groups into quantum groups for fermions.

[4]Which is something we would like to be able to describe, see section 2.9.1.

2.3 Many-body operators: $\mathcal{D}_{2h}^{T}$ and $\mathcal{D}_{2h}^{TD}$

We can straightforwardly construct many-body operators from the single-particle operators defined in the previous section. We denote the many-body operator $\hat{\mathcal{U}}$ as

$$\hat{\mathcal{U}} = \bigotimes_{i=1}^{A} \hat{U}_i \tag{2.17}$$

where $\hat{U}$ is the corresponding single-particle operator. We will distinguish between single-particle and many-body operators by way of the font. If we define the many-body operators in this way, the group structure survives and we get the full many-body group $\mathcal{D}_{2h}^{TD}$.

$$\mathcal{D}_{2h}^{TD} = \left\{ \hat{\mathbb{1}}, -\hat{\mathbb{1}}, \hat{\mathcal{P}}, -\hat{\mathcal{P}}, \check{\mathcal{T}}, -\check{\mathcal{T}}, \hat{\mathcal{R}}_\mu, -\hat{\mathcal{R}}_\mu, \hat{\mathcal{S}}_\mu, -\hat{\mathcal{S}}_\mu, \check{\mathcal{S}}_\mu^T, -\check{\mathcal{S}}_\mu^T \right\} \tag{2.18}$$

However, the multiplication table does not carry over naively. Definition (2.17) poses no problem for hermitian, linear operators like $\hat{P}$: $\hat{\mathcal{P}}$ is also hermitian and linear as a product of linear, hermitian operators. The case is different for antihermitian operators like $\hat{R}_\mu$. Depending if A is even or odd, $\hat{\mathcal{R}}_\mu$ is respectively hermitian or antihermitian. We have

$$\hat{\mathcal{R}}_\mu \hat{\mathcal{R}}_\mu = \prod_{i=1}^{A} \hat{R}_{\mu,i} \hat{R}_{\mu,i} = \prod_{i=1}^{A} -\hat{\mathbb{1}} = (-\hat{\mathbb{1}})^A \tag{2.19}$$

The same applies also to antilinear and antihermitian operators like $\check{T}$. Depending if A is even or odd, $\check{\mathcal{T}}$ is respectively hermitian or antihermitian.

$$\check{\mathcal{T}}\check{\mathcal{T}} = -\hat{\mathbb{1}} \text{ when A is odd,} \tag{2.20a}$$

$$\check{\mathcal{T}}\check{\mathcal{T}} = \hat{\mathbb{1}} \text{ when A is even.} \tag{2.20b}$$

In the end, we end up with two groups instead of one, with different multiplication tables

$$\mathcal{D}_{2h}^{T} = \left\{ \hat{\mathbb{1}}, \hat{\mathcal{P}}, \check{\mathcal{T}}, \check{\mathcal{P}}^T, \hat{\mathcal{R}}_\mu, \check{\mathcal{R}}_\mu^T, \hat{\mathcal{S}}_\mu, \check{\mathcal{S}}_\mu^T \right\}, \tag{2.21}$$

$$\mathcal{D}_{2h}^{TD} = \left\{ \hat{\mathbb{1}}, -\hat{\mathbb{1}}, \hat{\mathcal{P}}, -\hat{\mathcal{P}}, \check{\mathcal{T}}, -\check{\mathcal{T}}, \hat{\mathcal{R}}_\mu, -\hat{\mathcal{R}}_\mu, \check{\mathcal{R}}_\mu^T, -\check{\mathcal{R}}_\mu^T, \hat{\mathcal{S}}_\mu, -\hat{\mathcal{S}}_\mu, \check{\mathcal{S}}_\mu^T, -\check{\mathcal{S}}_\mu^T, \check{\mathcal{P}}^T, -\check{\mathcal{P}}^T \right\}. \tag{2.22}$$

Here we see the origin of the superscript D, standing for double, as $\mathcal{D}_{2h}^{TD}$ is essentially a doubling of $\mathcal{D}_{2h}^{T}$ with the extra element $-\hat{\mathbb{1}}$. The fact that we have different groups will have far-reaching consequences for the treatment of odd versus even nuclei. Note that $\mathcal{D}_{2h}^{TD}$ reduces to D_{2h}^{TD} when $A = 1$, as of course it should.

2.4 Z-isospin symmetry: the silent bystander

We have not mentioned another important operator yet: the isospin $\hat{\mathcal{I}}$ and in particular its third component $\hat{\mathcal{I}}_z$. The total isospin $\hat{\mathcal{I}}^2$ is in general not conserved by Slater determinants, similar to angular momentum. In this dissertation, we will however assume that the third component of the single-particle symmetry $\hat{I}_z$ is conserved, meaning that we only consider single-particle states that are definitely neutron or proton in nature. For the single-particle operators this implies

$$\left[\hat{I}_z \phi\right](x, y, z, \sigma, q) \quad = \quad q\phi(x, y, z, \sigma, q)\,. \tag{2.23}$$

It is linear and hermitian and thus permits eigenstates with real eigenvalues.
However, mean-field wavefunctions in general do not conserve the many-body operator $\hat{\mathcal{I}}_z$ but rather its exponential, denoted by $\hat{\mathcal{R}}_I$ for its similarity with the signature operators

$$\hat{\mathcal{R}}_I = \exp\left(-i\pi\hat{\mathcal{I}}_z\right). \tag{2.24}$$

$\hat{\mathcal{R}}_I$ commutes with both parity $\hat{\mathcal{P}}$ and the signature operators $\hat{\mathcal{R}}_\mu$ on both the single-particle and many-body level. It represents a rotation of 180° in isospin space and is in this sense the direct analog of the signature

operator $\hat{\mathcal{R}}_z$, while $\hat{\mathcal{I}}_z$ is the analog of $\hat{\mathcal{J}}_z$. Depending on the particle number, $\hat{\mathcal{I}}_z$ commutes or anticommutes with time-reversal

$$\left[\hat{\mathcal{R}}_I, \check{\mathcal{T}}\right] = 0 \qquad \text{if A is even}\,, \tag{2.25a}$$

$$\left\{\hat{\mathcal{R}}_I, \check{\mathcal{T}}\right\} = 0 \qquad \text{if A is odd}\,. \tag{2.25b}$$

We could redo the entire discussion, multiplying the possible symmetry combinations in the entire chapter by two, by including $\hat{\mathcal{R}}_I$ as a symmetry operator in the group structures

$$\mathcal{D}_{2h}^{D} \times \left\{\hat{\mathbb{1}}, \hat{\mathcal{R}}_I\right\} \qquad \text{and} \qquad \mathcal{D}_{2h}^{TD} \times \left\{\hat{\mathbb{1}}, \hat{\mathcal{R}}_I\right\}\,. \tag{2.26}$$

Many textbooks assume that the many-body state describes a nucleus with a fixed number of protons and neutrons and consequently that it is an eigenstate of $\hat{\mathcal{R}}_I$, what we will call z-isospin symmetry. Conserving this symmetry has the advantage of allowing every single-particle wavefunction to represent either a neutron or a proton, instead of a iso-spinor with isospin-up and isospin-down components. This has the consequence that the mean-field densities, mean-field potentials and the single-particle Hamiltonian can also be separated in a proton- and neutron part, as was already implicitly assumed in chapter 1 and Appendix A.
Z-isospin symmetry is not fundamentally different from the other symmetries discussed in this chapter and breaking it allows for a better description of many physical systems. See for example [37] for a recent overview. It is outside the scope of this text to treat the breaking of this symmetry and we will assume it to be conserved for the rest of this dissertation.[5] .

2.5 Generator sets: classifying subgroups of $\mathcal{D}_{2h}^{T}$ and $\mathcal{D}_{2h}^{TD}$

A group is generated by a set of generator elements $\hat{\mathcal{S}}_\mu$ if every element $\hat{\mathcal{U}}$ of that group can be written as a product of the $\hat{\mathcal{S}}_\mu$. We use the following notation

$$\mathcal{D}_{2h}^{T} = G\left\{\hat{\mathcal{P}}, \hat{\mathcal{R}}_z, \check{\mathcal{S}}_y^T, \check{\mathcal{T}}\right\}\,, \tag{2.27}$$

to denote that $\mathcal{D}_{2h}^{T}$ is generated by the set $\left\{\hat{\mathcal{P}}, \hat{\mathcal{R}}_z, \check{\mathcal{S}}_y^T, \check{\mathcal{T}}\right\}$. For a given subgroup, the choice of generators is far from unique and $\mathcal{D}_{2h}^{T}$ itself has many different generator sets.
The notion of generating sets allows us to explore the subgroups of $\mathcal{D}_{2h}^{T}$ and $\mathcal{D}_{2h}^{TD}$. We can denote every subgroup by specifying their generator sets. For $\mathcal{D}_{2h}^{T}$ the possible subgroups are listed in Table 2.1. One can divide all possible subgroups in various classes following a classification scheme proposed in [36], using the properties of the generating sets. A given subgroup is classified by two numbers and a letter, as follows

$$N^1 - N_X^2\,. \tag{2.28}$$

The first number N^1 is either 0, 1, 2, 3 or 4 and indicates the number of group elements in the generating set of the subgroup. The second number N^2 is either 0,1 or 3 and indicates the number of Cartesian axes explicitly referenced by the group elements. Note that N^2 cannot be equal to two: if the group includes two operators referencing Cartesian axes (signature, simplex and time-simplex operators) the third is also part of the group because of the commutation relations. The final letter X can be either A, B or D and denotes the number of signature operators in the group, either 0, 1 or 3. Again, a group with $X = C$ does not exist, as once two are included the third is too.
Not all of the possible subgroups of $\mathcal{D}_{2h}^{T}$ are systematically different, there is a large degree of isomorphism that corresponds to the freedom of labeling of the Cartesian axes. The subgroups $G\{\hat{R}_z\}$ and $G\{\hat{R}_y\}$ are clearly isomorphous and can thus be treated as the same group. The number of unique groups per type of subgroup is given in the third column of Table 2.1, while the total number of possible subgroups is given in the fourth column.
$\mathcal{D}_{2h}^{TD}$ has more group elements, and thus an expanded subgroup structure, summarized in Table 2.2. Note that Tables 2.2 and 2.1 share many groups on first inspection: while the notation for the generating sets is identical, the subgroups they represent are not the same because the multiplication tables are different.

[5] Although the data layout in `MOCCa` was designed with an extension in this direction in mind.

	Subgroups	Number	Total
$0-0_A$	$\emptyset$	1	1
$1-0_A$	$G\{\hat{\mathcal{P}}\}, G\{\check{\mathcal{T}}\}, G\{\check{\mathcal{P}}^T\}$	3	3
$1-1_A$	$G\{\hat{\mathcal{S}}_\mu\}, G\{\check{\mathcal{S}}_\mu^T\}, G\{\check{\mathcal{R}}_\mu^T\}$	3	9
$1-1_B$	$G\{\hat{\mathcal{R}}_\mu\}$	1	3
$2-0_A$	$G\{\hat{\mathcal{P}}, \check{\mathcal{T}}\}$	1	1
$2-1_A$	$G\{\check{\mathcal{T}}, \hat{\mathcal{S}}_\mu\}, G\{\hat{\mathcal{P}}, \check{\mathcal{S}}_\mu^T\}, G\{\check{\mathcal{P}}^T, \check{\mathcal{R}}_\mu^T\}$	3	9
$2-1_B$	$G\{\hat{\mathcal{P}}, \hat{\mathcal{R}}_\mu\}, G\{\check{\mathcal{P}}^T, \hat{\mathcal{R}}_\mu\}, G\{\check{\mathcal{T}}, \hat{\mathcal{R}}_\mu\}$	3	9
$2-3_A$	$G\{\hat{\mathcal{S}}_\mu, \check{\mathcal{S}}_\nu^T\}$	1	6
$2-3_B$	$G\{\hat{\mathcal{R}}_\mu, \check{\mathcal{R}}_\nu^T\}, G\{\hat{\mathcal{R}}_\mu, \hat{\mathcal{S}}_\nu\}, G\{\hat{\mathcal{R}}_\mu, \check{\mathcal{S}}_\nu^T\}$	3	9
$2-3_D$	$G\{\hat{\mathcal{R}}_\mu, \hat{\mathcal{R}}_\nu\}$	1	1
$3-1_B$	$G\{\hat{\mathcal{R}}_\mu, \check{\mathcal{T}}\}$	1	3
$3-3_B$	$G\{\hat{\mathcal{R}}_\mu, \hat{\mathcal{S}}_\nu, \check{\mathcal{T}}\}, G\{\hat{\mathcal{R}}_\mu, \check{\mathcal{S}}_\nu^T, \hat{\mathcal{P}}\}, G\{\hat{\mathcal{R}}_\mu, \check{\mathcal{R}}_\nu^T, \check{\mathcal{P}}^T\}$	3	9
$3-3_D$	$G\{\hat{\mathcal{R}}_\mu, \hat{\mathcal{R}}_\nu, \check{\mathcal{T}}\}, G\{\hat{\mathcal{R}}_\mu, \hat{\mathcal{R}}_\nu, \hat{\mathcal{P}}\}, G\{\hat{\mathcal{R}}_\mu, \hat{\mathcal{R}}_\nu, \check{\mathcal{P}}^T\}$	3	3
$4-3_D$	$\mathcal{D}_{2h}^T$	1	1

Table 2.1: Classification of subgroups of $\mathcal{D}_{2h}^T$ [36] with $\nu \neq \mu$. The third column gives the number of non-isomorphous subgroups while the fourth column gives the total number of subgroups, including isomorphous ones.

	Subgroups	Number	Total
$0-0_A$	$\emptyset$	1	1
$1-0_A$	$G\{\hat{\mathcal{P}}\}, G\{\check{\mathcal{T}}\}, G\{\check{\mathcal{P}}^T\}$	3	3
$1-1_A$	$G\{\hat{\mathcal{S}}_\mu\}, G\{\check{\mathcal{S}}_\mu^T\}, G\{\check{\mathcal{R}}_\mu^T\}$	3	9
$1-1_B$	$G\{\hat{\mathcal{R}}_\mu\}$	1	3
$2-0_A$	$G\{\hat{\mathcal{P}}, \check{\mathcal{T}}\}, G\{\hat{\mathcal{P}}, -\hat{\mathbb{1}}\}$	2	2
$2-1_A$	$G\{\check{\mathcal{T}}, \hat{\mathcal{S}}_\mu\}, G\{\hat{\mathcal{P}}, \check{\mathcal{S}}_\mu^T\}, G\{\check{\mathcal{P}}^T, \check{\mathcal{R}}_\mu^T\}, G\{\hat{\mathcal{R}}_\mu, -\hat{\mathbb{1}}\}, G\{\hat{\mathcal{S}}_\mu, -\hat{\mathbb{1}}\}$	5	15
$2-1_B$	$G\{\hat{\mathcal{P}}, \hat{\mathcal{R}}_\mu\}, G\{\check{\mathcal{P}}^T, \hat{\mathcal{R}}_\mu\}, G\{\check{\mathcal{T}}, \hat{\mathcal{R}}_\mu\}$	3	9
$2-3_A$	$G\{\hat{\mathcal{S}}_\mu, \check{\mathcal{S}}_\nu^T\}$	1	6
$2-3_B$	$G\{\hat{\mathcal{R}}_\mu, \check{\mathcal{R}}_\nu^T\}, G\{\hat{\mathcal{R}}_\mu, \hat{\mathcal{S}}_\nu\}, G\{\hat{\mathcal{R}}_\mu, \check{\mathcal{S}}_\nu^T\}$	3	9
$2-3_D$	$G\{\hat{\mathcal{R}}_\mu, \hat{\mathcal{R}}_\nu\}$	1	1
$3-1_A$	$G\{\check{\mathcal{S}}_\mu^T, \hat{\mathcal{P}}, -\hat{\mathbb{1}}\}, G\{\hat{\mathcal{S}}_\mu, \hat{\mathcal{P}}, -\hat{\mathbb{1}}\}$	1	3
$3-1_B$	$G\{\hat{\mathcal{R}}_\mu, \check{\mathcal{T}}\}$	1	3
$3-3_B$	$G\{\hat{\mathcal{R}}_\mu, \hat{\mathcal{S}}_\nu, \check{\mathcal{T}}\}, G\{\hat{\mathcal{R}}_\mu, \check{\mathcal{S}}_\nu^T, \hat{\mathcal{P}}\}, G\{\hat{\mathcal{R}}_\mu, \check{\mathcal{R}}_\nu^T, \check{\mathcal{P}}^T\}$	3	9
$3-3_D$	$G\{\hat{\mathcal{R}}_\mu, \hat{\mathcal{R}}_\nu, \check{\mathcal{T}}\}, G\{\hat{\mathcal{R}}_\mu, \hat{\mathcal{R}}_\nu, \hat{\mathcal{P}}\}, G\{\hat{\mathcal{R}}_\mu, \hat{\mathcal{R}}_\nu, \check{\mathcal{P}}^T\}$	3	3
$4-3_D$	$\mathcal{D}_{2h}^{TD}$	1	1

Table 2.2: Classification of subgroups of $\mathcal{D}_{2h}^{TD}$ [36] with $\nu \neq \mu$. The third column gives the number of non-isomorphous subgroups while the fourth column gives the total number of subgroups, including isomorphous ones.

2.6 Possible combinations of conserved symmetries

As in standard quantum mechanics textbooks, it is not possible to just pick any combination of symmetry operators and suppose the many-body wavefunctions conserve all of them. Note that the conservation of $\hat{\mathcal{R}}_I$ implies that we can split a Slater determinant in a proton and neutron part as

$$|\Psi_{\mathsf{HF}}\rangle = |\Psi_{\mathsf{HF},n}\rangle \otimes |\Psi_{\mathsf{HF},p}\rangle \,. \tag{2.29}$$

The many-body symmetry operators can also be separated into parts as

$$\hat{\mathcal{U}} = \hat{\mathcal{U}}_n \otimes \hat{\mathcal{U}}_p \,, \tag{2.30}$$

While we have separated the possible nuclear systems as either being time-even or time-odd, this separation implies that we have to make a slightly more involved separation of systems in the further discussion: either an even number of both particle species (even-even), an odd number of either one of the species (even-odd) or an odd number for both species (odd-odd).

2.6.1 Even-even systems

For even-even systems, the time-reversal operator $\check{\mathcal{T}}$ is hermitian, given that we have

$$\check{\mathcal{T}}\check{\mathcal{T}} = \check{\mathcal{T}}_{q_1}^2 \otimes \check{\mathcal{T}}_{q_2}^2 = \hat{\mathbb{1}} \,, \tag{2.31}$$

and the relevant group is $\mathcal{D}_{2h}^T$. In order to make our point we write down the commutators as deduced from the commutators of the single-particle operators

$$\left[\check{\mathcal{T}}, \hat{\mathcal{P}}\right] = \left[\hat{\mathcal{R}}_\mu, \hat{\mathcal{P}}\right] = 0 \,, \qquad \left[\check{\mathcal{T}}, \hat{\mathcal{R}}_\mu\right] = \left[\hat{\mathcal{R}}_\mu, \hat{\mathcal{R}}_\nu\right] = 0 \,, \tag{2.32}$$

and from this the commutation relations of the simplex $\hat{\mathcal{S}}_\mu$ and time-simplex $\check{\mathcal{S}}_\mu^T$ operators can easily be deduced. In short, every element in $\mathcal{D}_{2h}^T$ commutes with all the rest and the group is Abelian. Because of this[6] we know that we can construct Slater determinants $|\Psi\rangle$ that are eigenstates or invariants of any combination of elements of $\mathcal{D}_{2h}^T$. In fact, the mathematics of group theory starts to shine here: if a Slater determinant is an eigenstate of $\hat{\mathcal{U}}_1$ and $\hat{\mathcal{U}}_2$, then it is automatically an eigenstate of $\hat{\mathcal{U}}_1\hat{\mathcal{U}}_2$ too.
Every possible generator set in Table 2.1 thus defines a subspace in the space of all Slater determinants: the space of Hartree-Fock states that are eigenstates of all the generating operators. All of the operators in the subgroup correspond to a conserved symmetry, while all of the symmetry operators that are not in the subgroup correspond to broken symmetries.

2.6.2 Even-odd systems

For even-odd systems, the time-reversal operator is antihermitian, as we have

$$\check{\mathcal{T}}\check{\mathcal{T}} = \check{\mathcal{T}}_{q_1}^2 \otimes \check{\mathcal{T}}_{q_2}^2 = -\hat{\mathbb{1}} \,, \tag{2.33}$$

The relevant group is thus $\mathcal{D}_{2h}^{TD}$, which is not Abelian. Consider the following commutation relations

$$\left[\check{\mathcal{T}}, \hat{\mathcal{R}}_\mu\right] = \left[\check{\mathcal{T}}, \hat{\mathcal{P}}\right] = \left[\hat{\mathcal{R}}_\mu, \hat{\mathcal{P}}\right] = 0 \,, \qquad \left\{\hat{\mathcal{R}}_\mu, \hat{\mathcal{R}}_\nu\right\} = \left\{\hat{\mathcal{R}}_\mu^T, \check{\mathcal{R}}_\nu\right\} = \left\{\check{\mathcal{S}}_\mu^T, \hat{\mathcal{R}}_\nu\right\} = 0 \quad \text{for i} \neq \text{j} \,. \tag{2.34}$$

The commutation rules for the other operators can easily be deduced from these. The major difference with the even case is the behavior of the signature operators. They no longer commute among each other and render the group structure more complicated. In addition, $\check{\mathcal{T}}$ is in this case an antihermitian, antilinear operator.
This already shows that finding a Slater determinant that is an eigenstate of every operator in the $\mathcal{D}_{2h}^{TD}$ group is impossible: an antilinear, antihermitian operator does not admit eigenstates or invariants. Every subgroup in Table 2.2 that contains $\check{\mathcal{T}}$ is not a subgroup that characterizes a subspace of many-body wavefunctions. The subgroups containing more than one signature operator also do not generate possible symmetry combinations, since the signature operators do not commute for odd systems. These considerations severely limit the possible

[6] And the fact that there are no antihermitian, antilinear operators in the group.

Type	Subgroups	Number	Total
$0-0_A$	$\emptyset$	1	1
$1-0_A$	$G\{\hat{\mathcal{P}}\}, G\{\check{\mathcal{P}}^T\}$	2	2
$1-1_A$	$G\{\hat{\mathcal{S}}_\mu\}, G\{\check{\mathcal{S}}_\mu^T\}, G\{\check{\mathcal{R}}_\mu^T\}$	3	9
$1-1_B$	$G\{\hat{\mathcal{R}}_\mu\}$	1	3
$2-0_A$	$G\{\hat{\mathcal{P}}, -\hat{\mathbb{1}}\}$	1	1
$2-1_A$	$G\{\hat{\mathcal{P}}, \check{\mathcal{S}}_\mu^T\}, G\{\check{\mathcal{P}}^T, \check{\mathcal{R}}_\mu^T\}, G\{\hat{\mathcal{R}}_\mu, -\hat{\mathbb{1}}\}, G\{\hat{\mathcal{S}}_\mu, -\hat{\mathbb{1}}\}$	4	12
$2-1_B$	$G\{\hat{\mathcal{P}}, \hat{\mathcal{R}}_\mu\}, G\{\check{\mathcal{P}}^T, \hat{\mathcal{R}}_\mu\}$	2	6
$2-3_A$	$G\{\hat{\mathcal{S}}_\mu, \check{\mathcal{S}}_\nu^T\}$	1	6
$2-3_B$	$G\{\hat{\mathcal{R}}_\mu, \check{\mathcal{R}}_\nu^T\}, G\{\hat{\mathcal{R}}_\mu, \hat{\mathcal{S}}_\nu\}, G\{\hat{\mathcal{R}}_\mu, \check{\mathcal{S}}_\nu^T\}$	3	9
$3-1_A$	$G\{\check{\mathcal{S}}_\mu^T, \hat{\mathcal{P}}, -\hat{\mathbb{1}}\}, G\{\hat{\mathcal{S}}_\mu, -\hat{\mathbb{1}}\}$	1	3
$3-3_B$	$G\{\hat{\mathcal{R}}_\mu, \check{\mathcal{S}}_\nu^T, \hat{\mathcal{P}}\}, G\{\hat{\mathcal{R}}_\mu, \check{\mathcal{R}}_\nu^T, \check{\mathcal{P}}^T\}$	2	6

Table 2.3: Classification of subgroups of $\mathcal{D}_{2h}^{TD}$ that can be conserved by many-body states.

conserved symmetry combinations and the ones that survive are given in Table 2.3. While the group $\mathcal{D}_{2h}^{TD}$ has more elements than its even counterpart, the actual number of possible symmetry combinations is smaller for odd systems.
Note that these limitations do not apply to subgroups that contain a signature operator $\hat{\mathcal{R}}_\mu$ and either a time-signature operator $\check{\mathcal{R}}_\nu^T$ or a time-simplex operator $\check{\mathcal{S}}_\nu^T$. While these also do not commute, as antilinear hermitian operators they anticommute with the linear, antihermitian signature operators and thus can be simultaneously conserved, see Appendix B.

2.6.3 Odd-odd systems

For odd-odd systems, the total number of nucleons is again even, so time-reversal is again hermitian. Note that all of the commutation relations in Eq. (2.32) still hold because the total number of nucleons is even. The relevant group governing the system is thus once again $\mathcal{D}_{2h}^{T}$. At first sight the treatment of odd-odd nuclei is thus very much similar to the one for even-even nuclei, as we can conserve any subgroup listed in Table 2.1.
However, the situation is not as simple as that. While in general many-body states that are not Slater determinants can conserve time-reversal and $\hat{\mathcal{R}}_I$ at the same time, there is no Slater determinant that can. Indeed, consider

$$\check{\mathcal{T}}|\Psi_{\mathsf{HF}}\rangle = \left(\check{\mathcal{T}}_n \otimes \check{\mathcal{T}}_p\right)\left(|\Psi_{\mathsf{HF},n}\rangle \otimes |\Psi_{\mathsf{HF},n}\rangle\right) = \left(\check{\mathcal{T}}_n|\Psi_{\mathsf{HF},n}\rangle\right) \otimes \left(\check{\mathcal{T}}_p|\Psi_{\mathsf{HF},p}\rangle\right) , \tag{2.35}$$

and since both the proton and neutron number are odd, we know that

$$\check{\mathcal{T}}_n|\Psi_{\mathsf{HF},n}\rangle \neq |\Psi_{\mathsf{HF},n}\rangle , \qquad \check{\mathcal{T}}_p|\Psi_{\mathsf{HF},p}\rangle \neq |\Psi_{\mathsf{HF},p}\rangle . \tag{2.36}$$

It is thus the very structure of Eq. (2.29) that forbids the conservation of time-reversal and $\hat{\mathcal{R}}_I$ at the same time when the number of protons and neutrons is odd.
If we would allow for more general variational ansatzes that expand on the Slater determinants[7], the relevant group would thus be $\mathcal{D}_{2h}^{T}$. But we will maintain a) the variational space of Slater determinants and b) the assumption of z-isospin symmetry. We will not categorize the possible symmetry combinations as their description is well outside the scope of this dissertation.

[7] Similar arguments hold for the HFB ansatz that will be introduced in the next chapter.

2.7 Symmetries of the single-particle wavefunctions

A Slater determinant conserving a symmetry $\hat{\mathcal{U}}$ has consequences for the constituent single-particle wavefunctions. We already know that the space spanned by the occupied single-particle states is invariant under the action of $\hat{U}$ in that case, as the density matrix is invariant (up to a phase).
For linear operators this means that one can diagonalize the symmetry operator $\hat{U}$ in this subspace of the one-body Hilbert space. In practice, this means that one can freely choose the single-particle wavefunctions that make up the Slater determinant to be eigenstates of the symmetry operator $\hat{U}$. Since the diagonalization is a unitary transformation that does not mix occupied with unoccupied states, this will leave the density matrix invariant (up to a phase). Given a subgroup of conserved symmetries, we are thus free to only consider eigenstates of the linear operators and invariants of the hermitian, antilinear operators in the subgroup. We can even find a transformation that takes any antilinear, antihermitian operator into its normal form, see Appendix B.
Considering the single-particle wavefunctions to be eigenstates of single-particle symmetries also has direct consequences for the single-particle creation operators. If the single-particle states are eigenstates of a linear single-particle symmetry $\hat{U}$ with eigenvalues u_l we have the following relations for the creation and annihilation operators [32]

$$\hat{\mathcal{U}}^\dagger \hat{a}_l^\dagger \hat{\mathcal{U}} = u_l \hat{a}_l^\dagger \,, \tag{2.37a}$$
$$\hat{\mathcal{U}}^\dagger \hat{a}_l \hat{\mathcal{U}} = u_l^* \hat{a}_l \,. \tag{2.37b}$$

We have similar relations if the single-particle states are invariants of an antilinear, hermitian operator $\check{U}$

$$\check{\mathcal{U}}^\dagger \hat{a}_l^\dagger \check{\mathcal{U}} = \hat{a}_l^\dagger \,, \tag{2.38a}$$
$$\check{\mathcal{U}}^\dagger \hat{a}_l \check{\mathcal{U}} = \hat{a}_l \,. \tag{2.38b}$$

The single-particle states cannot be eigenstates of an antilinear, antihermitian operator $\check{U}$, but they can assume to come in normal pairs $(l, \bar{l})$, meaning that

$$\check{\mathcal{U}}^\dagger \hat{a}_l^\dagger \check{\mathcal{U}} = \hat{a}_{\bar{l}}^\dagger \,, \tag{2.39a}$$
$$\check{\mathcal{U}}^\dagger \hat{a}_l \check{\mathcal{U}} = \hat{a}_{\bar{l}} \,. \tag{2.39b}$$

As a practical example, let us select the entire group $\mathcal{D}_{2h}^T$, that corresponds to the case of the `ev8` code. Starting out, we can choose the single-particle wavefunctions as eigenstates of parity $\hat{P}$. We can now construct a set of $|\phi_l\rangle$ so that

$$\hat{P}|\phi_l\rangle = p_l|\phi_l\rangle \,, \tag{2.40}$$

where $p_l = \pm 1$. Another operator in the conserved subgroup is the z-signature $\hat{\mathcal{R}}_z$. It commutes with parity, so we are free to assume that

$$\hat{R}_z|\phi_l\rangle = \eta_l|\phi_l\rangle \,, \tag{2.41}$$

where $\eta_l = \pm i$. There are no more linear operators in $\mathcal{D}_{2h}^T$ that commute with $\hat{\mathcal{P}}$ and $\hat{\mathcal{R}}_z$, so we need to start looking at antilinear operators. $\check{\mathcal{S}}_y^T$ commutes with $\mathcal{P}$ but anticommutes with $\hat{\mathcal{R}}_z$, so that we again can consider

$$\check{S}_y^T|\phi_l\rangle = |\phi_l\rangle \,. \tag{2.42}$$

In addition, we can take $\check{\mathcal{T}}$ into its normal form, that is, we can assume that

$$\check{T}|\phi_l\rangle = |\phi_{\bar{l}}\rangle \,, \tag{2.43}$$

meaning that every single-particle wavefunction $|\phi_l\rangle$ has a time-reversed partner $|\phi_{\bar{l}}\rangle$. In the end we have a set of $|\phi_l\rangle$ that are simultaneous eigenstates of $\hat{P}, \hat{R}_z$, are invariants of $\check{S}_y^T$ and bring $\check{T}$ into normal form. This is the best we can do, as no remaining element of the single-particle group D_{2h}^{TD} can fulfill the necessary commutation relations to be added to the set.
`ev8` makes extensive use of the simplification these relations bring, as do `ev4`, `cr8` and `MOCCa` with some modifications. This comes in handy for the interpretation of mean-field states as we can use these quantum numbers to label single-particle states, similar to the spectroscopic notation of the states in in the hydrogen atom. The (immensely) practical numerical consequences will be further discussed in chapter 4.

2.8 Mean-field densities and mean-field potentials

Symmetries also impose relations on the mean-field densities. As example consider the parity operator $\hat{P}$ and the density $\rho(\mathbf{r})$. We are free to assume that the single-particle wavefunctions $|\psi_l\rangle$ are eigenstates of the single-particle parity operator $\hat{P}$[8]. We can then derive

$$\begin{aligned}\rho(-x,-y,-z) &= \sum_{l,\sigma=\pm1} \psi_l^*(-x,-y,-z,\sigma)\psi_l(-x,-y,-z,\sigma) \\ &= \sum_{l,\sigma=\pm1} p_l^2 \psi_l^*(x,y,z,\sigma)\psi_l(x,y,z,\sigma) \\ &= \rho(x,y,z)\,.\end{aligned} \tag{2.44}$$

The spatial symmetries $\hat{\mathcal{P}}, \hat{\mathcal{R}}_\mu, \hat{\mathcal{S}}_\mu$ and $\check{\mathcal{S}}_\mu^T$ all introduce similar spatial relations for the different mean-field densities. In general we have a symmetry rule for a density $d(x,y,z)$ as follows [38]

$$d(\epsilon_x x, \epsilon_y y, \epsilon_z z) = \epsilon d(x,y,z)\,. \tag{2.45}$$

These relations are summarised for all of the symmetries in Table 2.4. The signs $(\epsilon_x, \epsilon_y, \epsilon_z)$ are determined by the second row of the table, while the sign ϵ is the one that is tabulated.[9] The only exception is the time-reversal operator $\check{T}$, which does not induce any spatial relation of the symmetries. Instead, if it is conserved, several of the mean-field densities are zero. The column final in Table 2.4 thus tabulates the signs ϵ in the following relation

$$\rho(x,y,z) = \epsilon\rho(x,y,z)\,. \tag{2.46}$$

The densities with a minus-sign in the final column are thus time-odd and are strictly zero when time-reversal is conserved.

These relations directly transfer to the mean-field potentials, since they are sums of the mean-field densities and their derivatives. We tabulate which ones are time-even and time-odd in Table 2.5, and the spatial relations can be directly deduced from Table 2.4.

2.9 Breaking symmetries

As mentioned before, the space of all Slater determinants from chapter 1 represents only a tiny fraction of the entire Hilbert space of the many-body problem. Conserved many-body symmetries impose specific relations on these Slater determinants (as well as the single-particle wavefunctions in the Hartree-Fock basis). If more symmetries are imposed, the space of Slater determinants that conserve them shrinks drastically. From a variational point of view this is bad news, as the variational space becomes smaller and the upper bound we can put on ground-state energies thus becomes less strict. From a computational point of view symmetries are very welcome as they diminish the computational effort needed to find a solution of the Hartree-Fock equations.

Enlarging the variational space by breaking symmetries is key to enrich the variational space of Slater determinants. While the functional might be invariant under a given many-body symmetry, the Slater determinant that minimizes the Hartree-Fock energy does not have to be. This kind of symmetry breaking reminds of the spontaneous breaking of symmetries in particle physics: the simplified picture known as a 'Mexican hat'-potential is also very relevant here. Given a symmetry-broken solution, many different ones may be generated by applying the corresponding symmetry to the solution, but all of these will be degenerate.

We can also approach this from the other side: the exact many-body wavefunction is an eigenstate of the symmetries of the many-body Hamiltonian. However, this state is in general not a Slater determinant. While we could approximate the many-body state by a Slater determinant that is an eigenstate of the given symmetries, this does not mean this state is the best approximation (in the sense of lowest energy) to the exact many-body state. A Slater determinant that does not respect the given symmetries might have a lower energy and be therefore preferable. From this point of view it becomes clear that breaking symmetries in this context is not truly a physical phenomenon (the exact many-body state is an eigenstate of all relevant symmetries), but rather a consequence of our choice of variational space.

[8] This assumption makes the derivation more intuitive and shorter to write down, but is not necessary. The only necessary condition is that space of single-particle wavefunctions is closed under the action of $\hat{P}$, or equivalently that the density matrix $\hat{\rho}$ is invariant under $\hat{P}$.

[9] The table does not contain derivatives of the densities, but these obey similar relations. The signs under the transformations will of course not be the same, but it should be straightforward to further extend Table 2.4.

	$\hat{\mathcal{R}}_x$	$\hat{\mathcal{R}}_y$	$\hat{\mathcal{R}}_z$	$\hat{\mathcal{S}}_x$	$\hat{\mathcal{S}}_y$	$\hat{\mathcal{S}}_z$
$(x,y,z)\rightarrow$	$(x,-y,-z)$	$(-x,y,-z)$	$(-x,-y,z)$	$(-x,y,z)$	$(x,-y,z)$	$(x,y,-z)$
ρ,τ	$+1$	$+1$	$+1$	$+1$	$+1$	$+1$
s_x,T_x,F_x	$+1$	-1	-1	-1	$+1$	-1
s_y,T_y,F_y	-1	$+1$	-1	$+1$	-1	-1
s_z,T_z,F_z	-1	-1	$+1$	$+1$	$+1$	$+1$
j_x	$+1$	-1	-1	$+1$	-1	$+1$
j_y	-1	$+1$	-1	-1	$+1$	$+1$
j_z	-1	-1	$+1$	-1	-1	-1
$J_{xx},J_{yy},J_{zz},J^{(0)}$	$+1$	$+1$	$+1$	-1	-1	-1
$J_{yz},J_{zy},J_x^{(1)}$	$+1$	-1	-1	-1	$+1$	$+1$
$J_{xz},J_{zx},J_y^{(1)}$	-1	$+1$	-1	$+1$	-1	$+1$
$J_{xy},J_{yx},J_z^{(1)}$	-1	-1	$+1$	$+1$	$+1$	-1
	$\check{\mathcal{S}}_x^T$	$\check{\mathcal{S}}_y^T$	$\check{\mathcal{S}}_z^T$	$\hat{\mathcal{P}}$	$\check{\mathcal{P}}^T$	$\check{\mathcal{T}}$
$(x,y,z)\rightarrow$	$(-x,y,z)$	$(x,-y,z)$	$(x,y,-z)$	$(-x,-y,-z)$	$(-x,-y,-z)$	$N.A.$
ρ,τ	$+1$	$+1$	$+1$	$+1$	$+1$	$+1$
s_x,T_x,F_x	-1	$+1$	$+1$	$+1$	-1	-1
s_y,T_y,F_y	$+1$	-1	$+1$	$+1$	-1	-1
s_z,T_z,F_z	$+1$	$+1$	-1	$+1$	-1	-1
j_x	$+1$	-1	-1	-1	$+1$	-1
j_y	-1	$+1$	-1	-1	$+1$	-1
j_z	-1	-1	$+1$	-1	$+1$	-1
$J_{xx},J_{yy},J_{zz},J^{(0)}$	-1	-1	-1	-1	-1	$+1$
$J_{yz},J_{zy},J_x^{(1)}$	-1	$+1$	$+1$	-1	-1	$+1$
$J_{xz},J_{zx},J_y^{(1)}$	$+1$	-1	$+1$	-1	-1	$+1$
$J_{xy},J_{yx},J_z^{(1)}$	$+1$	$+1$	-1	-1	-1	$+1$

Table 2.4: Densities and the spatial relations they have when symmetries are conserved. See the explanation with Eqs. (2.45). and (2.46).

Time-even	$B_q, U_q, W_{\mu\nu,q}$
Time-odd	$\mathbf{A}_q, \mathbf{S}_q, \mathbf{C}_q, \mathbf{D}_q$

Table 2.5: Behavior under time-reversal of the mean-field potentials.

Since breaking symmetries is numerically costly, it is important to correctly identify the symmetry that adds relevant degrees of freedom and which one doesn't. Starting from either $\mathcal{D}_{2h}^{T}$ or $\mathcal{D}_{2h}^{TD}$, the amount of freedom to choose which symmetries to break and which to conserve is staggering. Every subgroup of both groups of which the generators satisfy the appropriate commutation rules is a possible combination of conserved symmetries (see Tables 2.1 and 2.2). The broken symmetries are then simply all of the elements in the parent group that are not part of the subgroup of conserved symmetries[10]. Note that these do not form a group.

2.9.1 Order parameters

Breaking symmetries enlarges the set of allowed Slater determinants in the variational procedure, and it is important to correctly identify and treat the new degrees of freedom this entails. When a given many-body operator $\hat{\mathcal{O}}$ obeys the following relation

$$\hat{\mathcal{U}}^{\dagger}\hat{\mathcal{O}}\hat{\mathcal{U}} = -\hat{\mathcal{O}} \tag{2.47}$$

for a given symmetry operator $\hat{\mathcal{U}}$ (that is possibly antilinear), then it follows that

$$\langle\Psi_{\mathsf{HF}}|\hat{\mathcal{O}}|\Psi_{\mathsf{HF}}\rangle = 0\,, \tag{2.48}$$

for a Slater determinant that is an eigenstate of $\hat{\mathcal{U}}$. A nonzero value of $\langle\hat{\mathcal{O}}\rangle$ is thus a clear indicator that the mean-field state is not symmetric. For this reason the value $\langle\hat{\mathcal{O}}\rangle$ can be regarded as an order parameter, in

[10] In addition to rotational symmetry, which is by default broken as SO(3) is not a subgroup of $\mathcal{D}_{2h}^{T}$ or $\mathcal{D}_{2h}^{TD}$.

Symmetry operator	Order parameters
$\hat{\mathcal{R}}(\alpha,\beta,\gamma)$	$\langle\hat{\mathcal{Q}}_{2m}\rangle, \langle\hat{\mathcal{Q}}_{4m}\rangle$
$\hat{\mathcal{P}}$	$\langle\hat{\mathcal{Q}}_{3m}\rangle, \langle\hat{\mathcal{S}}_z\rangle$
$\check{\mathcal{T}}$	$\langle\hat{\mathcal{J}}_x\rangle, \langle\hat{\mathcal{J}}_y\rangle, \langle\hat{\mathcal{J}}_z\rangle, \langle\hat{\mathcal{D}}\rangle, \langle\hat{\mathcal{S}}_z\rangle$
$\hat{\mathcal{R}}_x$	$\langle\hat{\mathcal{J}}_y\rangle, \langle\hat{\mathcal{J}}_z\rangle, \langle\mathrm{Re}\,\hat{\mathcal{Q}}_{21}\rangle, \langle\mathrm{Im}\,\hat{\mathcal{Q}}_{22}\rangle$
$\hat{\mathcal{R}}_y$	$\langle\hat{\mathcal{J}}_x\rangle, \langle\hat{\mathcal{J}}_z\rangle, \langle\mathrm{Im}\,\hat{\mathcal{Q}}_{21}\rangle, \langle\mathrm{Im}\,\hat{\mathcal{Q}}_{22}\rangle$
$\hat{\mathcal{R}}_z$	$\langle\hat{\mathcal{J}}_x\rangle, \langle\hat{\mathcal{J}}_y\rangle, \langle\hat{\mathcal{Q}}_{21}\rangle$
$\hat{\mathcal{S}}_x$	$\langle\hat{\mathcal{J}}_y\rangle, \langle\hat{\mathcal{J}}_z\rangle, \langle\mathrm{Re}\,\hat{\mathcal{Q}}_{21}\rangle, \langle\mathrm{Im}\,\hat{\mathcal{Q}}_{22}\rangle$
$\hat{\mathcal{S}}_y$	$\langle\hat{\mathcal{J}}_x\rangle, \langle\hat{\mathcal{J}}_z\rangle, \langle\mathrm{Im}\,\hat{\mathcal{Q}}_{21}\rangle, \langle\mathrm{Im}\,\hat{\mathcal{Q}}_{22}\rangle$
$\hat{\mathcal{S}}_z$	$\langle\hat{\mathcal{J}}_x\rangle, \langle\hat{\mathcal{J}}_y\rangle, \langle\hat{\mathcal{Q}}_{21}\rangle$
$\check{\mathcal{S}}_x^T$	$\langle\hat{\mathcal{J}}_x\rangle, \langle\mathrm{Re}\,\hat{\mathcal{Q}}_{21}\rangle, \langle\mathrm{Im}\,\hat{\mathcal{Q}}_{22}\rangle$
$\check{\mathcal{S}}_y^T$	$\langle\hat{\mathcal{J}}_y\rangle, \langle\mathrm{Im}\,\hat{\mathcal{Q}}_{21}\rangle, \langle\mathrm{Im}\,\hat{\mathcal{Q}}_{22}\rangle$
$\check{\mathcal{S}}_z^T$	$\langle\hat{\mathcal{J}}_z\rangle, \langle\hat{\mathcal{Q}}_{21}\rangle$

Table 2.6: Most relevant degrees of freedom mentioned that arise because of broken symmetries. Note that this list is far from comprehensive and that degrees of freedom listed under two symmetries are restricted by both. For the purpose of this list our choice of axes of the multipole moments is (x, y, z) following the conventions of Appendix C.

analogy to the quantities in thermodynamics that indicate phase transitions. Care should be taken however, as not every asymmetrical mean-field state gives rise to a nonzero value of $\langle\hat{\mathcal{O}}\rangle$, meaning that we should not take the analogy too far.
In what follows, we will consider a list of examples of order parameters and the physical situations they are relevant in. The first examples are the quadrupole deformation $\langle\mathcal{Q}_{20}\rangle$ and $\langle\mathrm{Re}\,\mathcal{Q}_{22}\rangle$, octupole deformation $\langle\mathcal{Q}_{3m}\rangle$ and the three components of the angular momentum vector. Less widespread in the literature, but not less interesting are the nuclear Schiff moment and the other quadrupole moments $\langle\mathcal{Q}_{21}\rangle$ and $\langle\mathrm{Im}\,\mathcal{Q}_{21}\rangle$ that characterize so-called scissor modes. We will go into detail briefly for all of these and try to give the reader references to some relevant applications.
These degrees of freedom (and some others) and the symmetries that constrain them are summarized in Table 2.6. The observables that can be considered as parameters are by no means limited to this table as presented here, as one can imagine many operators whose expectation value is restricted to zero by conserved symmetries. The main examples are of course the multipole moments with $\ell > 4$.

Quadrupole deformation

The deformation associated with non-zero values of the quadrupole moments $\langle\hat{\mathcal{Q}}_{20}\rangle$ and $\langle\mathrm{Re}\,\hat{\mathcal{Q}}_{22}\rangle$ is the most prevalent order parameter in the literature. Both quantities are actually not constrained by any of the discrete symmetries of $\mathcal{D}_{2h}^T$ or $\mathcal{D}_{2h}^{TD}$. They are more specifically order parameters of the rotational invariance, associated with SO(3) and the rotation operators of Eq. (2.9).
However, for many nuclei, the breaking of SO(3) is not complete and one of the cartesian axes can be chosen as a rotational symmetry axis of the nucleus, effectively conserving SO(2) as a subgroup of SO(3). Configurations that respect SO(2) are called axial and correspond, if the symmetry axis is the z-axis, to $\langle\hat{\mathcal{Q}}_{22}\rangle = 0$ and non-zero values of $\langle\hat{\mathcal{Q}}_{20}\rangle$ [11].
The mean-field minima for many nuclei are axial as was shown for light nuclei in the original application of Skyrme forces [8]. Mean-field configurations of this type have been used to interpret the ground state of many nuclei as either prolate or oblate and in many cases the rotational bands that correspond to the Bohr-Mottelson model of rotation of deformed states have been experimentally observed. Many applications were already performed in the '90s [39] and nowadays such deformation can be included in fits of parameterizations [18]. A more comprehensive review can be found in [3].
Triaxial mean-field minima that no longer respect SO(2) are also prevalent across regions of the nuclear chart, for instance the Mo isotopes [40] or more recently in the Ge isotopes [41]. Chiral doublet bands and wobbling bands are usually cited as the experimental signature of triaxial deformation. A body of evidence exists for this kind of deformation around $A \sim 130$ [7] and $A \sim 160$ [42] for excited triaxial rotational bands, but experimental evidence for static ground-state triaxial deformation is still questionable.

[11] Different choices of symmetry axis correspond to different conditions on the quadrupole moments, see Appendix C

Octupole deformation

For multipole moments with odd ℓ one has (see Appendix C)

$$\hat{\mathcal{P}}^\dagger \hat{\mathcal{Q}}_{\ell m} \hat{\mathcal{P}}^\dagger = -\hat{\mathcal{Q}}_{\ell m} \,. \tag{2.49}$$

The lowest degree ℓ that is a physical degree of freedom is 3 and consequently the octupole deformations $\langle \hat{\mathcal{Q}}_{3m} \rangle$ are widely used as order parameters for the breaking of parity $\hat{\mathcal{P}}$. Several nuclei show mean-field minima that are octupole deformed, mostly in the $A \sim 230$ region [43, 44, 45] but also in the rare earth region [46] and at high spin in light nuclei [47].
The experimental smoking gun for octupole correlations are significant electric dipole and octupole transitions $E1, E3$ between levels in the nucleus. A very clear experimental example are ^{220}Rn and ^{240}Ra [6]. But lighter nuclei can exhibit octupole deformation too, as strong octupole correlations were recently discovered in ^{144}Ba [48]. Octupole deformations are also important for the mean-field descriptions of fission barriers. For many actinide nuclei, the fission barrier height can be systematically lowered when one includes the octupole deformation [49, 50].

Angular momentum

The angular momentum $\hat{\mathcal{J}}$ is of course a very important observable of the nucleus. All of the projections $\hat{\mathcal{J}}_\mu$ are restricted by the conservation of time-reversal and time-parity since

$$\check{\mathcal{T}}^\dagger \hat{\mathcal{J}} \check{\mathcal{T}} = \check{\mathcal{P}}^{T,\dagger} \hat{\mathcal{J}} \check{\mathcal{P}}^T = -\hat{\mathcal{J}} \,, \tag{2.50a}$$
$$\tag{2.50b}$$

The conservation of every signature operator $\hat{\mathcal{R}}_\mu$ restricts the values of the other two projections of the angular momentum to zero. This is because of the following relations

$$\hat{\mathcal{R}}_\mu^\dagger \hat{\mathcal{J}}_\nu \hat{\mathcal{R}}_\mu = +\hat{\mathcal{J}}_j \text{ if } \mu = \nu \,, \tag{2.51a}$$
$$\hat{\mathcal{R}}_\mu^\dagger \hat{\mathcal{J}}_\nu \hat{\mathcal{R}}_\mu = -\hat{\mathcal{J}}_j \text{ if } \mu \neq \nu \,. \tag{2.51b}$$

The simplexes $\hat{\mathcal{S}}_\mu$ also restrict the other two components of the angular momentum. The time-simplexes $\check{\mathcal{S}}_\mu^T$ however restrict the angular momentum projection along the corresponding Cartesian axis, since one can check that

$$\check{S}_\mu^{T,\dagger} \hat{\mathcal{J}}_\mu \check{S}_\mu^T = -\hat{\mathcal{J}}_\mu \,. \tag{2.52}$$

In short, angular momentum is completely restricted by time-reversal conservation, but its orientation is heavily restricted by conserved spatial symmetries.
The description of excited states along rotational bands (in both even and odd nuclei) using mean-field theory is greatly improved by using mean-field states with non-zero expectation values of (at least) one Cartesian projection of the angular momentum operator [51, 52]. A special mention goes to the wobbling bands in rare earth nuclei that are subject to renewed interest like ^{138}Nd [7] and ^{158}Er [53]. A proper description of their high-spin bands (also related to triaxial deformation) necessitates orientations of the angular momentum that does not coincide with a principal axis of the nucleus [54].

Time-odd densities and terms in the functional

While not usually used as order parameters in the literature, the mean-field densities $\mathbf{s}, \mathbf{j}, \mathbf{T}$ and $\mathbf{F}$ are restricted by time-reversal symmetry. Once it is broken, they take non-zero values and give rise to new terms in the functional, often (improperly) called the time-odd terms[12]. These terms are the source of some problems when constructing new Skyrme parameterizations. Either one takes the view that the Skyrme functional should be strictly generated by a force, in which case the coupling coefficients of the time-odd terms are completely determined by the force coefficients. If on the other hand one takes the view that the fundamental object is the functional, then the coefficients of the time-odd terms can a priori be determined independently. In either approach, the determination of the time-odd coefficients is rudimentary at best, since none of the fits incorporate experimental data that depends strongly on time-reversal breaking, like binding energies of odd nuclei. The usual strategy is thus to simply put the time-odd terms to zero or relate them in some way to the time-even coefficients [3].[13]

[12] The actual terms are not themselves odd under time-reversal since the energy density has to be a time-reversal scalar. They are merely built out of time-odd densities.

[13] Although studies that aim to improve this situation exist, as an example see [55].

The nuclear Schiff moment

An observable of great interest to the physics community as a whole is the atomic electric dipole moment [56]. A non-zero value of this quantity can only be induced by parity- and time-reversal-violating contributions to interactions in a nucleus, something that is not incorporated in the Standard Model. Detection of a non-zero value of an atomic electric dipole moment would signal the existence of physics beyond the Standard model, just like the detection of an electron or neutron electric dipole moment would.
The dipole operator $\hat{\mathcal{D}}$ is proportional to

$$\hat{\mathcal{D}} \sim \sum_i q_i \hat{\mathbf{r}}_\mathbf{i} \,, \tag{2.53}$$

where q_i is the charge of particle i. The expectation value of the dipole moment is restricted to zero if parity is conserved. When parity is broken, $\hat{\mathcal{D}}$ can take finite values, and is directly proportional to the average position of the proton density $\rho_p(\mathbf{r})$ with respect to the centre-of-mass of the entire nucleus.
The electric dipole moment generated by a dipole deformation in the nucleus can not be detected due to the Schiff theorem [57], as its effect would be completely screened by atomic electrons. However, another type of deformation produces an interaction with the atomic electrons so that the end result is a non-zero atomic electric dipole moment. This nuclear Schiff moment (or at least its z-component) is defined as [58]

$$\hat{\mathcal{S}}_z = \frac{e}{10} \sum_{\text{protons}} \left(\hat{r}_i^2 - \frac{5}{3} \langle \hat{\mathbf{r}}_p^2 \rangle \right) \hat{z}_i \,. \tag{2.54}$$

As with the dipole moment, the expectation values of this operator are constrained to zero when parity is conserved. Mean-field studies [58, 59] suggest that the susceptibility of ^{225}Ra to parity and time-reversal violating interactions is much larger (and thus more easily measurable) due to its intrinsic octupole deformation when compared to ^{199}Hg, the system that at this point in time, provides the most stringent limit on the observation of the atomic electric dipole moment.

Scissor modes

Just like the proton and neutron centre-of-mass positions are physical degrees of freedom, while the total centre-of-mass coordinate is not, the proton and neutron values of $\langle \hat{\mathcal{Q}}_{21} \rangle_{n,p}$ and $\langle \mathrm{Im}\, \hat{\mathcal{Q}}_{22} \rangle_{n,p}$ are physical, while the total values $\langle \hat{\mathcal{Q}}_{21} \rangle_t, \langle \mathrm{Im}\, \hat{\mathcal{Q}}_{22} \rangle_t$ simply represent the orientation of the nucleus in space (see Appendix C).
A non-zero value of either $\langle \hat{\mathcal{Q}}_{21} \rangle_p$ or $\langle \mathrm{Im}\, \hat{\mathcal{Q}}_{22} \rangle_{n,p}$ implies that the proton distribution is rotated with respect to the neutron distribution. Given that the proton and neutron distribution are both ellipsoids, the image of two ellipsoids that are rotated with respect to one another gave rise to the name of 'scissors mode'. The typical experimental signature associated with this kind of collective excitation are low-lying 1^+ with a large M1 transition strength to the ground state [60, 61].
The multipole moment operators $\hat{Q}_{21}$ and $\mathrm{Im}\, \hat{Q}_{22}$ are proportional to

$$\hat{x}\hat{y} \,, \quad \hat{y}\hat{z} \,, \quad \hat{x}\hat{z} \,, \tag{2.55}$$

where which $Q_{\ell m}$ get linked to which combination of Cartesian directions is dependent on our choice of axes. If the expectation values of any of these needs to be non-zero, it is clear that at least two of the signature operators $\hat{\mathcal{R}}_\mu$ cannot be conserved, since

$$\hat{\mathcal{R}}_x^\dagger \hat{x}\hat{y} \hat{\mathcal{R}}_x = -\hat{x}\hat{y} \,, \qquad \hat{\mathcal{R}}_y^\dagger \hat{x}\hat{y} \hat{\mathcal{R}}_y = -\hat{x}\hat{y} \,, \tag{2.56a}$$

$$\hat{\mathcal{R}}_x^\dagger \hat{x}\hat{z} \hat{\mathcal{R}}_x = -\hat{x}\hat{y} \,, \qquad \hat{\mathcal{R}}_z^\dagger \hat{x}\hat{z} \hat{\mathcal{R}}_z = -\hat{x}\hat{y} \,, \tag{2.56b}$$

$$\hat{\mathcal{R}}_y^\dagger \hat{y}\hat{z} \hat{\mathcal{R}}_y = -\hat{x}\hat{y} \,, \qquad \hat{\mathcal{R}}_z^\dagger \hat{y}\hat{z} \hat{\mathcal{R}}_z = -\hat{x}\hat{y} \,. \tag{2.56c}$$

And because parity and time-reversal commute with any of operators in Eq. (2.55), it follows that at most one of the simplex operators $\hat{\mathcal{S}}_\mu$ and/or one of the time-simplex operators $\check{S}_\mu^T$ can be conserved.

2.10 Symmetry restoration

There is an important disadvantage that we incur when breaking a symmetry $\hat{\mathcal{U}}$: one can no longer assign to the Slater determinants the quantum numbers of the broken symmetry. Slater determinants that do not respect self-consistent symmetries are superpositions of eigenstates of the broken symmetry with different quantum numbers. With every broken symmetry, results obtained by a mean-field calculation become harder to interpret, as it is not clear a priori how to disentangle the information stored in a symmetry-broken Slater determinant.
As an example consider a Slater determinant that conserves all of the symmetries of $\mathcal{D}_{2h}^{T}$. This Slater determinant can in general not be assigned an angular momentum quantum number $\mathcal{J}^2$. If the configuration is axial, the situation can be partly salvaged as at least the component of the angular momentum along the symmetry axis of the nucleus (often denoted K) is conserved. But in many cases, the Slater determinant will thus be a superposition of many-body states with different values of $\mathcal{J}^2$ and on the mean-field level their contributions are impossible to disentangle.
Comparison with experiment thus becomes systematically harder as more symmetries get broken. For rotational symmetry this is most apparent, as experimental spectra of nuclei are often labeled by their angular momentum quantum numbers. The experimental observables that suffer most from this problem are the multipole transitions between different nuclear levels: they depend heavily on selection rules of the quantum numbers of the states involved and are simply not accessible in a pure EDF context. Other quantities, such as the binding energy and the rms radii are more easily comparable to experiment, but are still impacted.
The generator coordinate method described in chapter 1 offers a way out: by allowing for superpositions of symmetry-broken Slater determinants one can build a new many-body state that is an eigenstate of the symmetries broken on mean-field level. This symmetry restoration scheme is therefore often called multi-reference EDF while the formalism on the mean-field level as described here is called single-reference EDF. It is beyond the aim of this text to introduce this procedure more generally, but the case of rotational symmetry breaking as explained in [3] can serve as an educational example.
Consider a Slater determinant $|\Psi\rangle$ that breaks rotational symmetry. From it, one can then construct a many-body wavefunction $|\Psi_{JM}\rangle$ as

$$|\Psi_{JM}\rangle = \frac{\sum_K g_K^J \hat{P}_{MK}^J |\Psi\rangle}{\sum_K |g_K^J|^2 \langle\Psi(q)|\hat{P}_{KK}^J|\Psi(q)\rangle} \tag{2.57}$$

where the operator $\hat{P}_{MK}^J$ is defined as in [11]

$$\hat{P}_{MK}^J = \frac{2J+1}{16\pi^2} \int d\alpha \, \sin(\beta) \, d\beta \, d\gamma \, D_{MK}^{J,*}(\alpha,\beta,\gamma) \hat{\mathcal{R}}(\alpha,\beta,\gamma) \,, \tag{2.58}$$

where (α,β,γ) are three Euler angles, $D_{MK}^J(\alpha,\beta,\gamma)$ is a Wigner rotation matrix and $\hat{\mathcal{R}}$ is as before a rotation operator. $|\Psi_{JM}\rangle$ is a state with angular momentum quantum numbers J and M, even though the original Slater determinant $|\Psi\rangle$ was not rotationally invariant. The procedure is in fact a GCM on the set of states obtained by rotations of the original $|\Psi\rangle$. By solving a corresponding Hill-Wheeler equation (see section 1.6) the weights g_K can be determined.
In a way, restoration of broken symmetries is similar in spirit to breaking the symmetries. Symmetry breaking enlarged the variational space by allowing for many more different Slater determinants, while symmetry restoration enlarges the variational space by allowing for superpositions of Slater determinants. An ideal calculation would include the symmetry restoration in a variational scheme based on symmetry-breaking states. The correct generalization of the Hartree-Fock energy could then be varied across the space of symmetry-restored Slater determinants instead of only the Slater determinants. Such a scheme is often called 'variation after projection' or VAP for short. This method is however extremely computationally intensive and is in many cases not feasible[14].
'Projection after variation' (PAV) in contrast is feasible in many cases. Instead of varying the symmetry-restored Slater determinants, the projection procedure is carried out with the solution of an EDF optimization. The end result is of course less optimal from the viewpoint of enlarging the variational space, as the variation is only carried out in the space of Slater determinants. The main motivation is still the same however: the resulting many-body wavefunction can be assigned quantum numbers and observables such as the multipole transition rates become accessible.

[14] Only for restoring particle number, as will be discussed in chapter 3, VAP has been carried out in some cases, see for example [62, 63, 64, 65].

Projection after variation is still numerically very costly compared to an EDF calculation without beyond-mean-field procedures and many schemes to phenomenologically reintroduce quantum numbers have been devised. These are either applied after the mean-field optimization or during it. In the latter case the philosophy of an EDF is realized to its fullest extent: everything should be contained in the functional and correlations that cannot be captured by Slater determinants should be simulated by terms and coupling constants of the EDF. Rotational corrections [13] and Wigner energy terms [25, 26] are examples. Schemes applied after the mean-field optimization take a different view and want to truly add correlations to the Slater determinants, in the same spirit as exact projection. The Gaussian overlap approximation [3] for example, aims to approximate exact projection by proposing a Gaussian form for the norm kernel $\hat{I}_{\mathrm{GCM}}$. Other schemes map potential energy surfaces on effective collective Hamiltonians, see for example [11] and more recently [44, 46].

Chapter 3

Pairing

Any microscopic model of the nucleus needs to take into account pairing correlations. In this chapter, we will describe the HFB ansatz that will replace the Slater determinants from chapter 1. We introduce the Bogoliubov transformation in section 3.1 and explain how it generalizes the concept of a Slater determinant. Section 3.2 will treat the modifications pairing brings to the EDF and section 3.3 will present the analog of the Hartree-Fock equations. The pairing treatment in a HFB scheme can also be seen as a consequence of a broken symmetry, this will be explained briefly in section 3.4. The consequences of symmetry conservation and breaking are discussed in section 3.5. The HF+BCS ansatz will be introduced as a special case of the HFB ansatz in section 3.6. We will also spend some time discussing the subtleties of the treatment of systems with an odd number of particles in section 3.7. Section 3.8 briefly mentions an alternative representation of HFB vacua that will be useful in chapter 6. The final section 3.9 specifies the details of the pairing interaction and cutoff factors as it was employed in this dissertation.

3.1 The Hartree-Fock-Bogoliubov ansatz

The Hartree-Fock-Bogoliubov (HFB) ansatz is a more general ansatz than a Slater determinant. A typical textbook introduction starts by introducing a Bogoliubov transformation, which is a unitary transformation among the Hartree-Fock creation and annihilation operators in the Hartree-Fock basis, typically parametrized by complex matrices U and V as

$$\beta_j^\dagger \quad = \sum_{i=1} \left(U_{ij} \hat{a}_i^\dagger + V_{ij} \hat{a}_i \right) . \tag{3.1}$$

Combining this equation with its Hermitian conjugate we get the complete Bogoliubov transformation [11]

$$\begin{pmatrix} \hat{\beta} \\ \hat{\beta}^\dagger \end{pmatrix} = \begin{pmatrix} U^\dagger & V^\dagger \\ V^T & U^T \end{pmatrix} \begin{pmatrix} \hat{a} \\ \hat{a}^\dagger \end{pmatrix} \tag{3.2}$$

In order to make sure that the $\beta^\dagger$ operators create fermions, one needs to make sure that the Bogoliubov transformation is unitary. This means that the columns vectors $(U_k V_k)^T$ form a set of orthonormal vectors and translates to the following conditions on U and V

$$\begin{aligned} U^\dagger U + V^\dagger V = \mathbb{1} , \qquad & U^\dagger U + V^* V^T = \mathbb{1} , \\ U^T V + V^T U = 0 , \qquad & U V^\dagger + V^* U^T = 0 . \end{aligned} \tag{3.3}$$

The Bloch-Messiah-Zumino theorem [66, 67] states that one can decompose the transformation as

$$\begin{pmatrix} U & V^* \\ V & U^* \end{pmatrix} = \begin{pmatrix} D & 0 \\ 0 & D^* \end{pmatrix} \begin{pmatrix} \bar{U} & \bar{V} \\ \bar{V} & \bar{U} \end{pmatrix} \begin{pmatrix} C & 0 \\ 0 & C^* \end{pmatrix} . \tag{3.4}$$

This transformation is thus composed out of three parts

1. A unitary transformation $(\hat{a}, \hat{a}^\dagger) \to (\hat{c}, \hat{c}^\dagger)$ determined by the matrix D;

2. A Bogoliubov transformation using matrices $\bar{U}$ and $\bar{V}$ with a very specific structure, transforming particle operators $(\hat{c}, \hat{c}^\dagger)$ into quasiparticle operators $(\hat{\alpha}, \hat{\alpha}^\dagger)$;

3. A final unitary transformation among the quasiparticle operators $(\hat{\alpha}, \hat{\alpha}^\dagger) \to (\hat{\beta}, \hat{\beta}^\dagger)$, determined by the matrix C.

The first unitary transformation transforms the single-particle wave-functions $|\phi_l\rangle$ into a set of $|\psi_l\rangle$ called the canonical basis, for reasons to be explained below. The second transformation, in contrast to the first one, does mix creation and annihilation operators and determines the pairing properties of the levels in the canonical basis. In the canonical basis, a level i can be either fully occupied ($\bar{V}_{ll} = 1$), unoccupied ($\bar{V}_{ll} = 0$) or paired with another level $\bar{l}$ ($\bar{V}_{ll} = 0, \bar{V}_{l\bar{l}} \neq 0$). The level $\bar{l}$ is called the canonical conjugate partner of l. If we denote the number of empty orbits by N_e, the paired orbits by N_p and the filled/occupied orbit by N_f, then the total size of the Hartree-Fock basis is $\Omega = N_e + N_f + N_p$. Using this notation, the matrices $\bar{U}$ and $\bar{V}$ have a very specific structure:

$$\bar{U} = \begin{pmatrix} 0 & & & & & & & & & & & & \\ & \ddots & & & & & & & & & & & \\ & & 0 & & & & & & & & & & \\ & & & u_{N_f+1} & 0 & & & & & & & & \\ & & & 0 & u_{N_f+1} & & & & & & & & \\ & & & & & \ddots & & & & & & & \\ & & & & & & u_{N_f+N_p} & 0 & & & & & \\ & & & & & & 0 & u_{N_f+N_p} & & & & & \\ & & & & & & & & 1 & & & & \\ & & & & & & & & & \ddots & & & \\ & & & & & & & & & & 1 & & \\ & & & & & & & & & & & & \end{pmatrix},$$

$$\bar{V} = \begin{pmatrix} 1 & & & & & & & & & & & & \\ & \ddots & & & & & & & & & & & \\ & & 1 & & & & & & & & & & \\ & & & 0 & v_{\Omega_f+1} & & & & & & & & \\ & & & -v_{\Omega_f+1} & 0 & & & & & & & & \\ & & & & & \ddots & & & & & & & \\ & & & & & & 0 & v_{\Omega_f+\Omega_p} & & & & & \\ & & & & & & -v_{\Omega_f+\Omega_p} & 0 & & & & & \\ & & & & & & & & 0 & & & & \\ & & & & & & & & & \ddots & & & \\ & & & & & & & & & & 0 & & \\ & & & & & & & & & & & & \end{pmatrix}, \tag{3.5}$$

where the filled, paired and empty orbitals give rise to very specific block structure in both matrices. Note that the number of paired orbits is always even while there is no such restriction a priori on the number of filled and empty orbitals.

In the canonical basis the quasiparticle operators $(\hat{\alpha}_l, \hat{\alpha}_l^\dagger)$ become

$$\begin{pmatrix} \hat{\alpha}_l \\ \hat{\alpha}_l^\dagger \end{pmatrix} = u_l \begin{pmatrix} \hat{c}_l^\dagger \\ \hat{c}_l \end{pmatrix} + v_{\bar{l}} \begin{pmatrix} \hat{c}_{\bar{l}} \\ \hat{c}_{\bar{l}}^\dagger \end{pmatrix} . \tag{3.6}$$

The unitarity conditions imply that $|u_l|^2 + |v_l|^2 = 1$, $u_l = u_{\bar{l}}$ and $v_l = -v_{\bar{l}}$. It is important to note that one cannot identify additional relations between canonical partners without imposing extra assumptions, such as conserved symmetries.

Now that we have introduced the quasiparticle operators, we can introduce the HFB ansatz. We define the physical many-body state $|\Phi_{\mathsf{HFB}}\rangle$ as the vacuum state for all the quasiparticle annihilation operators β_k, meaning that

$$\beta_k |\Psi_{\mathsf{HFB}}\rangle = 0 \text{ for all k=}1, \ldots, \Omega\,. \tag{3.7}$$

Note that in the canonical basis, we can explicitly construct the HFB state by acting on the vacuum with creation operators (in the canonical basis) as follows [11]

$$|\Psi_{\mathsf{HFB}}\rangle = \prod_{f=1}^{N_f} \hat{c}_f^\dagger \prod_{p=N_f}^{N_f+N_p} \left(u_p + v_p \hat{c}_p^\dagger \hat{c}_{\bar{p}}^\dagger\right) |0\rangle \tag{3.8}$$

The density matrix ρ of a Slater determinant specified it completely, but this is no longer the case for a HFB wavefunction. The anomalous density matrix κ is needed in addition, and is defined as

$$\kappa_{ij} = \langle \Psi_{\mathsf{HFB}} | \hat{a}_j \hat{a}_i | \Psi_{\mathsf{HFB}} \rangle\,. \tag{3.9}$$

Together they form the generalized density matrix $\mathcal{R}$

$$\mathcal{R} = \begin{pmatrix} \rho & \kappa \\ -\kappa^* & 1-\rho^* \end{pmatrix} . \tag{3.10}$$

For a HFB wavefunction, both the density matrix and anomalous density matrix are related to the U and V matrices

$$\rho = V^* V^T , \qquad \kappa = V^* U^T . \tag{3.11}$$

The U and V matrices take on special forms in the canonical basis: ρ becomes diagonal in this basis and κ takes its canonical form, with the shorthand notation $(uv)_k = u_k v_k$,

$$\rho = \begin{pmatrix} 1 & & & & & & & & & & & & \\ & \ddots & & & & & & & & & & & \\ & & 1 & & & & & & & & & & \\ & & & v^2_{N_f+1} & 0 & & & & & & & & \\ & & & 0 & v^2_{N_f+1} & & & & & & & & \\ & & & & & \ddots & & & & & & & \\ & & & & & & v^2_{N_f+N_p} & 0 & & & & & \\ & & & & & & 0 & v^2_{N_f+N_p} & & & & & \\ & & & & & & & & 0 & & & & \\ & & & & & & & & & \ddots & & & \\ & & & & & & & & & & 0 & & \end{pmatrix} ,$$

$$\kappa = \begin{pmatrix} 0 & & & & & & & & & & & & \\ & \ddots & & & & & & & & & & & \\ & & 0 & & & & & & & & & & \\ & & & 0 & (uv)_{N_f+1} & & & & & & & & \\ & & & -(uv)_{N_f+1} & 0 & & & & & & & & \\ & & & & & \ddots & & & & & & & \\ & & & & & & 0 & (uv)_{N_f+N_p} & & & & & \\ & & & & & & -(uv)_{N_f+N_p} & 0 & & & & & \\ & & & & & & & & 1 & & & & \\ & & & & & & & & & \ddots & & & \\ & & & & & & & & & & 1 & & \end{pmatrix} . \tag{3.12}$$

3.2 The EDF with pairing

In the same way as the Slater determinants from chapter 1, the HFB wavefunctions form a subspace in the Hilbert space of the many-body problem for some many-body Hamiltonian $\hat{\mathcal{H}}$. As in chapter 1, we can define a HFB energy as

$$E_{\mathsf{HFB}} = \langle \Psi_{\mathsf{HFB}} | \hat{\mathcal{H}} | \Psi_{\mathsf{HFB}} \rangle . \tag{3.13}$$

The reasons why a functional was introduced in chapter 1 still apply and we will be replacing the expectation value of the many-body Hamiltonian by a functional. We will add a term to the functional from section 1.4:

$$E_{\mathsf{HFB}} = E_{\mathsf{Kin}} + E_{\mathsf{Coul}} + E_{\mathsf{Skyrme}} + E_{\mathsf{Corr}} + E_{\mathsf{Pair}} . \tag{3.14}$$

The pairing energy term is not the only change in the the functional, as the mean-field densities from section 1.4.1 need to be modified when dealing with HFB many-body wavefunctions [11]. The E_{Kin}, E_{Coul} and E_{Skyrme} maintain identical forms as functions of the mean-field densities, but they get calculated differently

$$\rho_q(\mathbf{r}) = \sum_{j,\sigma} v_j^2 \psi_j^*(\mathbf{r},\sigma,q)\psi_j(\mathbf{r},\sigma,q) \tag{3.15a}$$

$$\tau_q(\mathbf{r}) = \sum_{j,\sigma} v_j^2 \left[\boldsymbol{\nabla}\psi_j^*(\mathbf{r},\sigma,q)\right]\cdot\left[\boldsymbol{\nabla}\psi_j(\mathbf{r},\sigma,q)\right] , \tag{3.15b}$$

$$J_{\mu\nu,q}(\mathbf{r}) = \frac{1}{2i}\sum_{\sigma_1,\sigma_2}\sigma_{\nu,\sigma_1,\sigma_2}\sum_j v_j^2\left(\left[\psi_j^*(\mathbf{r},\sigma_1,q)\right]\left[\nabla_\mu\psi_j(\mathbf{r},\sigma_2,q)\right] - \left[\nabla_\mu\psi_j^*(\mathbf{r},\sigma_1,q)\right]\left[\psi_i(\mathbf{r},\sigma_2,q)\right]\right) , \tag{3.15c}$$

$$s_{\mu,q}(\mathbf{r}) = \sum_{j,\sigma_1,\sigma_2} v_j^2\sigma_{\mu,\sigma_1,\sigma_2}\psi_j^*(\mathbf{r},\sigma_1,q)\psi_j(\mathbf{r},\sigma_2,q)\,, \tag{3.15d}$$

$$j_{\mu,q}(\mathbf{r}) = \frac{1}{2i}\sum_{j,\sigma} v_j^2\left(\left[\psi_j^*(\mathbf{r},\sigma,q)\right]\left[\nabla_\mu\psi_j(\mathbf{r},\sigma,q)\right] - \left[\nabla_\mu\psi_j^*(\mathbf{r},\sigma,q)\right]\left[\psi_j(\mathbf{r},\sigma,q)\right]\right) , \tag{3.15e}$$

$$T_{\mu,q}(\mathbf{r}) = \sum_{j,\sigma_1,\sigma_2} v_j^2\sigma_{\mu,\sigma_1,\sigma_2}\left[\boldsymbol{\nabla}\psi_j^*(\mathbf{r},\sigma_1,q)\right]\cdot\left[\boldsymbol{\nabla}\psi_j(\mathbf{r},\sigma_2,q)\right] , \tag{3.15f}$$

$$F_{\mu,q}(\mathbf{r}) = \frac{1}{2}\sum_{\nu,\sigma_1,\sigma_2}\sigma_{\nu,\sigma_1,\sigma_2}\sum_j v_j^2\left(\left[\nabla_\mu\psi_j^*(\mathbf{r},\sigma_1,q)\right]\left[\nabla_\nu\psi_j(\mathbf{r},\sigma_2,q)\right] + \left[\nabla_\nu\psi_j^*(\mathbf{r},\sigma_1,q)\right]\left[\nabla_\mu\ \psi_j(\mathbf{r},\sigma_2,q)\right]\right) . \tag{3.15g}$$

The main difference with the Hartree-Fock case is that the single-particle wavefunctions that enter the mean-field densities are no longer the $|\phi_j\rangle$ in the Hartree-Fock basis but rather the $|\psi_j\rangle$ from the canonical basis, weighted with the diagonal elements of the HFB density matrix v_l^2 in the canonical basis.
The term centre-of-mass term changes slightly too

$$E_{\mathsf{cm},1} = \frac{\hbar^2}{2M}\sum_j v_j^2\langle\psi_j|\boldsymbol{\nabla}^2|\psi_j\rangle\,, \tag{3.16}$$

where the $|\psi_j\rangle$ are again single-particle wavefunctions in the canonical basis and the occupation factors v_j^2 appear.
The truely new term E_{Pair} term takes the following form in the canonical basis

$$E_{\mathsf{Pair}} = \sum_{kl} u_k v_k u_l v_l f_l f_k \bar{v}_{k\bar{k}l\bar{l}}\,, \tag{3.17}$$

where the $f_k f_l$ are cutoff factors and $\bar{v}_{k\bar{k}m\bar{m}}$ are the antisymmetrized matrix elements of a pairing interaction, both of which we will specify later.
We can now obtain the analog of the Hartree-Fock equations for the HFB ansatz, by varying the HFB energy. However, the HFB wavefunction is not an eigenstate of the neutron- and proton-particle number operators $\hat{\mathcal{N}}_n$ and $\hat{\mathcal{N}}_p$. In order to have some control over the number of particles, we introduce the Fermi energies λ_n, λ_p as Lagrange multipliers in order for the variation to satisfy extra conditions on the number of protons and neutrons.
The variation is now over the entire space of HFB wavefunctions instead of only over the Slater determinants

$$\delta\left(E_{\mathsf{HFB}} - \langle\Psi_{\mathsf{HFB}}|\lambda_n\hat{\mathcal{N}}_n + \lambda_p\hat{\mathcal{N}}_p|\Psi_{\mathsf{HFB}}\rangle\right) = 0\,, \tag{3.18}$$

and needs to satisfy the subsidiary conditions

$$\langle\Psi_{\mathsf{HFB}}|\hat{\mathcal{N}}_n|\Psi_{\mathsf{HFB}}\rangle = N\,, \qquad \langle\Psi_{\mathsf{HFB}}|\hat{\mathcal{N}}_p|\Psi_{\mathsf{HFB}}\rangle = Z\,. \tag{3.19a}$$

3.3 The HFB equations

This variational problem leads to the HFB equations [11] for the matrices U and V. The column vectors built out of the columns of U and V, denoted together by $(U_k V_k)^T$, satisfy the following eigenvalue equations

$$\mathcal{H}_{\mathsf{HFB},q}\begin{pmatrix}U_{k,q}\\V_{k,q}\end{pmatrix} = \begin{pmatrix}h-\lambda_q & \Delta_q\\ -\Delta_q^* & -h^*+\lambda_q\end{pmatrix}\begin{pmatrix}U_{k,q}\\V_{k,q}\end{pmatrix} = E_k^{qp}\begin{pmatrix}U_{k,q}\\V_{k,q}\end{pmatrix} . \tag{3.20}$$

Here q is an isospin index and we have decoupled the problem into two separate subproblems for protons and neutrons, since we assume z-isospin symmetry.
The numbers E_k^{qp} are necessarily real and are called the quasiparticle energies. The matrix $\hat{h}$ is the single-particle Hamiltonian from chapter 1, the derivative of the functional with respect to the density matrix ρ. The matrix Δ is its analogue [32]

$$\Delta_{ij,q} = \frac{\partial E_{\mathsf{HFB}}}{\partial \kappa^*_{ij,q}} = \frac{1}{2}\sum_{kl} f_k f_l \bar{v}_{ijkl}\kappa_{kl,q}\,, \tag{3.21}$$

where the cutoff factors and the pairing interaction are still left to be specified, and the sum is only over states with isospin q. The HFB equations can be summarized, using the generalized density matrix, as (dropping the isospin index for ease of notation)

$$\left[\hat{\mathcal{H}}_{\mathsf{HFB}}, \hat{\mathcal{R}}\right] = 0\,, \tag{3.22}$$

which is very reminiscent of the Hartree-Fock equations. As their analogs, the HFB equations also present a self-consistent problem: $\hat{\mathcal{H}}_{\mathsf{HFB}}$ depends on ρ and κ, which in turn can only be calculated starting from $\hat{\mathcal{H}}_{\mathsf{HFB}}$. We therefore need an iterative method to solve these equations. The practical details we defer to chapter 6. There is however an important subtlety to solving the HFB equations. They posses an innate symmetry, that is most easily visible from Eq. (3.20): for every eigenvector $(U_k V_k)^T$ of the HFB Hamiltonian with eigenvalue E_k^{qp}, there exists another eigenvector with eigenvalue $-E_k^{qp}$. One can easily check that

$$\hat{\mathcal{H}}_{\mathsf{HFB}} \begin{pmatrix} V_k^* \\ U_k^* \end{pmatrix} = -E_k^{qp} \begin{pmatrix} V_k^* \\ U_k^* \end{pmatrix}\,. \tag{3.23}$$

This symmetry is due to the inherent choice we make in assigning the transformation in Eq. (3.1) to the creation operator $\hat{\beta}_k^\dagger$ while we could just as easily have assigned it to the annihilation operator $\hat{\beta}_k$.
The HFB Hamiltonian has thus 2Ω eigenvectors, while we need only Ω of those eigenvectors to determine the quasiparticle operators, and we are thus forced to make a choice. This choice, for every index k, boils down to assigning the right-hand side of Eq. (3.1) to either a creation or annihilation operator. Note that we can never choose both eigenvectors with eigenvalues E_k^{qp} and $-E_k^{qp}$ as this would invalidate the unitarity of the transformation. In the end, the HFB vacuum in Eq. (3.7) is thus far from uniquely defined, as there are in fact 2^n possible choices. How this choice should be made is only seldom discussed in detail but of vital importance to select the configuration of interest. Notable exceptions are [68, 69, 70].
For most applications, it is usually silently assumed that the positive values of E_k^{qp} [11] should be chosen to have the configuration with minimal energy. This choice corresponds to the Hartree-Fock choice of groundstate in the limit of vanishing pairing. Usually, one uses conserved symmetries to guide the choice in HFB vacuum, and the choice of positive quasiparticle energies is usually a natural one. When one breaks symmetries however, this choice is not necessarily sound. We will come back to this topic in more detail in chapter 6.

3.4 Gauge invariance: pairing as a broken symmetry

The aim of the HFB ansatz is to enlarge the variational space of the Slater determinants by including some measure of correlations between particles. In chapter 2 we also enlarged the total variational space by breaking symmetries. It should come as no surprise that pairing in a mean-field approach can thus be viewed as breaking another symmetry. Consider the many-body particle number operator (of isospin q)

$$\hat{\mathcal{N}}_q = \sum_i \hat{a}_{i,q}^\dagger \hat{a}_{i,q}\,, \tag{3.24}$$

One can define unitary gauge rotation operators $\hat{R}_q(\alpha)$ as a function of a real parameter α

$$\hat{R}_q(\alpha) = \exp\left[-i\alpha\hat{\mathcal{N}}_q\right]\,. \tag{3.25}$$

A Slater determinant is always a an eigenstate of the number operators $\hat{\mathcal{N}}_q$ since it has a definite number of protons and neutrons. This automatically makes any Slater determinant invariant (up to a complex phase) under the action of the gauge rotation operators. The HFB states are in general no longer eigenstates of this operator. We could thus have added another group structure to both $\mathcal{D}_{2h}^T$ and $\mathcal{D}_{2h}^{TD}$ in chapter 2.
Number parity, however is a conserved symmetry in the HFB scheme. Its associated unitary operator Π_N is

$$\hat{\Pi}_{N,q} = e^{-i\pi\hat{\mathcal{N}}_q}\,, \tag{3.26}$$

	Linear, hermitian	Linear, antihermitian	$\check{\mathcal{P}}^T, \check{\mathcal{T}}$	Antilinear
$\rho =$	$\begin{pmatrix} \rho_1 & 0 \\ 0 & \rho_2 \end{pmatrix}$	$\begin{pmatrix} \rho_1 & 0 \\ 0 & \rho_2 \end{pmatrix}$	$\begin{pmatrix} \rho_1 & \rho_2 \\ \rho_2 & \rho_1 \end{pmatrix}$	ρ^*
$h =$	$\begin{pmatrix} h_1 & 0 \\ 0 & h_2 \end{pmatrix}$	$\begin{pmatrix} h_1 & 0 \\ 0 & h_2 \end{pmatrix}$	$\begin{pmatrix} h_1 & h_2 \\ h_2 & h_1 \end{pmatrix}$	h^*
$\kappa =$	$\begin{pmatrix} \kappa_1 & 0 \\ 0 & \kappa_2 \end{pmatrix}$	$\begin{pmatrix} 0 & -\kappa_1 \\ \kappa_1 & 0 \end{pmatrix}$	$\begin{pmatrix} \kappa_1 & -\kappa_2 \\ \kappa_2 & -\kappa_1 \end{pmatrix}$	κ^*
$\Delta =$	$\begin{pmatrix} \Delta_1 & 0 \\ 0 & \Delta_2 \end{pmatrix}$	$\begin{pmatrix} 0 & -\Delta_1 \\ \Delta_1 & 0 \end{pmatrix}$	$\begin{pmatrix} \Delta_1 & -\Delta_2 \\ \Delta_2 & -\Delta_1 \end{pmatrix}$	Δ^*

Table 3.1: Schematic representation of the structure imposed on the HFB and BCS pairing matrices due to conservation of various types of symmetries.

which corresponds to gauge rotations of $180°$. If a HFB state is a superposition of many-body states with even particle number, its number parity is equal to $+1$. If it is instead a super position of many-body states with odd particle number, its quantum number of -1. In practical calculations, the number parity of a HFB state can be determined by the number of eigenvalues v_k^2 of the density matrix ρ that are exactly equal to one [68]. This is of course equal to the number of filled orbitals N_f in Eq. (3.5).
The most natural order parameter associated with this symmetry is the dispersion $\Delta\mathcal{N}_q^2$.

$$\Delta\mathcal{N}_q^2 = \langle\hat{\mathcal{N}}_q^2\rangle - \langle\hat{\mathcal{N}}_q\rangle^2 \,. \tag{3.27}$$

It is zero when the mean-field state is an eigenstate of $\hat{\mathcal{N}}_q$ but is non-zero when at least some pairing is present. As with the other symmetry operators, gauge symmetry is subject to projection methods, either exactly or approximately, examples are [33] and [71], respectively.

3.5 Symmetry conservation

Conservation of symmetries often entail a significant simplification of the pairing equations discussed above. Just as isospin decouples the equations for neutrons and protons, conserved symmetries of $\hat{\mathcal{D}}_{2h}^T$ and $\hat{\mathcal{D}}_{2h}^{TD}$ imply specific structure of ρ and κ (and consequently Δ). In what follows, we will distinguish between linear and antilinear symmetry operators.
In Table 3.1 we summarize schematically the consequences that conserved symmetries have on the structure of the pairing matrices depending on their classification. Note that the same line of arguments that we used for ρ can be used for h, and the one for κ can be utilized for Δ, since these are closely related. While this section might seem rather technical and abstract, we will detail at length in chapter 6 how these considerations can be exploited in practice.

Linear operator $\hat{\mathcal{U}}$

For any conserved linear symmetry $\hat{\mathcal{U}}$, we are free to consider the single-particle states to be eigenstates of the corresponding single-particle operator $\hat{U}$ with eigenvalues u_k with module one. We then find for the density and anomalous density

$$\rho_{ij} = \langle\Psi|\hat{a}_j^\dagger\hat{a}_i|\Psi\rangle = \langle\Psi|\hat{\mathcal{U}}^\dagger\hat{a}_j^\dagger\hat{a}_i\hat{\mathcal{U}}|\Psi\rangle = u_j^* u_i \rho_{ij} \,, \tag{3.28a}$$

$$\kappa_{ij} = \langle\Psi|\hat{a}_j\hat{a}_i|\Psi\rangle = \langle\Psi|\hat{\mathcal{U}}^\dagger\hat{a}_j\hat{a}_i\hat{\mathcal{U}}|\Psi\rangle = u_j u_i \rho_{ij} \,. \tag{3.28b}$$

It directly follows that if $u_j^* u_i = -1$ that ρ_{ij} is necessarily zero and similarly when $u_j u_i = -1$ for κ_{ij}. If $\hat{U}$ is hermitian, this happens when the $|\phi_i\rangle$ and $|\phi_j\rangle$ have different quantum numbers $u_i \neq u_j$. Thus, pairing between both levels is forbidden, as both κ_{ij} and ρ_{ij} are zero. If $\hat{U}$ is antihermitian however, $\rho_{ij} = 0$ if $u_i \neq u_j$ while $\kappa_{ij} = 0$ if $u_i = u_j$. The hermitian and antihermitian conserved linear operators thus give rise to a different block structure in ρ, κ and Δ.
This block-structure is directly reflected in the Bogoliubov transformation. We have similar relations for the

$\hat{\beta}_k$ as we had for the $\hat{a}_k$

$$\hat{\mathcal{U}}^\dagger \hat{\beta}_k^\dagger \hat{\mathcal{U}} = u_k \hat{\beta}_k \,, \tag{3.29a}$$

$$\hat{\mathcal{U}}^\dagger \hat{\beta}_k \hat{\mathcal{U}} = u_k^* \hat{\beta}_k \,. \tag{3.29b}$$

For hermitian symmetries, the Bogoliubov transformation does not mix creation and annihilation operators of different eigenvalues. For antihermitian operators, the Bogoliubov mixes creation operators of levels with eigenvalue $+i$ with annihilation operators of levels with eigenvalue $-i$, and vice versa.

Antilinear operator $\check{\mathcal{U}}$

Consider this time an antilinear, hermitian[1] operator $\check{\mathcal{U}}$. The HFB wavefunction $|\Psi\rangle$ can be chosen as an invariant and we have then

$$\rho_{ij} = \langle\Psi|\hat{a}_j^\dagger \hat{a}_i|\Psi\rangle = \langle\Psi|\check{\mathcal{U}}^\dagger \hat{a}_j^\dagger \hat{a}_i \check{\mathcal{U}}|\Psi\rangle = \langle\Psi|\hat{a}_j^\dagger \hat{a}_i|\Psi\rangle^* = \rho_{ij}^* \,, \tag{3.30a}$$

$$\kappa_{ij} = \langle\Psi|\hat{a}_j \hat{a}_i|\Psi\rangle = \langle\Psi|\check{\mathcal{U}}^\dagger \hat{a}_j^\dagger \hat{a}_i \check{\mathcal{U}}|\Psi\rangle = \langle\Psi|\hat{a}_j \hat{a}_i|\Psi\rangle^* = \kappa_{ij}^* \,. \tag{3.30b}$$

Choosing the many-body state as an invariant of $\check{\mathcal{U}}$ does not introduce a block structure, but does imply ρ and κ to be real.
There is however, a block structure that is induced if the corresponding single-particle operator is antihermitian and antilinear[2]. In that case, we can assume the single-particle levels come in normal pairs $(k, \bar{k})$[3] We have then

$$\rho_{ij} = \langle\Psi|\hat{a}_j^\dagger \hat{a}_i|\Psi\rangle = \langle\Psi|\check{\mathcal{U}}^\dagger \hat{a}_j^\dagger \hat{a}_i \check{\mathcal{U}}|\Psi\rangle = +\rho_{\bar{i}\bar{j}} \tag{3.31a}$$

$$\kappa_{ij} = \langle\Psi|\hat{a}_j \hat{a}_i|\Psi\rangle = \langle\Psi|\check{\mathcal{U}}^\dagger \hat{a}_j \hat{a}_i \check{\mathcal{U}}|\Psi\rangle = -\kappa_{\bar{i}\bar{j}} \,, \tag{3.31b}$$

Note that this structure implies that the canonically conjugate states in the canonical basis form exactly the normal pairs of the antilinear operator $\check{U}$.

3.6 The HF+BCS approximation

If time-reversal[4] is conserved, we can impose an extra assumption: that the canonical basis is equal to the Hartree-Fock basis. In that case, the density matrix is diagonal in the Hartree-Fock basis and directly offers up the occupation factors v_k^2, while κ is in its canonical form in the Hartree-Fock basis: κ_{ij} is only non-zero if j is the time-reversed partner of i. The quasiparticle operators can then simply be built out of the single-particle operators and their time-reversed partners, as in Eq. (3.20). The Bardeen-Cooper-Schrieffer (BCS) many-body state can then be written as [72, 11]

$$|\Psi_{BCS}\rangle = \prod_{k>0} \left(u_k + v_k \hat{a}_k^\dagger \hat{a}_{\bar{k}}^\dagger\right) |0\rangle \,, \tag{3.32}$$

where the notation $k > 0$ signifies that the product is only over half of the single-particle states. This simplifies many equations considerably. One no longer needs to diagonalize the HFB Hamiltonian, and it is possible to write down immediately the quasiparticle energies E_k^{qp}[5]

$$E_k^{qp} = \sqrt{(\epsilon_k - \lambda_q)^2 + \Delta_{k\bar{k}}^2} \,. \tag{3.33}$$

where ϵ_k is the single-particle energy of the single-particle wavefunction $|\phi_k\rangle$ in the Hartree-Fock basis. From the quasiparticle energies, one can directly solve for the u_k^2 and v_k^2 [11]

$$v_k^2 = \frac{1}{2}\left[1 - \frac{\epsilon_k - \lambda_q}{E_k^{qp}}\right] \,, \tag{3.34a}$$

$$u_k^2 = \frac{1}{2}\left[1 + \frac{\epsilon_k - \lambda_q}{E_k^{qp}}\right] \,. \tag{3.34b}$$

[1] An antihermitian, antilinear operator can never be conserved and we omit this case.

[2] For the symmetry operators from the previous chapter, this is only the case for $\check{\mathcal{T}}$ and $\check{\mathcal{P}}^T$ in even systems.

[3] Note that the notation of the conjugate state $\bar{k}$ of k in the sense of the canonical basis and the normal partner $\bar{k}$ of k is the same, and these are not necessarily the same single-particle state. In the rest of this dissertation, the context should make it clear what the notation $\bar{k}$ means.

[4] Note that this implies that ρ and κ will always be real matrices when using the BCS ansatz, see the previous section.

[5] Note that this formula differs slightly from Eq. (22) in [72], since our definition of Δ includes another cutoff factor that is not incorporated in Eq. (23) in the same paper.

While the HF+BCS equations are significantly easier to solve compared to the HFB equations, they still represent a self-consistent problem. The gap equation [11] for the matrix Δ will be instrumental for the practical implementation in chapter 6.

$$\Delta_{k\bar{k}} = -\frac{1}{2}\sum_{l} f_l f_k \bar{v}_{k\bar{k}l\bar{l}} \frac{\Delta_{l\bar{l}}}{E_l^{qp}} \,. \tag{3.35}$$

3.7 Quasiparticle excitations

The treatment of nuclei with an odd number of particles (either protons, neutrons or protons and neutrons) merits some extra attention. Let us start by noting that the BCS approximation can never truly describe such a nucleus: the BCS ansatz Eq. (3.32) is a superposition of many-body states with an even number of particles. One can of course constrain the number of particles to be odd, using the Fermi energies as Lagrange multipliers. Such a construction is called a false vacuum, since the many-body state has the correct number of particles on average, but still conserves time-reversal.
In the case of full HFB treatment, one can also construct a false vacuum while still conserving time-reversal. But time-reversal conservation is not a necessity and we can do better. The possibility of choosing the HFB vacuum plays a fundamental role here. Consider an initial choice of eigenvectors of the HFB Hamiltonian that corresponds to an even-even configuration, with a set of eigenvectors $(U_k V_k)^T$. Let us now change from the original vacuum $|\Psi_{\text{HFB}}\rangle$ to another one $|\Psi'_{\text{HFB}}\rangle$ by making for one specific index k the following transformation

$$\begin{pmatrix} \beta_k \\ \beta_k^\dagger \end{pmatrix} \rightarrow \begin{pmatrix} \beta_k^\dagger \\ \beta_k \end{pmatrix} . \tag{3.36}$$

In terms of the eigenvectors of the HFB Hamiltonian this amounts to

$$\begin{pmatrix} U_k \\ V_k \end{pmatrix} \rightarrow \begin{pmatrix} V_k^* \\ U_k^* \end{pmatrix} . \tag{3.37}$$

This is a valid transformation, as one can check that the fermion commutation relations are still satisfied. Note that the following equation holds (with the original $\hat{\beta}_k^\dagger$)

$$\hat{\beta}_k^\dagger \hat{\beta}_k^\dagger |\Psi_{\text{HFB}}\rangle = 0 \,, \tag{3.38}$$

simply because we are dealing with fermions. This means that $\hat{\beta}_k^\dagger|\Psi_{\text{HFB}}\rangle$ is in fact annihilated by $\hat{\beta}_k^\dagger$, so $\hat{\beta}_k^\dagger|\Psi_{\text{HFB}}\rangle$ satisfies the conditions of the HFB vacuum to be annihilated by all of the quasiparticle annihilation operators, after the transformation in Eq. (3.36). It is thus safe to say that (up to a complex phase)

$$|\Psi'_{\text{HFB}}\rangle = \beta_k^\dagger |\Psi_{\text{HFB}}\rangle \,. \tag{3.39}$$

The HFB vacuum has changed dramatically by creating an extra quasiparticle, it is now an odd HFB state. Since $|\Psi_{\text{HFB}}\rangle$ is a superposition of many-body wavefunctions with even particle number, $|\Psi'_{\text{HFB}}\rangle$ is necessarily a superposition of many-body states with odd particle number, with odd number parity.
The creation of a quasiparticle excitation also fundamentally changes the density ρ' and anomalous density matrix κ'. One can check that [73], in terms of the original $(U, V)^T$,

$$\rho'_{ij} = \rho_{ij} + U_{ik}U^*_{jk} - V^*_{ik}V_{jk} \tag{3.40}$$

$$\kappa'_{ij} = \kappa_{ij} + U_{ik}V^*_{jk} - V^*_{ik}U_{jk} \,. \tag{3.41}$$

Note that from this follows that $\rho'_{kk} = 1$ in the canonical basis, since in this basis the V-matrices have no diagonal elements and the conditions in Eqs. (3.3) ensure the other terms combine to one. The quasiparticle with index k is thus fully occupied and does not engage in pairing correlations. This kind of HFB vacuum is thus often called a blocked state.
We can keep acting with quasiparticle creation operators on $|\Psi'_{\text{HFB}}\rangle$ to create even more quasiparticle excitations, provided we don't repeat creation operators, and in this way we can generate all of possible HFB vacua. Depending on the number of quasiparticle creation operators we get either even or odd HFB states. The practical challenge will be to identify the quasiparticles of interest and consistently block them in a self-consistent procedure. This is already difficult with conserved symmetries and gets progressively harder as more symmetries are broken. We will go more into detail about this in 6.

3.8 The Thouless theorem

An alternative characterization of HFB states that we will use in chapter 6 is due to Thouless [11]. Starting from a HFB state $|\Psi_{\mathsf{HFB}}\rangle$, we can use the the Thouless' operator $\hat{\theta}(Z)$ to construct a new HFB state $|\Psi'_{\mathsf{HFB}}\rangle$ as follows

$$|\Psi'_{\mathsf{HFB}}\rangle = \hat{\theta}(Z)|\Psi_{\mathsf{HFB}}\rangle = A \exp\left[-\frac{1}{2}\sum_{ij} Z_{ij}\beta_i^\dagger\beta_j^\dagger\right]|\Psi_{\mathsf{HFB}}\rangle\,, \tag{3.42}$$

where A is a normalization constant and the matrix Z_{ij} are the Thouless coefficients. Since the Thouless operator contains only products of even numbers of quasiparticle creation operators, it is impossible to change the number parity of a state by using it: $|\Psi'_{\mathsf{HFB}}\rangle$ shares the number parity of $|\Psi_{\mathsf{HFB}}\rangle$.
The Thouless theorem [74, 11], states that it is possible to construct *any* HFB wave-function $|\Psi_{\mathsf{HFB}}\rangle$ using an appropriate matrix Z, providing it is not orthogonal to the reference state $|\Psi'_{\mathsf{HFB}}\rangle$. In this sense, when a reference state is fixed, all HFB states that are not orthogonal to the reference state can be characterized by their corresponding matrix Z.

3.9 The pairing interaction

For all calculations that involve pairing in this dissertation we use the following pairing interaction, first introduced in [75]:

$$\hat{v}_q(\vec{r},\vec{r}') = -V_q\left[1-\frac{\alpha}{\rho_s}\rho_0(\vec{R})\right]\delta(\vec{r}-\vec{r}')\,, \tag{3.43}$$

where q is an isospin index, V_q is the pairing strength per particle species, ρ_s is the saturation density we fix at 0.16 fm^{-3} and $\vec{R} = \frac{\vec{r}+\vec{r}'}{2}$. This interaction enters the pairing equations through the pairing energy term in Eq. (3.14) and appears consequently in the matrix Δ.
Note that this interaction is purely phenomenological and has a priori nothing to do with the other terms of the EDF. In this dissertation we treat the EDF as the fundamental object, and the pairing interaction simply enters as an ingredient of an extra term of the functional that can be included in fits. If the relation between the expectation value of a many-body Hamiltonian and the functional needs to be enforced the same many-body Hamiltonian should be taken to generate pairing correlations [16].
Nevertheless, the parameters α, V_n and V_p[6] have historically only very rarely been incorporated in the fits of functionals to experimental data. The UNEDF family of parameterizations [76, 77, 78] are recent exceptions to this rule where the pairing interaction was included into the fits. Nevertheless, the effect of a given pairing interaction used during the fit is very dependent on the type of single-particle basis used for the fitting procedure, and it is in general very difficult to reproduce the calculations perfectly when using a different numerical scheme. In the case of the UNEDF parameterizations, the optimization was performed using a basis of harmonical oscillator wavefunctions and it is practically impossible for a method based on Lagrange meshes can reproduce the effect of this pairing interaction. Because of these considerations, the parameters V_n, V_p are usually adjusted ad-hoc to the mass region one wishes to study. This has historically been done to the experimental three-point pairing gaps of nuclei [79] or to moments of inertia along rotational bands [80]. In contrast, α is usually just set to 1.
As the interaction in Eq. (3.43) is zero-range, it diverges when we take into account more and more single-particle states. The cutoff functions in the pairing term in Eq. (3.14) are introduced precisely to combat this divergence. All of the calculations in this dissertation employ a symmetric Fermi cutoff around the Fermi energy f_k^{Fermi}, parametrized as [75]

$$f_k^{\mathsf{Fermi}} = \left[1+\exp\left[\mu^{-1}\left(\epsilon_k-\lambda_q-\Delta e_q\right)\right]\right]^{-\frac{1}{2}}\left[1+\exp\left[\mu^{-1}\left(\epsilon_k-\lambda_q+\Delta e_q\right)\right]\right]^{-\frac{1}{2}}\,, \tag{3.44}$$

where ϵ_k is the single-particle energy of the single-particle wavefunction $|\psi_k\rangle$ in the Hartree-Fock basis. This cutoff effectively limits the pairing correlations to single-particle states within roughly Δe_q around the Fermi energy λ_q. The parameters μ and Δe_q are input parameters of `MOCCa`, respectively denoted in chapter 11 by `PairingMu`, `CutProton` and `CutNeutron`.
Another parameterization of the cutoff functions f_k^{cosine} that is implemented in `MOCCa` (though not used in

[6] Or even more in general, the parameters of the pairing interaction, regardless of its prescription.

this dissertation) is given by [81]

$$f_k^{\text{cosine}} = \begin{cases} 1 & \text{if} \quad (\epsilon_k - \lambda_q) \leq E_{q,-} \\ \frac{1}{2}\left(\cos\left[\frac{\pi}{2}\left|\epsilon_k - \lambda\right| - E_{q,-}\right] + 1\right) & \text{if} \quad E_{q,-} \leq (\epsilon_k - \lambda_q) \leq E_{q,+} \\ 0 & \text{if} \quad (\epsilon_k - \lambda_q) \geq E_{q,+} \end{cases} \tag{3.45a}$$

$$E_{q,\pm} = \Delta e_q \pm \frac{\mu}{2}\,. \tag{3.45b}$$

This type of cutoff is dependent on the same input parameters μ and Δe_q that correspond to the same keywords. Switching between both can be achieved by the keyword `Cutofftype`: (1) for the Fermi cutoff and (2) for the cosine cutoff.

Part II

Numerical considerations

Chapter **4**

Numerical Implementation

In this chapter, we will detail how MOCCa represents the single-particle wavefunctions in coordinate space, and how this representation can use various assumptions of symmetries of the single-particle wavefunctions.
Section 4.1 introduces the concept of the cubic Lagrange mesh. The symmetry options of MOCCa are discussed in section 4.2, while the properties of the single-particle wavefunctions are introduced in section 4.3. The numerical optimization procedure, steepest descent, is introduced in section 4.4, while the difficulty of choosing a step size is briefly described in section 4.5. We will also compare to a different numerical scheme, as used in different mean-field codes in section 4.6. The calculation of the mean-field densities and the potentials, and more specifically the numerical implementation of density mixing and the calculation of the Coulomb potential is discussed in section 4.7. Particularly important is judging the convergence of the method, in section 4.8. As a final part of this chapter, section 4.9 presents some promising possibilities of improving the numerical scheme.

4.1 Coordinate space representation: The Lagrange mesh

In order to solve the Hartree-Fock equations from chapter 1 (and the pairing equations from chapter 3) we need to represent the single-particle wavefunctions $|\phi_l\rangle$ both in the Hartree-Fock and the canonical basis. A popular choice made in several other programs is expanding them on a basis of harmonic oscillator wavefunctions. Several different ways of doing this have been explored in the literature, see for instance [83, 84, 85].
MOCCa employs a cubic Cartesian mesh. Such a mesh is categorized by dx, the distance between nearest-neighbour points in fm and (N_X, N_Y, N_Z) the number of points in every Cartesian direction. The coordinates (x_i, y_j, z_k) of the mesh point in the full box are given by

$$x_i = \left(i - \frac{N_X}{2} - 1\right) dx \qquad i = 1, \ldots, N_X\,, \tag{4.1a}$$

$$y_j = \left(j - \frac{N_Y}{2} - 1\right) dx \qquad j = 1, \ldots, N_Y\,, \tag{4.1b}$$

$$z_k = \left(k - \frac{N_Z}{2} - 1\right) dx \qquad k = 1, \ldots, N_Z\,. \tag{4.1c}$$

Note that the origin is not part of the cubic mesh, thereby avoiding possible numerical difficulties when dealing with diverging potentials. Fig 4.1 offers a two-dimensional restriction of the point distribution of the points on the mesh.
As it turns out, this simple grid structure is a realisation of a Lagrange mesh [86, 87]. This allows us to define first and second derivatives of a function f on the mesh as follows [72]

$$\left.\frac{\partial_L f}{\partial x}\right|_{x=x_i} = \sum_{j=1,N_X}^{j\neq i} (-1)^{(i-j)} \frac{\pi}{N_X dx} \frac{1}{\sin\left(\pi(i-j)/N_X\right)} f(x_j)\,, \tag{4.2a}$$

$$\left.\frac{\partial_L^2 f}{\partial^2 x}\right|_{x=x_i} = -\frac{\pi^2}{3dx^2}\left(1 - \frac{1}{N_X^2}\right) f(x_i) + \sum_{j=1,N_X}^{j\neq i} (-1)^{i-j} \left(\frac{2\pi}{N_X dx}\right)^2 \frac{\cos\left[\pi(i-j)/N_X\right]}{\sin^2\left[\pi(i-j)/N_X\right]} f(x_j) \tag{4.2b}$$

with similar formulas for derivatives in the y- and z-directions. Thus, the calculation of a derivative on the Lagrange mesh amounts in practice to a matrix multiplication. This matrix is a dense matrix, and the total amount of operations to be done increases as $N_X^2 N_Y^2 N_Z^2$. Note that these definitions are internally consistent, meaning more precisely that

$$\boldsymbol{\nabla}_L \cdot \boldsymbol{\nabla}_L \neq \Delta_L\,. \tag{4.3}$$

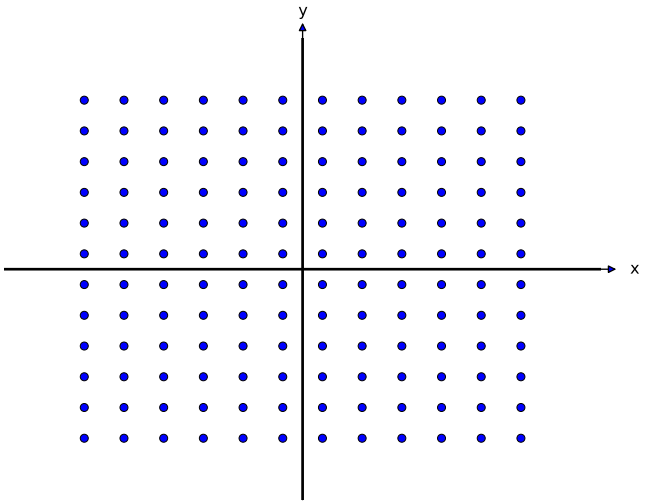

Figure 4.1: Two-dimensional representation of the point distribution on the Lagrange mesh.

Order	a_1	a_2	a_3	a_4	b_0	b_1	b_2	b_3	b_4
1	$\frac{1}{2}$				-2	1			
2	$\frac{2}{3}$	$-\frac{1}{12}$			$-\frac{5}{2}$	$\frac{4}{3}$	$-\frac{1}{12}$		
3	$\frac{3}{4}$	$-\frac{3}{20}$	$\frac{1}{60}$		$-\frac{49}{18}$	$\frac{3}{2}$	$-\frac{3}{20}$	$\frac{1}{90}$	
4	$\frac{4}{5}$	$-\frac{1}{5}$	$\frac{4}{105}$	$-\frac{1}{280}$	$-\frac{205}{75}$	$\frac{8}{5}$	$-\frac{1}{5}$	$\frac{8}{315}$	$-\frac{1}{560}$

Table 4.1: Finite difference coefficients for the first (a_j) and second derivative (b_j) on the mesh [82].

Since the cost of dense matrix multiplication becomes prohibitive for large meshes, MOCCa is also able to use finite difference formula to approximate the derivatives. For completeness' sake, we write the general formulas for the finite difference scheme of order N

$$\left.\frac{\partial_{FD} f}{\partial x}\right|_{x=x_i} = dx^{-1} \left[\sum_{j=1,N} a_j \left[f(x_{i-j}) - f(x_{i+j}) \right] \right] , \tag{4.4a}$$

$$\left.\frac{\partial^2_{FD} f}{\partial^2 x}\right|_{x=x_i} = dx^{-2} \left[b_0 f(x_i) + \sum_{j=1,N} b_j \left[f(x_{i-j}) + f(x_{i+j}) \right] \right] , \tag{4.4b}$$

and similar for derivatives in the y- and z-directions. The coefficients a_j and b_j that are included with the current version of MOCCa are shown in Table 4.1.
Calculating derivatives with finite difference formulas still amounts to a matrix multiplication, but for lower orders N the matrix is sparse, resulting in a number of operations proportional to $N_X N_Y N_Z$. Compared to the quadratic effort needed for Lagrange derivatives, this linear scaling is most welcome. The price to pay is however is that finite differences do not share all qualities of exact derivatives: partial integration is not exact and more importantly

$$\boldsymbol{\nabla}_{FD} \cdot \boldsymbol{\nabla}_{FD} \neq \Delta_{FD} . \tag{4.5}$$

There is a an extra point of subtlety regarding the boundary conditions of both formulas. The Lagrange derivatives reflect a configuration that is periodic in space [86], the derivatives reflect periodic boundary conditions at the edges of the mesh. In contrast, the finite difference derivatives assume the nuclear density to go to zero at the edges of the box and the terms in Eq. (4.4) for which $i - j \leq 1$ or $i + j \geq N$ simply get set to zero. For sufficiently large mesh sizes (depending on the mesh discretisation as well as the nucleus under consideration) both effects are negligible.
All of these considerations mean that finite difference formulas imply a loss of accuracy compared to Lagrange

Generators	Broken	Equivalent code
$\hat{\mathcal{P}}, \check{\mathcal{S}}_y^T, \hat{\mathcal{R}}_z, \check{\mathcal{T}}$	None	ev8
$\check{\mathcal{S}}_y^T, \hat{\mathcal{R}}_z, \check{\mathcal{T}}$	$\hat{\mathcal{P}}$	ev4
$\check{\mathcal{S}}_y^T, \hat{\mathcal{R}}_z, \hat{\mathcal{P}}$	$\check{\mathcal{T}}$	cr8
$\hat{\mathcal{P}}, \hat{\mathcal{R}}_z, \check{\mathcal{T}}$	$\check{\mathcal{S}}_y^T$	None
$\hat{\mathcal{P}}, \check{\mathcal{S}}_y^T, \check{\mathcal{T}}$	$\hat{\mathcal{R}}_z$	None
$\check{\mathcal{S}}_y^T, \hat{\mathcal{R}}_z$	$\check{\mathcal{T}}, \hat{\mathcal{P}}$	None
$\check{\mathcal{S}}_y^T, \check{\mathcal{T}}$	$\hat{\mathcal{R}}_z, \hat{\mathcal{P}}$	None
$\hat{\mathcal{R}}_z, \check{\mathcal{T}}$	$\check{\mathcal{S}}_y^T, \hat{\mathcal{P}}$	None

Generators	Broken	Equivalent code
$\hat{\mathcal{P}}, \check{\mathcal{T}}$	$\check{\mathcal{S}}_y^T, \hat{\mathcal{R}}_z$	None
$\hat{\mathcal{P}}, \check{\mathcal{S}}_y^T$	$\check{\mathcal{T}}, \hat{\mathcal{R}}_z$	None
$\hat{\mathcal{P}}, \hat{\mathcal{R}}_z$	$\check{\mathcal{T}}, \check{\mathcal{S}}_y^T$	None
$\hat{\mathcal{P}}$	$\check{\mathcal{T}}, \check{\mathcal{S}}_y^T, \hat{\mathcal{R}}_z$	None
$\check{\mathcal{T}}$	$\hat{\mathcal{P}}, \check{\mathcal{S}}_y^T, \hat{\mathcal{R}}_z$	None
$\check{\mathcal{S}}_y^T$	$\check{\mathcal{T}}, \hat{\mathcal{P}}, \hat{\mathcal{R}}_z$	None
$\hat{\mathcal{R}}_z$	$\check{\mathcal{T}}, \check{\mathcal{S}}_y^T, \hat{\mathcal{P}}$	None
None	$\hat{\mathcal{P}}, \check{\mathcal{S}}_y^T, \hat{\mathcal{R}}_z, \check{\mathcal{T}}$	None

Table 4.2: Possible choices for the generators of the conserved symmetry groups in MOCCa.

derivatives. We will study the accuracy of the Lagrange mesh representation in more detail in chapter 8. Integrals on the other hand can be obtained by simple summation

$$\int dx\, dy\, dz\, f(x,y,z) = dx^3 \sum_{i=1}^{N_X} \sum_{j=1}^{N_Y} \sum_{k=1}^{N_Z} f(x_i, y_i, z_i)\,. \tag{4.6}$$

In fact, the Lagrange derivatives in Eq. (4.2) are constructed such that this special case of Gauss quadrature is the exact inverse of the Lagrange derivative, meaning that

$$\int dx\, \frac{\partial_L f(x,y,z)}{\partial x} = f(x,y,z)\,, \tag{4.7}$$

a property that again does not hold for finite difference derivatives.

4.2 Symmetries in MOCCa

The Cartesian Lagrange mesh presents a natural way of breaking spherical and axial symmetry: any possible function $f(\mathbf{r})$ is numerically never exactly invariant under rotations. The possible symmetry groups on the mesh are thus the subgroups of either $\mathcal{D}_{2h}^T$ or $\mathcal{D}_{2h}^{TD}$. MOCCa is unfortunately not constructed to be able to solve the mean-field equations for every possible subgroup. As in chapter 2, we will index the options currently implemented by their generator generators. The following four generators can either be conserved or broken

$$\hat{\mathcal{P}}, \hat{\mathcal{R}}_z, \check{\mathcal{T}} \text{ and } \check{\mathcal{S}}_y^T. \tag{4.8}$$

The sixteen possible choices of subgroups this gives the user are listed in Table 4.2. Among them are the three choices that can reproduce the old codes ev8, cr8 and ev4. Note that the full groups $\mathcal{D}_{2h}^T$ and $\mathcal{D}_{2h}^{TD}$ are also represented, as well as the trivial group $\left\{\hat{\mathbb{1}}\right\}$ that conserves no symmetries. These sixteen choices do not represent all of the subgroups discussed in chapter 2, especially when we include z-isospin symmetry breaking.
On the other hand, all of the physical cases discussed in section 2.9 can be studied using MOCCa. Table 4.3 lists all of these cases, and the corresponding set of symmetries to conserve and break in MOCCa. This list is not comprehensive, as each of these degrees of freedom can be combined with the others.

4.3 Single-particle wavefunctions and their quantum numbers

In order to solve the mean-field equations, MOCCa needs to represent a number N_ϕ of single-particle wavefunctions on the Cartesian mesh. Any such single-particle wavefunction $|\phi\rangle$ is represented on the Lagrange mesh as four real functions for the real and imaginary parts of the spin-up and spin-down components of their spinor structure

$$\phi(\mathbf{r}) = \begin{pmatrix} \mathrm{Re}\,\phi(\mathbf{r}, \sigma = +1) + i\,\mathrm{Im}\,\phi(\mathbf{r}, \sigma = +1) \\ \mathrm{Re}\,\phi(\mathbf{r}, \sigma = -1) + i\,\mathrm{Im}\,\phi(\mathbf{r}, \sigma = -1) \end{pmatrix}. \tag{4.9}$$

Note that we assume isospin symmetry, and all of the single-particle wavefunctions have a definite isospin, explaining why there is no isospin index in Eq. (4.9). The advantage of storing four real functions instead

	Conserved symmetries	Broken symmetries	Equivalent code
Quadrupole deformation	$\mathcal{D}_{2h}^T$	None	`ev8`
Octupole deformation	$G\left\{\check{\mathcal{T}}, \hat{\mathcal{R}}_z, \check{\mathcal{S}}_y^T\right\}$	$\hat{\mathcal{P}}$	`ev4`
Time-odd densities	$G\left\{\hat{\mathcal{P}}, \hat{\mathcal{R}}_z, \check{\mathcal{S}}_y^T\right\}$	$\check{\mathcal{T}}$	`cr8`
Angular momentum $\hat{\mathcal{J}}_z$	$G\left\{\hat{\mathcal{P}}, \hat{\mathcal{R}}_z, \check{\mathcal{S}}_y^T\right\}$	$\check{\mathcal{T}}$	`cr8`
$\hat{\mathcal{J}}_x$	$G\left\{\hat{\mathcal{P}}, \check{\mathcal{S}}_y^T\right\}$	$\hat{\mathcal{R}}_z$, $\check{\mathcal{T}}$	None
$\hat{\mathcal{J}}_y$	$G\left\{\hat{\mathcal{P}}\right\}$	$\check{\mathcal{T}}, \check{\mathcal{S}}_y^T$	None
Nuclear Schiff Moment	$G\left\{\hat{\mathcal{R}}_z, \check{\mathcal{S}}_y^T\right\}$	$\check{\mathcal{T}}, \hat{\mathcal{P}}$	None
Scissor modes	$G\left\{\hat{\mathcal{P}}, \check{\mathcal{T}}, \check{\mathcal{S}}_y^T\right\}$	$\hat{\mathcal{R}}_z$	None

Table 4.3: A list of the order parameters discussed in chapter 2 and the corresponding symmetry options in `MOCCa`.

of two complex functions is that it allows the programmer to avoid wasteful processor instructions when calculating properties that one knows will be either completely real or completely imaginary. This storage scheme is almost identical to the way the original codes store single-particle wavefunctions. The case described here stores the single-particle wavefunctions independently of their symmetries, while `cr8` has a varying storage pattern depending on the signature quantum number [22].
As discussed in Chapter 2, we can use the conserved symmetries to choose quantum numbers for our single-particle wavefunctions. The generators $\hat{\mathcal{P}}$ and $\hat{\mathcal{R}}_z$ are respectively hermitian and antihermitian and give rise to simple single-particle quantum numbers

$$\left[\hat{P}\phi\right](x,y,z,\sigma,q) = \pm\,\phi(x,y,z,\sigma,q)\,, \tag{4.10a}$$

$$\left[\hat{R}_z\phi\right](x,y,z,\sigma,q) = \pm i\,\phi(x,y,z,\sigma,q)\,. \tag{4.10b}$$

Conservation of the antilinear operator $\check{\mathcal{S}}_y^T$ implies that the single-particle wavefunctions can be considered invariants, so that we have

$$\left[\check{S}_y^T\phi\right](x,y,z,\sigma,q) = \phi(x,y,z,\sigma,q)\,. \tag{4.11}$$

We can not demand a similar relation for the antilinear, antihermitian $\check{\mathcal{T}}$, but we can demand that the single-particle wavefunctions are come in normal pairs, i.e. that for every state ϕ_k there is also a time-reversed state $\phi_{\bar{k}}$ so that

$$\left[\check{T}\phi_k\right](x,y,z,\sigma,q) = \phi_{\bar{k}}(x,y,z,\sigma,q)\,. \tag{4.12}$$

When either of the symmetries $\hat{\mathcal{R}}_z, \check{\mathcal{S}}_y^T$ or $\hat{\mathcal{P}}$ are conserved, we can use the spatial relations to significantly limit the computational load by using relations (4.10) and (4.11). In each of these cases, the spatial extent of the mesh can be reduced by a factor of two. For parity conservation we have

$$\left[\hat{P}\phi\right](x,y,z,\sigma,q) = \phi(-x,-y,-z,\sigma,q) = \pm\phi(x,y,z,\sigma,q)\,. \tag{4.13}$$

This allows us to only store half of the values of $\phi(\mathbf{r},\sigma,q)$ as we can apply $\hat{P}$ to find the other half. `MOCCa` uses this freedom to only calculate the single-particle wavefunctions on half of the z-axis when parity is conserved. In this case we the number of points in the z-direction can be halved $nz = \frac{N_Z}{2}$.
The z-signature and y-timesimplex give rise to similar relations

$$\left[\hat{R}_z\phi\right](x,y,z,\sigma,q) = -i\sigma\phi(-x,-y,z,\sigma,q) = \pm i\phi(x,y,z,\sigma,q)\,, \tag{4.14a}$$

$$\left[\check{S}_y^T\phi\right](x,y,z,\sigma,q) = \phi^*(-x,-y,z,\sigma,q) = \phi(x,y,z,\sigma,q)\,. \tag{4.14b}$$

When y-timesimplex is conserved we can eliminate half of the y-axis $ny = \frac{N_Y}{2}$, while z-signature conservation can eliminate half of the x-axis $nx = \frac{N_X}{2}$. These choices are not unique, as a calculation with only conserved z-signature could in principle use the symmetry to eliminate half of the y-axis. This particular choice is merely the most practical, since each symmetry is related to one Cartesian axis.
Note that these relations for the single-particle wavefunctions directly transfer their features to the mean-field

densities and potentials as described in section 2.8. The conservation of these spatial symmetries thus reduce the total memory and computation time needed for a calculation by a factor of 2[1] by reducing the effective number of mesh points in one Cartesian direction. Fig. 4.2 shows the part of the mesh that is numerically represented in MOCCa for every combination of conservation of the three symmetries $\hat{\mathcal{R}}_z, \hat{S}_y^T$ and $\hat{\mathcal{P}}$.
Time-reversal conservation does not give rise to a similar spatial relation for the single-particle wavefunctions. The number of single-particle wavefunctions that actually is stored is `nwt`, and in the case of time-reversal conservation is only half of N_ϕ. The half of single-particle wavefunctions that is stored is the set with signature $+1$ in the case of z-signature conservation. When z-signature is conserved, there is no such particular practical division of the single-particle wavefunctions in two sets and which half gets stored is arbitrary.
As a final remark note that we have already implicitly used z-isospin symmetry in Eq. (4.9). We suppose that every single-particle wavefunction is an eigenstate of $\hat{I}_z$ and that they carry a definite isospin, they represent either a proton or a neutron. Would we not have this symmetry, the structure in Eq. (4.9) would not be enough and we would need eight real functions to properly represent the spinor and isospin-spinor structure. In this way, z-isospin symmetry also hands us a factor of two in complexity[2].

4.4 Optimizing the energy: steepest descent aka imaginary timestep

Let us now focus on how we could solve the Hartree-Fock equations when represented on a mesh. We will leave aside the pairing equations for now and treat them in chapter 6. The clearest way of presenting the problem is as an optimization problem. We would like to find a set of N_ϕ single-particle wavefunctions so that the energy as calculated using the functional

$$E_{HF(B)} = \int d\mathbf{r}\, \mathcal{E}[\rho(\mathbf{r}), \tau(\mathbf{r}), \ldots] \tag{4.15}$$

is minimal.
The first thing to realize is that the relevant degrees of freedom are the single-particle wavefunctions and more specifically their values at the mesh points

$$\phi_l\left(x_i, y_j, z_k, \sigma\right) \text{ with } \begin{cases} l = 1, \ldots, \texttt{nwt} \\ i = 1, \ldots, nx \\ j = 1, \ldots, ny \\ k = 1, \ldots, nz \\ \sigma = -1, 1 \end{cases} \tag{4.16}$$

where we have eliminated (for now) the isospin index, since we assume z-isospin symmetry in any case. One should not forget that the optimization problem has a subsidiary condition that the single-particle wavefunctions should be orthonormal

$$\langle \phi_i | \phi_j \rangle = \delta_{ij}\,. \tag{4.17}$$

In computer science (and specifically AI learning) [88] the simplest solution for an optimization problem is steepest descent. Given a scalar function f of some variable $\mathbf{x}$, the steepest descent algorithm looks for the direction in which the objective function f decreases the fastest. It then takes a small step in that direction and looks again for the direction of steepest descent. More formally, starting from a guess $\mathbf{x}^{(i)}$ at iteration i the algorithm evaluates the derivative $\boldsymbol{\nabla} f(\mathbf{x})|_{\mathbf{x}=\mathbf{x}^{(i)}}$ and proposes for the next iteration

$$\mathbf{x}^{(i+1)} = \mathbf{x}^{(i)} - \alpha\, \boldsymbol{\nabla} f(\mathbf{x})|_{\mathbf{x}=\mathbf{x}^{(i)}}\,, \tag{4.18}$$

where we call the real number α the stepsize. This stepsize variable is highly problem dependent and will receive some attention later this chapter. That eventually this algorithm will find a local minimum of f is intuitively very clear: $-\boldsymbol{\nabla} f(\mathbf{x})|_{\mathbf{x}=\mathbf{x}^{(i)}}$ is at every iteration a vector pointing in the direction in which $f(\mathbf{x})$ decreases the fastest. For this reason, this algorithm is also know as 'gradient descent'.
This algorithm is also easily applied to our optimization of Eq. (4.15). Every mesh value of every single-particle wavefunction $\phi_l\left(x_i, y_j, z_k, \sigma\right)$ is one component of $\mathbf{x}$, while f is the functional. The remaining challenge is to evaluate $\boldsymbol{\nabla} f(\mathbf{x})$. We can write

$$\frac{\partial E_{HF(B)}}{\partial \phi_i} = \sum_\rho \int d\mathbf{r} \frac{\partial \mathcal{E}[\rho(\mathbf{r}), \tau(\mathbf{r}), \ldots]}{\partial \rho(\mathbf{r})} \frac{\partial \rho(\mathbf{r})}{\partial \phi_i} = [\hat{h}\phi_i](\mathbf{r}, \sigma, \tau) \tag{4.19}$$

[1] This is of course only approximate in reality as different symmetry combinations have slightly different numerical requirements, but the factors two are very close to the actual factors.
[2] In combination with time-reversal symmetry and isospin symmetry ev8 should really have been called ev32.

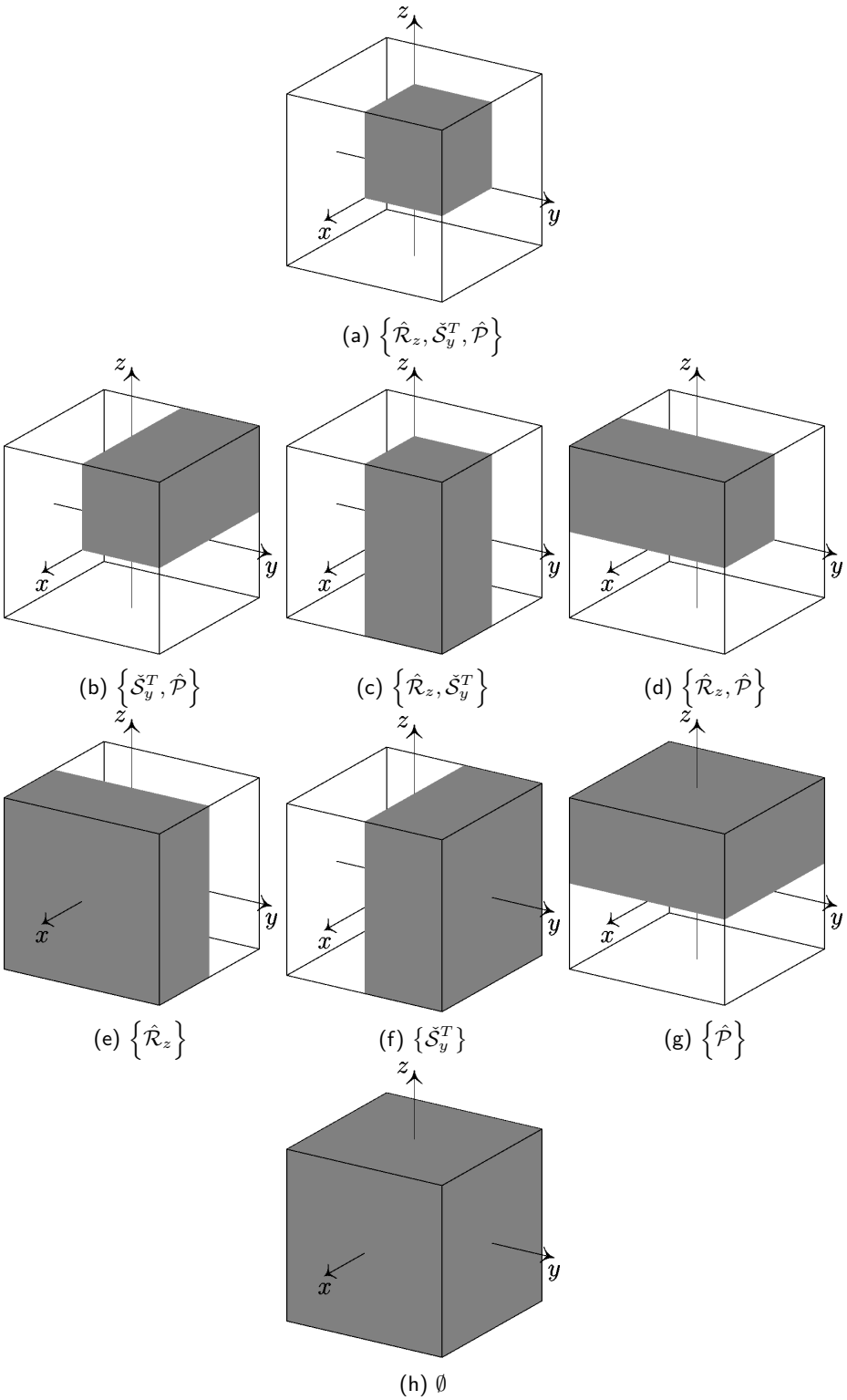

(a) $\left\{\hat{\mathcal{R}}_z, \check{\mathcal{S}}_y^T, \hat{\mathcal{P}}\right\}$

(b) $\left\{\check{\mathcal{S}}_y^T, \hat{\mathcal{P}}\right\}$ (c) $\left\{\hat{\mathcal{R}}_z, \check{\mathcal{S}}_y^T\right\}$ (d) $\left\{\hat{\mathcal{R}}_z, \hat{\mathcal{P}}\right\}$

(e) $\left\{\hat{\mathcal{R}}_z\right\}$ (f) $\{\check{\mathcal{S}}_y^T\}$ (g) $\left\{\hat{\mathcal{P}}\right\}$

(h) $\emptyset$

Figure 4.2: Spatial degrees of freedom actually represented in MOCCa when using different generator sets.

1 Start from a set of $|\phi_l^{(0)}\rangle$
2 **for** $i \to$ `MaxIter` **do**
3 | Compute mean-field densities $\rho, \tau, \ldots$
4 | Compute mean-field $U, W_{\mu\nu}, \ldots$
5 | Compute single-particle Hamiltonian $\hat{h}^{(i)}$
6 | Update single-particle wavefunctions $|\chi_l^{(i+1)}\rangle = |\phi_l^{(i)}\rangle - \alpha \hat{h}^{(i)} |\phi_l^{(i)}\rangle$
7 | Gramm-Schmidt to orthogonalize $|\chi_l^{(i+1)}\rangle \to |\phi_l^{(i+1)}\rangle$
8 **end**

Algorithm 2: Gradient descent algorithm for some maximum number of iterations `MaxIter`.

where the sum is over all the different mean-field densities that appear in $\mathcal{E}[\rho(\mathbf{r}), \tau(\mathbf{r}), \ldots]$. The derivative of our objective function is obtained by applying $\hat{h}$ on the single-particle wavefunction $|\phi_l\rangle$. Our version of Eq.(4.18) then becomes

$$\phi_l^{(i+1)}(\mathbf{r}, \sigma) = \phi_l^{(i)}(\mathbf{r}, \sigma) - \alpha \left[\hat{h}^{(i)} \phi_l^{(i)}\right](\mathbf{r}, \sigma)\,, \tag{4.20}$$

where we have added the superscript (i) to the single-particle Hamiltonian since it depends on the mean-field potentials and thus the single-particle wavefunctions at iteration (i).
The subsidiary condition of orthonormality can not be guaranteed by an update scheme as in Eq. (4.20). In practice, a simple Gram-Schmidt orthogonalization scheme is added as an extra update step[3] after the application of Eq. (4.20). With this addition the general steepest descent algorithm is complete; it is summarised below in Algorithm 2.
It is rather interesting that the update formula, Eq. (4.20) can also be obtained from a more physical point of view. Consider the time-dependent Schrödinger equation for the single-particle Hamiltonian $\hat{h}$

$$i\hbar \frac{\partial |\phi_l\rangle}{\partial t} = \hat{h}(t) |\phi_l\rangle\,. \tag{4.21}$$

Discretizing time and considering small time-steps δt, we can write the solution at $t = t_0 + \delta t$ as

$$|\phi_l^{(t+\delta t)}\rangle \approx \exp\left[-i \frac{\delta t}{\hbar} \hat{h}(t)\right] |\phi_l^{(t)}\rangle\,. \tag{4.22}$$

Schrödinger evolution conserves the energy of the system, but when we take $\delta t = -i dt$ with dt real we recover

$$|\phi_l^{(t+dt)}\rangle \approx \exp\left[-\frac{dt}{\hbar} \hat{h}(t)\right] |\phi_l^{(t)}\rangle \approx \left(\hat{\mathbb{1}} - \frac{dt}{\hbar} \hat{h}(t) + O(dt^2)\right) |\phi_l^{(t)}\rangle\,. \tag{4.23}$$

And to first order this is again Eq. (4.20) with α replaced by $\frac{dt}{\hbar}$ and iteration number (i) by the time t. Davies [89] took this approach to justify his first application of the steepest descent algorithm to the nuclear many-body problem. In what follows we will use the notation dt for historical reasons, it is equal to α up to a factor of $\hbar$.

4.5 Choosing the time-step dt

What value to pick for the time-step size in the update formula Eq. (4.23) is unfortunately non-trivial. Small values of dt will greatly impact the number of iterations we need to reach convergence as the single-particle wavefunctions will vary only slowly. Too big values unfortunately destroy convergence completely, as the direction $\hat{h}|\phi_l\rangle$ is only guaranteed to be a descent direction for infinitesimally small stepsizes. This situation is illustrated for ^{40}Ca in Fig. 4.3. Convergence is rather slow for small values of dt, but for values of dt higher than $\sim 0.03 \times 10^{-22}$s the iterative scheme diverges.[4]
A handwaving argument is readily available when $\hat{h}$ is independent of time in Eq. (4.23). In that case, the solution is integrable from $t = 0$ to $t = N dt$ and we have

$$|\phi_l^{(N dt)}\rangle = \left(\hat{\mathbb{1}} - \frac{dt}{\hbar} \hat{h}\right)^N |\phi_l^{(0)}\rangle\,. \tag{4.24}$$

[3] An alternative could also be to add Lagrange parameters to the problem of Eq. (4.15). In the end however, this is completely equivalent in both result and computational effort.
[4] The kinks in Fig. 4.3 appear when the error changes sign and are an artifact of the presentation on a logarithmic scale.

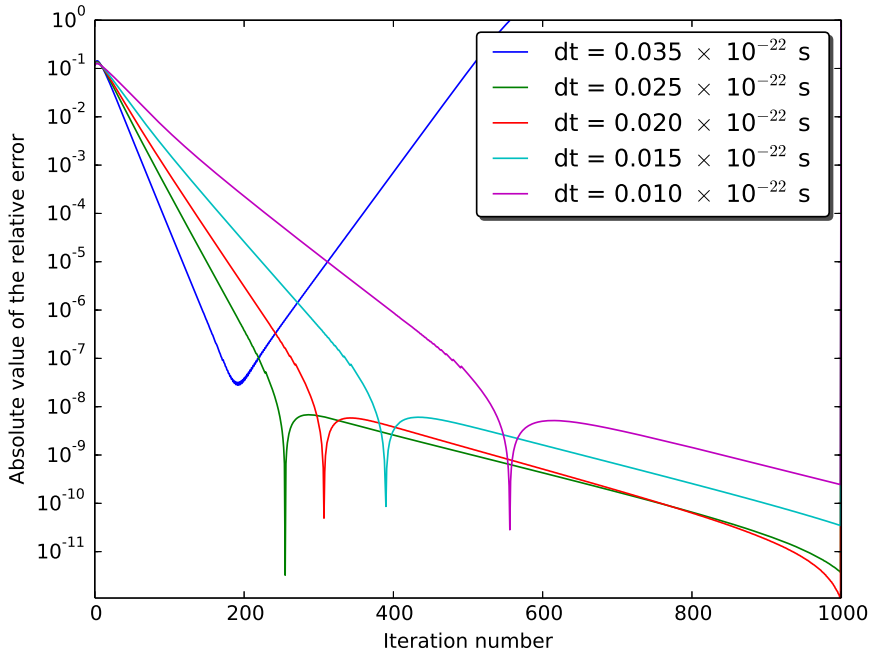

Figure 4.3: Absolute value of the relative error of the energy with respect to the converged value for a Hartree-Fock calculation of ^{40}Ca for various values of dt on a mesh with $dx = 1.0$ fm using the SLy4 parameterization. Note that the calculation with $dt = 0.035 \times 10^{-22}$ s diverges. The dips in the figure are places where the error changes sign.

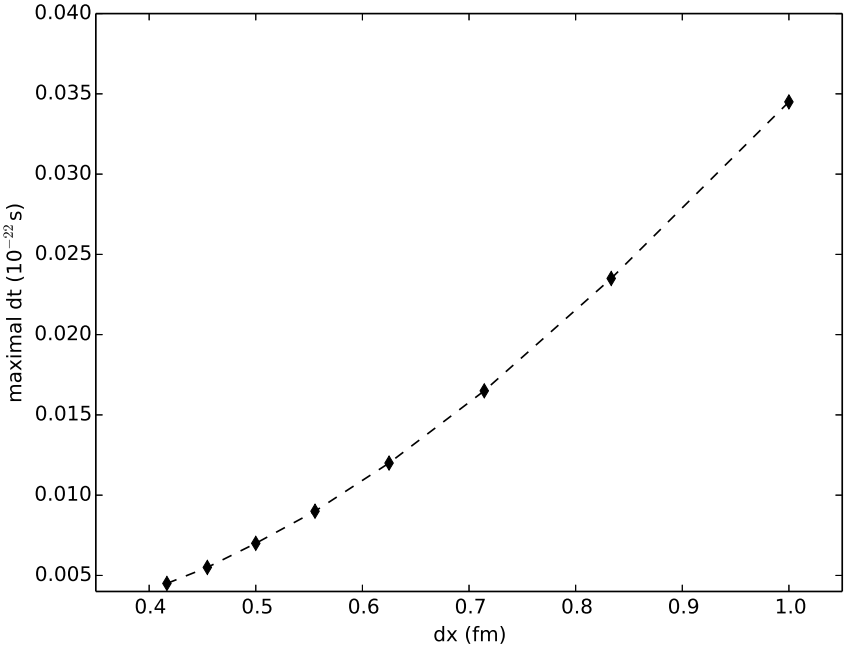

Figure 4.4: Maximal value of dt that results in a converging iterative scheme as a function of dx for a Hartree-Fock calculation of ^{40}Ca using the SLy4 parametrization, using the default finite difference derivatives.

```
Start from a set of |φ_l^(0)⟩
for i → MaxIter do
    Compute mean-field densities ρ, τ, ...
    Compute mean-field U, W_{μ,ν}, ...
    Compute single-particle Hamiltonian ĥ^(i)
    Diagonalise ĥ^(i) to find new φ_l^(i)
end
```

Algorithm 3: Sketch of the algorithm from [84].

We immediately see that it is the largest eigenvalue of $\frac{dt}{\hbar}\hat{h}$ that determines the behaviour of this series. If it is too large (> 1), then this series will diverge as N grows. If it is small (< 1), this series will converge.
As eigenstates of $\hat{h}$ climb in energy they become less and less bound and the very highest eigenstates will resemble plane waves. As such, the highest eigenvalues of $\hat{h}$ will be dominated by the kinetic energy which we can approximate for a Skyrme functional by

$$\hat{h} \approx -\boldsymbol{\nabla} \cdot B_q(\mathbf{r})\boldsymbol{\nabla} \approx -\frac{\hbar^2}{2m}\Delta\,, \tag{4.25}$$

where m is the nucleon mass. On a mesh with spacing dx, the highest representable plane wave has a momentum that is proportional to dx^{-1}. Thus, the maximum eigenvalue of $\hat{h}$ will be proportional to $\left(dx^2\right)^{-1}$. From this we can immediately see that smaller mesh sizes need smaller values of dt in order to converge. Fig. 4.4 show the dependence of dx of the maximal value of dt for a calculation of ^{40}Ca. When decreasing the mesh discretization from $dx = 1$ fm to $dx \sim 0.8$ fm the maximal value of dt drops already by one third. Calculations using small mesh discretisations are thus extra numerically burdened: they need more mesh points and more iterations to converge because of the smaller values of dt.

4.6 Comparing to the standard self-consistent scheme

A different scheme to solve self-consistent equations is sketched in Algorithm 3. It is more proliferated compared to the gradient descent scheme both in nuclear structure theory [84, 90, 83, 85], and computational chemistry. The overall idea is exactly the same, calculating $\hat{h}^{(i)}$ at every mean-field iteration and using a prescription to find a new set of single-particle wavefunctions in the Hartree-Fock base. Usually these are obtained by completely diagonalizing $\hat{h}^{(i)}$ at every mean-field iteration.
Gradient descent of course also diagonalises $\hat{h}^{(i)}$, as at convergence the single-particle wavefunctions are eigenstates of the single-particle Hamiltonian. One can regard update formula in Eq. (4.23) as the first iteration of an iterative process to diagonalize $\hat{h}^{(i)}$ at iteration (i). This is the main difference: gradient descent only performs a single iteration of the diagonalisation process of the single-particle Hamiltonian at every mean-field iteration.
Where gradient descent prefers to use CPU cycles to update the information contained in $\hat{h}^{(i)}$, the standard scheme prefers to capitalize on all of the information already contained in $\hat{h}^{(i)}$ at every iteration. Whether one or the other scheme is more efficient is probably very dependent on the type of numerical representation used, the number of single-particle wavefunctions taken into account and details of the implementation. It is however important to realize the difference between the two schemes as they will impact some numerical choices and more specifically why some numerical techniques that are in frequent use in other codes do not work as well for `MOCCa`.

4.7 Computing the mean-field densities and potentials

In order to successfully optimize the energy, one needs to calculate the single-particle Hamiltonian $\hat{h}^{(i)}$ at every mean-field iteration (i), using the mean-field potentials and the mean-field densities. The formulas in chapter 3 are easily implemented and the formulas in appendix A for the mean-field potentials are maybe hard to implement correctly but of no technical challenge.
However there are two points that merit some further attention. The first is the calculation of the Coulomb potential, which is fundamentally different from the other Skyrme mean-field potentials. The second is that without proper control and even with a well chosen parameter dt, a gradient descent step can produce quite

brutal changes of mean-field densities from iteration (i) to $(i+1)$. This directly influences the mean-field potentials and and in turn means that $\hat{h}^{(i)}$ has a rather different spectrum from one iteration to the next. In order to combat this, we mix the densities at different iterations.

4.7.1 Density mixing

At every mean-field iteration (i), we calculate all of the mean-field densities from the formulas in chapter 3 but then mix them in a simple linear way

$$\rho(\mathbf{r})^{(i)} = \texttt{DampingParam}\,\rho(\mathbf{r})^{(i-1)} + (1 - \texttt{DampingParam})\,\rho(\mathbf{r})^{(i)}\,, \tag{4.26}$$

where `DampingParam` is an input parameter of `MOCCa`. The other mean-field densities are mixed in similar fashion, using the same coefficient. This type of damping is effective at ensuring convergence when `DampingParam` is between 0.75 and 0.95, favoring the previous density and delaying new information to be incorporated in $\hat{h}^{(i)}$.
The main reason why using small values of `DampingParam` does not result in stable convergence is because the gradient descent scheme only performs a single update of the single particle wavefunctions at every mean-field iteration. This update is guaranteed to be in the correct direction to diagonalize $\hat{h}^{(i-1)}$ but it is not necessarily a proper descent direction for $\hat{h}^{(i)}$. The physical analog is that the time evolution in Eq. (4.21) can give rise to erratic behaviour if the variation of $\hat{h}(t)$ is too rapid compared to the timestep dt.
It is worth noting that one could achieve the same effect when mixing the mean-field potentials instead of the mean-field densities. This is the approach taken in [91]. One might argue that this is a more natural quantity to mix, but more study is needed to check whether this affects convergence (either positively or negatively).

4.7.2 Coulomb calculation

The exchange term in Slater approximation presents no technical challenge, as it is simply proportional to the proton density ρ_p[5]. The direct Coulomb energy density is generated by an interaction with infinite range and is thus more difficult to numerically represent than the Skyrme energy density. The direct Coulomb energy density is given by

$$\mathcal{E}^{\text{dir.}}_{\text{Coul}}(\mathbf{r}) = \frac{e^2}{2}\int d\mathbf{r}'\,\frac{\rho_p(\mathbf{r})\rho_p(\mathbf{r}')}{|\mathbf{r}-\mathbf{r}'|}\,. \tag{4.27}$$

Directly calculating this integral for every mesh point (x_i, y_j, z_k) by summing the integrand is both extremely costly and numerically unstable since there is always a point where the denominator is exactly zero. The numerically more sensible thing to do is to solve Poisson's equation on the mesh for the electrostatic Coulomb potential $V(\mathbf{r})$ of the point proton density $\rho_p(\mathbf{r})$

$$\Delta V(\mathbf{r}) = -4\pi e^2 \rho_p(\mathbf{r})\,, \tag{4.28}$$

where e is the proton charge. The energy density can then be written as

$$\mathcal{E}^{\text{direct}}_{\text{Coul}}(\mathbf{r}) = \int d\mathbf{r}\, V(\mathbf{r})\rho_p(\mathbf{r})\,, \tag{4.29}$$

which is numerically stable and not too resource-intensive to compute when $V(\mathbf{r})$ is known.
There are currently several different numerical schemes to solve Eq. (4.28) implemented in `MOCCa`. Dependent on the input parameter `CoulombSolver` one can use either a conjugate gradient scheme, a Gauss-Seidel solver or a symmetric-over-relaxation solver [88]. They are all iterative schemes and are tested to give the same solution. The interest of having different solvers was motivated by a search for a more efficient numerical scheme for this purpose[6]. All three implementations have comparable performance to within a factor two, but the relative importance of this part of the code is rather small on the mean-field level. For more details, see F.
Specifying Eq.(4.28) is however not enough to determine $V(\mathbf{r})$. We specify boundary conditions on the extremes of the mesh to uniquely determine the solution to Eq.(4.28) as follows [72]

$$U_{\text{bound}}(\mathbf{r}) = e^2 \sum_{\ell=0}^{\ell_{\text{max}}} \sum_{m=-l}^{l} \frac{\langle \hat{\mathcal{Q}}_{\ell m,p}\rangle^*}{r^{2\ell+1}} Y_{\ell m}(\mathbf{r})\,. \tag{4.30}$$

[5] Calculating the exact exchange energy density is a completely different story, but outside the scope of this text.

[6] A fourth solver based on a multigrid scheme was part of `MOCCa`, but was dropped because of subpar performance. This was to be expected as the number of mesh points we have is rather small compared to the typical application domain of multigrid methods [88].

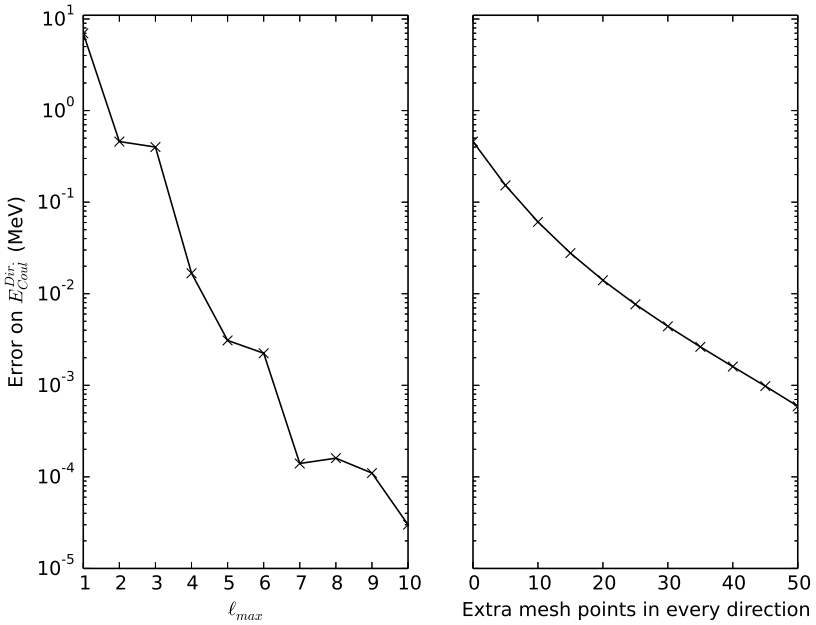

ℓ	1	2	3	4	5
$\beta_{\ell 0,p}$	0.006	0.816	0.408	3.071	2.881
ℓ	6	7	8	9	10
$\beta_{\ell 0,p}$	5.032	6.030	8.744	11.314	15.250

Figure 4.5: Accuracy of the direct Coulomb energy of an octupole deformed ^{226}Ra state as a function of ℓ_{max} and extra points added to the Coulomb mesh. The axial deformation parameters $\beta_{\ell 0,p}$ are given in the table below. The calculations adding extra points use Eq. (4.30) up to and including $\ell = 2$. Reference is the Coulomb energy calculated with 50 extra points and $\ell_{\text{max}} = 10$. The non-augmented mesh parameters are $(N_X, N_Y, N_Z) = (30, 30, 50)$ and $dx = 1.0$ fm.

where the $Y_{\ell m}(\mathbf{r})$ are the spherical harmonics, see Appendix C. ℓ_{max} is an input parameter and determines the highest degree ℓ of multipole moments that are taken into account in the calculation. These boundary conditions correspond to the expansion of the Coulomb potential in spherical harmonics far from the source charge. This approximation increases in quality as ℓ_{max} increases as the expansion gains more terms.
Another factor impacting the accuracy of this approximation is the size of the mesh. The denominator of the terms increases quickly with increasing r at the boundary of the box and higher order terms become less important. In addition, this expansion is only valid in regions where the charge density is zero, far enough away from the proton density. It is thus vitally important that the proton density is well contained in the mesh. `MOCCa` offers the option to take extra mesh points for the calculation of the Coulomb potential into account, in addition to those of the normal mesh, via the keywords `CEX`, `CEY` and `CEZ`.
Both effects can be used to increase the reliability of the boundary conditions, but increasing ℓ_{max} is numerically less costly than increasing the number of mesh points for the Coulomb solver. The calculation of some extra multipole moments $\langle \hat{\mathcal{Q}}_{\ell m,p} \rangle$ amounts to a few extra integrals over the mesh, while increasing the number of points for the iterative Poisson solver amounts to several matrix multiplications at every iteration over an enlarged mesh.
The accuracy of both approaches is shown in Figure 4.5 for a deformed mean-field state of ^{226}Ra at $\beta_2 \approx 0.8$ and $\beta_3 \approx 0.4$. The error is calculated by comparing with a calculation with $\ell_{max} = 10$ and 50 extra points in the z-direction. The accuracy increases rapidly both with increased ℓ_{max} and number of mesh points. The decrease in error by increasing ℓ_{max} is not a smooth function, as the different multipole moments are not all of comparable size and thus importance. For both methods the error can easily be controlled and be brought to acceptable levels. However, by increasing ℓ_{max} one does not incur any tangible numerical cost while this cannot be said for increasing the number of mesh points.

4.8 Judging convergence

When to stop iterating the procedure in Algorithm 4.20 is a valid question. Several checks are built into the code, that judge the stability of the iterative scheme. At a given iteration (i), one checks that a number of quantities have not varied too much over the past seven iterations $(i), (i-1), \dots (i-7)$.
Mainly the total energy $E^{(i)}_{HF(B)}$ is relevant: typically one stops the iteration when

$$\frac{\left|E^{(i-k+1)}_{HF(B)} - E^{(i-k)}_{HF(B)}\right|}{\left|E^{(i-k+1)}_{HFB}\right|} \leq \texttt{EnergyPrec} \qquad k = 1, \dots, 7\,, \tag{4.31}$$

The stability of the Fermi energy λ_q, for protons and neutrons alike, is also judged over the past seven iterations

$$\left|\lambda^{(i-k+1)}_q - \lambda^{(i-k)}_q\right| \leq \texttt{PairingPrec} \qquad k = 1, \dots, 7\,, \tag{4.32}$$

Other checks are in place when constraints are present [72]. If a multipole moment $\langle\hat{\mathcal{Q}}_{\ell m}\rangle$ is constrained to a value O, the code checks the values of the multipole moment at the previous seven iterations using either

$$\left|\langle\hat{\mathcal{Q}}_{\ell m}\rangle^{(i-k+1)}\right| \leq \texttt{MomentPrec} \qquad k = 1, \dots, 7 \text{ (if } O = 0) \quad , \tag{4.33a}$$

$$\frac{\left|\langle\hat{\mathcal{Q}}_{\ell m}\rangle^{(i-k+1)} - O\right|}{|O|} \leq \texttt{MomentPrec} \qquad k = 1, \dots, 7 \text{ (if } O \neq 0) \quad . \tag{4.33b}$$

A similar check is placed on the projection $\mu = x, y, z$ of the angular momentum if it is constrained to a non-zero value J

$$\frac{\left|\langle\hat{\mathcal{J}}_{\mu}\rangle^{(i-k+1)} - J\right|}{|J|} \leq \texttt{CrankPrec} \qquad k = 1, \dots, 7 \quad . \tag{4.34a}$$

The parameters `EnergyPrec`,`MomentPrec`,`PairingPrec` and `CrankPrec` are all input parameters of `MOCCa`, see chapter 11. While these are the check the code performs on its own, there are some other checks the user can look at themselves. The first is an alternative way to calculate the energy [72]

$$E_{\text{alt}} = \sum_{k=1}^{\texttt{nwt}} v_k^2 \epsilon_k + \frac{E_{\text{Kin}}}{2} + \frac{E^{\text{exch.}}_{\text{Coul}}}{3} + E_{\text{pair}} + E'_{\text{corr}} + E_{\text{SR}}\,(+\,E_{\text{Con}})\,. \tag{4.35}$$

Here the terms $E_{\text{Kin}}, E^{\text{exch.}}_{\text{Coul}}, E_{\text{pair}}$ take the same form as defined in the previous chapters. E'_{Cor} is slightly different from the term E_{Cor} in the Skyrme functional: if the one-body centre-of-mass correction (see sec. 1.4.5 and chapter 11) is treated self-consistently, it is comprised in the single-particle energies ϵ_k and thus should not be contribute to E_{Cor}. If it is added perturbatively, it is not part of the single-particle energies and should be included in E_{Cor}.
E_{SR} is an extra rearrangement term due to the density dependent terms in the Skyrme functional

$$E_{\text{SR}} = -\frac{1}{2}\int d^3r \sum_{x=a,b} \alpha_x\, \rho^{\alpha_x} \left[b_{7x}\,\rho^2 + \sum_{q=n,p}\left(b_{8x}\,\rho_q^2\right)\right]. \tag{4.36}$$

When constraints are added, an extra term needs to be added to E_{Alt}

$$E_{\text{Con}} = \sum_k \lambda^{(i)} \langle\hat{\mathcal{O}}_k\rangle^{(i)} \tag{4.37}$$

where the sum is over all constrained operators $\hat{\mathcal{O}}_k$ and the $\lambda^{(i)}$ are the Lagrange multipliers[7]. Note that this term has to be included here, as the constraints contribute to the single-particle Hamiltonian and are thus implicitly included in the sum in Eq. (4.35) and thus should be removed.
Theoretically, when convergence is reached E_{Alt} should match the energy calculated using the functional $E_{\text{HF(B)}}$. Because of the numerical approximations (mainly the use of finite-difference derivatives and the limited size of the mesh) that do not act in the same way on both sums, this equality will in general only hold

[7] We are running ahead of ourselves: see chapter 5 for more info on the constraints.

approximatively. Typical deviations between E_{Alt} and $E_{\text{HF(B)}}$ are tabulated in Table 3 in [72]. At convergence, using a sufficiently large mesh, the difference between E_{Alt} and $E_{\text{HF(B)}}$ should not be larger than a few hundred keV for $dx = 1$ fm and significantly smaller for smaller mesh discretisations.
Another indicator of convergence is the change in the change of all the mean-field densities. The output of `MOCCa` at every mean-field iteration contains

$$\delta\rho^{(i)} = 1 - \frac{\left[\sum_\rho \int d\mathbf{r}\rho^{(i)}(\mathbf{r})\rho^{(i-1)}(\mathbf{r})\right]}{\left[\sum_\rho \int d\mathbf{r}\rho^{(i)}(\mathbf{r})\rho^{(i)}(\mathbf{r})\right]} \tag{4.38}$$

where the sums range over all of the mean-field densities of Eq. (1.4.1). Note that this calculation is made before any damping procedure, so that $\rho^{(i)}$ is calculated without any damping procedure. Convergence is obviously better when $\delta\rho$ becomes smaller, and values around 10^{-8} should be reachable.

4.9 Points of possible improvement

The gradient descent algorithm as described in the previous sections (supplemented by a simple linear mixing of the densities) was already employed in the `ev8`, `cr8` and `ev4` codes. The overall scheme is rather straightforward and it is not hard to come up with possible improvements. In this section, we will discuss some of the possibilities that have been tried for `MOCCa`. In general, these alternatives show promise in decreasing the number of iterations needed to converge the numerical scheme. However, for all of them there are extra difficulties to make the schemes applicable to the most general problem we would like to solve or the numerical cost offsets the gain in convergence speed.
We will discuss the second-order expansion of Eq. (4.23), preconditioning the optimization problem, the Nesterov accelerated gradient scheme and the DIIS mixing of the mean-field densities. The properties of all of these schemes will be illustrated with their application to a calculation of ^{40}Ca using the SLy4 parameterization, without pairing and with conservation of the full $\mathcal{D}_{2h}^T$ group. This in order to keep the calculation as simple and straightforward as possible to clearly disentangle the effect of the different numerical schemes. All of the calculations were started from Nilsson model wavefunctions generated by the `nil8` [9] code, thereby granting every scheme the same (rather bad) starting point.

4.9.1 Second order imaginary time-step

Naïvely exanding Eq. (4.9) to second order in $\frac{dt}{\hbar}$ gives the following update formula for the single-particle wavefunctions

$$|\phi_l^{(i+1)}\rangle = \left[\hat{\mathbb{1}} - \frac{dt}{\hbar}\hat{h}^{(i)} + \frac{1}{2}\left(\frac{dt}{\hbar}\hat{h}^{(i)}\right)^2\right]|\phi_l^{(i)}\rangle\,. \tag{4.39}$$

This change in update formula is quite costly: the application of $\hat{h}^{(i),2}$ on the single-particle wavefunctions $|\phi_l\rangle$ involves the computation of numerical derivatives of $\hat{h}^{(i)}|\phi_l\rangle$. This almost doubles the computational effort for a single update step since the calculation of derivatives is by far the most numerically most costly part of every mean-field iteration. The gain of having a second order in dt on the other hand is meanwhile not that significant, as $\hat{h}^{(i)}$ changes from one iteration to the next. Two iterations of a first-order expansion in dt thus acquire more information than one iteration of a second-order expansion for roughly the same amount of numerical effort. This effect is illustrated in Fig. 4.6. The difference between the first order and second order expansion is negligible and the second order expansion does in fact slightly worse.
Another naïve improvement of the imaginary timestep, using a conjugate gradient algorithm (see Appendix D) in this context would also not really improve the convergence. The reason is again the fact that $\hat{h}^{(i)}$ is updated at the same speed as the single-particle wavefunctions: the conjugate direction that is constructed at every iteration is conjugate to directions determined by $\hat{h}^{(0)}, \hat{h}^{(1)}, \ldots, \hat{h}^{(i-1)}$ and is thus not very relevant for $\hat{h}^{(i)}$. In fact, I have not succeeded in getting a functional conjugate algorithm working in `MOCCa`, for what we suspect is this reason [8].

[8] Although any number of unsolved bugs might also be the cause, one can really never be sure.

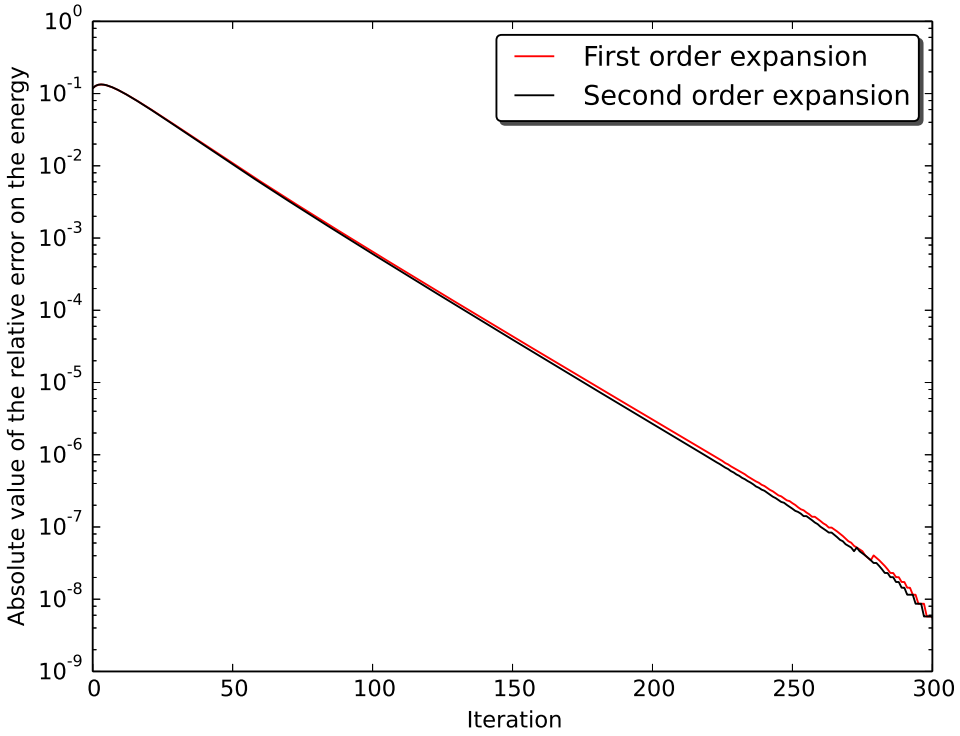

Figure 4.6: Energy difference with the converged value of a Hartree-Fock calculation for ^{40}Ca as a function of iteration number using the SLy4 parameterization for first or second order expansion of Eq. (4.23). The calculation was started from Nilsson model wavefunctions generated by `nil8`.

4.9.2 Preconditioning

Preconditioning the single-particle Hamiltonian is a promising strategy that was already studied in the context of the nuclear many-body problem several decades ago [92][9]. The idea is to transform $\hat{h}^{(i)}$ to a modified problem $\hat{h}_P^{(i)}$ that is easier to solve, i.e. that has a smaller spread in eigenvalues [88]. For the nuclear problem, this means that one tries to filter the components with high kinetic energy from $\hat{h}^{(i)}|\phi_l^{(i)}\rangle$ that slow convergence.
The most promising way to do this from [92] has been implemented in `MOCCa`. The preconditioning operator $\hat{P}$ is defined as

$$\hat{P} = \left(\hat{T} + E_0\right)^{-1} = \left(\frac{\hbar^2}{2m}\Delta + E_0\right)^{-1}, \tag{4.40}$$

where $\hat{T}$ is the kinetic energy operator. Note that $\hat{P}$ damps the eigenstates of the kinetic energy operator with high kinetic energy and amplifies the kinetic energy eigenstates with low kinetic energy. E_0 is a numerical parameter, typically of the order of 100 MeV, that is incorporated in order to make the method stable for components with very low kinetic energy. The modified single-particle Hamiltonian becomes

$$\hat{h}_P^{(i)} = \hat{P}\hat{h}^{(i)}\,. \tag{4.41}$$

The new update formula, replacing Eq. (4.20) becomes

$$|\phi_l^{(i+1)}\rangle = \left[\hat{\mathbb{1}} - \frac{dt}{\hbar}\hat{P}\left(\hat{h}^{(i)} - \langle\phi_l^i|\hat{h}^{(i)}|\phi_l^i\rangle\right)\right]|\phi_l^{(i)}\rangle\,. \tag{4.42}$$

Note that the extra term involving the expectation value of $\hat{h}^{(i)}$ is necessary in order not to filter the components of $\hat{h}^{(i)}$ in the direction of $|\phi_l^{(i)}\rangle$. These are of course the components of $|\phi_l^{(i)}\rangle$ that we want to keep. The main advantage of preconditioning is the increased maximum stepsize. The correct quantity to compare

[9] Although [92] does not use the term preconditioning.

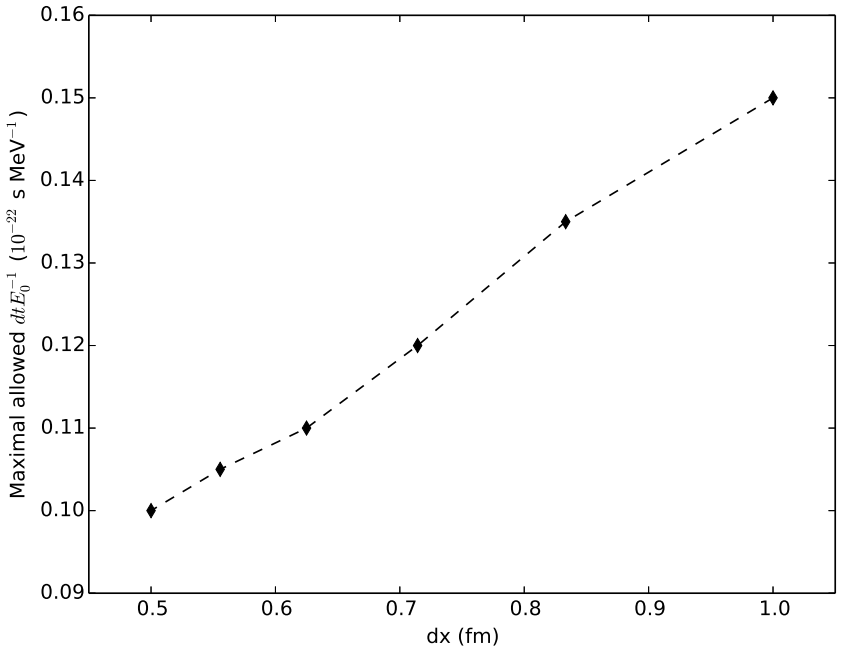

Figure 4.7: Maximum values of $\frac{dt}{E_0}$ that do not diverge as a function of the mesh discretisation dx.

to dt in the original gradient descent is $\frac{dt}{E_0}$[10]. In Fig. 4.7 the maximum value of $\frac{dt}{E_0}$ that does not produce a divergent iterative scheme is shown as a function of dx. The typical size of stepsize is significantly larger than the stepsizes for original gradient descent, compare with Fig. 4.4. Not only that, but the preconditioned scheme only suffers slight reductions of maximal $\frac{dt}{E_0}$ with decreasing dx compared to ordinary gradient descent.
The price to pay is the numerical cost of applying $\hat{P}$ to every single-particle wavefunction. While the application of Δ is essentially a sparse matrix multiplication (at least in the case of finite difference derivatives), its inverse and by extension $\hat{P}$ will in general be a matrix with the full dimension of the mesh. A conjugate gradient algorithm (see Appendix D) is currently implemented to solve the inverse problem, i.e. solving the following equation for χ,

$$\hat{P}^{-1}|\chi\rangle = \hat{h}^{(i)}|\psi_l^{(i)}\rangle\,. \tag{4.43}$$

This is again an iterative process that has to be completed at every mean-field iteration, for every single-particle wavefunction. The numerical cost of this process is consequently rather high. The current implementation limits the computational cost by using $\hat{h}^{(i)}|\psi_l^{(i)}\rangle$ as initial guess for χ instead of the zero-vector and using only first order finite difference derivatives when applying $\hat{P}^{-1}$. The number of iterations to calculate the action of $\hat{P}$ is in general on the order of 10, though the actual number depends heavily on the details of the calculation like the value of E_0 and the single-particle wavefunction under consideration. Higher values of dt will also increase the number of conjugate gradient applications necessary, as the high-kinetic energy components gain importance with increasing dt.
Inverting the complete operator at the start of the iterations once and for all, and then applying the full matrix-representation of $\hat{P}$ at every iteration might decrease the numerical cost. This procedure avoids the numerical cost of the iterative procedure of the conjugate gradient algorithm, but would incur a multiplication with a matrix with the full dimensions of the mesh. Depending on the precise implementation, this might be worth the effort, but it has not been implemented in the current version of `MOCCa`.

[10]Note that dt here does no longer have the dimensions of time, but this is not really relevant.

4.9.3 Nesterov gradient descent

Another possible iteration scheme is due to Nesterov [93] and is usually called Nesterov (accelerated) gradient descent. As a starting point, define a series of parameters $\alpha^{(i)}$ as

$$\begin{cases} \alpha^{(0)} = 0\,, \\ \alpha^{(i)} = \dfrac{1}{2}\left(1 + \sqrt{1 + 4\left(\alpha^{(i-1)}\right)^2}\right)\,. \end{cases} \tag{4.44}$$

Using these, we define a new updating scheme for the single-particle wavefunctions as

$$|\phi_l^{(i+1)}\rangle = \left(1 - \frac{dt}{\hbar}\hat{h}\right)|\chi_l^{(i)}\rangle\,, \tag{4.45}$$

$$|\chi_l^{(i+1)}\rangle = \frac{\alpha^{(i+1)} + \alpha^{(i)} - 1}{\alpha^{(i+1)}}|\phi^{(i+1)}\rangle + \frac{1 - \alpha^{(i)}}{\alpha^{(i+1)}}|\phi^{(i)}\rangle\,. \tag{4.46}$$

The vectors $|\chi_l^{(i+1)}\rangle$ are the result of a simple gradient descent step, but at every iteration this direction gets mixed with the previous step $|\chi_l^{(i)}\rangle$. This scheme is thus very reminiscent of so-called momentum methods [94], where the momentum in phase-space from previous updates carries over to further updates. There exist geometrical interpretations of this algorithm [95], and several elegant mathematical results, but we will limit ourselves here to the application to the nuclear many-body problem.

The ordinary gradient descent scheme guarantees that the error on the optimized quantity (in our case the energy of the many-body state[11]) decreases at least as t^{-1} with t the number of iterations. This is an upper bound and the maximum achievable convergence rate is in fact proportional to t^{-2}. Our main interest in Nesterov accelerated gradient descent is due to the fact that this algorithm is provably optimal [93], in the sense that it guarantees the maximum achievable error reduction, proportional to t^{-2}.

As the iterations build-up, the information contained in the $|\chi_l^{(i)}\rangle$ starts becoming irrelevant as $\hat{h}^{(i)}$ gets updated. This results in temporary increases in the energy, hindering convergence [96]. For this reason we augment the procedure by resetting the value of $\alpha^{(i)}$ to zero every 20 iterations and thus resetting the memory contained in the $|\chi^{(i)}\rangle$, in order to refresh the memory built into the scheme. This approach can probably be improved tremendously if one incorporates a detection mechanism that intelligently resets $\alpha^{(i)}$, instead of naïvely choosing a fixed value of iterations.

The result of this scheme can be seen in Fig 4.8 for a Hartree-Fock calculation for ^{40}Ca. Restarted Nesterov is clearly significantly faster than both alternatives and maintains a rather steep slope despite a residual wavy character of the convergence. Nesterov without restarts starts of strong, but as redundant information piles up, one observes a lot of iterations were the convergence actually worsens. In the end, this method is still roughly comparable to the ordinary gradient descent method.

The Nesterov scheme with restarts needs only mildly more computational power compared to ordinary gradient descent: one does need to apply $\hat{h}^{(i)}$ to the $|\chi_l^{(i)}\rangle$ vectors (involving derivatives), but one does not need to apply $\hat{h}^{(i)}$ to the actual single-particle wavefunctions $|\phi_l^{(i)}\rangle$. It is thus a very promising avenue for further optimizing `MOCCa`.

At the moment however, it is not used as default iterative scheme (and in fact anywhere else in this dissertation) due to two main disadvantages. The first is the issue of resetting α: the optimal resetting protocol seems in general very much problem dependent and a bad choice destroys the attractive properties of the method. A more intelligent resetting scheme is thus required. Secondly, it is at the moment unclear how predictor-corrector constraints (see chapter 5) would fit into the update scheme in Eqs. (4.46). While these constraints are not necessary for a well-functioning code, they are indeed very practical on a day-to-day basis and a very attractive point of the current version of the code.

4.9.4 Direct Inversion of the subspace (DIIS) density mixing

The linear mixing of the densities in Eq. (4.26) is rather naïve in two ways. Firstly, at iteration (i) it only uses the mean-field densities from the previous iteration $(i-1)$ and does not use any information that might have been gathered at iteration $(i-2)$ and before. Secondly, it does not take into account any features of $\rho^{(i)}$: if $\rho^{(i)}$ lowers the energy significantly one would like for it to make a significant contribution.

A method commonly employed in electronic structure calculations is called Direct Inversion in the Subspace

[11] Or in fact the Routhian, see chapter 5.

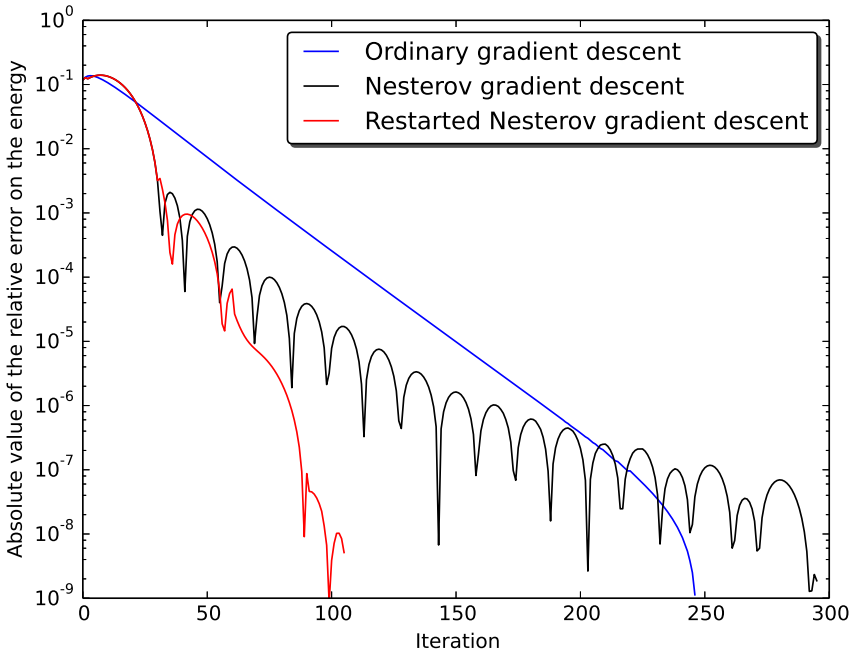

Figure 4.8: Comparison between ordinary gradient descent, Nesterov accelerated gradient descent and Nesterov accelerated gradient with restarts every 30 iterations for a calculation without pairing for ^{40}Ca using the SLy4 parameterization.

(DIIS in short) or Pulay mixing, after its inventor [97]. This method aims to remedy both deficiencies of the linear mixing scheme. For a given order n of the scheme, `MOCCa` mixes at iteration (i) the n values of all the mean-field densities at iteration $(i), (i-1), (i-2), \ldots,$ and $(i-n+1)$. They all get mixed with real coefficients c_k as follows

$$\rho^{(i)}(\mathbf{r}) = \sum_{k=1}^{n} c_k \rho^{(i-k+1)}(\mathbf{r}) \tag{4.47}$$

and similar for the other mean-field densities. The coefficients c_k satisfy the condition

$$\sum_{k=1}^{n} c_k = 1\,. \tag{4.48}$$

One then defines the residuals $p^{(k)}(\mathbf{r})$ as

$$p^{(k)}(\mathbf{r}) = \rho^{(k)}(\mathbf{r}) - \rho^{(k-1)}(\mathbf{r})\,. \tag{4.49}$$

The residual vector associated with the mixing in Eq. (4.47) is then

$$p^{(i)}(\mathbf{r}) = \sum_{k=1}^{n} c_k p^{(i-k+1)}(\mathbf{r})\,. \tag{4.50}$$

Our iterative scheme is converged when the density does not change from one iteration to the next, so one would like $p^{(i)}(\mathbf{r})$ to be small. Therefore, we wish to minimize its norm, which translates to the following objective function

$$|p^{(i)}(\mathbf{r})|^2 = \sum_{k,l=1}^{N} c_k c_l \int d\mathbf{r}\, p^{(i-k+1)}(\mathbf{r}) p^{(i-l+1)}(\mathbf{r}) - \lambda \left(1 - \sum_{k=1}^{N} c_k\right)\,, \tag{4.51}$$

with a Lagrange constraint on the sum of the coefficients c_k. We define the overlap between two residuals as

$$B_{kl} = \int d\mathbf{r}\, p^{(i-k+1)}(\mathbf{r}) p^{(i-l+1)}(\mathbf{r})\,, \tag{4.52}$$

and similar for the other mean-field densities. This leads us to an (n+1)-dimensional symmetric linear system

$$\begin{pmatrix} B_{11} & B_{12} & \dots & B_{1n} & -1 \\ B_{21} & B_{22} & \dots & B_{2n} & -1 \\ \vdots & \vdots & \ddots & \vdots & \vdots \\ B_{n1} & B_{n2} & \dots & B_{nn} & -1 \\ -1 & -1 & \dots & -1 & 0 \end{pmatrix} \begin{pmatrix} c_1 \\ c_2 \\ \vdots \\ c_n \\ \lambda \end{pmatrix} = \begin{pmatrix} 0 \\ 0 \\ \vdots \\ 0 \\ -1 \end{pmatrix} . \tag{4.53}$$

Unless this linear system is (almost) singular, the coefficients c_k can be found rather easily and the mixing of densities using Eq. (4.47) can be implemented. For modest values of n the numerical effort of calculating the B_{kl} and solving the linear system is completely negligible.
When the linear system is close to singular however, the system becomes unstable and the values of the c_k numerically deduced become numerically less than optimal. This is the case if the $p^{(k)}$ become (almost) linearly dependent, meaning that the gradient descent algorithm is exploring the same directions in phase-space during consecutive iterations. This means that in practice the memory order n is best limited to small values, typically 3 or 4.
Nevertheless, if the change in densities during the densities are not significant enough, the method in general fails to improve convergence, as shown in Fig. 4.9. Applied directly to the gradient descent algorithm for normal values of dt the overall trend of convergence is rather the same as with linear density mixing, only with more rather erratic oscillatory behaviour on top of the overall trend. If we change the iteration scheme to include preconditioning, the inclusion of DIIS significantly improves the convergence rate with respect to the linear mixing. This is due to the fact that preconditioned gradient descent manages a greater rate of change compared to ordinary descent, and therefore increases the stability of the DIIS scheme. Note that even for the preconditioned scheme there is still some erratic behaviour to be observed, indicating that the rate of change in the densities might not be large enough.
The DIIS method, applied to the mean-field potentials instead of the densities, is known in general as Broyden mixing[12]. The behaviour of this method for the nuclear many-body problem, reported in [91], is more beneficial to the convergence of the iterative scheme. This is primarily due to the fact that the code HFODD employs the more standard iterative scheme as explained in section 4.6. During successive mean-field iterations, the mean-field potentials change sufficiently due to the fact that the single-particle Hamiltonian is diagonalised at every iteration. This evades potential singularities of the linear system in Eq. (4.53).

4.9.5 Relative timing and conclusions

We have seen several points of possible improvement on the basic gradient descent scheme. All of them (except the expansion to higher order in dt) show some promise in speeding up the convergence of `MOCCa`. The number of iterations needed to converge the energy to within a relative error of 10^{-9} MeV for the various methods is given in Table 4.4.
For a mesh with $dx = 1$ fm, the CPU time is negligible for all of the methods and probably within the error margin of CPU time measurements. Only a scheme that combines the preconditioned gradient and DIIS density mixing does significantly better. For a finer mesh discretisation $dx = 0.5$ fm all schemes significantly improve upon the ordinary gradient descent scheme, with the preconditioned scheme with DIIS again a clear winner being almost five times as fast as ordinary gradient descent.
However, at this point in time ordinary gradient descent still takes precedence. Preconditioning is always effective in terms of number of iterations, but only significantly wins out when dx is small in the CPU time race. For most applications $dx = 0.8 \sim 1.0$ fm is quite accurate (see 8) and preconditioning does not bring appreciable benefit there. On the contrary, one should not forget that using preconditioning incurs the cost of human time to optimize $\frac{dt}{E_0}$, since contrary to the gradient descent case, the largest stepsize is not automatically the best in terms of CPU time.
Nesterov gradient descent is also very promising, but we need some further work in order to be able to reliable use this in applications. The current implementation of `MOCCa` needs a more reliable and intelligent restarting scheme and a way to incorporate the predictor corrector constraints into this method.
DIIS mixing also shows promise, but needs to be used in conjunction with preconditioning to have a beneficial effect. In order to use this method for practical applications, we would need to find a way to get rid of the erratic behaviour, as for example shown in Fig. 4.9, in order to be sure that activating the DIIS mixing procedure is not detrimental to convergence. Again here, a clever restarting scheme to wipe the memory of

[12] Although there are small differences.

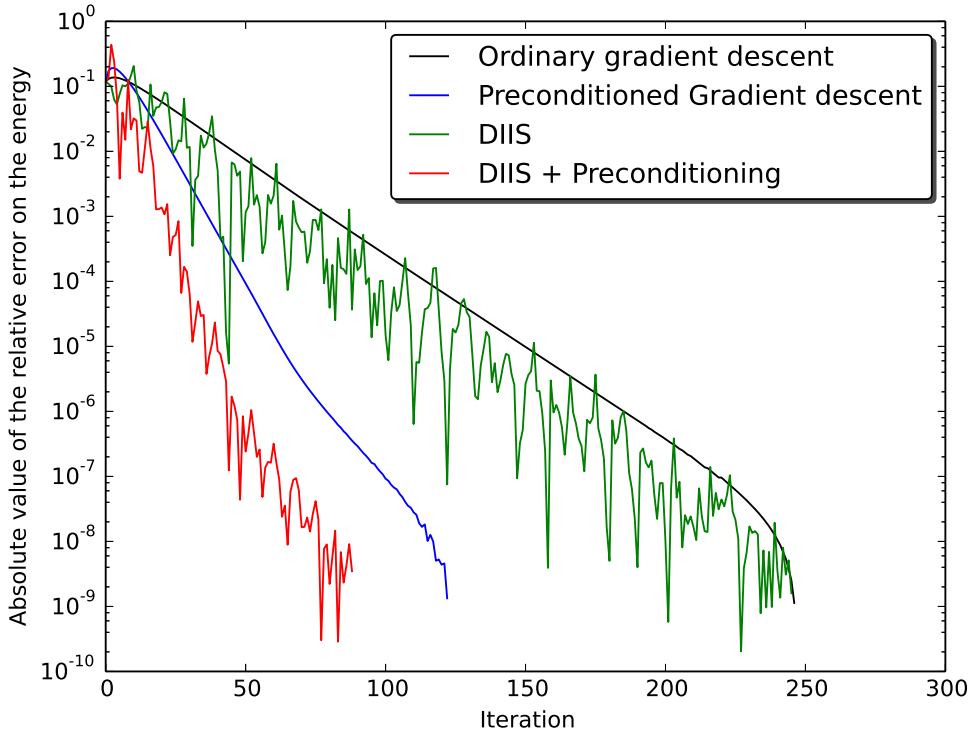

Figure 4.9: Calculation for ^{40}Ca using the SLy4 parameterization, using either ordinary gradient descent ($dt = 0.02 \times 10^{-22}$s) or preconditioned gradient descent ($\frac{dt}{E0} = 0.1 \times 10^{-22}$s) with linear mixing of the densities (`DampingParam` $= 0.75$) or with DIIS mixing of the densities ($n = 3$).

	dx=1.0 fm		dx=0.5 fm	
	Iterations	CPU time (s)	Iterations	CPU time(s)
Gradient descent	243	5.3	542	149.2
Preconditioned gradient descent	149	4.7	151	63.3
Nesterov gradient descent	108	3.9	235	70.8
Preconditioned gradient descent with DIIS	70	2.3	70	37.6

Table 4.4: Number of iterations and CPU time on a personal computer necessary to converge the energy to within a relative error of 10^{-9} of the converged value for a Hartree-Fock calculation of ^{40}Ca for different iteration schemes. The two different meshes have respectively $nx = ny = nz = 10$ with $dx = 1.0$ fm and $nx = ny = nz = 20$ with dx=0.5 fm.

the method might be useful.
Once the above issues have been addressed, the obvious next step would be to try to precondition the Nesterov scheme while using DIIS mixing. This is not possible in the current version of `MOCCa`, but due to the modularity of the code it would not be complicated to enable this possibility. Comparing the resulting method to the results in this section might be very interesting.

Chapter 5

Constraints

The point of breaking symmetries is of course moot if one can not generate symmetry-breaking configurations. MOCCa needs to be able to explore the degrees of freedom that are opened by broken symmetries in a controllable way. The problem we will explore in this chapter is: given a one-body operator[1] $\hat{\mathcal{O}}$, we would like to find a solution of the mean-field equations (either HF, BCS or HFB) that satisfies

$$\langle\Psi|\hat{\mathcal{O}}|\Psi\rangle = O\,, \tag{5.1}$$

where O is a number that is fixed before the start of the mean-field process. One can then find different solutions for different values of O and in this way explore the degrees of freedom associated with the operator $\hat{\mathcal{O}}$. Finding these solutions in a controlled way becomes even more important when one wants to do a GCM procedure afterward with O as the generator coordinate.
The obvious candidates for the operators $\hat{\mathcal{O}}$ are the order parameters discussed in chapter 2. They are fine examples (and often the most intuitive ones) of the degrees of freedom that broken symmetries imply and are very well suited to become generator coordinates in a GCM scheme. Historically, constraints have often (if not always) been put on the quadrupole deformation $(\langle\hat{\mathcal{Q}}_{20}\rangle, \langle\mathrm{Re}\,\hat{\mathcal{Q}}_{22}\rangle)$ in order to generate oblate, prolate and triaxial ellipsoid shapes. The octupole moments (particularly $\langle\hat{\mathcal{Q}}_{30}\rangle$) have been constrained to generate what one colloquially calls 'pear' or 'strawberry'[2] shapes. The interest of constraining various multipole moments is thus the generation of a veritable zoo of shapes.
The angular momentum is another prime example of an order parameter. Constraining a projection of the angular momentum to a certain value is also known as cranking. This model is widely spread in the literature and is not only limited to mean-field theory [98]. A similar case is the isocranking method [99], where one constrains the expectation value of isospin components. MOCCa is at the moment not able to do this, but the mathematical framework is completely analogous to the one of regular angular momentum.
Constraints can be imposed too on quantities as the total particle number and the dispersion $\Delta\mathcal{N}^2$. These are more related to the pairing subproblem than the mean-field iterations and will be dealt with separately in chapter 6.

5.1 Lagrange multipliers

The problem of minimizing the energy of the mean-field state thus becomes a constrained optimization problem. The most intuitive thing to do is to add a Lagrange multiplier λ_O to the energy [88].

$$E_{\mathsf{HF(B)}} \to E_{\mathsf{HF(B)}} + E_{\mathsf{Con}} = E_{\mathsf{HF(B)}} - \lambda_O\langle\Psi|\hat{\mathcal{O}}|\Psi\rangle\,. \tag{5.2}$$

For a functional that respects the link with a many-body Hamiltonian, this corresponds to creating a Routhian

$$\hat{\mathcal{H}} \to \hat{\mathcal{R}} = \hat{\mathcal{H}} - \lambda_O\hat{\mathcal{O}}\,. \tag{5.3}$$

The single-particle Hamiltonian also gets modified into the single-particle Routhian

$$\hat{h} \to \hat{R} = \hat{h} + \hat{h}_C = \hat{h} - \lambda_O\hat{O}\,, \tag{5.4}$$

The generalization to multiple constraints of the contributions to the energy and single-particle Hamiltonian is straightforward

$$E_{\mathsf{Con}} = -\sum_k \lambda_k\langle\Psi|\hat{\mathcal{O}}_k|\Psi\rangle\,, \tag{5.5a}$$

$$\hat{h}_C = -\sum_k \lambda_k\hat{O}_k\,. \tag{5.5b}$$

[1] This problem can be generalized to more general many-body operators, but the problem becomes numerically much and much harder.
[2] Thanks to V. Hellemans to point out the resemblance.

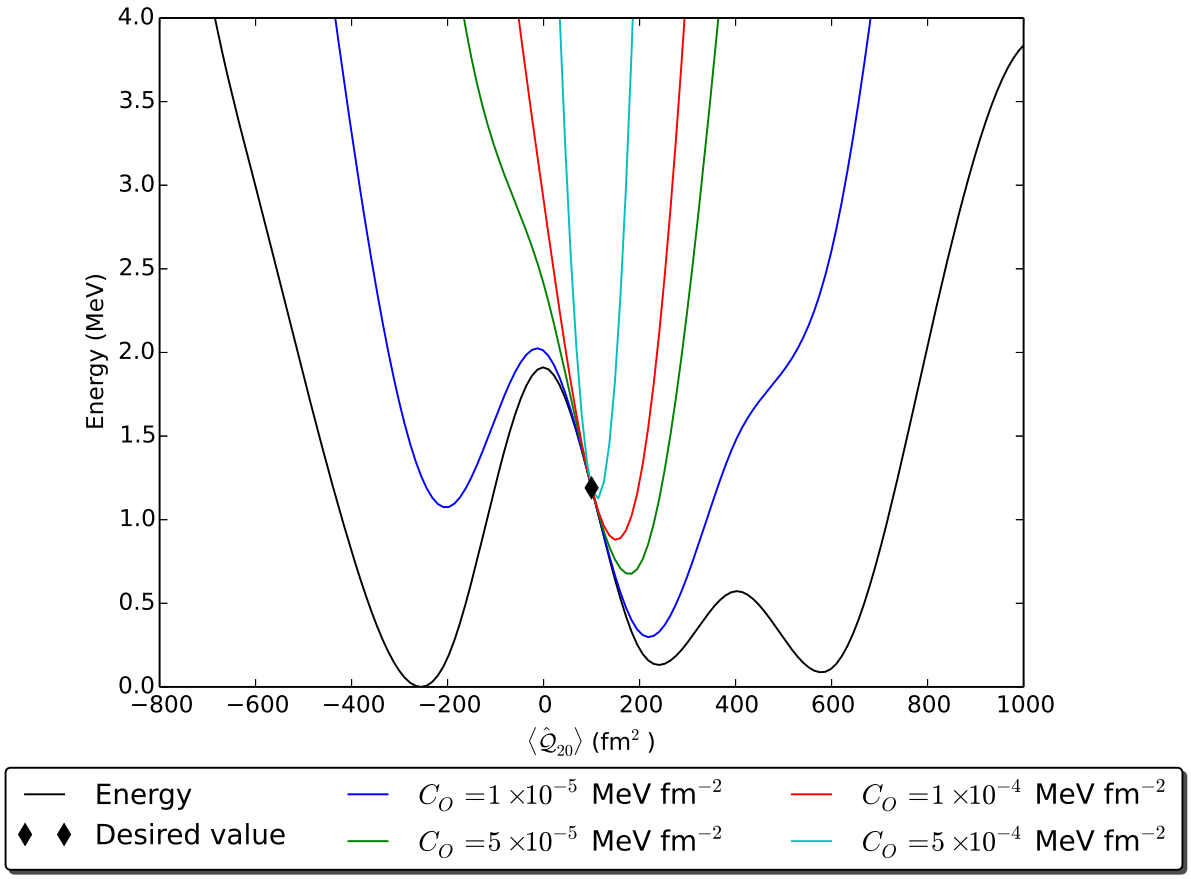

Figure 5.1: Energy of ^{178}Hg calculated with the SLy4 parameterization with HFB+LN pairing as a function of deformation $\langle \hat{\mathcal{Q}}_{20} \rangle$, superimposed with the Routhians with a quadratic penalty function for various values of C_O around $\langle \hat{\mathcal{Q}}_{20} \rangle = 100$ fm^2. Note that the minimum of the Routhians coincides more and more with the desired value of the quadrupole moment as C_O increases. Meanwhile the slopes of the Routhians become steeper and steeper, worsening the condition of the numerical problem.

When λ_O is taken as a constant, we refer to this type of constraint as linear. Note that this is a completely natural way to introduce symmetry breaking into our self-consistent scheme. While $\hat{h}$ might be symmetrical with respect to a symmetry operator $\hat{U}$, the operator $\hat{\mathcal{O}}$ need not be. The constrained optimization process will thus in general have a symmetry-breaking solution for non-zero values of O.
The challenge is now to find a value of λ_O so that the expectation value of our constrained operator takes the desired value. From Lagrangian mechanics we know that for the solution that minimizes Eq. (5.2) holds

$$\lambda_O = \frac{\partial E_{\text{HF(B)}}}{\partial \langle \hat{\mathcal{O}} \rangle}, \tag{5.6}$$

meaning that λ_O determines the slope of the energy with respect to variations in the value of $\langle \hat{\mathcal{O}} \rangle$. This determines the correct λ_O in hindsight, but is of no practical value when actually trying to calculate $E_{\text{HF(B)}}$. The next sections will focus on how to choose λ_O in order to solve this problem. All of these suggestions vary λ_O as a function of the many-body state at the current mean-field iteration.
For constant values of λ_O this has profound consequences on the accessibility of different parts of the energy surface: where the second derivative of the energy is positive, the energy surface is convex and the minimization of the Routhian will be unstable. In short, for constant values of λ_O the minimum of the Routhian will always be in a concave region of the energy surface. The convex regions of the energy surface will thus be completely inaccessible.

5.2 Penalty function method

A well known method from the constrained optimization literature is the penalty function method. In direct generalization of a Lagrange multiplier, one adds a function $f(\langle\hat{\mathcal{O}}\rangle)$ to the energy that has a minimum at $\langle\hat{\mathcal{O}}\rangle = O$. In this way, the energy rises at other values of $\langle\hat{\mathcal{O}}\rangle$ and is thus penalized. The simplest and most widely used form of f is quadratic

$$E_{\text{Con}} = C_O \left(\langle\hat{\mathcal{O}}\rangle - O\right)^2 , \tag{5.7}$$

where C_O is (for the moment) a free parameter. The corresponding contribution to the single-particle Routhian is

$$\hat{h}_C = 2C_O \left(\langle\hat{\mathcal{O}}\rangle - O\right)\hat{O} . \tag{5.8}$$

In this expression $-C_O(\langle\hat{\mathcal{O}}\rangle - O)$ has taken the role of the Lagrangian multiplier. Instead of the fixed number λ_O in Eq. (5.5) the Lagrange multiplier is now dependent on the mean-field state and thus on the iteration number (i).
The quadratic penalty functions suffers from a serious drawback: the minimum of Eq. (5.8) is only approximately at $\langle\hat{\mathcal{O}}\rangle = O$ for any finite value of C_O. As C_O grows in size, $\langle\hat{\mathcal{O}}\rangle$ for the minimizer of Eq. (5.8) becomes closer and closer to O. This is illustrated in Fig. 5.1 for the energy of ^{178}Hg as a function of the quadrupole deformation. Only as C_O grows does the minimum of the Routhian coincide with the desired deformation.
Any method using penalty functionals thus needs large enough penalties, which translates to large values for C_O in the case of the quadratic penalty function. Too large values of this parameter however severely limit the practical feasibility of a numerical algorithm. As C_O increases the conditioning of the problem becomes dramatically worse, as the penalty function completely dominates the nuclear part of the single-particle Hamiltonian. Numerical schemes will thus easily diverge, as the directions in the solution space that improve the constraint but are not physically feasible will be preferable to the algorithm.
In principle this problem is manageable, as one can take an iterative approach to this problem. First one minimizes the energy for $C_O^{(1)} = 0$, corresponding to an unconstrained minimization. One then takes this as an input for a minimization with C_O equal to some small value[3]. The result is of this minimization does not satisfy the desired constraint exactly, but can be used as a starting point for a calculation with an increased value of $C_O^{(2)}$. This process continues for ever increasing $C_O^{(i)}$ until the constraint is satisfied to the desired precision. Since every calculation will start progressively closer to the desired point, the conditioning of the problem can (hopefully) be controlled.
The quadratic form in Eq. (5.7) is the simplest and most widely spread form of penalty functions. Other forms of the penalty function $f(\langle\hat{\mathcal{O}}\rangle)$ are possible. In modern applications, they are mainly used for problems that are subject to inequality constraints, and are often called interior point or barrier methods. However, the deficiency related to the choice of any parameters in the form of $f(\langle\hat{\mathcal{O}}\rangle)$ is a critical weakness of the entire class of methods [88].

5.3 Augmented Lagrangian method and readjusting quadratic constraints

The augmented Lagrangian method is a well-known technique [88] that has also found its way into many nuclear structure codes [100]. This method solves the problem that finite values of C_O entail for quadratic penalty functions. Consider again the quadratic penalty function addition to the single-particle Hamiltonian

$$\hat{h}_C^{(i)} = 2C_O(\langle\hat{\mathcal{O}}\rangle^{(i)} - O^{(i)})\hat{O} , \tag{5.9}$$

where we have now given the target value of $\langle\hat{\mathcal{O}}\rangle$ an explicit iteration index. The idea is to cleverly adjust the target value $O^{(i)}$ during the mean-field iterations to obtain a Routhian with a minimum at $\langle\hat{\mathcal{O}}\rangle = O$.
The addition of $O^{(i)}$ can also be interpreted as the addition of a linear constraint on top of the quadratic constraint, meaning that

$$\hat{h}_C^{(i)} = -2C_O(O - O^{(i)})\hat{O} + 2C_O(\langle\hat{\mathcal{O}}\rangle^{(i)} - O)\hat{O} , \tag{5.10}$$

where there is now an extra linear constraint present with $\lambda_O = 2C_O(O - O^{(i)})\hat{O}$. By changing the value $O^{(i)}$ iteratively, one adjusts the parabola of the penalty function in order to get the minimum at the desired value of $\langle\hat{\mathcal{O}}\rangle$. This means that $O^{(i)}$ gets adjusted so that $C_O(O - O^{(i)})$ will approach the correct Lagrange multiplier. In contrast, the parameter C_O remains fixed and determines the stiffness of the parabola, thus

[3] It is of course, problem dependent what a small value of $C_O^{(1)}$ is and this is usually not that clear in practice.

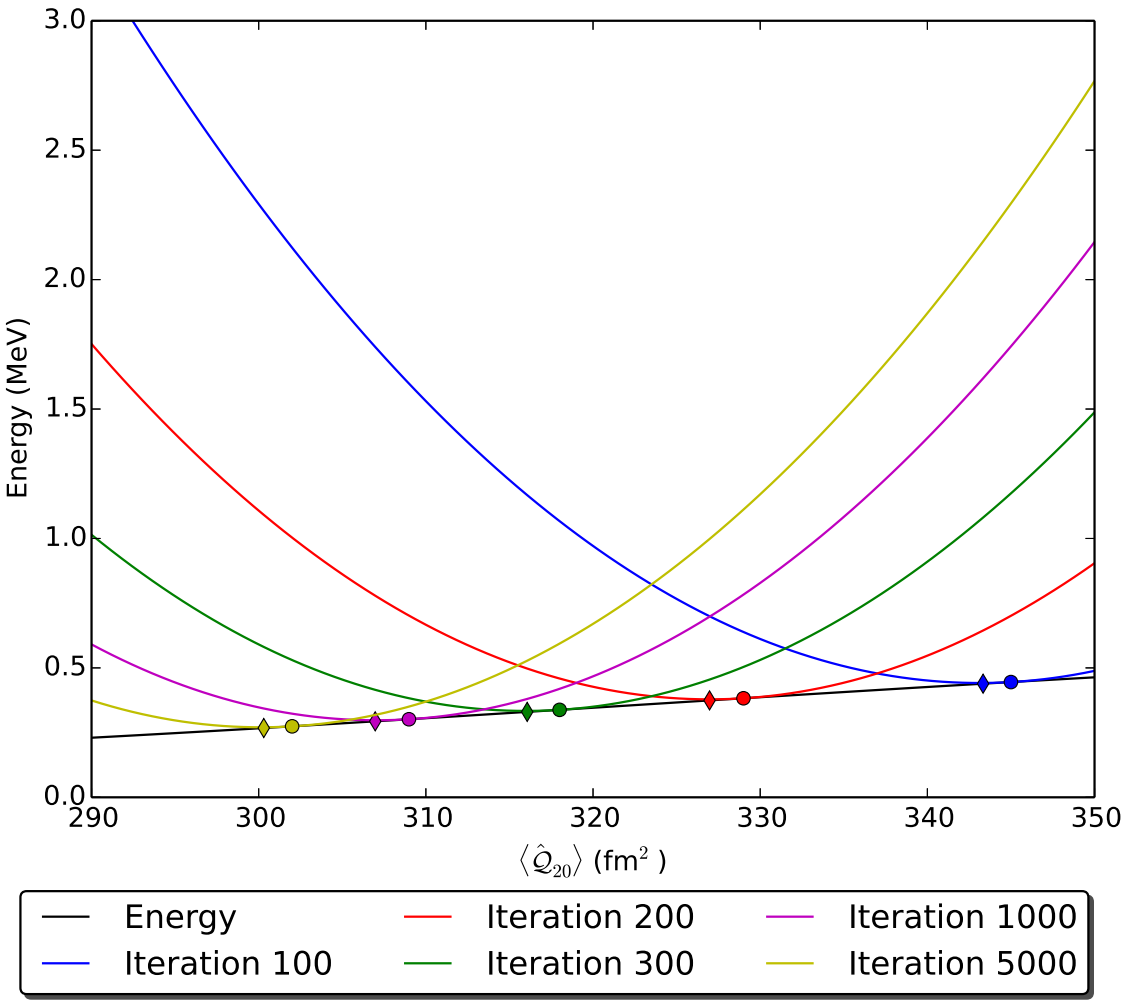

Figure 5.2: Energy of ^{178}Hg calculated with the SLy4 parameterization and HFB+LN pairing as a function of deformation $\langle \hat{\mathcal{Q}}_{20} \rangle$, superimposed with the Routhians at different mean-field iterations using the augmented Lagrangian method for $C_O = 10^{-3}$ MeV fm^{-2} and $v_{\text{readjustment}} = 0.02$. The targetted quadrupole deformation is $\langle \hat{\mathcal{Q}}_{20} \rangle = 300$ fm^2. The circle indicates the minimum of the parabolic constraint function of the corresponding color, while the diamond indicates the minimum of the total Routhian of the corresponding color.

guaranteeing the stability of the optimum of the Routhian, even where the energy surface is convex.
The explicit dependence of $O^{(i)}$ on the iterations is best taken as [101]

$$O^{(i)} = O^{(i-1)} + \langle \hat{\mathcal{O}} \rangle^{(i)} - O \,. \tag{5.11}$$

and the initial value $O^{(0)}$ can either be taken as O (corresponding to a linear constraint with Lagrange multiplier zero) or as some value obtained from a previous calculation that might constitute a better guess of the slope of the energy surface.
Note that there is an intrinsic ambiguity in the definition of an iteration here. The original augmented Lagrangian method inherently assumed that the minimization problem posed by Eq. (5.9) was solved for fixed $O^{(i)}$. Then $O^{(i)}$ is updated to $O^{(i+1)}$ and the minimization can be done again. This idea is perfectly in line with the spirit of ordinary mean-field algorithms, discussed in section 4.6. For the imaginary time-method as employed in `MOCCa`, `cr8`, `ev8` and `ev4`, this is absolutely not the case, as only a single iteration of the minimization is performed at every mean-field iteration. In practice this means that it is unreliable to perform the update in Eq. (5.11) every mean-field iteration, as $\langle \hat{\mathcal{O}} \rangle^{(i)}$ can vary wildly especially at the start of the iterative process.
The practical and time-honored way [9] to remedy this problem is simply by introducing the readjustment speed to the update formula in Eq. (5.11)

$$O^{(i)} = O^{(i-1)} + v_{\text{readjustment}}(\langle \hat{\mathcal{O}} \rangle^{(i)} - O) \,, \tag{5.12}$$

where $v_{\text{readjustment}}$ is significantly smaller than one. For example, the default value in the case of quadrupole constraints is 0.02, thereby splitting one full update like Eq. (5.11) over roughly of 50 to 100 mean-field iterations. Remark that the method reduces to the straight-forward penalty function method when $v_{\text{readjustment}}$ is set to zero.
The application of the augmented Lagrangian method with $C_O = 10^{-3}$ MeV fm^{-2} and $v_{\text{readjustment}} = 0.02$ is shown in Fig. 5.2. The initial Routhian is simply the corresponding quadratic penalty function and as the iterations progress the parabola gets adjusted to in order to put the minimum of the Routhian at $\langle \hat{\mathcal{Q}}_{20} \rangle = 300$ fm^2. The circles indicate the minimum of the parabolic constraint function, while the diamonds indicate the minimum of the total Routhian. Note that the diamonds approach the targeted deformation as the iterations progress, while the circles maintain a finite distance.

5.4 Predictor-corrector constraints

The augmented Lagrangian method solves the need of penalty functions to have their parameter C_O go to infinity. The dependence on the parameter C_O still remains in the sense that large values of C_O still make the problem numerically hard and too low values make convergence very slow[4]. Unfortunately, the optimal value of C_O is highly problem dependent, as constraints are imposed on different operators. For constraints on the multipole moments this is readily apparent: centre-of-mass coordinates are on the scale of some fm, while quadrupole deformations take values in the range of hundreds of fm^2 and octupole deformations take values in the several thousands of fm^3. In addition, there is significant variation in the size of typical deformations as a function of nuclear mass.
In the case of a single constraint, this problem is easily solved by a little human trial-and-error search for a good parameter C_O. When dealing with multiple constraints however, this becomes significantly harder. A calculation that breaks parity has typically constraints on $\langle \hat{\mathcal{Q}}_{20} \rangle$, $\langle \mathrm{Re}\, \hat{\mathcal{Q}}_{22} \rangle$, $\langle \hat{\mathcal{Q}}_{30} \rangle$ and the centre-of-mass coordinate $\langle \hat{\mathcal{Q}}_{10} \rangle$. Finding a working combination of C_{10}, C_{20}, C_{22} and C_{30} is a four-dimensional search with directions that are characterized by significantly different scales, and is in many cases if not impossible at least very time-consuming.
A method that is very much less reliant on parameters was introduced in [102] and further explained in [103]. Since both authors did not introduce a specific name for this method, we take the freedom of proposing the name predictor-corrector constraints.
Consider the imaginary-time step method with a linear constraint on an operator $\hat{\mathcal{O}}$. The single-particle wavefunctions at iteration $(i+1)$ are obtained from those at iteration (i) as[5]

$$|\phi_l^{(i+1)}\rangle = \left[\mathbb{1} - \frac{dt}{\hbar}\left(\hat{h} - \lambda_O^{(i)}\hat{O}\right)\right]|\phi_l^{(i)}\rangle\,. \tag{5.13}$$

The expectation value of $\hat{\mathcal{O}}$ at iteration (i) can easily be computed (up to linear order in $\frac{dt}{\hbar}$)

$$\begin{aligned}\langle\hat{\mathcal{O}}\rangle^{(i+1)} &= \sum_l v^{2,(i)}\langle\phi_l^{(i+1)}|\hat{O}|\phi_l^{(i+1)}\rangle \\ &= \langle\hat{\mathcal{O}}^{(i)}\rangle + 2\frac{dt}{\hbar}\left[\sum_l v_l^{2,(i)}\langle\phi_l^{(i)}|\hat{h}\hat{O}|\phi_l^{(i)}\rangle - \lambda_O^{(i)}v_l^{2,(i)}\langle\phi_l^{(i)}|\hat{O}^2|\phi_l^{(i)}\rangle\rangle\right] + O\left(dt^2\right)\,,\end{aligned} \tag{5.14}$$

where the v_l^2 are obtained by solving the pairing equations and the $|\phi_l\rangle$ are the single-particle wavefunctions in the case of the HF and BCS schemes, but the single-particle wavefunctions in the canonical basis in the case of the HFB ansatz. If we require that $\langle\hat{\mathcal{O}}\rangle^{(i+1)} = O$ and solve for $\lambda_O^{(i)}$ one gets

$$\lambda_O^{(i)} = \left[\sum_l\left(v_l^{2,(i)}\langle\phi_l^{(i)}|\hat{h}^{(i)}\hat{O}|\phi_l^{(i)}\rangle\right) - \hbar\frac{\langle\hat{\mathcal{O}}^{(i)}\rangle - O}{2dt}\right]\left[\sum_l v_l^{2,(i)}\langle\phi_l^{(i)}|\hat{O}^2|\phi_l^{(i)}\rangle\right]^{-1}\,. \tag{5.15}$$

[4] The dependence on the parameter $v_{\text{readjustment}}$ is more benign and the default value seems to works most (if not all) of the time.

[5] Note that this derivation can easily be performed for other iteration schemes like the preconditioned gradient descent too. The only difficulty are two-step schemes, like the Nesterov iteration scheme, where the generalization is not immediately apparent.

In the case of multiple constraints on several operators O_k, the formula is largely unchanged, except for the denominator and one has for each multiplier λ_k[6]

$$\begin{aligned}\lambda_k^{(i)} &= \sum_k \left(\hat{K}^{-1}\right)_{kk'} \left[\sum_l \left(v_l^{2,(i)} \langle \phi_l^{(i)} | \hat{h}^{(i)} \hat{O}_{k'} | \phi_l^{(i)} \rangle\right) - \hbar \frac{\langle \hat{\mathcal{O}}_{k'}^{(i)} \rangle - O_{k'}}{2dt}\right], \\ K_{kk'} &= \sum_l v_l^{2,(i)} \langle \phi_l^{(i)} | \hat{O}_k \hat{O}_{k'} | \phi_l^{(i)} \rangle\end{aligned} \tag{5.16}$$

In principle, this formula would allow one to calculate the values of all the Lagrange multipliers λ that one would need to use to construct the Routhian that leads one to the desired expectation values of the constrained operators. In an iterative mean-field procedure this would not lead to a direct satisfaction of the constraints and Eq. (5.16) should be regarded as an update formula for the multipliers that will iteratively lead to the satisfaction of the constraints.
The practical implementation of Eq. (5.16), especially the calculation and inversion of the matrix K, is rather involved when many constraints are present. In practice, `MOCCa` does not calculate the value of $\lambda^{(i)}$ before evolving the single-particle wavefunctions in imaginary time. We first execute the standard evolution step as a trial step, denoted by iteration number $(i + \frac{1}{2})$

$$|\phi_l^{(i+\frac{1}{2})}\rangle = \left[\mathbb{1} - \frac{dt}{\hbar}\left(\hat{h} - \sum_k \lambda_k^{(i)} \hat{O}_k\right)\right] |\phi_l^{(i)}\rangle \,. \tag{5.17}$$

After orthonormalisation of the single-particle wavefunctions and solving the pairing equations for the occupation numbers $v_l^{2,(i+\frac{1}{2})}$, the expectation values $\langle \hat{\mathcal{O}}_k^{(i+\frac{1}{2})} \rangle$ are calculated. Because the λ_k did not have the proper values suggested by Eq. (5.16) we execute a corrective step

$$|\phi_l^{(i+1)}\rangle = \left[\mathbb{1} - \frac{dt}{\hbar} \sum_k \hat{q}_k \hat{O}_k\right] |\phi_l^{(i+\frac{1}{2})}\rangle \,. \tag{5.18}$$

where the corrective potential $\hat{q}_k$ is given by

$$\hat{q}_k = C_0 \frac{\langle \hat{\mathcal{O}}^{(i+\frac{1}{2})} \rangle - O_k}{\sum_l v_l^{2,(i+1/2)} \langle \phi^{(i+\frac{1}{2})} | \hat{O}_k^2 | \phi^{(i+\frac{1}{2})} \rangle\rangle + d_0} \,. \tag{5.19}$$

and where C_0 and d_0 are numerical parameters. The value of d_0 is rather unimportant and simply serves as a safeguard for when the denominator is small. The value of C_0 determines the strength of the corrective potential and is by default taken to be 0.2 for constraints on multipole moments and 0.8 for constraints on (projections of) the angular momentum. Note that C_0 has different units depending on the operator O_k that is constrained.
In addition, the Lagrange multipliers are updated as

$$\lambda_k^{(i+1)} = \lambda_k^{(i)} + \epsilon \frac{\langle \hat{\mathcal{O}}_k^{(i+\frac{1}{2})} \rangle - \langle \hat{\mathcal{O}}_k^{(i)} \rangle}{\sum_l v_l^{2,(i)} \langle \phi^{(i)} | \hat{O}_k^2 | \phi^{(i)} \rangle} \,, \tag{5.20}$$

where ϵ is again a numerical parameter that defaults to 7.0 for constraints on multipole moments and to 1.0 for constraints on (projections of) angular momentum. Note that this update of the Lagrange multipliers can not be easily related to formula for the total Routhian, as was the case for both quadratic penalty functions and the augmented Lagrangian method. This is the reason why we started directly from the single-particle Routhians in Eq. (5.13). The application of Eq. (5.20) concludes the iteration (i) and the scheme can proceed to the next iteration $(i + 1)$. The entire algorithm is summarized in 4.
The predictor-corrector constraint scheme is an ad-hoc approximation to Eq. (5.16) and has (to the best of our knowledge) never been rigorously derived. A first observation that one might make that is that the term $\sum_l v_l^2 \langle \hat{h}\hat{O} \rangle_l$ is approximated by $\langle \hat{\mathcal{O}}^{(i+\frac{1}{2})} \rangle$. As this can only be calculated after the trial step, this update is only taken into account afterwards, directly translating to the corrective potential $\hat{q}_k$. Another element is that

[6] Note that we conveniently forgot to include the orthonormalisation procedure in all of this as in [103]. Aside from this issue, this formula also does not agree with the one in [102] where the single-particle Hamiltonian ($\hat{W}$ in their notation) is applied to a many-body wavefunction in a fantastically vague confusion of notation. These issues will not play an important role, as this formula mainly serves as a motivation for the iteration scheme presented below.

for $i \rightarrow$ *MaxIter* **do**
  Obtain trial wavefunctions $|\phi_l^{(i+\frac{1}{2})}\rangle$
  Orthonormalise the trial wavefunctions $|\phi_l^{(i+\frac{1}{2})}\rangle$
  Solve the pairing subproblem to obtain the occupation factors $v_l^{(i+\frac{1}{2})}$
  Do the correction step to obtain the $|\phi_l^{(i+1)}\rangle$
  Orthonormalise the $|\phi_l^{(i+1)}\rangle$
  Solve the pairing subproblem to obtain the occupation factors $v_l^{(i+1)}$
  Update the Lagrange multipliers to obtain $\lambda_k^{(i+1)}$
end

Algorithm 4: Schematic of the gradient descent algorithm with predictor-corrector constraints incorporated.

the matrix K is assumed to be diagonal, massively simplifying its calculation and inversion.
Even though the argumentation is rather flimsy, the algorithm converges easily and does not depend sensitively on any numerical parameters like the augmented Lagrangian method. The default values of the numerical parameters ϵ, c_0 and d_0 ensure good convergence in virtually all of the systems that we have ever tried[7].
The numerical cost of this algorithm is however far from negligible. For every mean-field iteration the code now needs to execute two updates for all of the single-particle wavefunctions, including two orthogonalisation steps and solving the pairing subproblem twice. If the constrained operators $\hat{O}$ do not include derivatives (as for example the multipole operators $\hat{\mathcal{Q}}_{\ell m}$), the total cost per iteration is significantly less than twice the cost of an iteration of the augmented Lagrangian method as MOCCa doesn't need to derive the single-particle wavefunctions at the intermediate iteration. When any of the constrained operators do include derivatives (like the angular momentum operators $\hat{\mathcal{J}}_{x/y/z}$), we need to derive the intermediate single-particle wavefunctions and the numerical cost compared to the augmented Lagrangian method effectively doubles. Luckily this method does not scale with added constraints, as once the double-step scheme is used, the addition of extra constraints does not significantly impact CPU time, as the quantities involved are all easily computable.
The advantage of predictor-corrector constraints over the augmented Lagrangian method is shown in Fig. 5.3. A calculation of ^{80}Zr breaking parity is presented, that has four active constraints: one on the redundant z-coordinate of the centre-of-mass, two on both physical components of the quadrupole deformation $\langle\hat{\mathcal{Q}}_{20}\rangle, \langle\hat{\mathcal{Q}}_{22}\rangle$ and one on the axial octupole moment $\langle\hat{\mathcal{Q}}_{30}\rangle$. The predictor-corrector method has no troubles whatsoever steadily converging on all fronts using the default parameters: the errors on the energy, quadrupole moment and octupole moment all steadily decrease as a function of the iteration count. The augmented Lagrangian method is significantly slower in the case of all sets and is still far from converged after 4000 iterations especially for the first set of constraint intensities.
We emphasize that the augmented Lagrangian method is heavily dependent on the correct choice of its parameters, and it is probably not impossible to find a set of constraint parameters that are competitive with the predictor-corrector method. The third set for example, is only slightly slower compared to the predictor-corrector constraints. The problem is finding this set of optimal parameters, which is a significant investment of human time, while the predictor-corrector method can solve virtually any problem using the default parameters, at the price of only a moderate CPU time cost.

5.5 Possible constraints in MOCCa

MOCCa is equipped to deal with constraints on different quantities in a rather general way. Several different possibilities are implemented at the moment, but the system is easily extensible to accommodate constraints that users may wish to code themselves. As a general remark: the default constraint type employed is the predictor-corrector type, as it has shown to be easily the most easy to use and reliable of the methods discussed.

[7] The only slight exception are constraints on angular momentum, where one might occasionally want to lower the corresponding value of c_0 from 0.8 to somewhere in the range $0.2 - 0.8$.

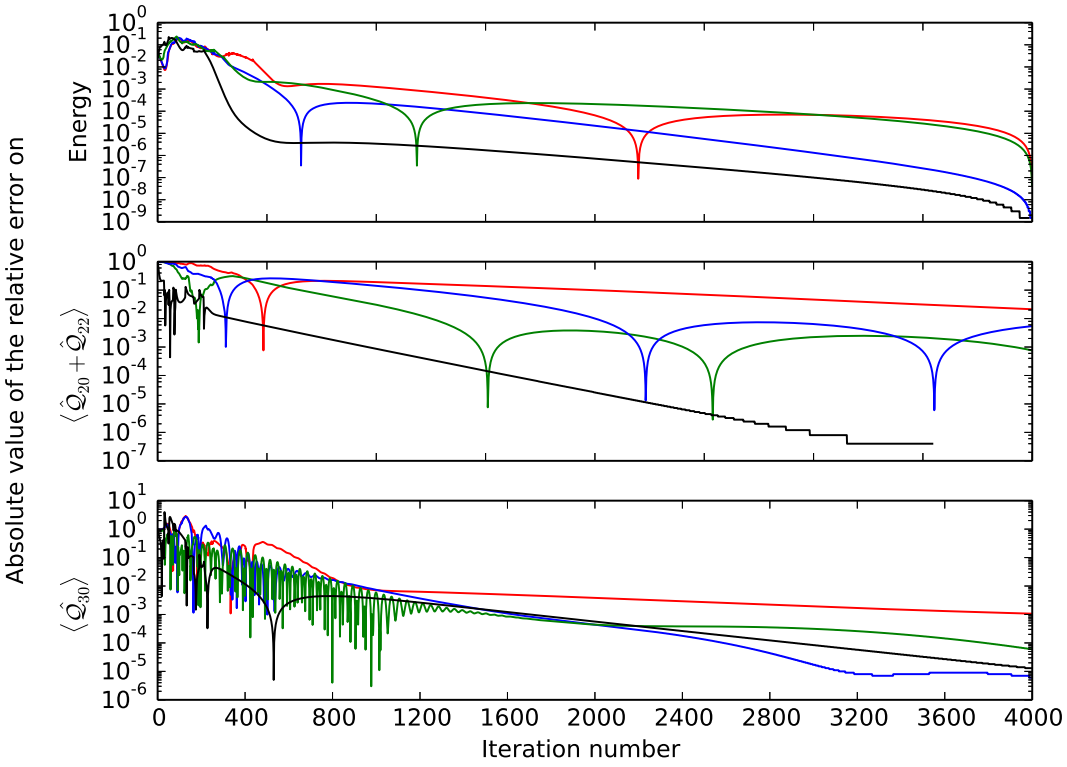

Set	1	2	3
C_{10} (MeV fm^{-2})	1.0	1.0	1.0
C_{20} (MeV fm^{-4})	0.0001	0.0005	0.0002
C_{22} (MeV fm^{-4})	0.0001	0.0005	0.0002
C_{30} (MeV fm^{-6})	0.0001	0.0001	0.0005

Figure 5.3: Convergence of energy, quadrupole moment and octupole moment for a parity-breaking calculation of ^{80}Zr using the SLy4 parameterization with BCS pairing using either the augmented Lagrangian method (red/green/blue) or predictor-corrector (black) constraints. The active constraints are the centre-of-mass coordinate $\langle \hat{\mathcal{Q}}_{10} \rangle$ (not shown), quadrupole constraints on $\langle \hat{\mathcal{Q}}_{20} \rangle = 250$ fm^2 and $\langle \hat{\mathcal{Q}}_{22} \rangle = 0$ fm^2 and on $\langle \hat{\mathcal{Q}}_{30} \rangle = 100$ fm^3. The constraint intensities as used by the augmented Lagrangian method are tabulated in the table below the figure, for their respective color. Sudden dips in the lines are associated with changes of the sign of the error.

5.5.1 Multipole constraints

Most calculations are interested in constraining the expectation values of multipole operators $\hat{\mathcal{Q}}_{\ell m}$, as has been demonstrated in the examples given in this chapter and will be further shown in the applications in part III of this dissertation.

The current code is capable of constraining any set combination of $\langle \hat{\mathcal{Q}}_{\ell m} \rangle$ for any value of (ℓ, m). The only two limitations are imposed by the input parameter `MaxMoment`, which determines the maximum value of ℓ that is calculated and by the conserved symmetries requested by the user[8]. The user is thus free to specify constraints on $\langle \hat{\mathcal{Q}}_{87} \rangle$ or similar exotic deformations. The only caveat is that high-ℓ multipole moments are not very well represented on Cartesian meshes with limited number of points and one should take into account that their computed values are not necessarily very reliable.

The constraints can all be put either on the multipole moments of the total density

$$\langle \hat{\mathcal{Q}}_{\ell m} \rangle_t = \langle \hat{\mathcal{Q}}_{\ell m} \rangle_0 = O\,, \tag{5.21}$$

[8]The other limitation is a constraint on Q_{00}, which represents the number of particles. This constraint is in practice automatically taken into account by the pairing subproblem solvers, see 6.

as was demonstrated throughout this chapter or separately on proton and neutron values

$$\begin{aligned}\langle\hat{\mathcal{Q}}_{\ell m}\rangle_p &= O_p\,,\\ \langle\hat{\mathcal{Q}}_{\ell m}\rangle_n &= O_n\,.\end{aligned} \tag{5.22}$$

The isovector density can also be constrained

$$\langle\hat{\mathcal{Q}}_{\ell m}\rangle_1 = O_1\,, \tag{5.23}$$

which can be useful when one is looking for the scissors mode for example.
It is worth noting that the code allows for all of these options to be set independently for different multipole constraints, including the options described in the previous section regarding the type of constraints. One can easily set a quadratic penalty constraint on $\langle\hat{\mathcal{Q}}_{20}\rangle_1$ with $C_O = 10^{-4}$ while also putting a predictor-corrector constraint on $\langle\hat{\mathcal{Q}}_{22}\rangle_0$. The only thing fixed for all of the multipole moments commonly (although still input parameters) are C_0, ϵ and d_0, since they are intrinsically linked to the two-step scheme.
When symmetries are broken, MOCCa selects itself which multipole constraints are redundant, following the conventions from Appendix C. These constraints are by default predictor-corrector constraints, but if the user so wishes he can override these settings for the redundant multipole moments by simply specifying input for them.

5.5.2 Constraints on the total multipole moments Q_ℓ

Constraints on the total multipole moments of order ℓ are also possible. The definition of the total multipole moment of degree ℓ $\mathcal{Q}_\ell$ is (see Appendix C)

$$Q_\ell = \sqrt{\frac{16\pi}{2\ell+1}\sum_{m=-\ell,..,\ell}|\langle\hat{\mathcal{Q}}_{\ell m}\rangle|^2}\,. \tag{5.24}$$

Constraints on this quantity merit their own little subsection since they differ in an important way from constraints on ordinary multipole moments: the $\hat{Q}_\ell$ are not expectation values of a one-body operator and thus do not fit directly in the procedures explained above.
For augmented Lagrangian constraints that target $Q_\ell = O$, MOCCa solves the problem by adding the following term to the energy

$$E_{\text{Con}} = C_\ell(Q_\ell - O)^2\,. \tag{5.25}$$

This gives rise to a different contribution to the single-particle Hamiltonian at iteration (i)

$$\hat{h}_C^{(i)} = 2C_\ell\sqrt{\frac{16\pi}{2\ell+1}}\left(1-\frac{O^{(i)}}{\mathcal{Q}_l}\right)\sum_{m=-\ell}^{\ell}\langle\hat{\mathcal{Q}}_{\ell m}^{(i)}\rangle\hat{\mathcal{Q}}_{\ell m} \tag{5.26}$$

Readjusting $O^{(i)}$ as a function of the iterations is still performed using Eq. (5.11).
For the moment, only augmented Lagrangian constraints are allowed on the total multipole moments Q_ℓ as we have not (yet) succeeded in finding an appropriate two-step scheme that is the analog of Eq. (5.20).

5.5.3 Cranking constraints

Constraints on the projections of the total angular momentum of the nucleus $\hat{\mathcal{J}}_\mu$ are very useful to probe the structure of rotational bands. Note that historically, the Lagrange multipliers of the cranking constraints are not denoted by λ_μ, but by frequencies ω_μ, making the following equation the analog of Eq. (5.4)

$$\hat{h}_C = -\omega_\mu\hat{\mathcal{J}}_\mu\,. \tag{5.27}$$

MOCCa can constrain any combination of all three components with either a linear, quadratic, augmented Lagrangian or predictor-corrector constraint. This, of course, under the condition of the symmetries of the many-body state allowing for non-zero values. Note that this is also the case for symmetries that are approximately conserved. The main example is cranking an oblate or prolate configuration around its symmetry axis: it is impossible to make quantum mechanical system rotate around a symmetry axis and the code will

in general[9] not converge when trying to do this[10].
In the current version, it is only possible to constrain the total angular momentum of the nucleus and not separately the neutron and proton contributions. This would be easy to implement, but has not been done yet since the need did not yet arise.
Note that using predictor-corrector cranking constraints is significantly more costly than their multipole counterparts, since $\hat{\mathcal{J}}$ involves derivatives and we thus need to derive the single-particle wavefunctions one more time per iteration compared to an unconstrained calculation. Nevertheless, they are still the constraining method of choice, especially when dealing with simultaneous constraints on multiple components of $\hat{\mathcal{J}}$ since one does not need to spend time looking for appropriate constraint parameters.

5.5.4 Other constraints

There are currently two other quantities that can be constrained when using `MOCCa`. The root-mean-square radius is physically speaking the most intuitive one. It is defined in `MOCCa` as

$$r_{\text{rms},t} = \sqrt{\frac{\int d\mathbf{r}\, \rho_t(\mathbf{r})\mathbf{r}^2}{\int d\mathbf{r}\, \rho_t(\mathbf{r})}}\,, \tag{5.28}$$

and similar for $r_{\text{rms},n}, r_{\text{rms},p}$ and $r_{\text{rms},1}$. The practical implementation of the constraint needs an extra trick, as there is no operator $\hat{\mathcal{O}}$ of which r_{rms} is the expectation value. For this reason we constrain in practice the mean-square radius, which is $\hat{r}^2_{\text{rms}}$. The output is translated into terminology reflecting the rms radius, but the contributions to the Routhian and single-particle Routhians are calculated in terms of the ms radius. Other than this internal trick, constraints on the rms radius behave exactly like constraints on the multipole moments and they can be given the same calculation options.
The operator $\hat{\mathcal{S}}_z$ was defined in chapter 2 and can be used to constrain the nuclear Schiff moment of a parity breaking configuration in `MOCCa`. It can be accessed by specifying the `SchiffMoment` input parameter in a `MOCCa` run. No calculations using this feature will be reported in this dissertation, but the main aim of the implementation is to serve as an example for future users wishing to constrain other operators that are at the moment not implemented.

5.6 Damping and cutoffs

The constraints discussed in this chapter all contribute to the mean-field Hamiltonian and are thus subject to the numerical difficulties described in chapter 4. The mean-field potential due to the constraints should thus be damped. The contribution to the single-particle Hamiltonian at iteration (i) thus becomes

$$\hat{h}_C^{(i)} = (1 - \texttt{Damping}) \sum_k \lambda_k^{(i)} \hat{O}_k + \texttt{Damping}\, \hat{h}_C^{(i-1)}\,, \tag{5.29}$$

where `Damping` is an input parameter of `MOCCa`, with a default value of 0.9. This mixing of the constraint potential has exactly the same aim as the density mixing discussed in chapter 4. That we introduce a new mixing parameter `Damping` instead of reusing `DampingParam` is a historical artifact.
The mean-field potentials discussed in chapter 1 are all more or less contained to the nuclear volume. They are clearly small where the single-particle wavefunctions are negligible. In practice this means that the mean-field potentials vanish at the edges of the Cartesian mesh, at least if the number of points (N_X, N_Y, N_Z) is sufficiently large. This is not the case for many of the operators $\hat{O}$ one wants to constrain. The multipole operators $\hat{Q}_{\ell m}$ scale as r^ℓ at the edge of the box and are thus decidedly non-zero. Non-zero values of the constraint potential close to the box edges are problematic. This modifies the boundary conditions of both the mean-field and pairing problem, leading to non-physical bubbles in the density in the most extreme cases. For this reason we modify Eq. (5.29) by adding a cutoff factor $\hat{f}^{(i)}$

$$\hat{h}_C^{(i)} = (1 - \texttt{Damping}) \sum_k \lambda_k^{(i)} \hat{f}^{(i)} \hat{O}_k + \texttt{Damping}\, \hat{h}_C^{(i-1)}\,. \tag{5.30}$$

[9] Although it is possible to create quasi-particle excitations using such procedure.
[10] And I've tried many times by accident during my PhD.

Using the keyword `CutoffType` the cutoff operator $\hat{f}$can be chosen to be either spherical (`CutoffType` $= 1$) or dependent on the nuclear density(`CutoffType` $= 0$). In the first case it is simply given by

$$\hat{f}(\mathbf{r}) = \begin{cases} \dfrac{\exp(-d)}{1+\exp(-d)} \text{ if } d > 0\,, \\ \dfrac{1}{1+\exp(d)} \text{ if } d < 0 \end{cases} \tag{5.31}$$

$$d = \frac{|\mathbf{r}| - \texttt{radd}}{\texttt{acut}}\,. \tag{5.32}$$

This cutoff function severely limits the contribution of constraints when $r >$ `radd` and does so with an exponential width of `acut`, both of which are input parameters of `MOCCa`. Since this cutoff is essentially spherical in nature, it is not very suited to very deformed nuclear configurations. A density-dependent cutoff was proposed in [104] and is implemented in `MOCCa` as

$$\hat{f}(\mathbf{r}) = \left(1 + \exp\left[\frac{\Delta R(\mathbf{r}) - \texttt{radd}}{\texttt{acut}}\right]\right)^{-1}\,. \tag{5.33}$$

The function $\Delta R(\mathbf{r})$ is the distance to the equidensity surface where $\rho_t(\mathbf{r}) = \rho_{\text{treshold}}$, where ρ_{treshold} is usually fixed to one tenth of the maximum value of the total density. On the mesh, $\Delta R(\mathbf{r})$ at mesh point $\mathbf{r}_i$ can then be calculated as

$$\Delta R(\mathbf{r}_i) = \begin{cases} \min\left\{|\mathbf{r}_i - \mathbf{r}_j| \text{ where } \rho_t(\mathbf{r}_j) \geq \rho_{\text{treshold}}\right\} \text{ when } \rho_t(\mathbf{r}_i) \leq \rho_{\text{treshold}} \\ -\min\left\{|\mathbf{r}_i - \mathbf{r}_j| \text{ where } \rho_t(\mathbf{r}_j) < \rho_{\text{treshold}}\right\} \text{ when } \rho_t(\mathbf{r}_i) > \rho_{\text{treshold}} \end{cases}\,. \tag{5.34}$$

This cutoff restricts the components of the multipole operators at the edges of the box, again exponentially with parameters `radd` and `acut`. The main difference is that the cutoff takes the nuclear density distribution approximately into account, and thus restricts the operators $\hat{O}$ less in space along elongated directions while restricting them more along shortened directions of the nuclear density.

Chapter 6

Solving the pairing problem

While chapter 4 has dealt with the numerical aspects of the Hartree-Fock part of a mean-field calculation, this chapter will detail how MOCCa approaches the pairing equations of either the HF, BCS or HFB ansatzes from chapter 3. Finding a solution to the pairing equations, while maintaining the stability of the iterative scheme, is not straightforward, in particular when dealing with symmetry broken HFB calculations.
Section 6.1 introduces the general framework of the pairing equations, while sections 6.2, 6.3 and 6.4 go more into detail on the cases for respectively Hartree-Fock, HF+BCS and HFB calculations. In general, the Hartree-Fock solution is not a desirable solution and section 6.5 details the options to evade solutions with vanishing pairing when doing HF+BCS or HFB calculations. The problem of selecting the correct HFB vacuum will be discussed in great length in section 6.6 at the hand of a toy model. The treatment of quasiparticle blocking is the subject of section 6.8. The final section, section 6.9 details how the eigenvalues of ρ can be used to characterize HFB configurations.

6.1 The pairing subproblem

We start by treating the common elements for the three ansatzes (HF, HF+BCS and HFB) and detail the common solving strategy employed in MOCCa. That such a common strategy exists is of course due to the fact that the Slater determinant is the zero-pairing limit of the BCS wavefunction, which is in turn a particular HFB wavefunction. The general solving scheme is iterative and decoupled from the mean-field iterations: the pairing problem is solved at every mean-field iteration, using the single-particle wavefunctions $|\phi_l\rangle$ in the Hartree-Fock basis at that particular mean-field iteration. There are three main steps that make up the pairing solver, summarised in Algorithm 5: calculation of the pairing gaps Δ, finding suitable Fermi energies so that the average number of protons and neutrons is correct and calculating the occupation factors v_l^2.
While the overall idea is straightforward and one could naively implement the formulas from chapter 3, there will be some nontrivial computational details to contend with. In particular the search for the Fermi energies merits some attention, as it is rife with pitfalls. Every step for every type of pairing treatment will be discussed separately for this reason.

```
1 for i ← 1 to PairingIter do
2 |   for q ← −1, 1 do
3 |   |   Compute gaps Δ_ij
4 |   |   Find correct λ_q and λ_{2,q}
5 |   |   Compute occupation numbers v_l^2
6 |   end
7 |   if Convergence then exit;
8 end
```

Algorithm 5: Schematic general algorithm for the pairing subproblem. `PairingIter` is an input parameter of MOCCa, with default value 50 in the case of BCS pairing and a default value of 1 in the case of HFB pairing.

6.2 Hartree-Fock

The Hartree-Fock ansatz treats all particles as independent and there is no complicated pairing problem: the pairing gaps are all strictly zero and one can simply set the occupation factors of the occupied levels to one, while setting the others to zero. As $\frac{\partial E}{\partial N}$ is discontinuous, any value for the Fermi energy λ is not unambiguous: MOCCa simply takes it as the single-particle energy of the highest-lying occupied state.

As discussed in chapter 1 however, there is an inherent choice to be made for any practical Hartree-Fock calculation: which single-particle wavefunctions to occupy. A completely traditional calculation will select at each mean-field iteration the single-particle operations with lowest single-particle energies. For unconstrained calculations that aim to reach the minimum of the energy surface this usually poses no problem, and calculations usually converge.
A way of identifying Hartree-Fock configurations is by counting the number of occupied single-particle wavefunctions with certain quantum numbers. When both z-signature and parity are conserved, `MOCCa` uses the notation from [105] for both isospins to indicate the current Hartree-Fock configuration

$$[N_{++}, N_{+-}, N_{+-}, N_{++}] \qquad [Z_{++}, Z_{+-}, Z_{+-}, Z_{++}] \ , \tag{6.1}$$

where $N_{\pm\pm}$ ($Z_{\pm\pm}$) is the number of occupied neutron (proton) states in the corresponding (parity,z-signature) block[1].[2] This notation is obviously dependent on the conservation of both parity and z-signature. When this is not the case, the notation simplifies to

$$[N_+, N_-] \qquad [Z_+, Z_-] \tag{6.2}$$

where $N_\pm$ ($Z_\pm$) is now the number of occupied neutron (proton) levels in either the corresponding parity or signature block.
This configuration labeling is far from unique, as counting the number of occupied single-particle wavefunctions does not tell us which orbitals are occupied. This touches on the primary practical problem when doing symmetry broken Hartree-Fock calculations: single-particle wavefunctions are very hard to label/identify without quantum numbers. A spherical Hartree-Fock calculation for example can label its single-particle wavefunctions with angular momentum quantum numbers (both J^2, J_z and L^2) and parity quantum number resulting in an (almost) unique identification of every configuration. For `MOCCa` this is not possible, as at the maximum only parity, z-signature and isospin can be used to label Hartree-Fock configurations, corresponding to Eq. (6.2). Theoretically the labeling problem is not severe: one can simply specify that the states with correct quantum numbers with the lowest energy are occupied. In calculations however, this is not always ideal as during the mean-field iterations single-particle energies might change ordering, making the mean-field states changes abruptly from one iteration to the next, which makes the calculation very difficult to converge. `MOCCa` offers the user three possibilities to perform Hartree-Fock calculations, depending on the input parameters `FreezeOccupation` and `HFConfig`:

1. At every mean-field iteration, occupy the lowest orbitals,
2. The occupations are taken from the input file and don't change during the mean-field iterations
3. The occupations are specified by the user at the start and don't change during the mean-field iterations

All three have advantages and disadvantages. When using option 1) the user forfeits all control over the particular configuration (and thus quantum numbers of the many-body state) but obtains the lowest state. This might present a problem for constrained calculations, as the configuration might change from one data point to the next. Convergence problems might show up due to crossings of the single-particle levels. Option 2) has the advantage of (almost) always converging, as no abrupt changes in the mean-field state are possible. When the user has access to a starting point that has the desired Hartree-Fock configuration, this is the option of choice. Option 3) offers the user more direct control on the Hartree-Fock configuration, at the price that the user knows ahead of time what configuration he is interested in. Note that for both options 2) and 3) that nothing guarantees that the converged solution has the lowest energy among all the possible configurations corresponding to the quantum numbers specified (6.2).

6.3 BCS

The BCS pairing problem is in a certain sense the most straightforward of the three ansatzes. The single-particle wavefunctions and their single-particle energies at every mean-field iteration present the inputs of the BCS pairing equations from chapter 3. We can obtain the solution in a straightforward way without too much technical complications by simple fixed-point iteration of these equations. This simplicity is of course completely due to the conservation of time-reversal symmetry that allows for the direct identification of the canonical partners.

[1] The $\pm$ does not indicate the signature quantum number, which is still $\pm i$.
[2] If time-reversal is conserved, this constrains the number of positive and negative signature states to be equal in every parity block.

6.3.1 Computing the gaps

At every pairing iteration (i) one can use the gap equation to calculate the gaps from the values at the previous iteration $(i-1)$.

$$\Delta_{j\bar{j}}^{(i)} = -\frac{1}{2}\sum_{k} \bar{v}_{j\bar{j}k\bar{k}} \frac{\Delta_{k\bar{k}}^{(i-1)}}{E_{qp,k}^{(i-1)}} , \tag{6.3}$$

where the sum is over all of the single-particle wavefunctions. The pairing interaction matrix elements that figure in this equation are not that computationally nor memory intensive to calculate as we do not need the full matrix $\bar{v}_{ijkl}$. For future expansion and for analogy with the HFB case, we do however split the calculation of these matrix elements somewhat. The pairing field $\Delta^{(i)}(\mathbf{r})$ is defined as

$$\Delta^{(i)}(\mathbf{r}) = -v(\mathbf{r}) \sum_{k\geq 0,\sigma} u_k^{(i-1)} v_k^{(i-1)} \left|\psi_k(\mathbf{r},\sigma)\right|^2 , \tag{6.4}$$

where the sum is now over only half of the single-particle states of isospin q. This quantity is useful, as it allows us to calculate the pairing gaps as

$$\Delta_{j\bar{j}}^{(i)} = \int d\mathbf{r}\, \Delta(\mathbf{r})^{(i)} \sum_{\sigma} \left|\psi_j(\mathbf{r},\sigma)\right|^2 . \tag{6.5}$$

6.3.2 Finding a Fermi energy

The values of the pairing gaps at hand, we can now look for a Fermi energies $\lambda_q^{(i)}$ so that the particle number is on average correct. For the BCS ansatz, one can simply sum the occupation numbers calculated with the new pairing gaps and demand that the result is the desired particle number, i.e.

$$N_q(\lambda^{(i)}) = \sum_{k\geq 0} \left[1 - \frac{\epsilon_k^{(i)} - \lambda_q^{(i)}}{E_k^{qp,(i-\frac{1}{2})}}\right] , \tag{6.6a}$$

$$E_k^{qp,(i-\frac{1}{2})} = \sqrt{\left(\epsilon_k^{(i)} - \lambda_q^{(i-1)}\right)^2 + \left(\Delta_{k\bar{k}}^{(i)}\right)^2} , \tag{6.6b}$$

where the sum is only over half of the single-particle wavefunctions. The notation $E_k^{qp,(i-\frac{1}{2})}$ is a shorthand for the BCS quasiparticle energy at iteration (i) but calculated with the Fermi energy from the previous iteration. This allows us to easily solve for the new Fermi energy

$$\lambda_q^{(i)} = \left[N_q - \sum_{k\geq 0}\left(1 - \frac{\epsilon_k^{(i)}}{E_k^{qp,(i-\frac{1}{2})}}\right)\right]\left[\sum_{k>0}\left(E_k^{qp,(i-\frac{1}{2})}\right)^{-1}\right]^{-1} . \tag{6.7}$$

With this we can then finally compute the individual occupation probabilities $v_k^{(i)}$.

$$v_k^{(i)} = \frac{1}{2}\left(1 - \frac{\left(\epsilon_k^{(i)} - \lambda^{(i)}\right)}{E_k^{qp,(i)}}\right) . \tag{6.8}$$

Note that, for given non-zero values of the pairing gaps and single-particle energies, $N_q(\lambda_q)$ is a continuous and derivable function for all values of λ_q. This guarantees that `MOCCa` will without problem find a suitable Fermi energy[3]. While this might seem trivial, this conclusion is not valid for HFB pairing as we will see in section 6.6.

6.3.3 Judging convergence

The calculation of the occupation factors $v_k^{2,(i)}$ is the end of iteration i and we can proceed to iteration $(i+1)$. The process completes when the Fermi energy $\lambda^{(i)}$ does not vary too much from iteration to iteration and

[3] At least for BCS ground states, which are the only ones that `MOCCa`is currently equipped to handle.

the occupation numbers and pairing gaps satisfy the self-consistent equations.
We judge the BCS iterations to be converged when

$$|\lambda_q^{(i)} - \lambda_q^{(i-1)}| < \texttt{PairingPrec} \tag{6.9}$$

for every isospin and `PairingPrec` is an input variable that defaults to 10^{-6}. The iteration scheme nearly always converges without problems, mostly because the degrees of freedom are rather limited (there are only `nwt` pairing gaps values and `nwt` occupation numbers to compute).

6.4 HFB

The HFB ansatz is the most general of the three ansatzes. The price to pay for this generality is the host of technical problems that need to be tackled. As we will see, the solution method we employ involves diagonalizing several (potentially large) matrices repeatedly and the iterative process can be time-consuming. In order to gain time, the iterative process from algorithm 5 is only executed for one iteration at every mean-field iteration.[4]

6.4.1 Structure of the HFB equations in `MOCCa`

Before we start however, it will be useful to discuss the structures of the HFB matrices, meaning that we will apply the general considerations of section 3.5 to the specific symmetry combinations that are implemented in `MOCCa`.

Y-time-simplex $\check{\mathcal{S}}_y^T$

`MOCCa` is currently not capable of doing HFB calculations without conserving the y-time-simplex $\check{\mathcal{S}}_y^T$ symmetry. Conserving this antilinear, hermitian symmetry implies that all of the relevant quantities $U, V, \rho_{\mathsf{HFB}}, \kappa, \Delta, \ldots$ are real instead of complex matrices. This is good news from a computational point of view, as this effectively halves all of the computational effort required. Time-simplex breaking was originally included in the HFB routines, but since no application was readily planned, we opted to remove it in favor of the CPU time gains of working with real numbers instead of complex ones. We will assume it is conserved for the rest of this chapter. A future implementation of time-simplex breaking will be straightforward, [5] as new routines that differ only from the time-simplex conserving routines can almost be copy-pasted into the code.

Parity $\hat{\mathcal{P}}$ and z-isospin symmetry $\hat{\mathcal{I}}_z$

The parity symmetry introduce a simple block structure into the HFB Hamiltonian when it is conserved

$$\hat{\mathcal{H}}_{\mathsf{HFB}} = \begin{pmatrix} h_{++} & 0 & \Delta_{++} & 0 \\ 0 & h_{--} & 0 & \Delta_{--} \\ \Delta_{++} & 0 & -h_{++} & 0 \\ 0 & \Delta_{--} & 0 & -h_{--} \end{pmatrix} . \tag{6.10}$$

The block structure introduced by a conserved isospin symmetry is of course completely analogous, and it suffices to replace $(+,-)$ in Eq. (6.10) by (n,p) to obtain it.
Diagonalising the HFB Hamiltonian is thus remarkably easier if parity and/or isospin symmetry are conserved. Each of them allows for the splitting of $\hat{\mathcal{H}}_{\mathsf{HFB}}$ into two smaller matrices to diagonalise, again effectively halving the numerical cost. These symmetries also affect the eigenvectors of the HFB Hamiltonian, which can be one of either

$$\begin{pmatrix} U_+ \\ 0 \\ V_+ \\ 0 \end{pmatrix} \text{ or } \begin{pmatrix} 0 \\ U_- \\ 0 \\ V_- \end{pmatrix} . \tag{6.11}$$

[4] Users that do want to iterate the pairing problem can simply increase the value of `PairingIter` in `MOCCa`'s input.
[5] Of course, the job of finding the correct places to insert complex conjugates will be rather tedious.

Z-signature $\hat{\mathcal{R}}_z$

The case of the z-signature $\hat{\mathcal{R}}_z$ is slightly more complicated. This linear, antihermitian symmetry induces the following block structure

$$\hat{\mathcal{H}}_{\mathsf{HFB}} = \begin{pmatrix} h_+ & 0 & 0 & \Delta \\ 0 & h_- & -\Delta^T & 0 \\ 0 & -\Delta^T & -h_+ & 0 \\ \Delta & 0 & 0 & -h_- \end{pmatrix} . \tag{6.12}$$

As a consequence, the diagonalisation of $\hat{\mathcal{H}}_{\mathsf{HFB}}$ can be split into two subproblems

$$\hat{\mathcal{H}}_{\mathsf{HFB},(1)} = \begin{pmatrix} h_+ & \Delta \\ \Delta & -h_- \end{pmatrix} \qquad \hat{\mathcal{H}}_{\mathsf{HFB},(2)} = \begin{pmatrix} h_- & -\Delta^T \\ -\Delta^T & -h_+ \end{pmatrix} . \tag{6.13}$$

The eigenvectors of the entire HFB matrix come in two types, depending if they belong to $\hat{\mathcal{H}}_{\mathsf{HFB},(1)}$ or $\hat{\mathcal{H}}_{\mathsf{HFB},(2)}$.

$$\begin{pmatrix} U_+ \\ 0 \\ 0 \\ V_- \end{pmatrix} \text{ or } \begin{pmatrix} 0 \\ U_- \\ V_+ \\ 0 \end{pmatrix} . \tag{6.14}$$

As noted already in chapter 3, the Bogoliubov transformation mixes creation operators of levels with positive signature with annihilation operators of negative signature and vice versa. We will denote the quasiparticles by the signature of the creation operators, we will refer to the first (second) type in Eq. 6.14 as positive (negative) signature quasiparticles. Conservation of signature symmetry thus also allows for gaining a factor of two in the computational effort: it is sufficient to diagonalize two matrices of dimension `nwt` instead of a single matrix of dimension `nwt`^{2}.

Time-reversal $\check{\mathcal{T}}$

Time-reversal conservation implies another totally different kind of structure of the HFB Hamiltonian. Assuming the single-particle wavefunctions to come in time-reversed pairs $(k, \bar{k})$ we have that

$$\hat{\mathcal{H}}_{\mathsf{HFB}} = \begin{pmatrix} h_1 & h_2 & \Delta_1 & -\Delta_2 \\ h_2 & h_1 & \Delta_2 & -\Delta_1 \\ -\Delta_1 & \Delta_2 & -h_1 & -h_2 \\ -\Delta_2 & \Delta_1 & -h_2 & -h_1 \end{pmatrix} . \tag{6.15}$$

Given an eigenvector $(U_{1,k}, U_{2,k}, V_{1,k}, V_{2,k})^T$ with eigenvalue E_k^{qp}, one can check that $(U_{2,k}, U_{1,k}, -V_{2,k}, -V_{1,k})^T$ is also an eigenvector of $\hat{\mathcal{H}}_{\mathsf{HFB}}$ with the same eigenvalue. This does not come as a surprise, as this is simply a manifestation of the fact that the quasiparticles come in time-reversed pairs $(\beta_k, \beta_{\bar{k}})$.
When z-signature is conserved, both symmetries conspire to further simplify the problem: the submatrices $\hat{\mathcal{H}}_{\mathsf{HFB},(1)}$ and $\hat{\mathcal{H}}_{\mathsf{HFB},(2)}$ from Eq. (6.13) are equal up to a sign and a permutation of rows and columns. It is thus sufficient to diagonalise just one of them and get half of the quasiparticles. The other half can then be obtained by time-reversal.
Leveraging the structure implied by time-reversal into a numerical advantage without conservation of z-signature symmetries is not straightforward: we would need a diagonalisation routine that is able to somehow exploit the Kramers degeneracy of $\hat{\mathcal{H}}_{\mathsf{HFB}}$ to reduce the amount of operations needed. Note that this is not trivial, since $\hat{\mathcal{H}}_{\mathsf{HFB}}$ is in general a full matrix and cannot easily be split into two sub-matrices as was the case when z-signature was conserved. The straightforward diagonalisation routine in `MOCCa` cannot take this into account and thus the full matrix $\hat{\mathcal{H}}_{\mathsf{HFB}}$ is diagonalised[6].

6.4.2 Calculating the gaps

The pairing gaps Δ_{kl} now form a complete matrix, but we can still define a pairing field $\Delta(\mathbf{r})$ at iteration (i)

$$\Delta^{(i)}(\mathbf{r}) = -v(\mathbf{r}) \sum_{kl} \kappa_{kl}^{(i-1)} \left[\sum_{\sigma} \sigma \psi_l^*(\mathbf{r}, -\sigma) \psi_k(\mathbf{r}, \sigma) \right] , \tag{6.16}$$

[6]Note that this is the only simplification not exploited: the symmetries of Δ are exploited for its computation for example.

and the pairing gaps can be calculated from that as

$$\Delta_{kl}^{(i)} = \int d\mathbf{r}\, \Delta^{(i)}(\mathbf{r},\tau) \sum_{\sigma} \left[\sigma \psi_k^*(\mathbf{r},-\sigma)\psi_l(\mathbf{r},\sigma)\right] . \tag{6.17}$$

Note that the anomalous density matrix κ has taken the role of the factors $u_k v_k$ from the BCS case.
The advantage of introducing the pairing field $\Delta(\mathbf{r})$ is more clear here than in the BCS case: calculating all of the $\bar{v}_{klmn}$ matrix elements is more costly than calculating the pairing field and afterwards the pairing matrix. However, this is still a quite a time-consuming calculation when dealing with heavy nuclei. Symmetries help in this case, as isospin, z-signature, time-simplex and parity allow MOCCato reduce the numerical cost by bringing the matrices to specific block structures, see 3.

6.4.3 Finding the Fermi energy

Given the pairing gaps and the single-particle energies ϵ_i from the mean-field iterations, we can build the HFB Hamiltonian in the Hartree-Fock basis

$$\hat{\mathcal{H}}_{q,HFB}(\lambda_q^{(i-1)}) = \begin{pmatrix} \epsilon - \lambda_q^{(i-1)} & \Delta \\ -\Delta & -\epsilon + \lambda_s^{(i-1)} \end{pmatrix} , \tag{6.18}$$

where the matrix Δ is as defined before, but the diagonal matrix $\epsilon - \lambda$ is an approximation to the single-particle Hamiltonian $\hat{h}$ that is given by [52]

$$\epsilon - \lambda^{(i-1)} = \begin{pmatrix} \epsilon_1 - \lambda^{(i-1)} & 0 & 0 & 0 \\ 0 & \epsilon_2 - \lambda^{(i-1)} & 0 & 0 \\ \vdots & \vdots & \ddots & 0 \\ 0 & 0 & 0 & \epsilon_{\mathtt{nwt}} - \lambda^{(i-1)} \end{pmatrix} . \tag{6.19}$$

The next step is diagonalizing the HFB Hamiltonian $\hat{\mathcal{H}}_{q,HFB}$ to obtain its eigenvectors and the corresponding quasiparticle energies. This diagonalization gives us double the number of eigenvectors we need. The choice we face is which of the possible HFB vacua we choose to construct, as already discussed in chapter 3. We will defer how to make this choice to section 6.6, but this step is crucial for the construction of a working algorithm.
Assuming for the moment we can reliably select the correct half of the quasiparticle spectrum we can then proceed to calculate the number of particles by simply tracing the density matrix

$$N_q(\lambda_q^{(i-1)}) = \mathsf{Tr}\rho_q = \sum_{k=1}^{\mathtt{nwt}} \sum_{j=1}^{\mathtt{nwt}} V_{kj}^* V_{jk} . \tag{6.20}$$

We have made the dependence on the Fermi energy explicit in this formula, since nothing guarantees us that $N_q(\lambda_q^{(i-1)})$ is close to the desired number of particles N_q. Now we are faced with the problem of finding a new Fermi energy $\lambda_q^{(i)}$ so that the number of particles is correct. Unfortunately $N_q(\lambda_q)$ is not a simple function that can be inverted as in the BCS case and neither can we assume a simple 'level-occupying scheme' as in the HF case. We need to turn to numerical schemes in order to solve this problem.

MOCCa offers two algorithms to find a proper Fermi energy: a straight-forward bisection algorithm and a more advanced Broyden scheme. Both are iterative schemes[7] that probe $N_q(\lambda)$ and slowly converge to the desired number of particles.

The bisection algorithm

The aim of the bisection algorithm is to quickly find a good Fermi energy λ so that

$$f(\lambda) = N(\lambda) - N = 0 . \tag{6.21}$$

Starting from an initial guess $\lambda^{(i-1)}$ MOCCa searches for a bracketing interval $[\lambda_<, \lambda_>]$ so that

$$f(\lambda_<) < 0 < f(\lambda_>) . \tag{6.22}$$

[7] Note that we arrive here at the third iterative level: we solve for a Fermi energy at every iteration of the pairing problem which we solve at every iteration of the gradient-descent algorithm.

When found, MOCCa takes as next guess $\lambda^{(i)}$

$$\lambda^{(i)} = \frac{\lambda_< + \lambda_>}{2} \,. \tag{6.23}$$

Depending on the sign of $f(\lambda^{(i)})$ we then select a new bracketing interval by either replacing $\lambda_<$ or $\lambda_>$

$$\lambda_< = \lambda^{(i)} \quad \text{if } f(\lambda^{(i)}) < 0 \tag{6.24}$$
$$\lambda_> = \lambda^{(i)} \quad \text{if } f(\lambda^{(i)}) > 0 \,. \tag{6.25}$$

This process is repeated until $|f(\lambda^{(i)})| <$PairingPrec.
The main advantage of the bisection method is that it is extremely reliable in finding a zero of $f(\lambda)$. Finding an initial bracketing interval is the only possible problem of the algorithm, but in nuclear applications several rough guesses can easily work. The disadvantage is that this algorithm is quite costly computationally, as every evaluation of $f(\lambda)$ involves diagonalizing the HFB Hamiltonian, a matrix that can be rather large for heavy nuclei when symmetries are broken. If the initial bracketing interval is large, the number of evaluations of $f(\lambda)$ can grow quickly.

The Broyden solver

The Broyden algorithm as presented here is a method to solve a problem of two variables λ and λ_2. The use of a second variable is not immediately clear at this point in the text, but will become clear in section 6.5. Consider this time an objective function $f(\lambda_q, \lambda_{2,q}) = N_q(\lambda_q, \lambda_{2,q})$ and a second objective function $g(\lambda_q, \lambda_{2q})$ that we leave unspecified for now. We are interested in finding the zeros of both objective functions f and g. From the value of the Fermi energies and $\lambda_{2,q}$ at iteration $(i-1)$, we construct new values at iteration (i) as [88]

$$\begin{pmatrix} \lambda^{(i)} \\ \lambda_2^{(i)} \end{pmatrix} - \begin{pmatrix} \lambda^{(i-1)} \\ \lambda_2^{(i-1)} \end{pmatrix} = \frac{1}{2} \left(G^{(i-1)} \right)^{-1} \begin{pmatrix} f(\lambda^{(i-1)}, \lambda_2^{(i-1)}) \\ g(\lambda^{(i-1)}, \lambda_2^{(i-1)}) \end{pmatrix} \,, \tag{6.26}$$

where G is an iteratively constructed approximation to the Jacobian of the problem, i.e.

$$G^{(i-1)} = \left. \begin{pmatrix} \frac{\partial f}{\partial \lambda} & \frac{\partial f}{\partial \lambda_2} \\ \frac{\partial g}{\partial \lambda} & \frac{\partial g}{\partial \lambda_2} \end{pmatrix} \right|_{\lambda_q = \lambda_q^{(i-1)}, \lambda_{2,q} = \lambda_{2,q}^{(i-1)}} \,. \tag{6.27}$$

After the update of (λ, λ_2), one then updates the approximate Jacobian to $G^{(i)}$ using the following formula

$$G^{(i)} = G^{(i-1)} + G^{(i-1)} \frac{\delta \boldsymbol{\lambda}}{\delta \boldsymbol{\lambda}^T \delta \boldsymbol{\lambda}} \tag{6.28}$$

where

$$\delta \boldsymbol{\lambda} = \begin{pmatrix} \lambda^{(i)} \\ \lambda_2^{(i)} \end{pmatrix} - \begin{pmatrix} \lambda^{(i-1)} \\ \lambda_2^{(i-1)} \end{pmatrix} \,. \tag{6.29}$$

In order for this scheme to work, one needs an initial guess for G. We approximate the partial derivatives in Eq. (6.27) with a simple second order finite difference formula between $(\lambda^{(1)}, \lambda_2^{(1)})$ and $(\lambda^{(1)} + 0.01, \lambda_2^{(1)} + 0.01)$. Note that in the case of a one-dimensional problem, finding a zero of $f(\lambda_q)$, this method simply reduces to a version of Newtons method, as the Jacobian G becomes a simple derivative [88].
The Broyden scheme works very well in almost all applications and in general needs only a few iterations and evaluations of $N(\lambda)$ to converge to a Fermi energy that fixes the average number of particles correctly, in contrast to the bisection method. However, this performance is completely dependent on the quality of the initial guess $\lambda^{(0)}$: if this guess is rather bad the number of necessary iterations will increase drastically. In practice however, MOCCa uses the Fermi energy at the previous mean-field iteration as a starting point and convergence is very quick. At the first mean-field iteration this is not possible, but MOCCa saves the Fermi energy to files and so this value (resulting from a BCS calculation or HFB calculation of a similar configuration) is usually sufficient.
When this algorithm fails however, it fails spectacularly. When at a certain iteration the vector $(\lambda^{(i)}, \lambda_2^{(i)})$ is a rather bad approximation to the zeros of both objective functions f and g, the update to $G^{(i)}$ will not improve the approximation to the true Jacobian. In a snowball effect the iterative process will diverge. Numerically, this process will end up producing a singular Jacobian, leading Eq. (6.26) to be ill-defined. This kind of

failure only happens when either one of the objective functions is discontinuous or otherwise irregular.[8]
The algorithm in `cr8` that solves the same problem is somewhat less efficient. Instead of updating the approximation of the Jacobian at every pairing iteration with Eq. (6.28) a new approximation is constructed at every Fermi-iteration using the finite-difference formula. This results in double the evaluations of $N_q(\lambda_q)$ and thus double the amount of diagonalisations of the HFB Hamiltonian at every iteration of the pairing problem except for the very first.

Summary

The above steps to find a proper Fermi energy that fixes the correct particle number on average are summarised in Algorithm 6. As usual this seems deceptively simple.

```
for i ← 1 to HFBIter do
    Select half of the eigenvectors of Ĥ(λ^(i)) to correctly identify the HFB vacuum
    Compute ⟨N̂⟩ = Trρ_HFB
    Get a new guess of λ^(i+1) using the bisection or Broyden formula
    if Convergence then exit;
end
```

Algorithm 6: Schematic algorithm to determine λ at every iteration in Algorithm 5 for the HFB problem.

6.5 Evading the Hartree-Fock solution

All of the numerical algorithms for both the BCS and HFB ansatz work quite well, but have a fundamental flaw. Due to the iterative nature of our solution, the Hartree-Fock limit is an attractor of the pairing problem. If at any mean-field iteration (i) the pairing gaps $\Delta^{(i)}$ become zero (or small), the iterative nature of the pairing solver guarantees that at the following iteration $\Delta^{(i)}$ will stay zero. Once the many-body wavefunction is sufficiently close to the Hartree-Fock solution, we can no longer sample possible solutions with non-zero pairing at the following mean-field iterations.
This situation can be understood easily when looking at pairing as a broken symmetry. When $\Delta^{(i)}$ is zero (or close to it) at a given mean-field iteration and the many-body symmetry has a small particle number dispersion, particle number symmetry is (approximately) conserved. Since the HFB Hamiltonian respects this symmetry, the iterative mean-field process will not break this symmetry, similar to the case for the other symmetries discussed in chapter 2.
This situation is however highly undesirable [52, 32]. If `MOCCa` insists on the Hartree-Fock solution when there is a paired solution that is lower in energy, one would like to force `MOCCa` to break the symmetry. Even when the non-paired solution has the lowest energy, one would like the many-body wavefunction to exhibit some pairing. The reason is that after projection on particle number, the paired states in general gain enough energy to overtake the non-paired solution and become the minimum after projection [106].
There is also a practical side to the discussion: a Hartree-Fock calculation is more tricky to converge in the sense that one needs to identify the exact configuration one is interested in, especially when doing systematic calculations of energy surfaces. Paired solutions vary much more smoothly in the solution space, since they can use the occupation numbers v_l^2 to change occupation of single-particle levels gradually. Guaranteed pairing is thus very useful to have a practical way of generating energy surfaces.

6.5.1 Resetting or fixing pairing gaps in BCS

In the BCS case it is Eq. (6.3) that is the culprit. If the pairing gaps $\Delta^{(i-1)}$ vanish, the factors $u_k v_k$ will be zero, ensuring the pairing-field to be equal to zero which in turn makes the pairing gaps at the next iteration vanish. Without extra intervention, `MOCCa` is unable to exit this cycle.
Two methods are used to combat this phenomenon. The first consists of simply re-initializing the pairing gaps to

$$\Delta_{k\bar{k}} = 1.0 \text{ MeV} \tag{6.30}$$

[8] An interesting historical observation is that I debugged and debugged this solver on and off over the course of about one year, thinking there was something wrong with my implementation. It kept on failing spectacularly when doing time-reversal broken calculations, but as it turned out, there was a more fundamental physical reason: $N(\lambda)$ was discontinous in many cases due to careless selection of HFB quasiparticles, see section 6.6.

for all single-particle levels when MOCCa detects that the pairing (almost) vanishes. This method has the property that it fixes very nicely the problem when there the minimum of the functional is a many-body state with pairing but the solver has gotten stuck on a zero-pairing solution. By simply breaking the symmetry in an arbitrary direction (setting Δ to non-zero values), MOCCa will be able to find the correct minimum. Another method implemented in MOCCa is simply keeping the pairing gaps constant. With the input parameter ConstantGap users can choose the gaps Δ to have constant values for all single-particle levels (per isospin), fixed by the input parameters protongap and neutrongap [72].
Both of these methods can make sure that the pairing solver does not get stuck with the Hartree-Fock solution, provided the actual minimum has non-vanishing pairing. Neither of these however can force the many-body state to have pairing if the minimum of he functional has zero pairing, in which case the BCS solver will (after some iterations) find the correct minimum again, without pairing.

6.5.2 Constraining the dispersion in HFB

Since the HFB ansatz makes the pairing gaps Δ into matrices instead of numbers, a simple resetting scheme or constant value scheme as proposed for BCS will not work. In order to break rotational symmetry, one constrains the quadrupole moment[9] and so in order to break global gauge symmetry, we add a constraint on an order parameter related to the symmetry, the dispersion $\Delta\mathcal{N}^2$.
This constraint is intimately tied to the pairing subproblem and thus does not fall into the framework from chapter 5. Instead, we modify the HFB Hamiltonian by adding some terms

$$\hat{\mathcal{H}}_{q,\text{HFB}}(\lambda_q) \to \hat{\mathcal{H}}_{q,\text{HFB}}(\lambda_q) - 2\lambda_{2,q} \begin{pmatrix} \left(\hat{\mathbb{1}} - 2\rho_q\right) & 0 \\ 0 & \left(\hat{\mathbb{1}} - 2\rho_q\right) \end{pmatrix} . \tag{6.31}$$

As the Fermi energy was a constraint on the average particle number N_q, this term can be derived as a constraint on the dispersion $\Delta\mathcal{N}^2$ with Lagrange multiplier $\lambda_{2,q}$. MOCCa offers the user this constraint using the input parameter ConstrainDispersion. Two further options are available, the first is keeping $\lambda_{2,q}$ fixed, corresponding to a linear constraint from chapter 5, with values fixed by input parameter LNFixN and LNFixP, for respectively the neutron and proton dispersion.
The other option is to fix the dispersion to a predetermined value fixed by input parameters DN2N (neutrons) and DN2P (protons). This is achieved by the introduction of the objective function $g(\lambda, \lambda_2)$ for the Fermi solvers of the previous section. We can now specify this function as

$$g(\lambda_q, \lambda_{2,q}) = \left(\Delta\mathcal{N}^2\right)(\lambda_q, \lambda_{2,q}) - \texttt{DN2N/P}\,, \tag{6.32}$$

where the notation $\left(\Delta\hat{\mathcal{N}}^2\right)(\lambda_q, \lambda_{2,q})$ highlights the dependency of the dispersion on the many-body state, which in turn depends on the values of λ_q and $\lambda_{2,q}$ through the HFB Hamiltonian.

6.5.3 Lipkin-Nogami for HFB

Constraining the dispersion of a HFB state can avoid that the pairing solver gets stuck at the zero-pairing solution, provided there exists a HFB state with non-vanishing pairing that is lower in energy. This is however not always the case, and as argued above it can be preferable to construct HFB states that have guaranteed non-zero pairing.
The Lipkin-Nogami method is a tried-and-true method of guaranteeing a non-zero pairing solution. In practice, one modifies the HFB Hamiltonian in the same way as in Eq. (6.31), introducing the parameter λ_2. This parameter however is not held fixed or modified to satisfy a constraint, instead we calculate it from the mean-field state using the following expression [52]

$$\lambda_{2,q}^{LN} = \frac{\left\langle \hat{\mathcal{H}}\left(\Delta\hat{\mathcal{N}}_q^2 - \langle\Delta\hat{\mathcal{N}}^2\rangle\right)\right\rangle - \langle\hat{\mathcal{H}}\Delta\hat{\mathcal{N}}_q\rangle\langle\Delta\hat{\mathcal{N}}_q^3\rangle\langle\Delta\hat{\mathcal{N}}_q^2\rangle^{-1}}{\langle\Delta\hat{\mathcal{N}}_q^4\rangle - \langle\Delta\hat{\mathcal{N}}_q^2\rangle^2 - \langle\Delta\hat{\mathcal{N}}_q^3\rangle^2\langle\Delta\hat{\mathcal{N}}_q^2\rangle^{-1}} . \tag{6.33}$$

[9] Or any multipole moment with $\ell \neq 0$ in fact.

The following equations help to calculate this horrendous expression in practice

$$\gamma = 1 - 2\rho\,, \tag{6.34a}$$
$$\chi = \rho(1-\rho)\,, \tag{6.34b}$$
$$\langle \Delta\hat{\mathcal{N}}_q^2 \rangle = 2\,\mathrm{Tr}\,\chi\,, \tag{6.34c}$$
$$\langle \Delta\hat{\mathcal{N}}_q^3 \rangle = 4\,\mathrm{Tr}\,\gamma\chi\,, \tag{6.34d}$$
$$\langle \Delta\hat{\mathcal{N}}_q^4 \rangle = 3\langle \Delta\hat{\mathcal{N}}_q^2 \rangle + 8\,\mathrm{Tr}\left[\chi(1-6\chi)\right]\,, \tag{6.34e}$$
$$\langle \hat{\mathcal{H}}\Delta\hat{\mathcal{N}}_q^2 \rangle = 2\,\mathrm{Tr}\,h\chi - \mathrm{Re}\,\mathrm{Tr}\left[\Delta\kappa^*\gamma\right]\,, \tag{6.34f}$$
$$\begin{aligned}\left\langle \hat{\mathcal{H}}\left(\Delta\hat{\mathcal{N}}_q^2 - \langle\Delta N^2\rangle\right)\right\rangle &= 4\,\mathrm{Tr}\left[\left(\hat{h}\gamma + \sum_{kl}\bar{v}_{ijkl}\chi_{lk}\right)\chi\right] - \frac{1}{2}\,\mathrm{Tr}\left[\sum_{kl}\bar{v}_{ijkl}\left(\gamma\kappa\right)_{kl}\right] \\ &\quad - \mathrm{Tr}\left[\Delta\kappa^*\left(1-8\chi\right)\right]\,.\end{aligned} \tag{6.34g}$$

The addition of this constraint modifies the pairing energy term

$$E_{\mathsf{Pair}} \to E_{\mathsf{Pair}} - \lambda_2 \Delta\mathcal{N}^2\,. \tag{6.35}$$

Historically, the aim of this addition to the HFB Hamiltonian was to approximate the energy of the many-body state after projection on particle number [107]. Following this idea the $\lambda_{2,q}$ variable becomes an expansion parameter of a Kamlah expansion. The contribution to the energy of the system should thus be taken literally as an energy and added to the functional, in contrast to ordinary constraints on the dispersion that contribute to the Routhian, but not to the functional .

One can seriously doubt the validity of the Lipkin-Nogami method as a way to approximate projection on particle number [32], especially in the form of Eq. (6.33) which contains many hidden assumptions compared to the exact treatment [108]. In addition, this kind of modification of the many-body Hamiltonian makes it state-dependent. It is unclear what the optimization of such an object over our variational space entails exactly, and can in practice lead to pathologies [109].

For these reasons, we employ the Lipkin-Nogami method to ensure that pairing does not vanish as well and add its contribution to the energy, but does not correct other one-body operators in the spirit of [110]. Further interpretation as an approximation of particle number will not be attempted in the remainder of this document, and in general should be made with care.

A final note on the numerical implementation: the addition of the $\lambda_{2,q}^{LN}$ parameter is added in a rather peculiar way to `cr8` and `MOCCa`. At every pairing iteration (i), λ_2^{LN} is calculated from Eq. (6.33). The objective function for the Fermi solver g is then

$$g(\lambda_q, \lambda_{2,q}) = \lambda_{2,q} - \lambda_{2,q}^{LN}\,. \tag{6.36}$$

In the code, the λ_2 parameter is thus slowly varied and matched to the calculated λ_2^{LN}. The reason for this peculiarity seems to be, as always, letting the mean-field process occur in a controlled way and direct calculation of λ_2 as λ_2^{LN} might lead to large changes in configurations from one iteration to the next.

6.5.4 Some remarks on the implementation of the $\lambda_{2,q}$ contribution

The contribution to the HFB Hamiltonian in Eq. (6.38) should be handled with care. First of all, the actual calculation of it as presented is impossible to implement, since ρ is constructed from the diagonalisation of $\hat{\mathcal{H}}_{\mathsf{HFB}}$. For this reason, the term is added using the density at the previous mean-field iteration and the more practical version of Eq. (6.31) reads

$$\hat{\mathcal{H}}^{(i)}(\lambda) - 2\lambda_2^{(i)}\begin{pmatrix}\left(\hat{\mathbb{1}} - 2\rho^{(i-1)}\right) & 0 \\ 0 & \left(\hat{\mathbb{1}} - 2\rho^{(i-1)}\right)\end{pmatrix}\,, \tag{6.37}$$

where the subscripts (i) for once in this chapter do not denote pairing iterations, but mean-field iterations. Note that the value of $\lambda_2^{(i)}$ is adjusted within the pairing iterations using the value of $\rho^{(i)}$.

A second remark is related to structure of the extra term. The HFB equations are in fact invariant under a set of transformations, as shown in Appendix G. We can use this freedom to alter the λ_2 contribution to the HFB Hamiltonian, with a free parameter α,

$$\hat{\mathcal{H}}_{\mathsf{HFB}}(\lambda) + 2\lambda_2\left[(1-\alpha)\begin{pmatrix}-\left(\hat{\mathbb{1}} - \rho\right) & 0 \\ 0 & -\left(\hat{\mathbb{1}} - \rho\right)\end{pmatrix} - \alpha\begin{pmatrix}0 & 4\kappa \\ -4\kappa & 0\end{pmatrix}\right]\,. \tag{6.38}$$

Ignoring the constant matrix $\begin{pmatrix} \hat{\mathbb{1}} & 0 \\ 0 & -\hat{\mathbb{1}} \end{pmatrix}$, this modification can be found by simply adding a multiple of the generalized density matrix $-\alpha\lambda_2\hat{\mathcal{R}}$ to the expression. This modification does not change the eigenvectors of the HFB Hamiltonian, and correspondingly it has no effect on the eventual many-body solution[10]. However, numerically, the value of α can be used to improve convergence. This fact has been known for a long time [52, 110] and has been argued to be due to the size of some off-diagonal elements of ρ. By (partially) removing them by using positive values of α one could possibly improve the conditioning of the numerical problem. It is however, also very much related to the possible crossings of quasiparticle energies and their conjugate partners, as higher values of α increase the absolute value of the quasiparticle energies.

6.6 Choosing the correct HFB vacuum

Algorithm 6 is not usable in practice without a good way to select the HFB vacuum from all of the possibilities. As was already discussed in chapter 3 this choice is related to the freedom in the Bogoliubov transformation. We repeat it here

$$\begin{pmatrix} \hat{\beta} \\ \hat{\beta}^\dagger \end{pmatrix} = \begin{pmatrix} U^\dagger & V^\dagger \\ V^T & U^T \end{pmatrix} \begin{pmatrix} \hat{a} \\ \hat{a}^\dagger \end{pmatrix} . \tag{6.39}$$

For a given linear superposition of single-particle creation and annihilation operators we are in principle free to assign to it either a quasiparticle creation operator $\hat{\beta}^\dagger$ or an annihilation operator $\hat{\beta}$. For every index k, we can thus assign the operators as

$$\begin{aligned} \beta_k^\dagger &= \sum_{i=1} U_{ij}\hat{a}_i^\dagger + V_{ij}\hat{a}_i \,, \\ \beta_k &= \sum_{i=1} V_{ij}^*\hat{a}_i^\dagger + U_{ij}^*\hat{a}_i \,, \end{aligned} \tag{6.40}$$

or the other way round

$$\begin{aligned} \beta_k &= \sum_{i=1} U_{ij}\hat{a}_i^\dagger + V_{ij}\hat{a}_i \,, \\ \beta_k^\dagger &= \sum_{i=1} U_{ij}\hat{a}_i^\dagger + V_{ij}\hat{a}_i \,. \end{aligned} \tag{6.41}$$

Notice that this is reminiscent of the treatment of odd nuclei with HFB pairing. By going from Eq. (6.40) to Eq. (6.41) we have exchanged $(\hat{\beta}_k, \hat{\beta}_k^\dagger)$ with $(\hat{\beta}_k^\dagger, \hat{\beta}_k)$ (or equivalently $(U_k, V_k)^T$ with $(V_k^*, U_k^*)^T$), thereby creating a quasiparticle excitation on top of the original vacuum determined by Eq. (6.39).
This freedom of choice for the HFB vacuum is analogous to the choice of the Hartree-Fock vacuum. For every single-particle level one can either occupy it or leave it unoccupied, resulting in a possible set of $2^{\mathtt{nwt}}$ Slater determinants, or Hartree-Fock vacua in a rather suggestive wording. While this choice in the Hartree-Fock case is rather intuitive and well-known, the HFB problem faces rather the same problem in a more obscure way, formulated in terms of quasiparticles instead of particles.
We will use this analogy with the Hartree-Fock case in the next subsection to hazard a first guess at a practical rule to make the choice between Eq. (6.40) and Eq. (6.41) for all quasiparticle indices k.
For future reference, we say that a quasiparticle eigenvector from a pair of eigenvectors of $\hat{\mathcal{H}}_{HFB}$ with conjugate eigenvalues $(E_k, -E_k)$ is 'picked' when we use it to define the $(U_k, V_k)^T$ eigenvector that will be used to construct the density and anomalous density matrix. From a numerical point of view, we thus only have to represent the 'selected' or 'picked' half of the eigenvectors of $\hat{\mathcal{H}}_{\mathtt{HFB}}$ that determine the (U, V) matrices. The conjugate quasiparticle, that was not 'picked' is then simply given by $(V_k^*, U_k^*)^T$.

6.6.1 A first try: the lessons of the zero pairing limit

When the pairing gaps vanish, we would like the HFB vacuum to revert to a Slater determinant, the Hartree-Fock solution. This solution is characterized by single-particle levels with single-particle energies ϵ_k that can either be occupied or empty. One can see that in this case the eigenvectors of the HFB Hamiltonian come in the following pairs

$$\hat{\mathcal{H}}_{\mathsf{HFB}} \begin{pmatrix} \delta_k \\ 0 \end{pmatrix} = (\epsilon_k - \lambda_q) \begin{pmatrix} \delta_k \\ 0 \end{pmatrix} , \qquad \hat{\mathcal{H}}_{\mathsf{HFB}} \begin{pmatrix} 0 \\ \delta_k \end{pmatrix} = -(\epsilon_k - \lambda_q) \begin{pmatrix} 0 \\ \delta_k \end{pmatrix} , \tag{6.42}$$

[10] The only change is the quasiparticle spectrum, see Appendix G.

where $(\delta_k)_j = \delta_{jk}$ and ϵ_k are the single-particle energies. We let the Fermi energy λ_q unspecified for the moment. One is then free to choose which of the both eigenvectors to select for $\beta_k^\dagger$. Choosing the left option in Eq. (6.42) gives rise to

$$\hat{\beta}_k^\dagger = \hat{a}_k^\dagger\,, \qquad \hat{\beta}_k = \hat{a}_k\,, \tag{6.43}$$

while the right-most option corresponds to

$$\hat{\beta}_k^\dagger = \hat{a}_k\,, \qquad \hat{\beta}_k = \hat{a}_k^\dagger\,. \tag{6.44}$$

Suppose now that the level k is occupied in the Hartree-Fock solution: $\hat{a}_k^\dagger$ annihilates the Hartree-Fock state. For the HFB vacuum to match the Hartree-Fock state, Eq. (6.44) is the correct association between quasi-particle and particle operators. For an empty single-particle level, Eq. (6.43) is the correct one, as the Hartree-Fock state is instead annihilated by $\hat{a}_k$.
Supposing we make the correct choice for every level k, matching the HFB vacuum to the Hartree-Fock state. The density matrix ρ has only diagonal elements equal to one or zero

$$\rho_{kk} = \begin{cases} 1 & \text{if k is occupied}\,, \\ 0 & \text{if k is empty}\,. \end{cases} \tag{6.45}$$

The number of particles $\langle\hat{\mathcal{N}}\rangle = \mathrm{Tr}\rho_{\mathsf{HFB}}$ is then automatically fixed correctly.
In practice of course, we do not have the reference Hartree-Fock state and it is not clear whether we should use Eq. (6.43) or Eq. (6.44) for a specific level k. The Fermi energy can come to our aid however. The natural expectation for Hartree-Fock states is that the levels beneath the Fermi level should be occupied and the ones above empty. We can use this rule in the HFB case too: we choose Eq. (6.44) for all $\epsilon_k \leq \lambda$ and Eq. (6.43) for all $\epsilon_k > \lambda$. By then fixing the Fermi energy to be slightly larger than the N_q-th level (and smaller than the N_q+1-th level) we get a HFB vacuum with N_q particles that corresponds to the Hartree-Fock state with the lowest N_q single-particle levels occupied.
The most commonly used 'rule of thumb' to pick quasiparticles is inspired by the zero-pairing limit [11, 68] and is remarkably straightforward. One picks the eigenvectors of the HFB Hamiltonian with positive eigenvalues (corresponding to $\epsilon_k - \lambda < 0$ in the zero-pairing limit) to signify $(U_k, V_k)^T$. The negative eigenvalues (corresponding to $\epsilon_k - \lambda > 0$ in the zero-pairing limit) are then taken to be $(V_k^*, U_k^*)^T$, meaning that they do not get 'picked'. This fixes the freedom of choice for every single-particle level k and uniquely determines the annihilation and creation operators $(\hat{\beta}_k, \hat{\beta}_k^\dagger)$.

6.6.2 A toy model

In further sections, we will demonstrate how the naive selection of quasiparticles with positive quasiparticle energies can fail in different cases. In order to keep the discussion clear, we will make use of a simple four-level toy model, inspired by B. Avez [81]. It is characterized by the following HFB Hamiltonian

$$\hat{\mathcal{H}}_{\mathsf{HFB}}^{\mathsf{Toy}} = \begin{pmatrix} h-\omega & 0 & \Delta_{sig} & \Delta \\ 0 & h+\omega & -\Delta & \Delta_{sig} \\ -\Delta_{sig} & \Delta & -h+\omega & 0 \\ -\Delta & -\Delta_{sig} & 0 & -h-\omega \end{pmatrix}, \tag{6.46}$$

where the real-valued (2x2) matrices h, Δ_{sig} and Δ are given by

$$\begin{aligned} h &= \begin{pmatrix} -8 & 0 \\ 0 & -7 \end{pmatrix}, \\ \Delta &= \begin{pmatrix} 2\alpha & \alpha \\ \alpha & 2\alpha \end{pmatrix}, \\ \Delta_{sig} &= \begin{pmatrix} 0 & \gamma \\ -\gamma & 0 \end{pmatrix}. \end{aligned} \tag{6.47}$$

The model describes a system with four single-particle levels in the Hartree-Fock basis, which are two-by-two degenerate with energies of -8 and -7 MeV. These levels are also characterized by quantum numbers $\eta = \pm i$ that are generated by the z-signature operator $\hat{R}_z$. The precise symmetry is not important however

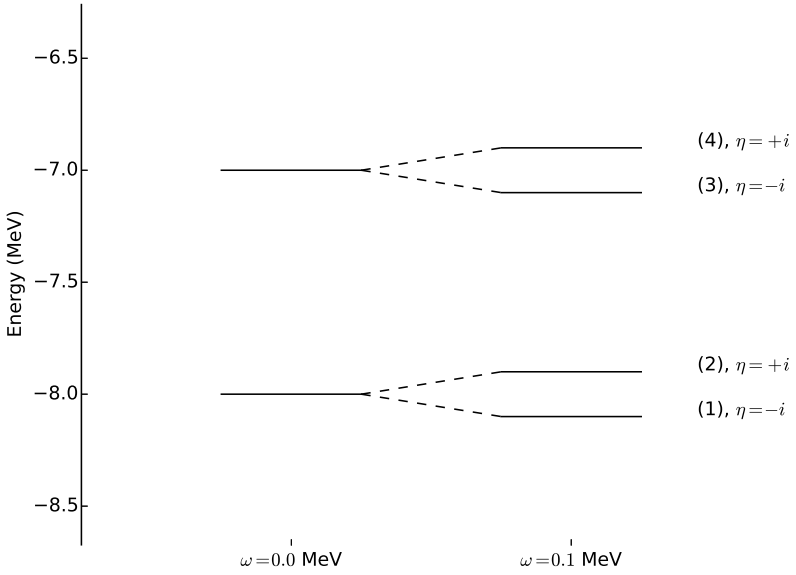

Figure 6.1: Level scheme and numbering of the single-particle levels in the toy model of Eq. (6.46). η is the z-signature quantum number and levels (1,2) and (3,4) form time-reversal normal pairs when $\omega = 0$.

and everything that follows remains valid for different linear, antihermitian symmetry operators.
We consider the degenerated pairs of levels to be time-reversed partners. Again, this is the most practical case for discussion centered on the application in MOCCa, but any antilinear, antihermitian conserved symmetry operator would do.
The parameter ω then determines the amount of time-reversal breaking in the system by simulating a cranking frequency, effectively lifting the Kramers degeneracy. The four-level system and numbering of the four states (1,2,3,4) is illustrated in Fig. 6.1. The parameter α determines the strength of the pairing between levels of different values of η, and due to the factor two on the diagonal of κ the pairing between time-reversed pairs always dominates. In what follows we will always choose $\alpha = 0.1$, as the strength of the pairing interaction will not play a significant role[11]. The matrix Δ_{sig} finally simulates pairing between levels with equal η. If γ is non-zero, z-signature is thus not conserved.
The interest of the toy model is that we can investigate the behaviour of the system as a function of the Fermi energy λ in controlled conditions, where an investigation of a typical system in MOCCa with rather large numbers of single-particle levels would be difficult to understand. More precisely, we can study this system to evaluate different methods of selecting quasiparticles after diagonalization of the HFB Hamiltonian.
The simplest case is the time-reversal conserving, signature conserving problem with $\omega = 0$, and $\gamma = 0$. Note that we are interested in even HFB vacua, since time-reversal is conserved, meaning that the selected HFB vacua should always have positive number parity. This case is demonstrated in Fig. 6.2 where we see $N(\lambda)$, the number parity and the quasiparticle spectrum as a function of the Fermi energy. Notice that the number parity is always positive, and $N(\lambda)$ is a smooth function. Note that the energies of the picked quasiparticles never actually reach zero, and their minimum value is about 0.19 MeV. This miminum value is reached at $\lambda = -8$ MeV and $\lambda = -7$ MeV where the Fermi energy matches the single-particle energies in the Hartree-Fock basis. Selecting the quasiparticles with positive quasiparticle energies is thus a sound (and easy to implement) strategy in the case of time-reversal conservation.

6.6.3 Breaking time-reversal: quasiparticle crossings

Selecting the quasiparticles with positive quasiparticle energy is not reliable when time-reversal symmetry is broken. To see why, consider Fig. 6.3, where the behaviour of the toy model for $\omega = 0.1$ and $\omega = 0.4$ MeV is plotted. In a realistic calculation with MOCCa, this would correspond to a cranked calculation of an even system, meaning that we would be interested in HFB vacua with even number parity.

[11] Provided it is non-zero of course.

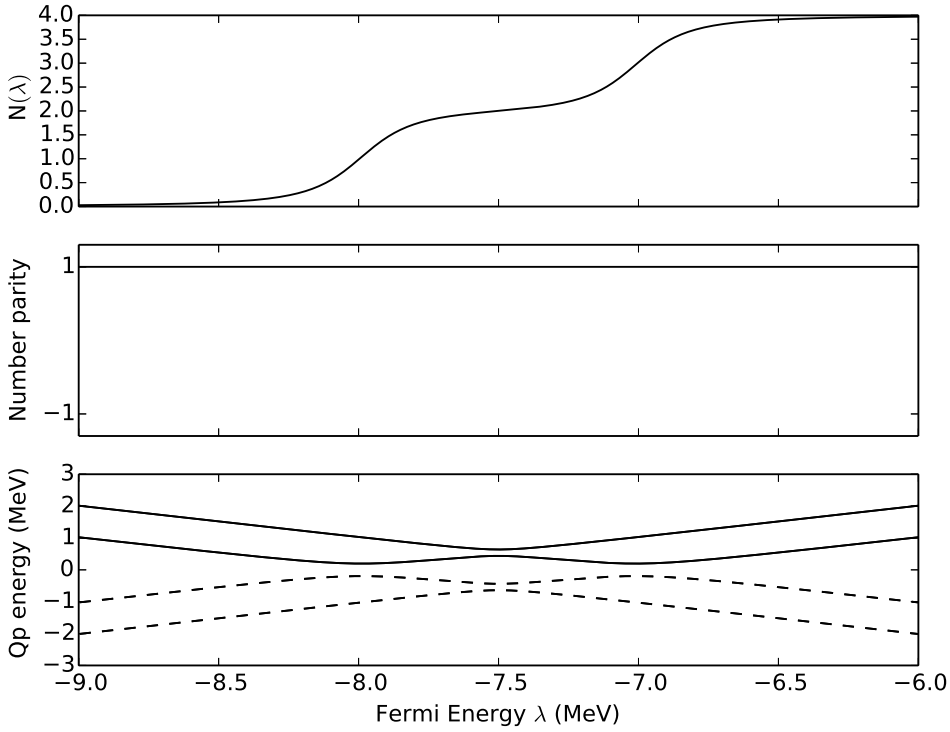

Figure 6.2: Number of particles, number parity and quasiparticle energies as a function of Fermi energy λ for the toy model from Eq. (6.46) for $\omega = \gamma = 0$ and $\alpha = 0.1$, selecting quasiparticles with positive quasiparticle energies. The toy Hamiltonian conserves time-reversal and z-signature in this case. 'Selected' quasiparticles are drawn in solid lines, their conjugates in dashed lines. The quasiparticle spectrum is two-fold degenerate, but this can not be seen on the figure.

For $\omega = 0.1$, there is no problem. The Kramers degeneracy gets lifted as the single-particle levels are slightly shifted by $\pm\omega$. Note that half of the quasiparticle energies move towards their conjugate partner by 2ω, while the other half move away from their conjugate partner by the same amount. For this small value of ω, this shift cannot overcome the distance between conjugate partners observed in the time-reversal invariant case. This means that no selected quasiparticle crosses with a non-selected quasiparticle. For this case selecting on the positive quasiparticle energies is still a valid strategy, as we obtain the correct particle number parity for all values of λ and $N(\lambda)$ is a smooth function.
The strategy fails however for $\omega = 0.4$ MeV. The shift of quasiparticle energies is enough to overcome the minimum distance between conjugate quasiparticles in the time-reversal invariant case. At $\lambda = -8.4$ MeV a quasiparticle energy goes to zero and thus becomes degenerate with its conjugate, non-selected partner. At higher values of λ quasiparticles have changed places. This change signals a transition to a completely different HFB vacuum with a different number parity: the new selection of quasiparticles is in effect a one-quasiparticle excitation with respect to the previous vacuum. At this point $N(\lambda)$ is discontinuous as the number of particles jumps up, as the density matrix ρ suddenly gets an extra eigenvalue equal to 1 due to the blocking of the quasiparticle that made the crossing. At $\lambda = -7.6$ MeV, another quasiparticle energy goes to zero and the HFB model creates an extra quasiparticle excitation to get to the vacuum. This gives rise to another discontinuity in $N(\lambda)$ and changes the number parity of the state again, reverting back to the correct value. This situation repeats itself around $\lambda = -7.0$ when λ crosses the two remaining single-particle energies and the quasiparticle energies of two selected quasiparticles go to zero.
Why does this problem not arise when time-reversal is conserved? This is equivalent to asking why the selected quasiparticle levels in Fig. 6.2 never approach zero. The answer from many-body physics is that only states with even number parity can arise when time-reversal is conserved, and thus no one-quasiparticle excitations are allowed and no transitions of single quasiparticles can occur. Mathematically, this is encoded in the Kramers degeneracy. The two lowest quasiparticle energies do tend to zero, but at the same location of the Fermi energy λ. However, each of these two selected quasiparticles is free to mix with the non-selected

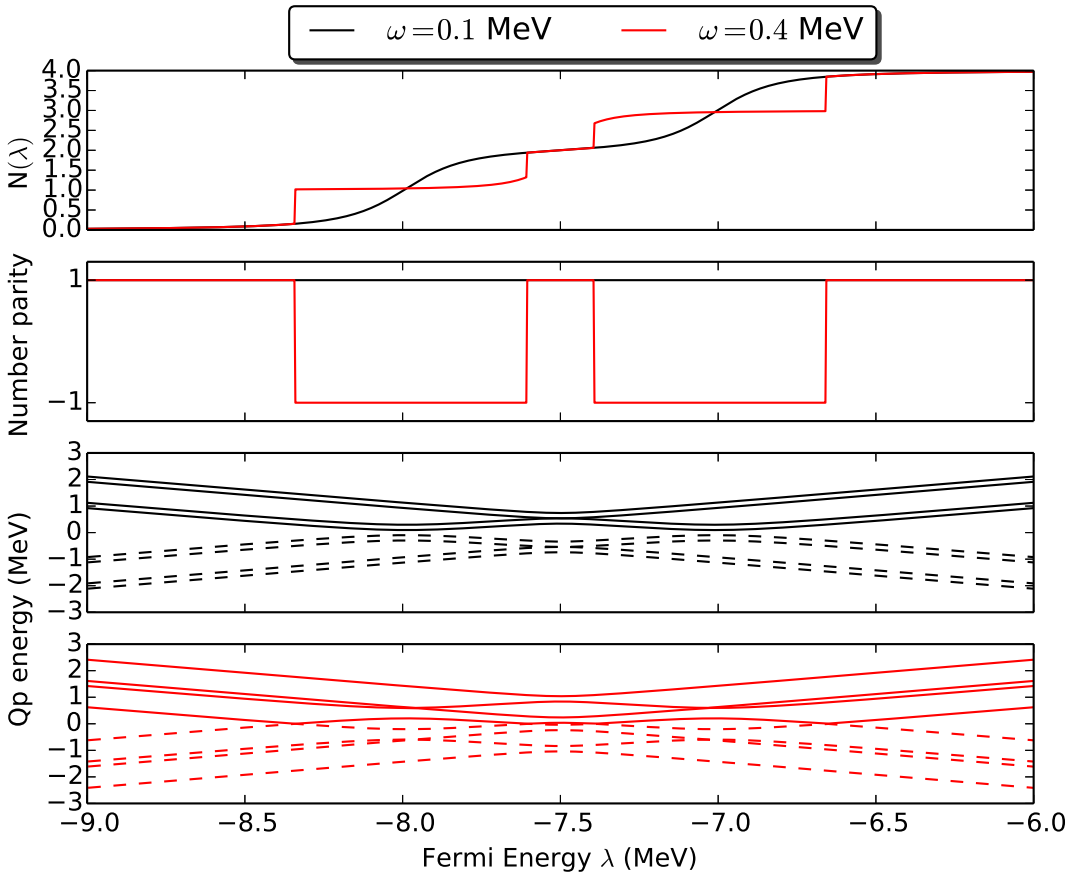

Figure 6.3: Average number of particles, number parity and quasiparticle spectra as a function of Fermi energy λ for the toy model from Eq. (6.46) for $\gamma = 0$, $\alpha = 0.1$ for varying ω, when selecting quasiparticles with positive quasiparticle energy. The toy Hamiltonian conserves z-signature, but breaks time-reversal in this case. 'Selected' quasiparticles are drawn in solid lines, their conjugates in dashed lines. Note that for $\omega = 0.1$ MeV no quasiparticle energies cross zero, while this does happen for $\omega = 0.4$ MeV.

partner of the other selected quasiparticle due to the structure of the Δ matrix that encodes the pairing. Since these eigenvectors of the HFB Hamiltonian can mix pairwise, what is known in quantum mechanics as an avoided crossing occurs and in the end no quasiparticle energies reach zero. In the time-reversal broken case, the selected eigenvector cannot mix with its non-selected partner and thus a crossing cannot be avoided.

6.6.4 A new selection rule: using signature blocks

In order to find a selection rule that does not fail when time-reversal is broken we restrict ourselves first to the case when z-signature is conserved. As seen before, the eigenvectors $(U_k, V_k)^T$ can be separated in two categories, see Eq. (6.13),

$$\begin{pmatrix} U_k \\ 0 \\ 0 \\ V_k \end{pmatrix} \text{ or } \begin{pmatrix} 0 \\ U_k \\ V_k \\ 0 \end{pmatrix}, \tag{6.48}$$

where the left-hand side option corresponds to a positive signature quasiparticles and the righthand side to a negative signature quasiparticle.

In the time-reversal invariant case, one would like to select all of the quasiparticle states (there are `nwt` total of them) with positive quasiparticle energies, ignoring categories. Due to the Kramers degeneracy, this would result in taking half of the quasiparticles in every category. This suggests that taking half of the quasiparticles in every category with the highest quasiparticle energy is a valid strategy.

When time-reversal is broken, this new strategy stays robust. The problem of quasiparticle energies crossing zero is completely avoided: a quasiparticle will not change its signature and the quasiparticle will stay 'picked'

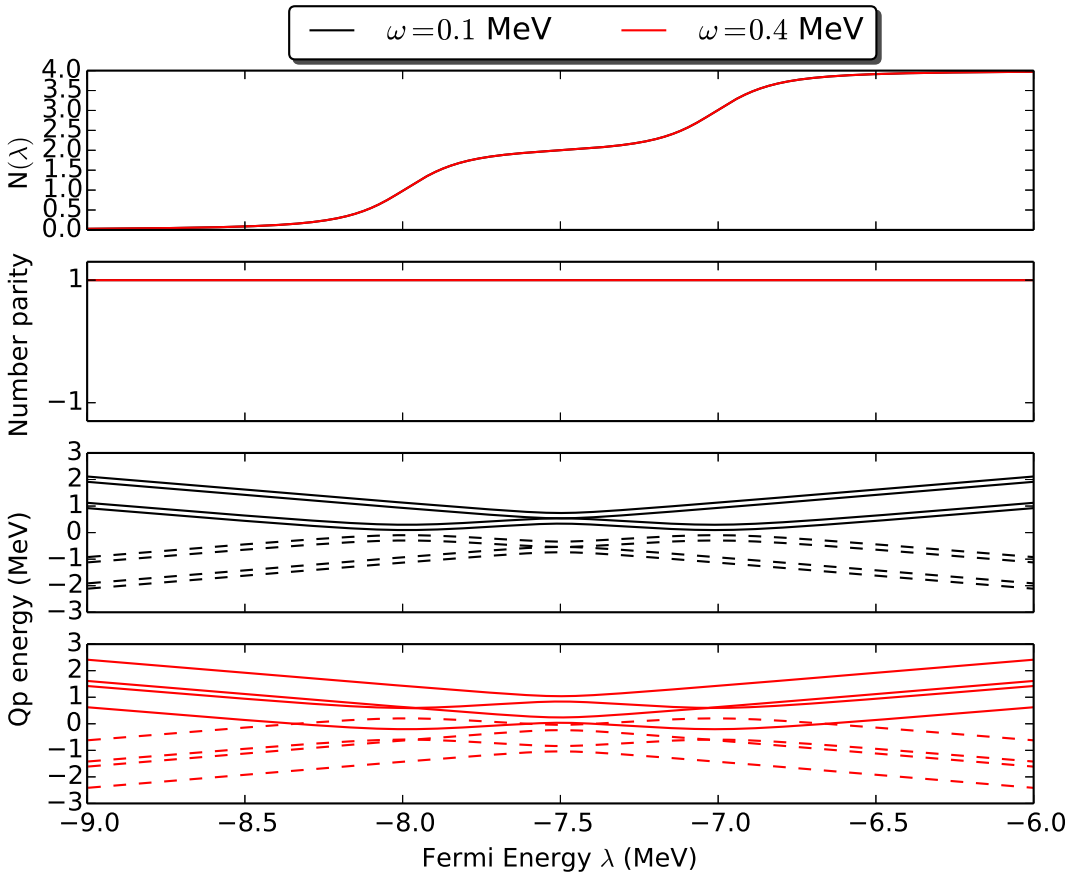

Figure 6.4: Average number of particles, number parity and quasiparticle spectra as a function of Fermi energy λ for the toy model from Eq. (6.46) for $\gamma = 0$, $\alpha = 0.1$ for varying ω, when selecting quasiparticles based on their signature structure. The toy Hamiltonian conserves z-signature, but breaks time-reversal in this case. 'Selected' quasiparticles are drawn in solid lines, their conjugates in dashed lines. Note that for $\omega = 0.1$ MeV no quasiparticle energies cross zero, while this does happen for $\omega = 0.4$ MeV.

even when its quasiparticle energy becomes negative. In this way we can ensure that the HFB configuration evolves continuously with the Fermi energy. Fig. 6.4 is a revised version of Fig. 6.3, now selecting quasiparticles on their signature structure instead of on their quasiparticle energies. Note that all of the discontinuities in $N(\lambda)$ have disappeared and the number parity is a constant over the entire range of λ.[12]

6.6.5 Quasiparticle selection without signature and time-reversal

Time-reversal and signature conservation both divided the quasiparticles in two groups, either through the Kramers degeneracy or through the signature quantum number. Severe problems arise when neither of those symmetries are conserved, as there is no natural way to divide the eigenvectors of the HFB Hamiltonian in two groups. One could still select quasiparticles based on their positive quasiparticle energy, but one runs into the same trouble as in section 6.6.3.
Possible remaining symmetries in `MOCCa` are parity and y-time-simplex, both of which do not offer any help. Parity provides a completely different block structure than signature, and y-time-simplex simply makes all of the relevant quantities real, see section 3.5. In short, there is no way of consistently choosing quasiparticles from among the eigenvectors of the HFB Hamiltonian to allow for smooth behavior of $N(\lambda)$ and avoiding quasiparticle energies that cross zero.

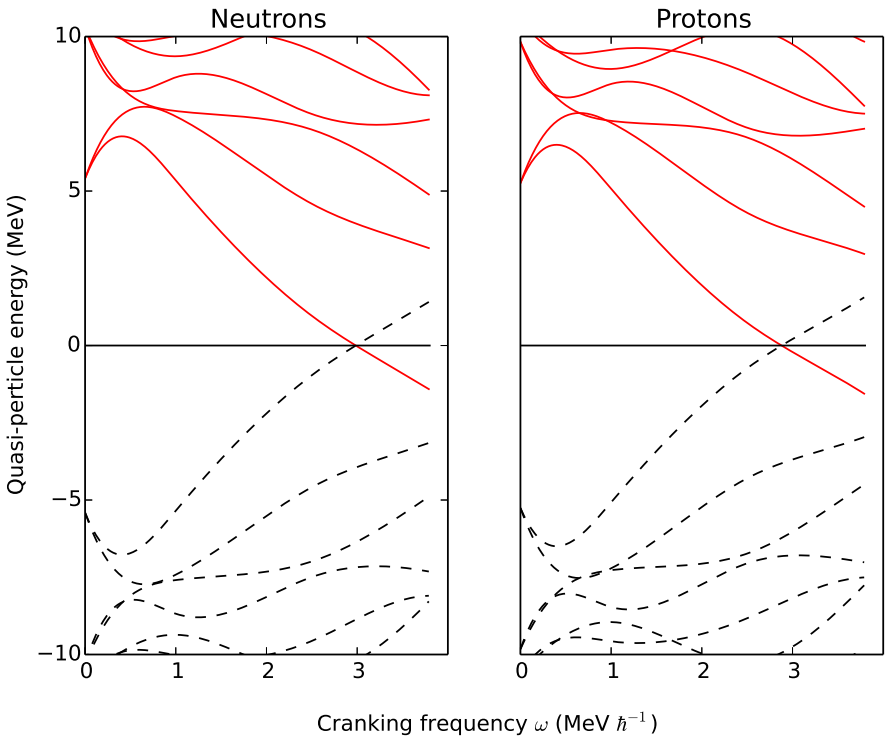

Figure 6.5: Negative parity quasiparticle spectrum of ^{24}Mg in a HFB calculation as a function of cranking frequency ω with z-signature conserved. The SLy4 parameterization was used with $V_n = V_p = 750$ MeV fm^3. The neutron and proton dispersion $\Delta\hat{\mathcal{N}}^2$ was constrained to 1.0 in order to enforce pairing. Selected quasiparticles are in red, and their conjugate partners in black.

6.6.6 Why is quasiparticle selection crucial?

The gradient descent process in `MOCCa` is very sensitive to configuration changes when doing Hartree-Fock calculations (see section 6.2) and the same is true for HFB calculations. Especially when looking for a Fermi energy to fix the number of particles on average, discontinuities in $N(\lambda)$ like we encountered in Fig. 6.3 will destroy the convergence of either of the Fermi solvers. This is easily explained: there are values of N for which there are no solutions, which is debilitating to the bisection solver, and there are locations where the derivative of $N(\lambda)$ becomes infinite which completely derails the Broyden solver.
As detailed above, when breaking time-reversal but conserving signature, this problem is solvable by selecting quasiparticle using signature blocks. That the situation from Fig. 6.3 is not an artefact of our toy model can be seen in Fig. 6.5. As a function of the cranking frequency ω, the negative parity proton and neutron quasiparticles of ^{24}Mg show one quasiparticle going to zero at $\omega \approx 3$ MeV $\hbar^{-1}$. If `MOCCa` selected on positive quasiparticle energy, the HFB configuration would have changed number parity and would rather be describing ^{23}Mg or ^{25}Mg than ^{24}Mg. The selection of quasiparticles using signature blocks is thus essential for `MOCCa` to be able to do time-reversal breaking calculations.
Changes in number parity are also destructive towards the iterative process: due to the mixing between mean-field iterations traces from the wrong number parity [13] end up persisting throughout the mean-field process and destroying convergence. We have never been able to converge a signature-broken and time-reversal broken calculation with `MOCCa` while simply selecting quasiparticles based on their energy.

6.7 Solving the HFB problem with the Thouless theorem

Another way of solving the HFB equations has been in use for a quite long time [11, 111, 112] and is based on the Thouless theorem, see section 3.8.We start by applying the Thouless operator on a reference HFB state

[12] Note that the curves of N(λ) for $\omega = 0.1$ MeV and $\omega = 0.4$ MeV are so similar because of the simplicity and symmetries of the toy model.
[13] -1 or +1, depending on if we are looking for an even or odd solution

$|\Psi_0\rangle$

$$|\Psi(Z)\rangle = \hat{\theta}(Z)|\Psi_0\rangle = \left[-\frac{1}{2}\sum_{ij} Z_{ij}\beta_i^\dagger\beta_j^\dagger\right]|\Psi_0\rangle\,. \tag{6.49}$$

The energy of this state is

$$E(Z,\Psi_0) = \frac{\langle\Psi(Z)|\hat{\mathcal{H}}_{\mathsf{HFB}}|\Psi(Z)\rangle}{\langle\Psi(Z)|\Psi(Z)\rangle}\,. \tag{6.50}$$

which is a function of the Z matrix, but also of the initial HFB state $|\Psi_0\rangle$. Keeping $|\Psi_0\rangle$ fixed as a reference point, we can vary this energy with respect to the Thouless coefficients Z_{ij} and try to find the minimum energy. One can calculate that [113]

$$\frac{\partial E(Z)}{\partial Z_{ij}^*} = \left[U^\dagger h V^* - V^\dagger h^T U^* - V^\dagger\Delta^* V^* + U^\dagger\Delta U^*\right]_{ij}\,. \tag{6.51}$$

Using this expression, one can easily set-up an optimization algorithm for the value of the matrix Z. The implementation in `MOCCa` is a conjugate gradient algorithm, based on [111], but with some practical modifications. See Appendix E for details.

The nature of the ansatz $|\Psi(Z)\rangle$ is what makes this method special. Note that the Thouless operator $\hat{\theta}(Z)$ can only create two-quasiparticle excitations on top of $|\Psi_0\rangle$. This means that the number parity of $|\Psi(Z)\rangle$ will in all cases be equal to the number parity of $|\Psi_0\rangle$. This property also solves the problems of selecting the proper quasiparticles at every diagonalisation of $\hat{\mathcal{H}}_{\mathsf{HFB}}$. The selected quasiparticles in the HFB state $|\Psi_0\rangle$ can be followed continuously through the iterative solution and in this way the selected quasiparticles of $|\Psi(Z)\rangle$ are the continous evolution of the selected quasiparticles in $|\Psi_0\rangle$. Physically, this is due to the specific form of the Thouless operator, since changing quasiparticle configuration would imply changing number parity, which is forbidden. This method is thus not plagued by the problems of the preceding section, and can be applied without modification to time-reversal breaking, signature breaking and time-reversal and signature breaking calculations.

Figure 6.6 demonstrates the application of this method for our toy model when $\gamma = 0.4$ MeV, with a much stronger pairing between levels with equal signature than opposite signature. No irregularities are present and the selected quasiparticles stay the same for all values of λ.

The price to pay is the dependence on the initial guess $|\Psi_0\rangle$. In order for this method to work, the initial wavefunction must have the correct quantum numbers, as the Thouless operator does not allow for changing any of them. This is a direct consequence of the ansatz $|\Psi(Z)\rangle$, which results in significantly smaller variational space than the one explored by direct diagonalisation of the HFB Hamiltonian. In practice, this means that the user should take care that the initial wavefunction does have the desired number of completely occupied orbitals, as it is impossible for the method to decrease this number.

6.8 Quasiparticle blocking

HFB theory for systems with an odd number of particles is more complicated compared to the theory for even systems, due to the need to create quasiparticle excitations, see section 3.7. In practice this presents a rather technical challenge for mean-field codes, as one needs to identify and evolve several quasiparticles self-consistently, thereby multiplying the computational time. In addition, the description of one-quasiparticle excitations implies the breaking of time-reversal symmetry. `MOCCa` is equipped for all of this, but several remarks need to be made. We first explain how `MOCCa` identifies the quasiparticle to block and afterwards split our discussion depending on which solution method is used.

6.8.1 Identification of quasiparticles

In a completely spherical calculation, the single-particle levels $|\phi_l\rangle$ carry several quantum numbers. In that case one could (almost) uniquely identify interesting quasiparticles by simply specifying J, J_z and parity quantum numbers. In `MOCCa`, this is not the case at all and many quantum numbers are in general not available. Given an initial HFB state $|\Psi_0\rangle$, the user can indicate to `MOCCa` the index of a single-particle level in the Hartree-Fock basis, say $|\phi_k\rangle$, and `MOCCa` will then scan the U and V matrices of the Bogoliubov transformation. We then select the column of these matrices, the eigenvector (U_l, V_l), that has the largest overlap with $|\phi_k\rangle$, meaning that

$$l = \text{maximum}\,\{|U_{jk}||j = 1,\ldots,\texttt{nwt}\}\,. \tag{6.52}$$

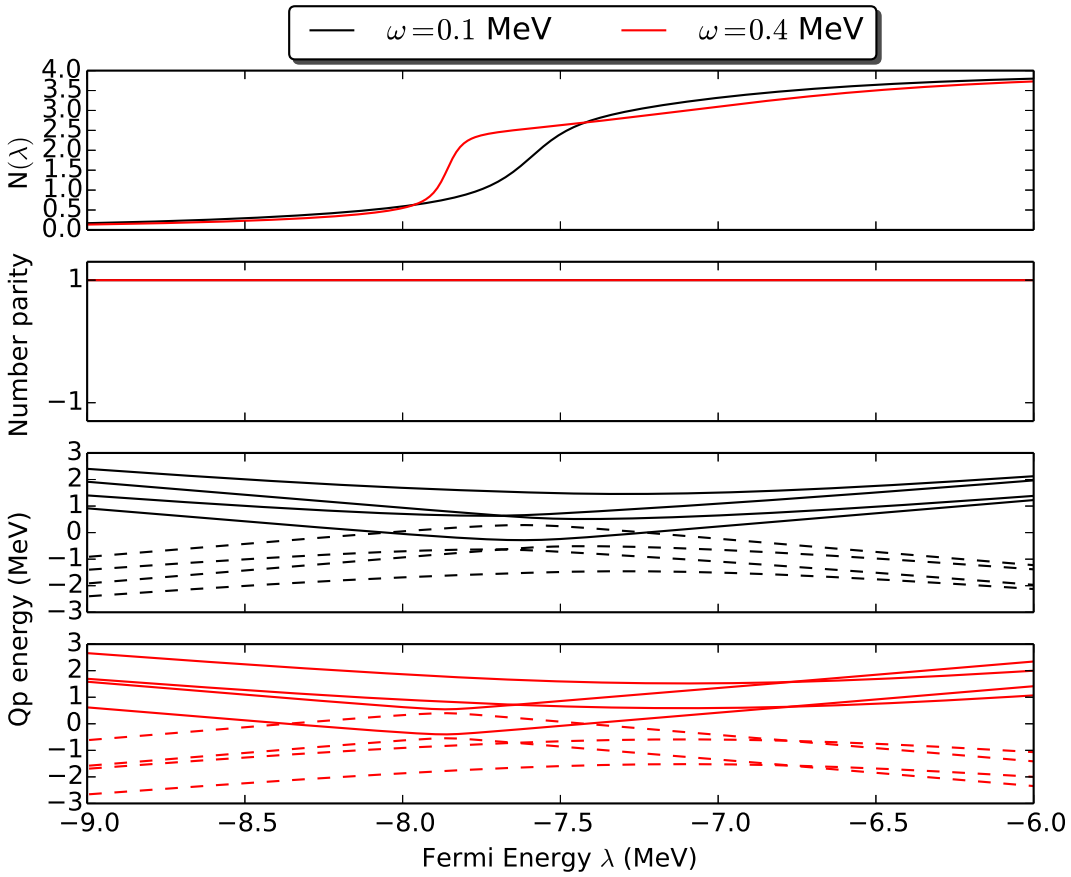

Figure 6.6: Average number of particles, number parity and quasiparticle spectra as a function of Fermi energy λ for the toy model from Eq. (6.46) for $\alpha = 0.1$ MeV for varying ω, when using the Thouless method. The toy Hamiltonian breaks z-signature strongly with $\gamma = 0.4$ MeV. 'Selected' quasiparticles are drawn in solid lines, their conjugates in dashed lines, although no explicit selection is necessary in this case. Note that quasiparticle crossings happen for every value of ω.

This can be interpreted as the quasiparticle that looks most like the single-particle level $|\phi_k\rangle$. Upon identifying this quasiparticle, `MOCCa` makes the switch

$$\begin{pmatrix} \hat{\beta}_l \\ \hat{\beta}_l^\dagger \end{pmatrix} \rightarrow \begin{pmatrix} \hat{\beta}_l^\dagger \\ \hat{\beta}_l \end{pmatrix} , \tag{6.53}$$

which is equivalent to

$$\begin{pmatrix} U_l \\ V_l \end{pmatrix} \rightarrow \begin{pmatrix} V_l^* \\ U_l^* \end{pmatrix} . \tag{6.54}$$

This is of course the practical implementation of applying the quasiparticle creation operator $\hat{\beta}_l^\dagger$ (before the switch) on the HFB state $|\Psi_0\rangle$, that is to say the state numerically represented changes like

$$|\Psi_0\rangle \rightarrow \hat{\beta}_l^\dagger |\Psi_0\rangle . \tag{6.55}$$

Note that the selection of largest overlap automatically takes the quantum numbers that are present into account. Indeed, if particles don't share the same quantum numbers (parity, isospin, z-signature), the corresponding entries in U will be zero. The quantum numbers that are broken however, do not enter anywhere in this procedure and one simply cannot draw any conclusions without restoring symmetries by projection. The direct diagonalization and Thouless methods will mainly differ in when they apply this blocking procedure.

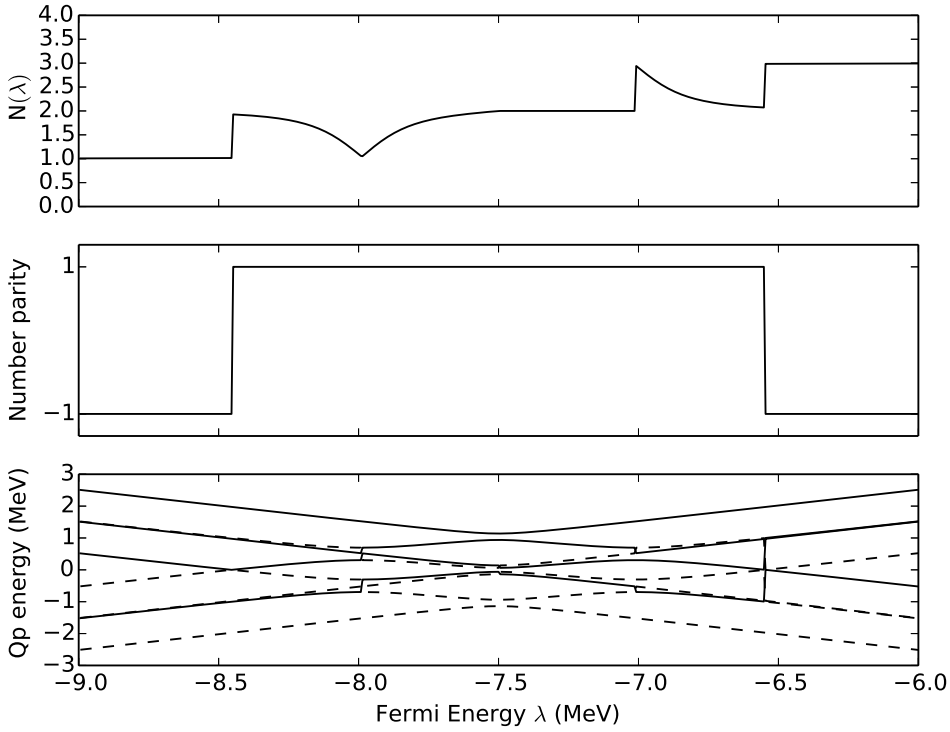

Figure 6.7: Same as Fig. 6.8 but with $\omega = 0.5$ MeV and selection of quasiparticles based on quasiparticle energies.

6.8.2 Blocking for direct diagonalization

The blocking procedure enters into the direct diagonalisation in a rather straightforward way. Every time the selection of quasiparticles is made after the diagonalisation of the HFB Hamiltonian, it is supplemented by blocking the desired quasiparticle. This way of implementing blocking has been used in `cr8` since its conception and has proven its worth in several applications [114, 115, 116, 117].
There are however some problems that are rather non-intuitive. In order to demonstrate these problems, let us go back to the toy model of Eq. 6.46. In Fig. 6.8 we show the function $N(\lambda)$ of the toy-model (without breaking signature) when blocking the single-particle level labeled 1 in Fig. 6.1. ω was taken to be zero, but the blocking procedure itself breaks time-reversal symmetry. For low values of λ, Nλ) is equal to one, corresponding to a particle blocked in level 1. For high values of λ, the particle number is equal to three, corresponding to a hole blocked in level 1 with levels 2-4 filled. The number parity is -1 for all configurations, corresponding to an odd system.
There are two fundamental problems with Fig. 6.8. The first problem is the discontinuity of $N(\lambda)$, which spells death for any Fermi solver. This is due to the blocking procedure, since at that point the overlap of level 1 with a different quasiparticle index becomes the largest and the HFB configuration changes drastically. A second problem emerges around $\lambda \approx -7.5$ MeV: another change in the index of the blocked quasiparticle introduces another irregularity. $N(\lambda)$ is still continuous here and this problem is thus less severe. However, there is no longer a unique Fermi energy for some values of N, as N(λ) is no longer injective.
One can make these problems very severe if one is not careful, especially when selecting quasiparticles through their quasiparticle energies. While we've already established the problems with this selection rule, Fig. 6.7 shows what happens if we add a non-zero value of ω on top of the blocking. The results are clearly disastrous and any Fermi solver looking for a suitable Fermi energy would fail in this type of landscape. This is the type of situation `MOCCa` encounters when breaking time-reversal and z-signature without using the Thouless method.

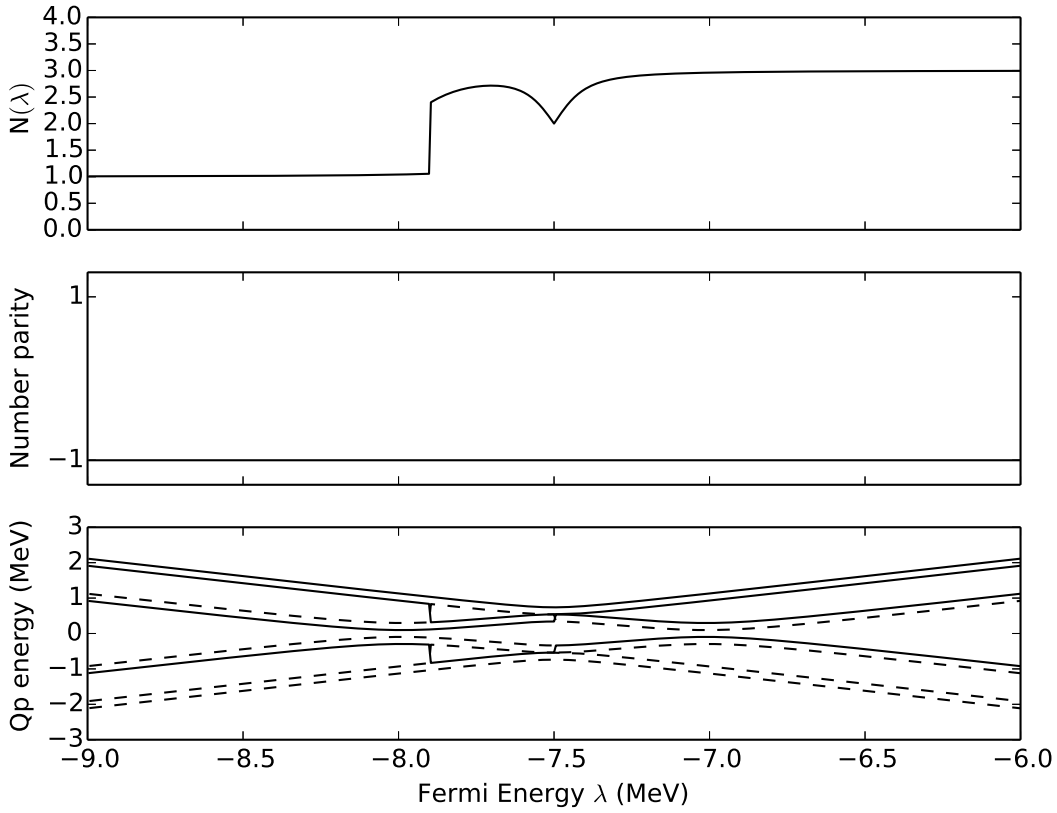

Figure 6.8: Average number of particles, number parity and quasiparticle spectra as a function of Fermi energy λ for the toy model from Eq. (6.46) for $\gamma = \omega = 0$ MeV and $\alpha = 0.1$ MeV for varying ω, blocking the state labeled 1. The toy Hamiltonian conserves z-signature but breaks time-reversal. Quasiparticle selection was based on positive quasiparticle energies. Selected quasiparticles are drawn in solid lines, their conjugates in dashed lines.

6.8.3 Blocking for the Thouless method

In principle the blocking procedure as described above has no place in the Thouless method. In order to obtain a one-quasiparticle blocked state, one has to start from a one-quasiparticle blocked state, since the number parity is among the symmetry quantum numbers that cannot be changed by the Thouless operator $\hat{\theta}(Z)$. In order to obtain a negative number parity state as a starting point, `MOCCa` offers the user to do the blocking procedure once at the start of the iterative process. By selecting the appropriate quasiparticle, the user can thus generate a starting state with the desired symmetries, which will remain fixed for the rest of the iterative process.
The advantage of this method is that it is variational, meaning that it will find the lowest state with the given quantum numbers determined by the initial blocking. If the initial quasiparticle blocked had positive parity, the final state will have positive parity. The entire process depends continuously on the matrix Z and nowhere does one have to do a selection procedure of quasiparticles. This is demonstrated in Fig. 6.9, which shows again the results of blocking the quasiparticle with largest overlap with single-particle level 1 but this time using the Thouless method. All of the pathologies of Fig. 6.9 have disappeared. Note that far from the crossings of the quasiparticles the methods give identical results.

6.8.4 Comparing both methods

The differences between direct diagonalisation and the Thouless method when studying states with negative number parity are subtle. The disadvantage of the direct diagonalisation method is obvious: the irregularities are very serious and make it very hard for `MOCCa` (but also `cr8`!) to converge. This problem only becomes more dramatic when one adds more single-particle levels and breaks more symmetries, thereby creating more

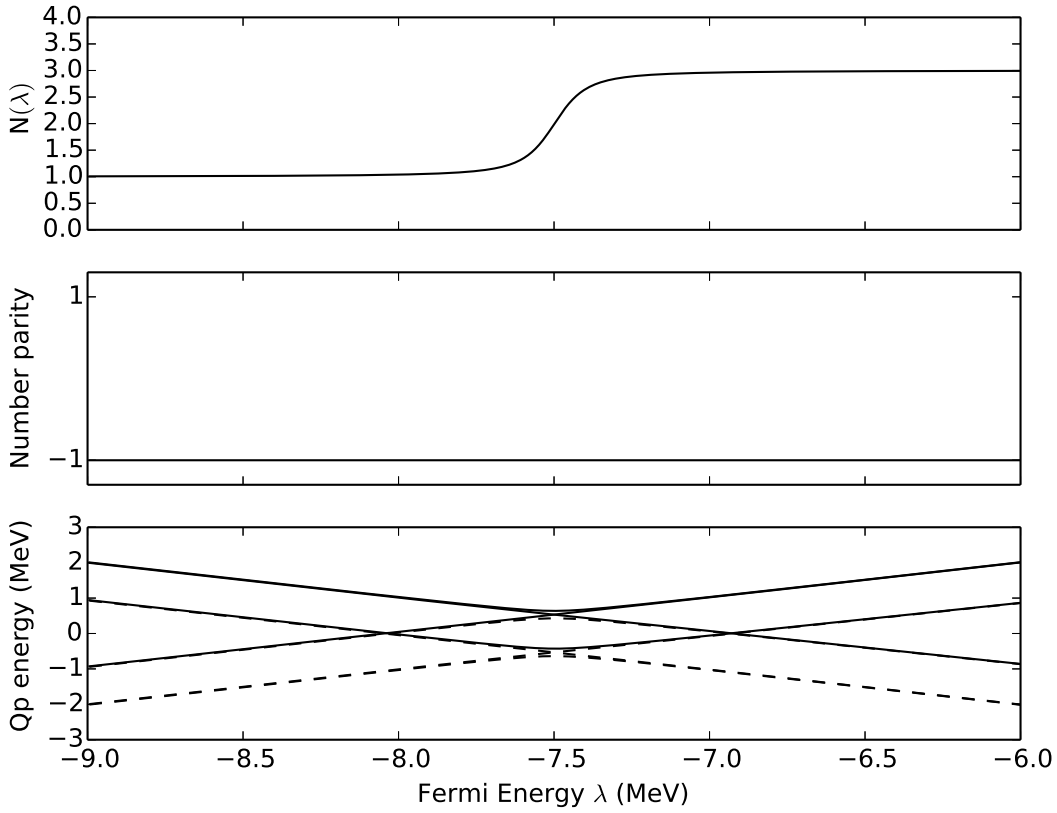

Figure 6.9: Same as Fig. 6.8, but using the Thouless method for blocking the quasiparticle with the largest overlap with level 1. Note that far from the crossings of the quasiparticles the methods give identical results.

quasiparticle crossings. States that originate from $J = \frac{1}{2}$ spherical states for example, are notoriously hard to converge, because their sheer number makes quasiparticle crossings plentiful.
The disadvantage of the Thouless method compared to direct diagonalisation is also that it is variational. Given a set of quantum numbers of all conserved symmetries the Thouless method will always converge towards the same many-body state with that set of quantum numbers, the lowest one in energy. For a calculation that conserves signature and parity, this method can thus only build four different quasiparticle states upon a given even reference state. This is a limitation that direct diagonalisation does not have, as in general different indices of Hartree-Fock basis states give rise to different final many-body states.
From a mean-field point of view, the Thouless method makes the most sense, as it will automatically give the quasiparticle configuration that is lowest energy for a given sets of quantum numbers[14]. From a beyond-mean-field point of view, the direct diagonalisation can be seen as more preferable, since one is able to generate more different states to include in a configuration-mixing calculation.
For heavy nuclei the difference between the lowest quasiparticle of a given set of quantum numbers obtained by direct diagonalisation and the one obtained by the Thouless blocking method is very small. Consider Table 6.1 comparing results of both methods for a positive parity, positive signature state in ^{219}Ac. The direct diagonalisation method result is the lowest negative-parity positive-signature proton quasiparticle excitation[15] on top of the even ^{218}Ra. The results for the Thouless method were obtained by exciting two different proton, negative parity, positive signature quasiparticle excitations on top of ^{218}Ra at the start of the iterations using the blocking procedure. The results are completely equivalent both between the different Thouless results and the direct diagonalisation result.

[14] Although it is possible to calculate excited states using the Thouless method [111], several technical developments are still needed.

[15] That I was able to converge, as it is by far not trivial to converge all possible selection of quasiparticles with direct diagonalisation.

	Direct diagonalisation	Thouless (1)	Thouless (2)
Energy (MeV)	-1672.165	-1672.166	-1672.166
Time-odd contribution to energy (MeV)	-0.098	-0.098	-0.098
$\langle\hat{\mathcal{J}}_z\rangle(\hbar)$	0.056	0.000	-0.004
Proton Fermi energy (MeV)	-2.710	-2.710	-2.710
Proton dispersion ΔN^2	5.724	5.724	5.725
Proton Lipkin-Nogami parameter λ_2 (MeV)	0.084	0.084	0.084
q_t (fm^2)	219.778	220.359	219.803
γ_t	-60.652	-60.493	-60.550

Table 6.1: Properties of ^{219}Ac, obtained by exciting a negative parity, positive signature proton quasiparticle on top of axially deformed ^{218}Ra, either the quasiparticle lowest in energy obtained by direct diagonalisation or by the Thouless method started from two different quasiparticles (1) and (2). The Skyrme parameterization was SLy5s1 [118], supplemented by HFB+LN pairing with $V_n = V_p = 1100$ MeV fm^3.

6.9 Investigating the HFB configuration: eigenvalues of ρ

As a practical means of distinguishing one HFB configuration from another one, `MOCCa` prints at every iteration summary the number of eigenvalues of the density matrix ρ that are equal to one. We denote these numbers by N_{block}. For every hermitian linear symmetry that is conserved, one can unambiguously define a value N_{block} for every quantum number combination of these symmetries. In `MOCCa`, the code will count N_{block} in every available parity-isospin block.
The interpretation of N_{block} is rather straightforward: it is the number of single-particle states in the canonical basis that do not partake in pairing, since their occupation factor v^2 is equal to one. They are directly related to the number parity of the many-body state: the number-parity of a given parity-isospin block is $+1$(-1) if the corresponding N_{block} of the parity-isospin block is even (odd).
The most practical use of quantity N_{block} lies thus in the quantification of the number-parity per isospin-parity block. In particular for the Thouless method: since this method can not induce any changes in the quasiparticle configuration during the search for the Fermi energy, this method effectively conserves the number of eigenvalues of ρ that are equal to one. If `MOCCa` can reliably identify the quasiparticle to be blocked in the direct diagonalisation method, the values of N_{block} should also be constant during the search for the Fermi energy. Note that this does not completely preclude any changes in N_{block} during the mean-field iterations. As single-particle levels in the Hartree-Fock basis enter or exit the pairing window dictated by the pairing cutoff (see section 3.9) they can decrease or raise the values of N_{block} in the case of the direct diagonalisation method. While at the start of a calculation the values of N_{block} can change, they should stabilize rather fast when approaching convergence. If these values change significantly, something is probably very wrong with the calculation.

Chapter 7

Numerical Tests

The aim of this chapter is to investigate the validity of MOCCa by comparing with the older codes where possible. As system of choice, we will investigate the nucleus ^{64}Ge because its energy surface has a simple triaxial structure. In section 7.1 we will compare the full triaxial energy surface of ^{64}Ge calculated by MOCCa with the surfaces as calculated by ev8, cr8 and ev4 in different conditions that are indicative of the applicability of all the codes. Section 7.2 details a number of checks on the internal consistency of MOCCa. Finally, 7.3 deals with the CPU time needed by MOCCa for various symmetry combinations.

7.1 Comparison with ev8, cr8 and ev4: ^{64}Ge

In order to have faith in any new results of MOCCa, we will demonstrate in this section that it is consistent with the older codes for the cases where they can be used. For future reproduction purposes, the versions of all the codes used are given in Table 7.1. All the calculations in this chapter were done on a $(N_X, N_Y, N_Z) = (32, 32, 32)$ Lagrange mesh with a mesh discretisation of $dx = 1.0$ fm. When all symmetries are conserved, this corresponds to a $(nx, ny, nz) = (16, 16, 16)$ mesh that is numerically represented. The derivatives used were finite-difference formulas during the mean-field iterations (3rd order for the first and 4th order for the second derivative[1]) with a recalculation with Lagrange energies at convergence for ev8 and ev4. The Coulomb problem was solved with a second order discretization of the Laplacian, without extra mesh points. The pairing interaction was characterized by a strength $V_n = V_p = 1250$ MeV fm^3 with $\alpha = 1.0$, supplemented by a symmetric Fermi cutoff at 5 MeV around the Fermi energy. It is worth noting that where we show constrained results the ev8, ev4 and cr8 results used readjusted quadratic constraints, while MOCCa employed predictor-corrector constraints. In practice this means that some getting converged results from the old codes (and specifically ev4) was significantly more human-time-consuming than with MOCCa.
Figure 7.1 shows the structure of the energy surface as a function of β_2 and γ for the SLy4 parameterization and HF+BCS pairing, obtained with ev8 and MOCCa. The minimum is convincingly triaxial, with $\gamma \approx 30°$. The spherical configuration is a local minimum and a barrier of somewhat less than 2 MeV separates it from the minimum. Any differences that are present between the two codes are not visible by eye. The energy difference between the two codes is generally on the order of a few keV and for all calculated points is strictly less than 10 keV.
Figure 7.2 shows the energy surface obtained with MOCCa and ev4. This time parity is broken in both cases by a constraint on the octupole moment $\langle \hat{\mathcal{Q}}_{30} \rangle = 250$ fm^3. The surface is significantly flatter compared to the parity-conserved case. The same energy difference on the order of at most a few keV is observed. We can conclude that MOCCa correctly treats breaking of the parity symmetry, at least in combination with BCS pairing.
HFB+LN calculations by cr8 and MOCCa are shown in Figure 7.3. The conditions of the calculation are identical to the conditions employed before, aside from the pairing treatment. Note that the configurations are time-reversal conserving as time-reversal is not explicitly broken. The minimum is significantly more smeared out, likely because of the Lipkin-Nogami contribution. The surfaces obtained with MOCCa and cr8 are again not distinguishable by eye. The largest error among all of the calculated points was 5 keV. Finally, Fig. 7.4 shows again a comparison between MOCCa and cr8 with HFB+LN pairing, but this time explicitly breaking time-reversal by including a cranking frequency around the z-axis of $\omega_z = 0.25$ MeV $\hbar^{-1}$. The surface does not change very much when this constraint is introduced, and both codes agree on the keV level. Two points

[1] This is only derivative option which is consistently present in all codes.

Code	ev8	cr8	ev4
Version	1.4.0	1.8.3	1.3.6

Table 7.1: Version of the codes used for the comparisons.

on the surface show an error of 11 keV, but this can likely be improved by further converging both codes. These results evidence the fact that MOCCa is correctly coded, at least on the level of a few keV and at least for the physics cases that ev8, ev4 and cr8 can access. As final evidence, consider Table 7.2 that directly compares various terms of the energy between MOCCa and cr8 for the cranked case.
In general, it should be possible to demonstrate the equivalence of MOCCa and the older codes on levels below on 1 keV. This is however very hard to do in practice because of the enormous control needed over all of the ingredients of the code. The binding energy of ^{64}Ge is on the order of 550 MeV, and 10 keV represents one thousandth of a percent of the total binding energy. Any small discrepancy can have profound impacts. Rounding errors on the values of the Skyrme parameterizations can easily have an impact on the order of 100 keV (see the appendix of [72]). The same applies to the numerical values of constants such as $\frac{\hbar^2}{2m_q}$ and e^2, which play the role of coupling constants for the kinetic energy and Coulomb term respectively.[2]

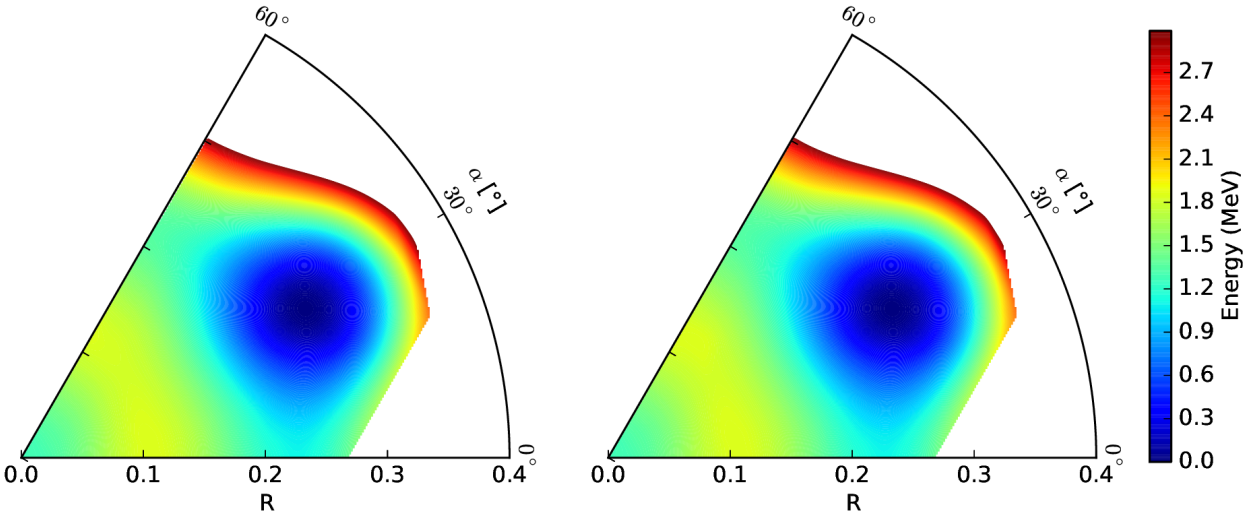

(a) ev8 (b) MOCCa

Figure 7.1: Energy surface of ^{64}Ge as a function of (β_2, γ) using the SLy4 interaction with BCS pairing with a pairing strength of 1250 MeV fm^3 obtained with ev8 and MOCCa. The largest difference observed over all of the calculated points is 8 keV.

[2]The reason why the codes do not simply use the numerical values of these constants, as for instance provided by CODATA [119] is because various Skyrme parameterizations have been fitted with different values.

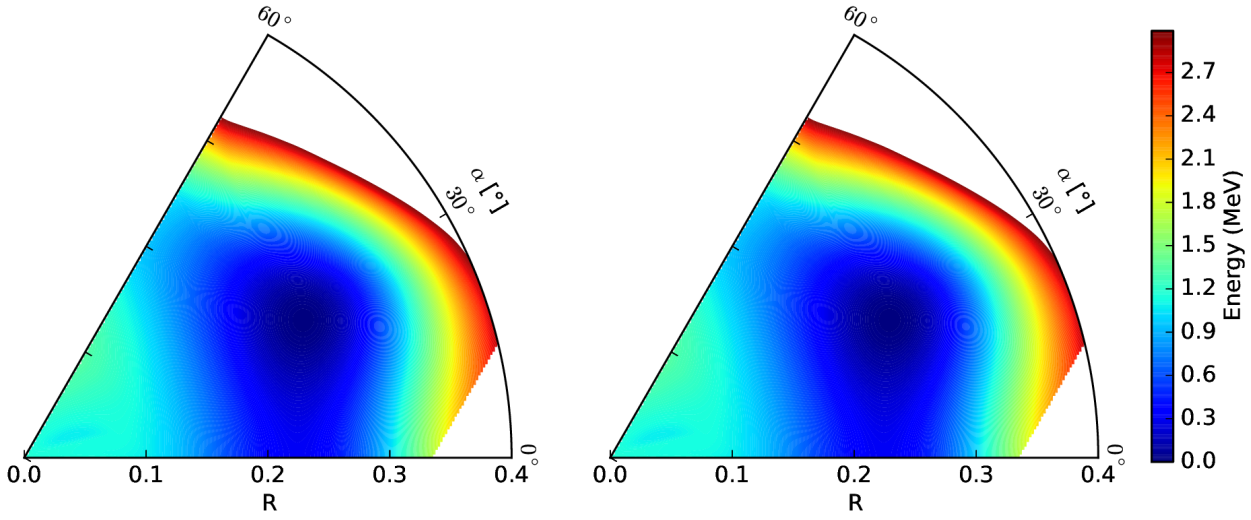

(a) ev4 (b) MOCCa

Figure 7.2: Energy potential surface of ^{64}Ge using the SLy4 interaction with HFB+LN pairing with a pairing strength of 1250 MeV fm^3 obtained with ev4 and MOCCa. The configurations break parity, with $\langle \hat{Q}_{30} \rangle$ constrained to 250 fm^3.

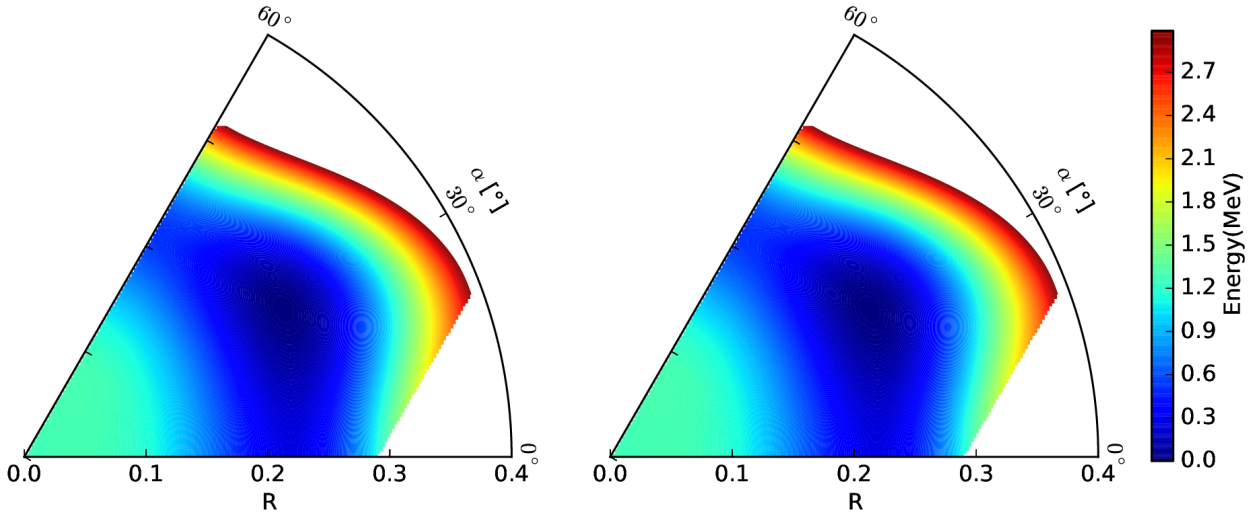

(a) cr8 (b) MOCCa

Figure 7.3: Energy potential surface of ^{64}Ge using the SLy4 parameterization with HFB+LN pairing with a pairing strength of 1250 MeV fm^3 obtained with cr8 and MOCCa. Note that the configurations do not break time-reversal.

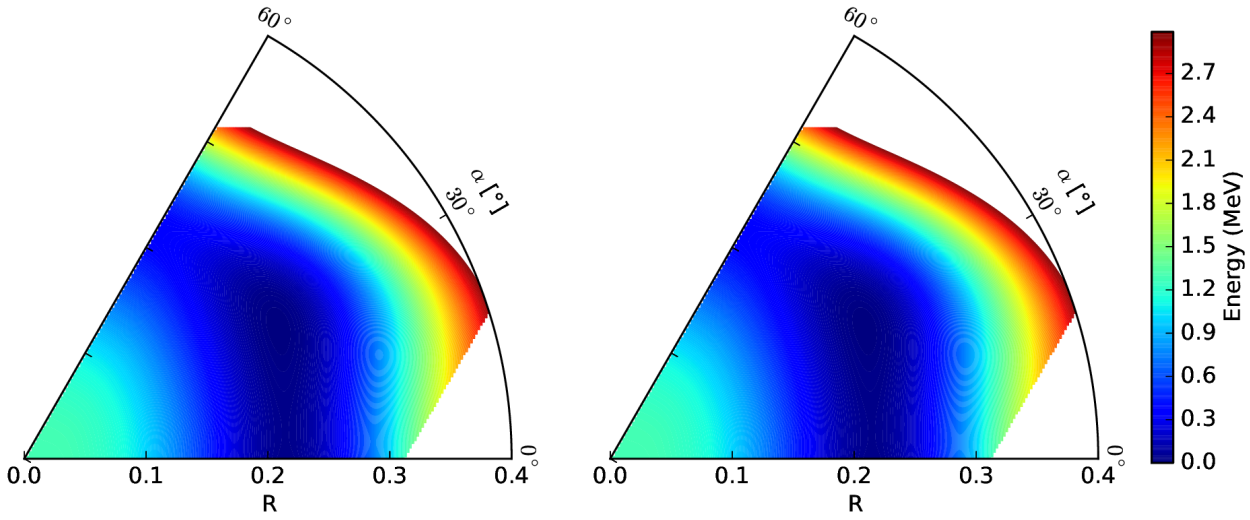

(a) cr8 (b) MOCCa

Figure 7.4: Cranked energy potential surface of ^{64}Ge using the SLy4 interaction with HFB+LN pairing with a pairing strength of 1250 MeV fm^3 obtained with cr8 and MOCCa. The configurations break time-reversal this time, with and angular frequency of $\omega_z = 0.25$ MeV $\hbar^{-1}$. The largest difference between the codes at the calculated points was 5 keV.

	MOCCa	cr8
Kinetic energy	1142.253	1142.250
Skyrme energy (time-even terms)	−1830.942	−1830.942
Skyrme energy (time-odd terms)	−0.028	−0.028
Coulomb energy (direct)	178.517	178.517
Coulomb energy (exchange)	−12.379	−12.379
Pairing energy	−6.381	−6.379
Lipkin-Nogami energy	−2.175	−2.175
Total energy (from functional)	−548.984	−548.984
Total energy (from single-particle energies)	−549.105	−549.108

Table 7.2: Comparison of contribution of different terms of the functional to the energy compared between cr8 and MOCCa for a calculation of ^{64}Ge with the SLy4 parameterization and HFB+LN pairing, constrained to $(\beta_2, \gamma) = (0.186, 27°)$ and with a cranking frequency $\omega_z = 0.25$ MeV $\hbar^{-1}$. All entries are in MeV. Note that these energies were computed using finite-difference derivative formulas.

Conserved	$\mathcal{D}^T_{2h}$	$G\{\hat{\mathcal{P}}, \hat{\mathcal{R}}_z, \check{\mathcal{S}}^T_y\}$	$G\{\hat{\mathcal{R}}_z, \check{\mathcal{S}}^T_y\}$	$G\{\check{\mathcal{S}}^T_y\}$	$\emptyset$
Broken	None	$\check{\mathcal{T}}$	$\hat{\mathcal{P}}$, $\check{\mathcal{T}}$	$\hat{\mathcal{P}}, \check{\mathcal{T}}, \hat{\mathcal{R}}_z$	$\hat{\mathcal{P}}, \check{\mathcal{T}}, \hat{\mathcal{R}}_z, \check{\mathcal{S}}^T_y$
$nx \times ny \times nz$	$(16 \times 16 \times 16)$	$(16 \times 16 \times 16)$	$(16 \times 16 \times 32)$	$(32 \times 16 \times 32)$	$(32 \times 32 \times 32)$
nwt	64	128	128	128	128
Energy	−542.9579	−542.9579	−542.9589	−542.9589	−542.9581
$r_{\text{rms},t}$(fm)	3.8858	3.8858	3.8858	3.8858	3.8858
β_2	0.8104	0.8104	0.8105	0.8105	0.8105
β_4	0.1387	0.1387	0.1387	0.1387	0.1387
β_6	0.0474	0.0474	0.0474	0.0474	0.0474

Table 7.3: Comparison of various quantities of the Hartree-Fock minimum of ^{64}Ge using the SLy4 parameterization. Energies are recalculated after convergence with Lagrange derivatives.

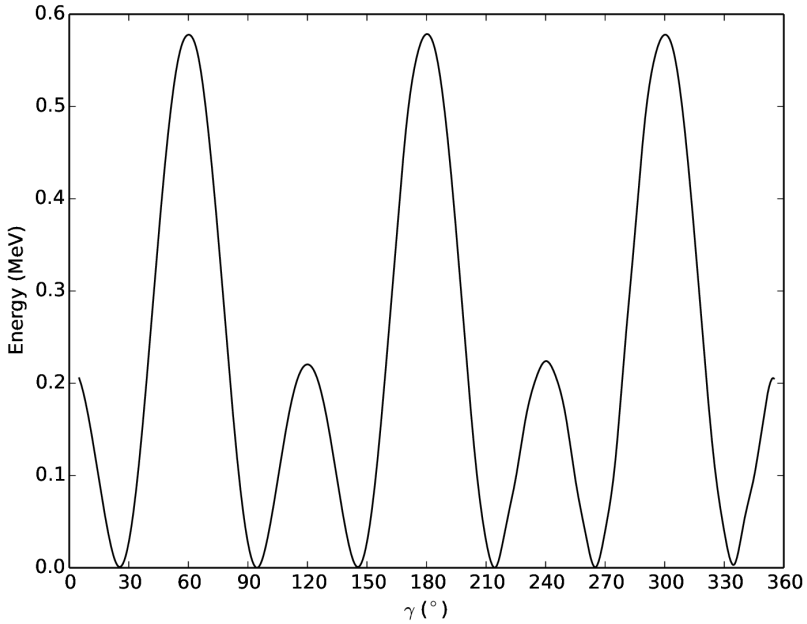

Figure 7.5: Energy of ^{64}Ge with $q = 250$ fm^2 as a function of γ calculated with the SLy5s1 parametrization and BCS pairing, conserving the entire $\mathcal{D}_{2h}^T$ group. The energy is symmetric around $\gamma = n \times 60^\circ$ for $n = 0, 1, 2, \ldots$.

7.2 Internal Consistency

Several other checks are possible that allows us to test the internal consistency of MOCCa. A first test is checking whether all the different symmetry combinations are represented in a consistent way. Table 7.3 summarizes the energy and shape quantities of the triaxial minimum in the energy surface of ^{64}Ge, calculated with the SLy5s1 parameterization. No constraints were added aside from the ones on redundant degrees of freedom. Starting from a symmetric mean-field state that conserves the entire group $\mathcal{D}_{2h}^T$, MOCCa should converge to a solution respecting all symmetries of $\mathcal{D}_{2h}^T$, regardless of the symmetry breaking the numerical representation allows. That this is the case can be seen in Table 7.3 for calculations that progressively break more symmetries. Energy differences are on the level of some tenths of keV while the shape parameters differ only slightly.

A second test is if the orientation of the nucleus in the box does not matter, i.e. that interchanging the axis labels (x, y, z) does not change the energy. As explained in Appendix C, the physically relevant values of γ can be chosen in any sextant of the plane, e.g. $[0^\circ, 60^\circ]$. The other values of γ describe the same shapes of the density distribution. Fig 7.5 show the energy of ^{64}Ge as a function of the triaxiality γ for constant total deformation $Q_2 = 250$ fm^2. As expected, the energy surface is completely symmetrical around integer multiples of 60°. Note that it is tempting from the shape of the surface to identify the triaxial minimum at $(\gamma \sim 30^\circ + n \times 60^\circ)$ as another symmetry axis, but that this is not the case can be identified from the fact that the prolate deformations $(\gamma = 2n \times 60^\circ)$ are favored energetically compared to the oblate deformations $(\gamma = (2n + 1) \times 60^\circ)$.

A third test is similar in nature, but more stringent. For a given triaxial shape, the energy should be invariant under a change in its direction: - $\langle \mathcal{J}_\mu \rangle$ should give rise to the same energy as $\langle \mathcal{J}_\mu \rangle$. Figure 7.6 shows the energy of ^{64}Ge as a function of the angle θ between the angular momentum and the z-axis. The shape of the nucleus was kept fixed by constraining all components of the quadrupole deformation while the total size of the angular momentum was kept fixed at $4\hbar$. Only the orientation of the angular momentum was changed in the $x - z$-plane: for $\theta = 0$ the angular momentum points in the positive z-direction, while for $\theta = 90$ the angular momentum points in the positive x-direction. The energy clearly does not depend on the sign of both the x and z component of the angular momentum. Note that this calculation needs to break z-signature in order to accommodate non-zero values of $\langle \hat{\mathcal{J}}_x \rangle$. Since pairing was treated using the HFB+LN formalism, the Thouless method was necessary to perform the calculation.

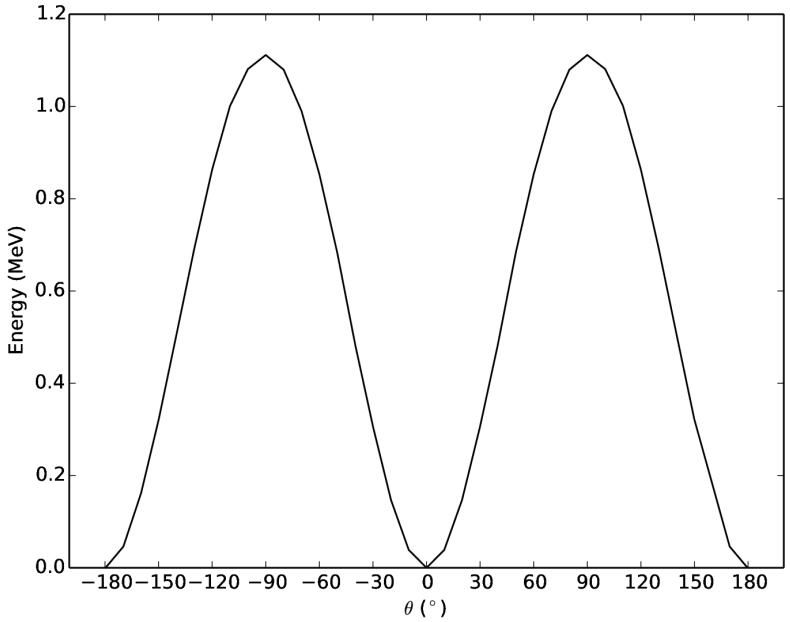

Figure 7.6: Energy as a function of the angle θ between the $\langle \mathcal{J} \rangle$ and the z-axis for ^{64}Ge at fixed quadrupole deformation $\langle \hat{\mathcal{Q}}_{20} \rangle = 5.97$ fm^2 and $\langle \mathrm{Re}\, \hat{\mathcal{Q}}_{22} \rangle = 56.90$ fm^2 and fixed total size of the angular momentum $\langle \hat{\mathcal{J}}_x \rangle^2 + \langle \hat{\mathcal{J}}_z \rangle^2 = 16\hbar^2$, using the SLy4 parameterization. At $\theta = 0^\circ$ the angular momentum is parallel to the z-axis, at $\theta = \pm 90^\circ$ the angular momentum is parallel to the x-axis. HFB+LN was used as pairing treatment using the Thouless method. Note that this calculation breaks both signature and time-reversal.

7.3 Timing

The CPU times demanded by `MOCCa` vary greatly depending on the calculation: the size of the numerical mesh, the number of single-particle wavefunctions, the pairing option selected and most importantly the number of conserved symmetries. Figure 7.7 shows the CPU time used by `MOCCa` on the HYDRA cluster at ULB for 1000 iterations for ^{64}Ge in selected symmetry combinations. The mesh previously defined in this chapter was used, as well as the same options for the finite difference derivatives. Predictor-corrector constraints were imposed on both physical quadrupole degrees of freedom, and on the centre-of-mass coordinate when parity is broken. Note that these numbers should be taken as indicative, as we have no precise control over the resources allocated by the cluster nor over the precise optimization done by the compiler[3].

Note that Hartree-Fock calculations are always cheaper in CPU time compared to both HF+BCS and HFB options: the difference between HF and HF+BCS is mainly due to the calculation of the matrix elements of the pairing interaction [10]. HFB is consistently the most costly of the pairing options, as the two-basis method needs the numerical representation of both the Hartree-Fock basis as well as the canonical basis, resulting in twice the numerical effort needed. The factor is slightly more than two compared to the Hartree-Fock case however, mostly due again to the calculation of the matrix elements of the pairing interaction $\bar{v}$.

The scaling with more broken symmetries in the Hartree-Fock case is almost exactly a factor of two: in the case of parity breaking due to a doubling of the represented points on the z-axis, in the case of time-reversal breaking due to the doubling of the number of single-particle wavefunctions represented. When both symmetries are broken, the total factor in CPU time is of course roughly four.

A comparison with the CPU times needed by `ev8`, `ev4` and `cr8` is made in Table 7.4 for calculations on the same mesh. The corresponding `MOCCa` calculation was performed in identical conditions. Note that it concerns unconstrained calculations, as the predictor-corrector constraints add an extra factor to the CPU time required. `MOCCa` is significantly slower than `ev4` and `ev8`. The treatment of derivatives is the culprit, as the data structures in `ev8` and `ev4` are significantly simpler and thus more straightforward to optimize for a compiler. This can definitely be improved in future versions of `MOCCa`. It is however striking that `cr8` and `MOCCa` take almost the same time to do a calculation for this particular choice of parameters.

[3] All of the compilations for the calculations of this section were performed with the gfortran compiler, using the -O3 optimization option.

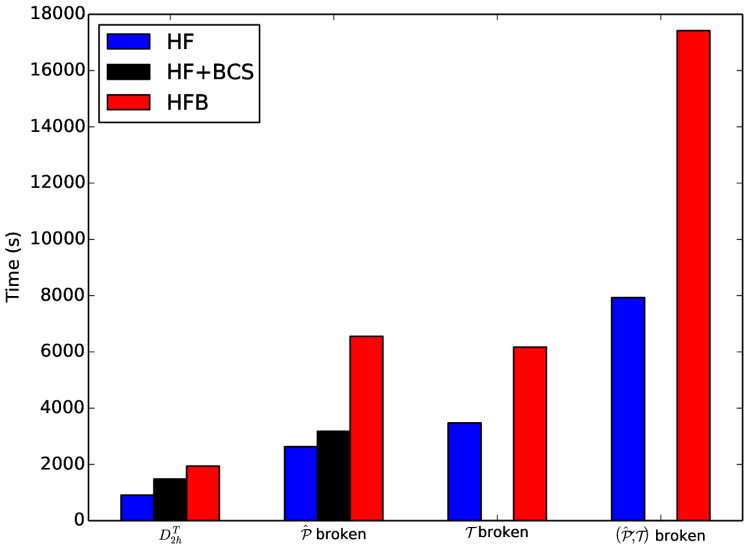

Figure 7.7: CPU time in seconds used by `MOCCa` on the HYDRA cluster for 1000 iterations on a $(N_X, N_Y, N_Z) = (32, 32, 32)$ mesh with $dx = 1.0$ using finite-difference derivatives for the three pairing options and either full symmetry conservation, parity broken, time-reversal-broken and parity and time-reversal broken calculation.The Skyrme parameterization used was SLy5s1 [118]. Predictor-corrector constraints were imposed of $\langle \hat{\mathcal{Q}}_{20} \rangle$, $\langle \hat{\mathcal{Q}}_{22} \rangle$ for all calculations, as well as on $\langle \hat{\mathcal{Q}}_{10} \rangle$ in the case of parity breaking.

	`ev8`	`cr8`	`ev4`
Time (s)	348	1380	840
Time by `MOCCa` (s)	820	1370	1930

Table 7.4: CPU time needed by `ev8`, `cr8`, `ev4` and `MOCCa` for 1000 iterations of ^{64}Ge with the SLy4 parameterization on a $(N_X, N_Y, N_Z) = (32, 32, 32)$ mesh with $dx = 1.0$ using finite-difference derivatives on the HYDRA cluster. In the case of `ev8` and `ev4` it concerns a HF+BCS calculation, while in the case of `cr8` it concerns a HFB calculation. The `MOCCa` calculation is identical to the one performed by the corresponding older code.

Chapter 8

Accuracy

In the view of the recent interest to quantify the statistical uncertainties associated with the readjustment of EDF [120, 121], it is imperative that the numerical error due to the solution method of the mean-field equations is well controlled.
The representation of the single-particle wavefunctions on the Lagrange mesh from chapter 4 offers a very intuitive grasp over this numerical accuracy. The numerical accuracy is determined by three factors: the treatment of derivatives, the size of the mesh and the discretisation length of the mesh dx. Attached is an extensive study of all three factors on various quantities of interest as the total energy, rms radii, two-neutron separation energies, density profiles as well as the fission barrier of ^{240}Pu.
The main conclusion is that modest mesh discretisations $dx \approx 1$ fm already give a rather accurate result for the energy, provided the numerical mesh is large enough to accommodate the nucleus and provided the Lagrange derivatives are used to reanalyze energies after convergence. The typical accuracy is on the order of (in a worst-case scenario) a few hundred keV in absolute sense, but in general much smaller when dealing with differences of energies such as two-neutron separation energies. Other quantities as the single-particle spectrum, as well as the deformation parameters β_ℓ profit from a comparable accuracy, even though it is only the total energy that is optimized. If further accuracy is required, the choice of $dx \approx 0.8$ fm or 0.7 fm shrinks the numerical error further down to levels that are far below the typical uncertainty associated with the mean-field model.

PHYSICAL REVIEW C **92**, 064318 (2015)

Numerical accuracy of mean-field calculations in coordinate space

W. Ryssens* and P.-H. Heenen†
PNTPM, CP229, Université Libre de Bruxelles, B-1050 Bruxelles, Belgium

M. Bender
Université de Bordeaux, Centre d'Etudes Nucléaires de Bordeaux Gradignan, UMR5797, F-33175 Gradignan, France
and CNRS/IN2P3, Centre d'Etudes Nucléaires de Bordeaux Gradignan, UMR5797, F-33175 Gradignan, France
(Received 2 September 2015; published 23 December 2015)

Background: Mean-field methods based on an energy density functional (EDF) are powerful tools used to describe many properties of nuclei in the entirety of the nuclear chart. The accuracy required of energies for nuclear physics and astrophysics applications is of the order of 500 keV and much effort is undertaken to build EDFs that meet this requirement.
Purpose: Mean-field calculations have to be accurate enough to preserve the accuracy of the EDF. We study this numerical accuracy in detail for a specific numerical choice of representation for mean-field equations that can accommodate any kind of symmetry breaking.
Method: The method that we use is a particular implementation of three-dimensional mesh calculations. Its numerical accuracy is governed by three main factors: the size of the box in which the nucleus is confined, the way numerical derivatives are calculated, and the distance between the points on the mesh.
Results: We examine the dependence of the results on these three factors for spherical doubly magic nuclei, neutron-rich ^{34}Ne, the fission barrier of ^{240}Pu, and isotopic chains around $Z = 50$.
Conclusions: Mesh calculations offer the user extensive control over the numerical accuracy of the solution scheme. When appropriate choices for the numerical scheme are made the achievable accuracy is well below the model uncertainties of mean-field methods.

DOI: 10.1103/PhysRevC.92.064318 PACS number(s): 21.60.Jz

I. INTRODUCTION

The self-consistent mean-field approach, based on an energy density functional (EDF), is a tool of choice to study nuclei in any region of the nuclear chart [1]. It allows one to calculate the properties of the ground state but also of alternative configurations, like shape isomers, or to follow the behavior of a nucleus along rotational bands or along fission paths. Often, one is directly interested not in the total binding energy of a specific nucleus but in its evolution along a series of isotopes or isotones, which can signal structural changes for given neutron or proton numbers.

Motivated by the needs of the nuclear physics and astrophysics communities, major efforts are under way to push the predictive power of nuclear mass models well below the 500-keV level. To reach this goal, the protocols used to adjust the EDF parameters have been revisited. In particular, methods are being developed [2–4] to quantify the statistical uncertainty of these parameters. However, besides the errors in observables due to these uncertainties, there is also a numerical error due to the way the self-consistent mean-field equations are solved. One needs to verify that the numerics does not introduce errors that are larger than the maximum error tolerated for mass models. More importantly, these errors should not vary too rapidly from one nucleus to another, to avoid spurious behavior of mass differences.

The numerical methods used to solve mean-field equations can be classified according to the way the single-particle wave functions are represented: by coordinate-space techniques or by a basis expansion. Coordinate-space techniques represent the single-particle wave functions in a discretized, finite volume. Several discretization techniques exist, utilizing finite-difference (FD) formulas [5], Fourier transformations [6], B splines [7], wavelets [8,9], and the Lagrange-mesh (LM) method [10–12].

The second family of numerical representations involves expanding single-particle wave functions in some chosen (finite) set of basis states. Usually these basis states are harmonic oscillator (HO) eigenstates, although the details often vary.

While the origin of numerical errors is quite different for the two families of representations, the type of EDF does not seem to influence the accuracy of the methods very much. The three main families (relativistic EDFs, zero-range Skyrme EDFs, and finite-range EDFs) require similar numbers of basis states to achieve a similar precision (see, e.g., [13–17]). In what follows, we limit ourselves to the study of zero-range Skyrme EDFs.

It is the aim of this paper to study the numerical accuracy of a specific implementation of coordinate-space techniques: representation on a three-dimensional (3D) Cartesian mesh of equidistant points. We focus on two specific techniques—FD formulas and the LM method—which are the ones implemented in our codes. As far as we can infer from the tests published in the literature, the accuracy obtained with the other techniques mentioned above is similar to that obtained

*wryssens@ulb.ac.be
†phheenen@ulb.ac.be

within our LM scheme. Most of the information relative to the tools that we have developed has been presented for the particular implementation made in the EV8 code [18,19]. More involved implementations have also been used, which differ from EV8 only in that they impose fewer symmetries on the nucleus. The presence of these symmetries in general allows for a reduction of the dimension of the problem; e.g., in EV8 it allows for the reduction of the space by a factor of 1/8.

The article is organized as follows: First, we define precisely the quantities that are used to characterize the accuracy of mean-field calculations. Next, we review the basic ingredients needed to define wave functions on a Cartesian mesh and to calculate derivatives and integrals in this representation. We then discuss the main sources of numerical errors: the size of the box in which the nucleus is confined and the step size of the mesh. We discuss the numerical accuracy that can be achieved by comparing energies and radii of doubly magic nuclei with those obtained with a spherical code. Finally, we check the convergence of energies, radii, and multipole moments of deformed nuclei by comparing results obtained with decreasing mesh discretization lengths.

II. DEFINITION OF USEFUL QUANTITIES

A mean-field configuration is characterized by its energy, its root-mean-square (rms) radius, and multipole moments. In this section we define these quantities, whose dependence on the mesh parameters is studied.

A. Total energy

For a time-reversal-invariant system as assumed here, the total (tot) energy is composed of the kinetic (kin) energy, the Skyrme energy describing the strong interaction in the particle-hole channel, the pairing (pair) energy, the Coulomb (Coul) energy, and a center-of-mass (c.m.) correction [19]:

$$E_{\rm tot} = E_{\rm kin} + E_{\rm Skyrme} + E_{\rm pair} + E_{\rm Coul} + E_{\rm c.m.}. \tag{1}$$

For the parametrizations used throughout this article, the Skyrme EDF takes the form of the sum of various bilinear combinations of the isoscalar ($t = 0$) and isovector ($t = 1$) local densities $\rho_t(\mathbf{r})$, kinetic densities $\tau_t(\mathbf{r})$, and spin-current densities $J_{t,\mu\nu}(\mathbf{r})$, where $\mu, \nu = x, y, z$,

$$\begin{aligned} E_{\rm Skyrme} &= E_{\rho^2} + E_{\rho^{2+\alpha}} + E_{\rho\tau} + E_{\rho\Delta\rho} + E_{\rho\nabla J} + E_{JJ} \\ &= \sum_{t=0,1} \int d^3r \left(C_t^{\rho}[\rho_0]\,\rho_t^2 + C_t^{\rho^\alpha}\,\rho_0^\alpha\,\rho_t^2 + C_t^{\tau}\,\rho_t\,\tau_t \right. \\ &\quad \left. + C_t^{\Delta\rho}\,\rho_t\,\Delta\rho_t + C_t^{\nabla\cdot J}\,\rho_t \nabla\cdot\mathbf{J}_t - C_t^{T} \sum_{\mu,\nu} J_{t,\mu\nu}\,J_{t,\mu\nu} \right), \end{aligned} \tag{2}$$

with coupling constants as defined in Ref. [19]. The kinetic energy just depends on the kinetic density

$$E_{\rm kin} = \sum_{q=n,p} \int d^3r\, \frac{\hbar^2}{2m_q}\,\tau_q(\mathbf{r}) \tag{3}$$

of protons and neutrons. While the Skyrme and kinetic energies are local functionals of the densities, the direct Coulomb energy is a nonlocal functional of the proton density $\rho_p(\mathbf{r})$:

$$E^d_{\rm Coul} = \frac{e^2}{2} \iint d^3r\, d^3r'\, \frac{\rho_p(\mathbf{r})\,\rho_p(\mathbf{r}')}{|\mathbf{r}-\mathbf{r}'|}. \tag{4}$$

Compared to the other terms contributing to the total energy, (1), the exact calculation of the Coulomb exchange energy is orders of magnitude more costly, as it is a functional of the complete nonlocal one-body density matrix. As a consequence, the local Slater approximation, whose numerical cost is similar to that of the Skyrme energy, (2), is used instead:

$$E^e_{\rm Coul} = -\frac{3e^2}{4}\left(\frac{3}{\pi}\right)^{1/3} \int d^3r\, \rho_p^{4/3}(\mathbf{r}). \tag{5}$$

The pairing energy contribution to the energy is

$$E_{\rm pair} = \sum_{k,m>0} f_k\,u_k v_k\,f_m\,u_m v_m\,\bar{v}^{\rm pair}_{k\bar{k}m\bar{m}}, \tag{6}$$

where the $\bar{v}_{k\bar{k}m\bar{m}}$ are antisymmetrized matrix elements of the pairing interaction and the f_i are cutoff factors, both of which are specified in Appendix B.

The expression for the cm correction, which is not relevant for our discussion, can be found in Ref. [19].

B. Dimensionless multipole moments

As in [19], the dimensionless multipole moments $\beta_{\ell m}$ are related to the matrix elements of the multipole operators $\hat{Q}_{\ell m} \equiv r^\ell\, Y_{\ell m}(\mathbf{r})$ by

$$\beta_{\ell m} = \frac{4\pi}{3R_0^\ell A}\langle \hat{Q}_{\ell m}\rangle, \tag{7}$$

where $R_0 = 1.2A^{1/3}$ fm. When m is omitted we imply it to be 0.

C. Radii

Another set of observables, related to the density profile of the nucleus, is the mean-square (ms) radii, rms radii, and isotopic shifts. The ms radius of the proton ($q = \mathrm{p}$), neutron ($q = \mathrm{n}$), and total density distribution is defined as

$$r_q^2 = \frac{1}{N_q}\int d^3r\, \rho_q(\mathbf{r})\, r^2, \tag{8}$$

$$r_t^2 = \frac{1}{A}\int d^3r\, [\rho_n(\mathbf{r}) + \rho_p(\mathbf{r})]\, r^2. \tag{9}$$

The rms radii are then the square root of the corresponding ms radius.

Similarly, we present results for the isotope shift of charge radii, which are calculated as the difference between the proton ms radius of an isotope with N neutrons and that of a reference isotope with N_0 neutrons,

$$\delta r^2(N,Z) = r_p^2(N,Z) - r_p^2(N_0,Z), \tag{10}$$

without any corrections.

III. COORDINATE-SPACE REPRESENTATION

Assuming a 3D Cartesian mesh, a function $\Phi(\mathbf{r}) = \Phi(x,y,z)$ is represented by the tensor Φ_{pqs} of its values at the collocation points (x_p, y_q, z_s):

$$\Phi(\mathbf{r}) = \{\Phi(x_p, y_q, z_s)\} = \{\Phi_{pqs}\}. \tag{11}$$

A mesh can be defined in several ways, depending on the choice of the collocation points. For example, the origin of the coordinate system and the boundaries of the box can be included as collocation points or not. Different choices can also be made for the boundary conditions at the edge of the box.

To set up self-consistent mean-field equations, one has to vary the EDF with respect to Φ_{pqs}. This requires defining the prescriptions to calculate derivatives and integrals from the values of Φ_{pqs} on the mesh. Several choices for derivatives have been explored over the years.

A. Derivatives on a mesh

The most straightforward possibility for setting up a coordinate-space representation of self-consistent mean-field equations is provided by the FD method, a widely used tool for solving partial differential equations [20]. In this scheme, the derivatives are calculated with n-point FD formulas, and the integrals are obtained by summing up the integrand at the mesh points multiplied by a suitable volume element.

There are three factors that determine the accuracy that can be achieved with the FD method. First is the overall resolution scale provided by the mesh spacing; decreasing the distance between mesh points improves the accuracy. Second, the higher the order of the FD formulas used for a given mesh spacing, the better the accuracy. In both cases, however, a higher accuracy means also an increase in the numerical cost. Third, there are internal inconsistencies introduced by the method itself. For example, taking twice the numerical first-order derivatives of a given function is not equivalent to applying the numerical second-order derivatives. Also, the numerical derivatives are not the inverse of the numerical integrations. Only for very small step sizes, well below 0.1 fm, do these internal inconsistencies become irrelevant. While such small step sizes can be easily handled in spherical 1D codes [21], the required storage is prohibitive in axial 2D and Cartesian 3D codes. In addition, such step sizes are much smaller than what can be expected to be the physically relevant resolution scale; see, for example, the arguments brought forward in Ref. [22].

Several other schemes have been developed in the past with a better consistency between derivation and integration. For instance, derivatives have been defined through a Fourier transformation to momentum space [6,23,24], which is equivalent to the assumption that the functions on the mesh can be developed into a set of plane waves. In this method, the derivatives are quasiexact for a given resolution of the mesh, and first- and second-order derivatives are internally consistent. Similar ideas have been developed in quantum chemistry under the label *discrete variable representation* (DVR) [25–27]. A similar formalism that provides an internal consistent scheme for derivatives and integrals is the LM method, which we sketch in the following section.

B. Lagrange-mesh representation

The idea underlying the LM method is that for each Gauss quadrature one can construct a set of basis functions for which orthogonality and completeness relations are exactly fulfilled when evaluated with the given quadrature [10,28,29]. This additional condition makes the LM method a special case of the slightly less rigorous concept of DVR [26,29].

LMs have been constructed for a multitude of different geometries and used for a wide range of applications (see [29] and references therein). We use here the case of an equidistant 3D Cartesian mesh. Its three directions are separable in the formalism, such that presentation of the principles of the method for one dimension is sufficient.

The underlying basis of a 1D Cartesian equidistant LM is constructed as the set of functions $\varphi_k(x)$, whose orthogonality relations are exact when evaluated by a simple $2N$-point rectangular quadrature rule, sometimes called the *midpoint rule* [10],

$$\int_a^b dx\ \varphi_k^*(x)\,\varphi_{k'}(x) \to dx \sum_r \varphi_k^*(x_r)\,\varphi_{k'}(x_r) = \delta_{kk'}, \tag{12}$$

where dx is the distance between the collocation points located at

$$x_r = r\,dx = \pm dx/2, \pm 3\,dx/2, \ldots, \pm(N-1)\,dx/2 \tag{13}$$

and where a and b are the boundaries of the numerical box $[a,b] = [-N dx, +N dx]$. A convenient representation of the $2N$ basis functions $\varphi_k(x)$ are plane waves of the form

$$\varphi_k(x) = \frac{1}{\sqrt{L}} \exp\left(\frac{2\pi i}{L} k\,x\right), \tag{14}$$

where $L = 2N dx$ is the length of the numerical box and where $k = \pm\frac{1}{2}, \pm\frac{3}{2}, \ldots, \pm(N-\frac{1}{2})$. The real part of the $\varphi_k(x)$ is symmetric and has nodes on the boundaries of the box and a maximum at the origin, whereas their imaginary part is skew-symmetric and, consequently, has a node at the origin and maxima on the boundaries of the box. This also implies that $\varphi_k^*(x) = \varphi_{-k}(x)$.

The $\varphi_k(x_r)$ form a complete set of functions to describe any function on the mesh points

$$dx \sum_k \varphi_k^*(x_r)\,\varphi_k(x_s) = \delta_{rs}. \tag{15}$$

Note that the box size L is not a multiple of the wavelength of the basis functions. Instead, twice the box size is an odd multiple of the wavelengths, which take the values $2L = 2L/1, 2L/3, 2L/5, \ldots, 2L/(2N-1)$. Both the real and the imaginary parts of all plane waves in Eq. (14) are nonzero at all mesh points.

As recalled in Ref. [22], in Cartesian DVR and LM coordinate-space methods, where the derivatives are defined

through an expansion in plane waves, the analysis of a calculation's infrared and ultraviolet cutoffs introduced by the basis is straightforward. This has to be contrasted with the much more involved analyses required when working with an HO basis [30–32]. It is also argued in Ref. [22] that a DVR or LM representation of the nuclear many-body problem covers the relevant part of the phase space with a much smaller number of basis states than required by an HO basis. In practice, however, HO bases typically used for self-consistent mean-field calculations are much smaller than the typical number of mesh points used in the same kind of calculation. For a box with 20 points in every direction the number of linearly independent states is 64 000, compared with an HO expansion with 20 shells, which contains 14 168 states.

While the basis functions $\varphi_k(x)$ in Eq. (14) are useful to discuss the mathematical properties of the LM method, the actual coordinate representation then employs the set of $2N$ Lagrange interpolation functions $f_i(x)$ obtained as [10,28,29]

$$f_r(x) \equiv dx \sum_k \varphi_k^*(x_r)\,\varphi_k(x) = \frac{1}{2N}\,\frac{\sin\left[\frac{\pi}{dx}(x - r\,dx)\right]}{\sin\left[\frac{\pi}{dx}\frac{x-r\,dx}{2N}\right]}. \tag{16}$$

By construction, the Lagrange interpolation functions have the property of being equal to 1 at the mesh point, $x_r = r\,dx$, and 0 at all others, $f_r(x_s) = \delta_{rs}$ [10,28,29]. When developed into Lagrange functions, any function $\phi(x)$ on the mesh,

$$\phi(x) = \sum_r \phi(x_r)\,f_r(x) = \sum_r \phi_r\,f_r(x), \tag{17}$$

is then simply represented by its values $\phi_r \equiv \phi(x_r)$ at $2N$ mesh points.

The Lagrange functions are smooth and infinitely derivable. They can be used to define matrices representing the first and second derivatives of functions discretized through[1] Eq. (17):

$$D^{(1)}_{ji} \equiv \left.\frac{df(x)}{dx}\right|_{x=x_j} = \begin{cases} (-1)^{i-j}\,\frac{\pi}{(2N)dx}\,\frac{1}{\sin(\pi(i-j)/(2N))} & \text{for} \quad i \neq j, \\ 0 & \text{for} \quad i = j; \end{cases} \tag{18}$$

$$D^{(2)}_{ji} \equiv \left.\frac{d^2 f_i(x)}{dx^2}\right|_{x=x_j} = \begin{cases} (-1)^{i-j+1}\,2\left(\frac{\pi}{(2N)dx}\right)^2\frac{\cos\left[\pi(i-j)/(2N)\right]}{\sin^2\left[\pi(i-j)/(2N)\right]} & \text{for} \quad i \neq j, \\ -\frac{\pi^2}{3dx^2}\left(1 - \frac{1}{(2N)^2}\right) & \text{for} \quad i = j. \end{cases} \tag{19}$$

The first derivative of any function $\phi(x)$ on the mesh is obtained by multiplying the $2N \times 2N$ matrix $D^{(1)}_{rs}$ by the vector ϕ_r,

$$\phi'_r = \phi'(x_r) = \sum_s D^{(1)}_{rs}\,\phi_s, \tag{20}$$

and similarly for the second derivatives. Note that the derivative matrices have the property $D^{(2)} = D^{(1)}D^{(1)}$ by construction [29], which is not the case for FD formulas. As the derivatives of Eqs. (18) and (19) correspond to full $2N \times 2N$ matrices, their application is more time-consuming than that of FD derivatives, which correspond to a sparse band matrix.

The full Cartesian 3D representation of a function $\Phi(\mathbf{r})$ is then provided by

$$\Phi(\mathbf{r}) = \sum_{pqs} \Phi_{pqs}\,f_p(x)\,f_q(y)\,f_s(z), \tag{21}$$

where the number of discretization points does not have to be the same in each direction. In this case, the derivative matrices in Eqs. (18) and (19) have to be set up separately for each direction.

As pointed out in Refs. [26] and [33], a variational calculation using DVR or LM derivatives delivers very precise values for the total energy in spite of the individual matrix elements' being much less accurate. In what follows, we illustrate that this property implies very accurate total energies, while separate terms of the Skyrme EDF are less well represented. In addition, we show that using an LM results in a variational calculation.

IV. NUMERICAL CONSIDERATIONS

A. Numerical parameters of parameterizations

Unless explicitly stated, we have used the SLy4 parametrization. To explore the dependence of the numerical accuracy on the EDF, we have, in addition, tested a representative set of Skyrme parametrizations, as listed in Appendix A.

In the next two sections, we present calculations for the doubly magic spherical nuclei ^{40}Ca, ^{132}Sn, and ^{208}Pb; the neutron-rich nucleus ^{34}Ne; Cd, Sn, and Te isotope chains; and the fission path of ^{240}Pu. It is noteworthy that we only include pairing for the isotopic chains and for ^{240}Pu (see Appendix B for details). In all other cases, pairing has been neglected. In Appendix C we comment on the precise physical constants used during our calculations.

B. Measuring accuracy

The accuracy of a coordinate-space calculation is limited by the size of the box, the discretization length dx, and the way derivatives and integrals are calculated. In order to properly judge these effects we employ two ways of analyzing results.

[1] Unfortunately, the corrections of these expressions as given in the corrigendum to Ref. [19] still contain a typographical error: the formula for the second derivative has a superfluous factor of 2 when $i \neq j$.

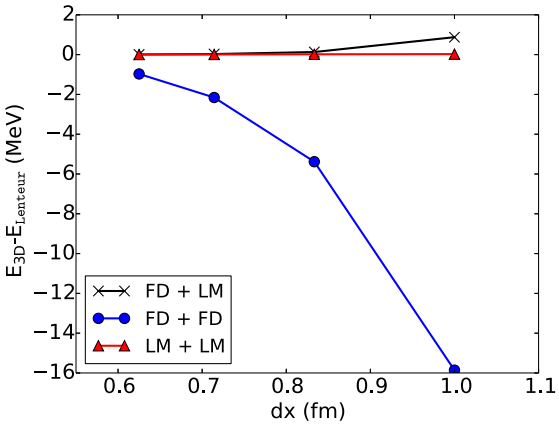

FIG. 1. (Color online) Comparison between the errors in the total energy of ^{208}Pb obtained in calculations using different combinations of formulas for the derivatives (see text). Differences are taken with respect to the total energy obtained with LENTEUR [21].

For spherical nuclei we can compare our 3D results with a 1D spherical code that also represents the single-particle wave functions in coordinate space. Because of spherical symmetry, we can use extremely fine discretizations and the results can thus be considered exact to a very high precision. For this purpose we use LENTEUR [21] as a reference.

For deformed nuclei, we no longer have access to such a comparison. Here we have to resort to looking at 3D results as a function of both box size and mesh spacing: we compare results in small boxes with a large mesh spacing to results in very large boxes with a very fine mesh spacing.

C. Use of derivatives and the variational principle

The numerical cost of using LM derivatives is much higher than that of the FD alternative. To control the computational time, three options have been considered: they differ in the way derivatives are calculated during the mean-field iterations and after convergence. The first option (FD + FD) has been used in the first applications of the codes [5], where derivatives were exclusively calculated by FD. The second one (FD + LM) has been the most used for more than 20 years: FD derivatives are used during the iterations but the energies are recalculated after convergence by LM formulas. Finally, in the last option (LM + LM), the LM formulas are used during the iterations and after convergence.

In practice, we use a seven-point difference formula for the first-order and a nine-point formula for the second-order derivatives when employing FD formulas. It is shown in Ref. [34] that this provides an efficient compromise in terms of overall speed and precision.

Figure 1 illustrates the accuracy of the total energy obtained using these three options. The LM + LM choice is by far the most accurate. As reported in Table II, the result obtained with a mesh size of 1.0 fm differs by only 25 keV from the LENTEUR result. The FD + LM option is less accurate but already sufficient for most applications, with an error of around 100 keV for $dx = 0.8$ fm. It is better by nearly an order of magnitude than the FD + FD choice. Results presented in the following were obtained with the FD + LM option, unless otherwise stated.

Both the FD + LM and the LM + LM calculations underestimate the binding energy, as it should be for a variational calculation. This is due to the fact that the single-particle wave functions are expanded on a complete and closed basis for a given box size and mesh discretization length [see Eq. (14)]. Increasing the box size and/or decreasing the mesh discretization length enlarges the accessible subspace of the Hilbert space [29] and leads to a monotonous convergence of the energy. In contrast, such a basis cannot be defined for the FD + FD option, for which the calculation systematically overestimates the binding energy of ^{208}Pb.

The same applies to mesh calculations with Fourier derivatives, as can be deduced from the convergence analyses in Refs. [6] and [23]. While for a given dx the overall accuracy of the binding energy found there is very similar to that we find for LM + LM calculations, the energy does not converge monotonically with decreasing dx.

While the use of LM derivatives after having used FD ones during the iterations (FD + LM) is sufficient to obtain an upper bound of the total energy since any wave function discretized on a mesh can be expanded on the LM basis, the errors in the various individual terms of the Skyrme EDF can be very large, as reported in Table I. While the total energy varies by slightly less than 1 MeV when dx is decreased from 1.0 to 0.549 fm, the variation in the kinetic energy is of the order of 40 MeV, counterbalanced by a similar change in the Skyrme energy. The situation for the LM + LM scheme is reported in Table II. It indicates a similar effect, but on a much smaller scale: the total energy varies by 20 keV, while the kinetic energy varies by roughly 150 keV.

When performing symmetry restoration and configuration mixing by the generator coordinate method, a high level of accuracy is required to avoid buildup numerical noise while solving the Hill-Wheeler-Griffin equation. This calls for the use of LM derivatives in these calculations, as done since our first applications [35].

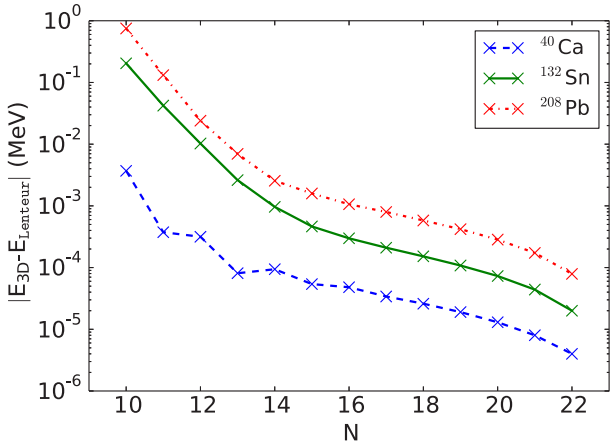

FIG. 2. (Color online) Energy difference between a reference calculation performed with 23 points and calculations performed with N points for the three nuclei ^{40}Ca, ^{132}Sn, and ^{208}Pb. In all cases, the step size is equal to 1.0 fm.

TABLE I. Decomposition of the total energy between the terms of the Skyrme parametrization SLy4 for ^{208}Pb, using the FD + LM option. All energies are in MeV. See Sec. II A fore definitions of terms. Values obtained with the spherical 1D code LENTEUR are given for comparison.

	Energy (MeV)				
	$dx = 1.0$ fm	$dx = 0.83$ fm	$dx = 0.71$ fm	$dx = 0.549$ fm	LENTEUR
Kinetic + c.m. correction	3908.548	3880.647	3872.035	3867.506	3866.190
Direct Coulomb	831.801	829.241	828.433	828.004	827.876
Coulomb exchange	−31.415	−31.319	−31.289	−31.273	−31.269
E_{ρ^2}	−22749.578	−22510.048	−22435.391	−22395.941	−22384.379
$E_{\rho\tau}$	1368.924	1343.506	1335.611	1331.436	1330.206
$E_{\rho^{2+\alpha}}$	14812.851	14631.848	14575.413	14545.584	14536.832
$E_{\rho\Delta\rho}$	323.771	318.147	316.431	315.539	315.287
$E_{\rho\nabla J}$	−99.730	−97.595	−96.917	−96.554	−96.445
Total Skyrme energy	−6343.762	−6314.142	−6304.854	−6299.937	−6298.501
Total energy	−1634.828	−1635.574	−1635.675	−1635.700	−1635.703

D. Determining box sizes and mesh spacings

The first requirement for a coordinate-space calculation is that the box in which the nucleus is confined is large enough to avoid any spurious effect due to the truncation of the wave functions. The influence of the box size on the total energy for three spherical nuclei is represented in Fig. 2. The same mesh size, $dx = 1.0$ fm, is used in all calculations while the number of discretization points is varied, thus changing the volume of the box. The calculation in the largest box, using 23 points, is taken as a reference. The errors decrease quickly when the box size is enlarged. If one requires that the error is smaller than 1 keV, we see that taking boxes with half-sides of 11 fm for ^{40}Ca, 15 fm for ^{132}Sn, and 20 fm for ^{208}Pb is sufficient. Since the numerical effort required for ^{40}Ca is very low we opted to use the slightly larger half-side of 13 fm in order to further increase our accuracy to about 0.1 keV.

Similar analyses have been performed for all nuclei considered in this paper. Since several nuclei in the isotopic chains around $Z = 50$ are deformed, we have performed all calculations with the same box size as ^{208}Pb. This choice allows us to calculate all isotopes with the same numerical conditions. The box dimensions are listed in Table III. The columns C_x, C_y, and C_z indicate the size of the box in which the Coulomb problem is solved. For every system, the box size was varied for fixed dx until the energy did not change by more than 0.1 keV, with the exception of ^{240}Pu, for which this limit was 1 keV.

A nonambiguous comparison between calculations performed with different mesh discretizations dx can only be achieved when the volume of the box is conserved. This is realized by determining the value of dx in such a way that the box has the same size for each number of mesh points.

E. Convergence of the iterative procedure

Decreasing the mesh size improves the accuracy. However, this has a price in computing time. First, keeping the same box size requires increasing the number of discretization points. Second, the time step of the imaginary-time-step method [36,37] implemented in the codes [19] has to be decreased with decreasing mesh size, thus increasing the number of iterations necessary to reach convergence and, by consequence, also the computing time. This considerably slows down the convergence. In Fig. 3 we show the evolution of the error in the total energy relative to LENTEUR during the iterations for the ^{40}Ca nucleus for different mesh discretizations dx. The most accurate result after 100 iterations is obtained with $dx = 1.0$ fm. Gaining an order of magnitude of accuracy after

TABLE II. Same as Table I, but for the LM + LM option.

	Energy (MeV)				
	$dx = 1.0$ fm	$dx = 0.83$ fm	$dx = 0.71$ fm	$dx = 0.549$ fm	LENTEUR
Kinetic + c.m. correction	3866.323	3866.165	3866.182	3866.182	3866.190
Direct Coulomb	827.922	827.889	827.882	827.878	827.876
Coulomb exchange	−31.269	−31.268	−31.268	−31.268	−31.269
E_{ρ^2}	−22384.936	−22384.188	−22384.322	−22384.320	−22384.379
$E_{\rho\tau}$	1330.300	1330.193	1330.201	1330.200	1330.206
$E_{\rho^{2+\alpha}}$	14537.174	14536.691	14536.789	14536.787	14536.832
$E_{\rho\Delta\rho}$	315.238	315.275	315.284	315.284	315.287
$E_{\rho\nabla J}$	−96.430	−96.444	−96.445	−96.445	−96.445
Total Skyrme energy	−6298.657	−6298.473	−6298.493	−6298.494	−6298.501
Total energy	−1635.678	−1635.687	−1635.696	−1635.700	−1635.703

TABLE III. Edge lengths (in fm) of boxes used to solve self-consistent mean-field equations (L_μ) and to determine the Coulomb potential (C_μ) for nuclei studied in this paper. Depending on the symmetries imposed on the nucleus, only half of of the length is treated numerically in most cases.

Nucleus	$L_x = L_y$	L_z	$C_x = C_y$	C_z
^{40}Ca	26	26	26	26
^{132}Sn	30.8	30.8	46.8	46.8
^{208}Pb	40	40	60	60
$Z \approx 50$	40	40	60	60
^{240}Pu	40	60	80	120

convergence requires carrying out roughly 100 more iterations for the step sizes represented in the figure.

F. Treatment of the long-range Coulomb interaction

The direct Coulomb energy requires a special treatment because of its long range. One of the spatial integrations in Eq. (4) can be eliminated through the calculation of the Coulomb potential of the protons, which satisfies the electrostatic Poisson equation

$$\Delta U(\mathbf{r}) = -4\pi e^2 \rho_p(\mathbf{r}), \tag{22}$$

where e^2 is the square of the elementary charge. When solving this equation, boundary conditions need to be imposed at the edge of the box. These can be easily constructed when recalling that at large distances the potential is entirely determined by the multipoles of the nuclear charge distribution $\langle \hat{Q}_{\ell m} \rangle$. Expanding the Coulomb potential on spherical harmonics and keeping the terms up to $\ell = 2$, the Coulomb potential outside the box is approximated by

$$U(\mathbf{r}) = \frac{e^2 Z}{r} + e^2 \frac{\langle \hat{Q}_{20} \rangle Y_{20}(\mathbf{r}) + \langle \hat{Q}_{22} \rangle \, \mathrm{Re} Y_{22}(\mathbf{r})}{r^3}, \tag{23}$$

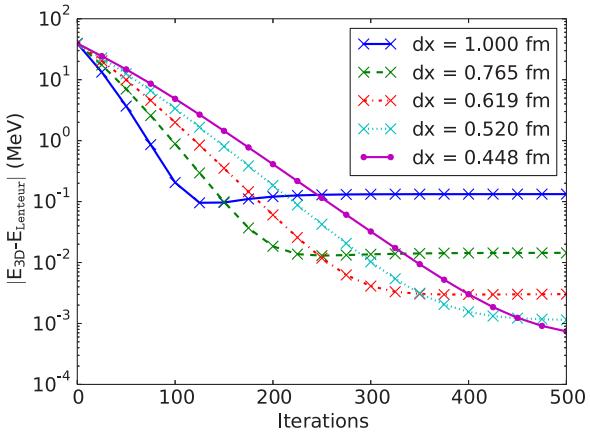

FIG. 3. (Color online) Error in the total energy using the FD + LM option as a function of the number of mean-field iterations for ^{40}Ca for different values of dx. Calculations were initialized with Nilsson-model single-particle wave functions. The box length is 26 fm.

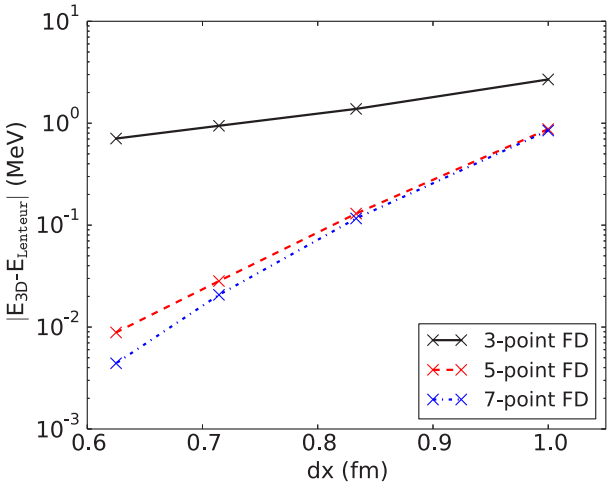

FIG. 4. (Color online) Differences between the total energy of ^{208}Pb calculated on a 3D mesh with different approximations in the calculation of the Coulomb energy and that obtained with LENTEUR. The three lines correspond to the use of three-, five-, and seven-point FD formulas for calculation of the Laplacian in the Poisson equation.

which provides the boundary condition for the numerical solution of Eq. (22). The direct Coulomb energy is then calculated as

$$E^d_{\mathrm{Coul}} = \frac{1}{2} \int d^3r \; U(\mathbf{r}) \, \rho_p(\mathbf{r}). \tag{24}$$

As for the nuclear part of the energy, the accuracy of the electrostatic potential, obtained by solving Eq. (22), is limited by three factors: the size of the box, the mesh discretization length dx, and the way derivatives are calculated.

A suitable box size for the Coulomb problem has to be larger than that for the Skyrme EDF. This is a direct consequence of the long range of the Coulomb force. To make negligible the contributions to the boundary conditions of terms higher than $\ell = 2$ [see Eq. (23)], one has to calculate the Coulomb potential in a box larger than the one used for the nuclear part of the interaction. Typical values are listed in Table III. For light nuclei such as ^{40}Ca, no extra points for Coulomb need to be added, while the box has to be significantly enlarged for heavier systems in the ^{132}Sn and ^{208}Pb regions. For calculation of the fission barrier of heavy nuclei such as ^{240}Pu up to very large deformations, the Coulomb box size has to be two times larger than the one needed for the Skyrme EDF to obtain the same nuclear accuracy in all the energies.

The Laplacian in Eq. (22) has to be approximated on the mesh in such a way that the accuracy of the Coulomb energy is similar to that of the other terms in the EDF. We show in Fig. 4 the gain in accuracy of the total energy of ^{208}Pb obtained by going from a three-point to a seven-point FD formula for the Laplacian. Already a five-point formula provides the required accuracy and is used in all other calculations reported here. One can easily understand that a lower-order FD formula than the one used to calculate the kinetic energy is sufficient for the Laplacian in Eq. (22): the typical length scale of the variation of the Coulomb potential is much larger than the scale on which the wave functions vary.

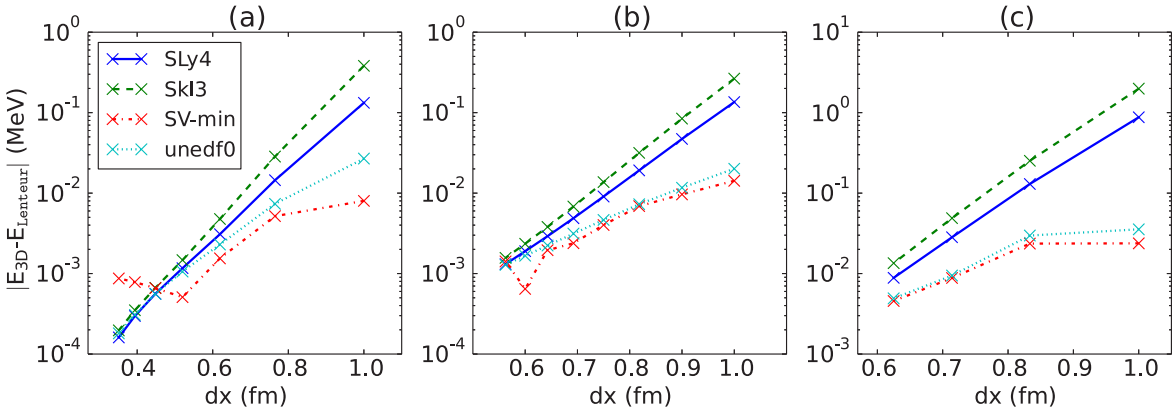

FIG. 5. (Color online) Differences between the total energy calculated with our 3D code and that calculated with the spherical code LENTEUR for ^{40}Ca (a), ^{132}Sn (b), and ^{208}Pb (c), as a function of the mesh distance dx. Results are plotted for a representative set of Skyrme parametrizations, without pairing. Results for SLy5, T22, and T65 are not shown but are indistinguishable from the SLy4 results at the scale of this graph.

The final factor for the accuracy of the Coulomb solution is the mesh discretization length dx. As the effect of the Coulomb term is already incorporated in all of the applications, we do not discuss it separately.

V. DISCUSSION

A. Binding energies

Provided that the box size is large enough, the main factor determining the accuracy of our implementation of mesh calculations is the discretization length. In Fig. 5 the energy difference with respect to LENTEUR results is plotted for three doubly magic spherical nuclei, as a function of the mesh discretization dx for a representative set of Skyrme parametrizations. It is remarkable that the interactions are grouped according to their effective mass (see Appendix A for the actual values): interactions with a larger effective mass m^* give systematically more accurate results than interactions with a smaller mass. This property is related to the term $E_{\rho\tau}$ term of the Skyrme EDF in Eq. (2), which, in our experience, is the least well represented on a mesh. Since the magnitude of this term increases when the effective mass decreases, the accuracy obtained for a given mesh size deteriorates for a lower effective mass.

One can see that the accuracy obtained with a mesh discretization as large as $dx = 1.0$ fm is less than 1.0 MeV for ^{208}Pb. The energy difference decreases to a few hundred keV for $dx = 0.8$ fm and to a few keV for $dx = 0.6$ fm. Note that a similar accuracy for $dx = 0.6$ fm was found for a 2D code based on splines [8]. To obtain an agreement between the spherical code LENTEUR and our 3D codes below the 1-keV level would require increasing the box size but also making the codes more similar. For a nucleus with a binding energy higher than 1 GeV, this implies a relative discrepancy of better than 10^{-7} and there are several sources of differences in the codes that can play a role, none of which is easy to control.

B. Deformation energy curves

Let us now study the convergence properties of our numerical scheme for the fission path of ^{240}Pu. Our motivation is twofold: ^{240}Pu is a frequent benchmark for models that describe fission [39–44] but also for numerical algorithms [8,13]. The energy curve of this nucleus presents two minima at prolate deformations, the ground state and a fission isomer. In Fig. 6, we show the variation of the energy with deformation.

The box used for these calculations has the same size for all discretizations, as indicated in Table III. When the left-right symmetry is broken, the number of points along the z direction is doubled. We have performed calculations with four mesh discretizations, $dx = 1.0$, 0.82, 0.69 and 0.60 fm, and tested the convergence as a function of dx by taking the difference with respect to the results obtained with $dx = 0.6$ fm. For each value of dx, the energy at each deformation is the energy relative to the prolate ground state.

The energy curve obtained with $dx = 0.6$ fm is shown in Fig. 6. The topography obtained for other values of dx is the same. Shapes are triaxial in the vicinity of the first barrier, whereas everywhere else they remain axial. At deformations

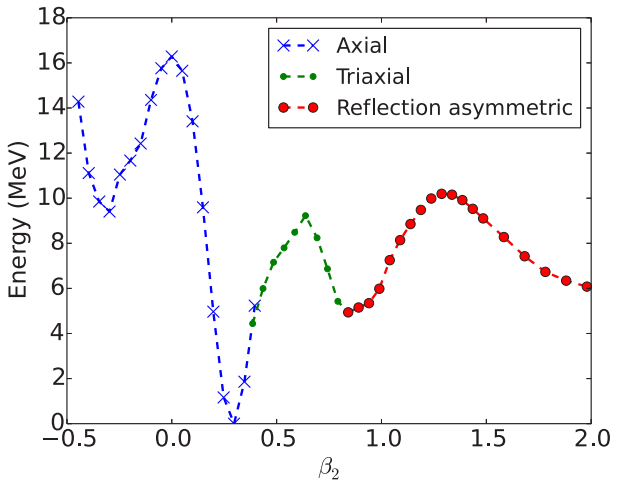

FIG. 6. (Color online) Energy curve for ^{240}Pu calculated with $dx = 0.6$ fm. Regions where the deformation is axial [(blue) crosses], triaxial [small (green) filled circles], or axial and reflection asymmetric [large (red) filled circles] are indicated.

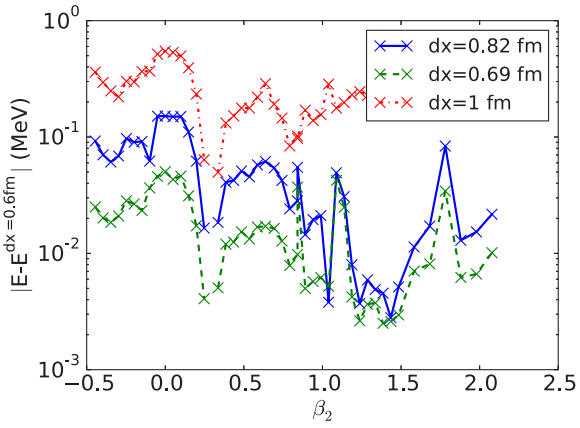

FIG. 7. (Color online) Energy differences between the results obtained for ^{240}Pu with $dx = 1.0$, 0.82, and 0.69 fm and those corresponding to $dx = 0.6$ fm.

smaller than the one of the fission isomer the configurations are reflection symmetric, whereas at larger deformations they are increasingly asymmetric.

We use this curve as a reference to determine the accuracy of the calculations carried out for other values of dx. For each dx, the ground-state energy is taken as the 0 of the energy. The results are shown in Fig. 7. The properties of the minimum are listed in Table IV. The error decreases roughly by an order of magnitude upon going from $dx = 1.0$ to $dx = 0.82$ fm and from $dx = 0.82$ to $dx = 0.69$ fm. At $dx = 1.0$ fm the error is of the order of a few hundred keV, with a rather large oscillation. For a mesh discretization of 0.82 fm, the error becomes lower than 100 keV (except in the vicinity of the spherical configuration, where it reaches 150 keV, but this configuration is very excited) and is quite acceptable for the calculation of energy curves. Decreasing the discretization further, to 0.69 fm, reduces the error to values of a few tens of keV at most.

Some published results allow for a comparison between the accuracy of mesh calculations and that of calculations using an expansion on an HO basis. Pei *et al.* [8] have performed calculations on an axial mesh using B splines and on HO bases, either spherical or deformed, with 20 oscillator shells in both cases. The accuracy obtained in [8] on a mesh of $dx = 0.65$ fm seems very similar to the one we obtain. The use of a spherical HO basis is rather unreliable, with an error larger than 1 MeV already for the excitation energy of the fission isomer and that quickly increases to several MeV at larger deformations. For an axial oscillator basis, the results are similar to those we obtain with a mesh size of 0.82 fm up to the first barrier but the accuracy deteriorates rapidly for larger deformations, being several hundred keV at the deformation corresponding to the fission isomer. Similar results can be found in [46] for ^{194}Hg and in [47] for ^{256}Fm.

As a number of shells significantly larger than 20 is numerically prohibitive, either one has to resort to a two-center oscillator basis or one has to construct a suitable subspace within a much larger one-center HO basis by carefully selecting the low-lying single-particle states. The former option is developed in Ref. [48], whereas the latter has been used during the construction of the unedf1 parametrization [49], where the lowest 1771 basis states of a basis of 50 HO shells have been kept. The accuracy obtained in this way for the excitation energy of the fission isomer is of the order of 100 keV. As a comparison, the experimental excitation energies of the fission isomer found in the literature are 2.4 ± 0.3 MeV [50], approximately 2.8 MeV [51], and 2.25 ± 0.20 MeV [52]. In the light of these error bars, a numerical accuracy of 100 keV is sufficient for the adjustment of an EDF. However, from the published results of Pei *et al.* [8], it can be estimated that the numerical error in the fission barrier height is a few times these 100 keV. Similar results have been obtained in the case of the relativistic mean-field method [13,53].

C. Radial density distribution

The rms radius is intimately linked to the radial density distribution of a nucleus. One can expect that it is particularly sensitive to the box size for nuclei with a large excess of neutrons. Tests have been performed for the very neutron-

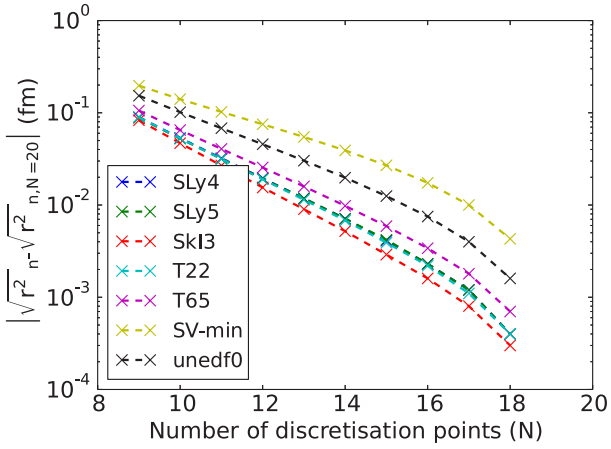

FIG. 8. (Color online) Absolute difference in neutron rms radius for different Skyrme parametrizations for ^{34}Ne at $dx = 0.8$ fm. The reference calculation was performed in a box with $N = 20$.

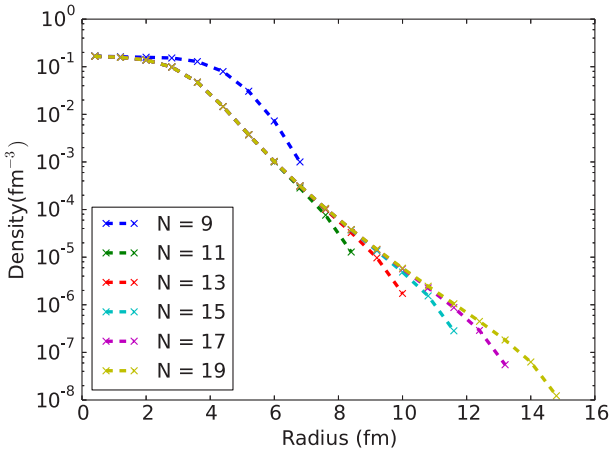

FIG. 9. (Color online) Radial density profile of ^{34}Ne in different box sizes with $dx = 0.8$ fm.

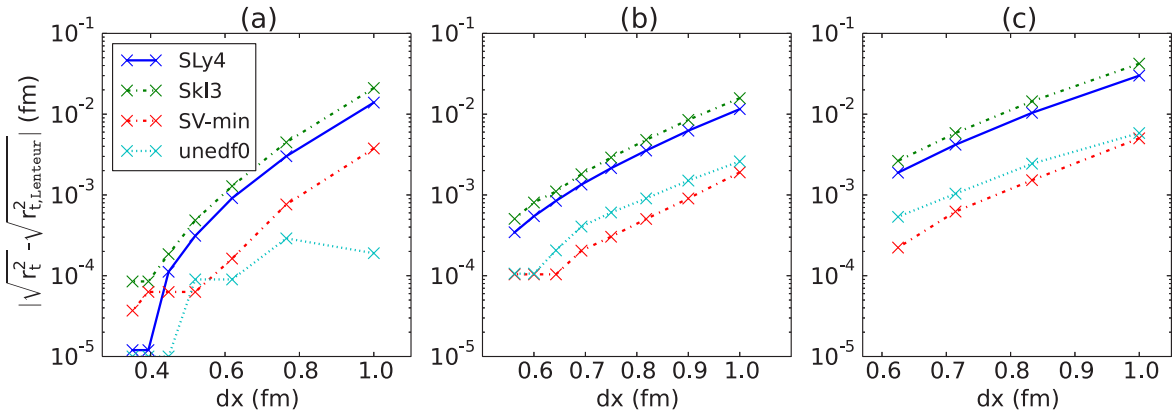

FIG. 10. (Color online) Absolute difference between the total rms radii calculated on a 3D mesh with respect to those of LENTEUR as a function of the step size dx for the spherical nuclei ^{40}Ca (a), ^{132}Sn (b), and ^{208}Pb (c) and those calculated with the Skyrme parametrizations as indicated.

rich nucleus ^{34}Ne by varying the box size for a fixed mesh discretization $dx = 0.8$ fm. To avoid any ambiguity in the calculation, pairing has been omitted. The results are presented in Fig. 8, where we show the difference in total rms radius as a function of the box size for a representative set of EDF parametrizations. For the size of the box recommended for ^{40}Ca in Table III, the number of points is 16 for a mesh size of 0.8 fm. It leads to an error of the order of 10^{-2} fm for most interactions, the results being slightly less accurate for SV-min. For smaller boxes, the accuracy of radii is lower and depends on the interaction.

In Fig. 9 the radial profile of the total density of ^{34}Ne is plotted as a function of the box size. The distortion of the density in the smallest box is large and demonstrates that half the box size must be larger than 8.0 fm. In all other boxes, the exponential tail of the density distribution is well described, up to the point before the last one. For a box size of around 12 fm, the density is well described up to a decrease in the central density by six orders of magnitude.

The confinement in a volume is less evident in an expansion on a basis than in a mesh calculation, but it is also present. While oscillator basis functions extend to infinity, they are in practice strongly localized by their Gaussian form factor. If one takes its classical turning point as a measure of the extension of an HO state, one obtains, for ^{208}Pb and 20 oscillator shells, a value for the turning point that varies from 14 fm for $\ell = 0$ to 16 fm for $\ell = 20\hbar$. To increase the value of this turning point to 20 fm would require using 28 oscillator shells for $\ell = 0$. This effect of confinement by an oscillator basis has been reported in Ref. [54] for the case of ^{112}Zr.

For comparison, the experimental uncertainty in rms charge radii for the Ne isotopes (up to $A = 28$) varies from 0.002 fm close to stability to 0.02 fm for exotic isotopes [55]. It is interesting to note that the numerical accuracy of a mesh mean-field calculation has a similar level (provided the box is large enough) but that the model already introduces uncertainties in the rms radii that are at least one order of magnitude larger [2].

In Fig. 10, we compare the total rms radii calculated with decreasing mesh sizes to those obtained with LENTEUR for three spherical nuclei: ^{40}Ca, ^{132}Sn, and ^{208}Pb. The agreement is already very satisfactory for the large mesh size of 1.0 fm, with one order of magnitude gained in accuracy upon decreasing the mesh size to 0.8 fm, which is the usual value of production calculations. An interesting feature that cannot be deduced from Fig. 10 is that all of the parametrizations, with the exception of unedf0, always produce an rms radius that is smaller than the LENTEUR result.

In Fig. 11, we present the isotopic shifts $\delta r^2(N,Z)$ for a range of even-even Sn nuclei, the reference being ^{132}Sn. All curves almost exactly coincide. This demonstrates that the isotopic shifts are quite reliable even with coarse meshes. Similar results are obtained for Cd, Xe, and Te isotopes.

D. Two-neutron separation energies

To put into evidence changes in nuclear structure with nucleon number, one often uses mass filters that are computed by taking specific differences between the binding energies of neighboring nuclei. The simplest filter is the two-nucleon separation energy, which is defined as the energy difference between two isotopes (or isotones) whose nucleon numbers differ by 2. In Fig. 12, we show the evolution of the

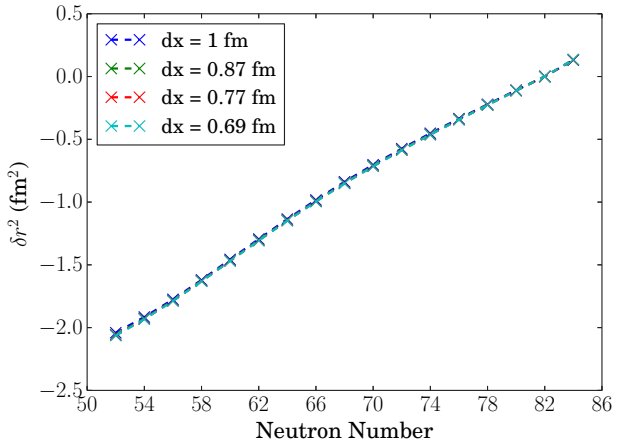

FIG. 11. (Color online) Isotopic shifts $\delta r^2(N,Z)$ with respect to ^{132}Sn for different Sn isotopes and different mesh sizes.

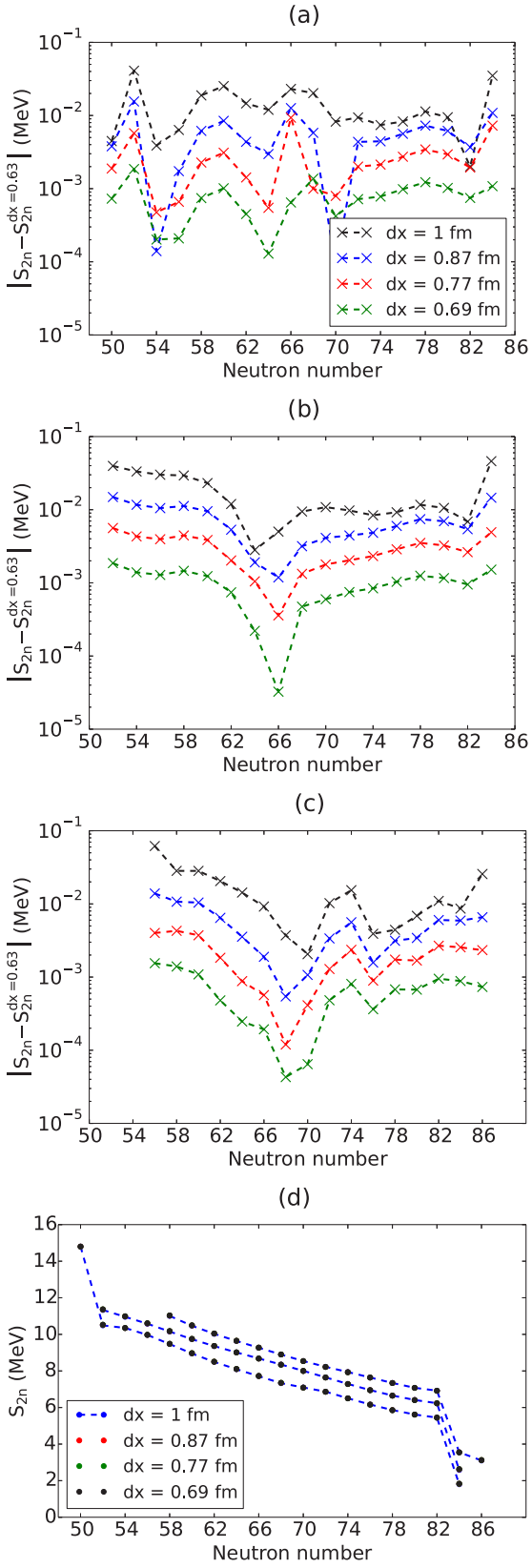

FIG. 12. (Color online) Absolute differences of two-neutron separation energies between four mesh discretizations and a calculation with a mesh size of $dx = 0.63$ fm for Cd (a), Sn (b), and Te (c) isotopes. (d) Plot of the two-neutron separation energies of all of these isotope chains as a reference.

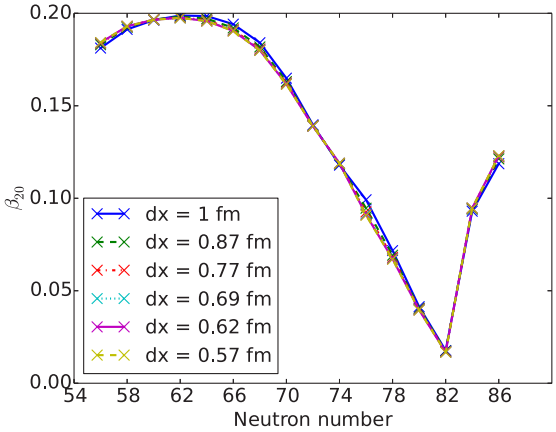

FIG. 13. (Color online) Mass β_2 quadrupole moment as a function of neutron number for a series of Te isotopes.

two-neutron separation energies, S_{2n}, of even-even nuclei for three neighboring isotopic chains when the mesh size dx is decreased. For each discretization dx we have plotted the difference in the S_{2n} values from the one obtained at $dx = 0.63$ fm. Even with a mesh size as large as $dx = 1.0$ fm, the accuracy of the S_{2n} is already better than 100 keV, which is small enough for most applications. The mesh size used in most of our published applications, $dx = 0.8$ fm, leads to an accuracy better than 10 keV. In Fig. 12(d), the two-neutron separation energies of the three isotope chains are plotted for four values of dx. The curves cannot be distinguished using a scale adapted to the variation of S_{2n} as a function of the neutron number. This result is in strong contrast with respect to some published calculations using an expansion on an oscillator basis [56], where special algorithms have to be devised to smooth numerical irregularities, which can be of the order of a few hundred keV.

E. Multipole moments

The dimensionless ground-state quadrupole moments β_2 of even-even Te isotopes are shown in Fig. 13. Differences

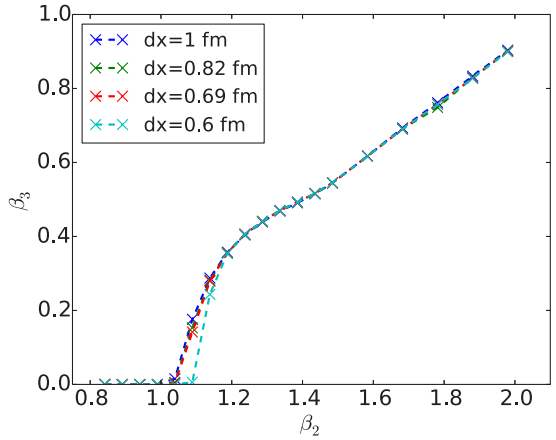

FIG. 14. (Color online) Mass octupole moment β_3 along the fission path for ^{240}Pu.

TABLE IV. Properties of the ground state of ^{240}Pu as obtained from nonconstrained calculations.

dx (fm)	E (MeV)	β_2	β_4	β_6	β_8	β_{10}
1.0	−1801.909	0.288	0.160	0.043	−0.002	−0.003
0.849	−1802.770	0.289	0.163	0.045	0.001	0.001
0.739	−1802.929	0.292	0.164	0.046	0.002	0.002
0.653	−1802.969	0.290	0.165	0.046	0.002	0.001

TABLE V. Properties of the superdeformed fission isomer obtained from nonconstrained calculations.

dx (fm)	E (MeV)	β_2	β_4	β_6	β_8	β_{10}
1.0	−1796.929	0.832	0.494	0.344	0.279	0.255
0.849	−1797.950	0.840	0.510	0.367	0.303	0.278
0.739	−1798.099	0.847	0.528	0.388	0.319	0.268
0.653	−1798.123	0.841	0.516	0.375	0.312	0.259

between the curves corresponding to different values of dx are tiny and not significant. Similar results were obtained for the Cd and Sn isotopes.

We now examine how the multipole moments of ^{240}Pu along the fission path are affected by the mesh size. In Figs. 14 and 15 we show the octupole and hexadecapole moments, respectively, in the region of the fission path where parity is broken. Similar results obtained for the axial and triaxial cases are not shown. In Tables IV and V we list the multipole moments of the ground state and fission isomer of ^{240}Pu for the different mesh discretizations as obtained by unconstrained calculations.

From Figs. 14 and 15 we see that the overall sequence of shapes along the fission path is robust with respect to the mesh spacing. The fission path is already precisely defined at the coarsest mesh ($dx = 1.0$ fm) we used. A single exception can be seen at the onset of octupole deformation; in the vicinity of this point, however, the energy surface is very flat in the β_3 direction.

On a smaller scale, the multipole moments do vary as a function of the mesh discretization. This is clearly shown in Tables IV and V. Since our method hinges on the variation of the total energy in Eq. (1), there is no guarantee that the values of the multipole moments converge in a predictable way. It is, however, reassuring to see that the typical variation of these moments is of the order of a few percent to, at most, about 10%. The larger variations present themselves in the higher-order β_6, β_8, and β_{10} moments. These are more difficult to resolve on coarse meshes because of the high number of nodes their associated Legendre polynomials have.

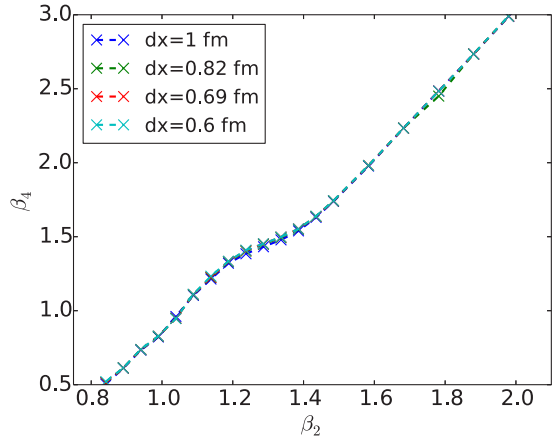

FIG. 15. (Color online) Mass hexadecapole moment β_4 for the parity-breaking configurations along part of the fission path for ^{240}Pu.

F. Single-particle levels

In Fig. 16 we show the evolution of the neutron single-particle levels within 1.5 MeV of the Fermi energy in the ground state of ^{240}Pu as a function of the mesh spacing dx. While slight shifts in the position of the levels are observed as a function of the mesh size, the largest error at $dx = 1.0$ fm is of the order of 100 keV. One can also note that the level ordering within the parity subspaces is the same for all values of dx. A similar dependence on box parameters is found for the proton states and the lighter nuclei studied here.

VI. CONCLUSION

The aim of this paper was to study the numerical accuracy of the solution of self-consistent mean-field equations using a discretization on a 3D Cartesian coordinate-space mesh. Three elements permit control of its numerical accuracy. The first one is the method used to calculate derivatives. Using LM derivatives leads to much more accurate results than using FD formulas for derivatives. In addition, a Cartesian LM corresponds to a representation in a closed subspace of the Hilbert space, such that it always provides an upper bound to the binding energy that becomes tighter when adding points outside a given box or when decreasing the distance of mesh points in a given box. Neither is the case for FD derivatives. However, we have shown quantitatively that the accuracy of a calculation that uses FD formulas during the iterations

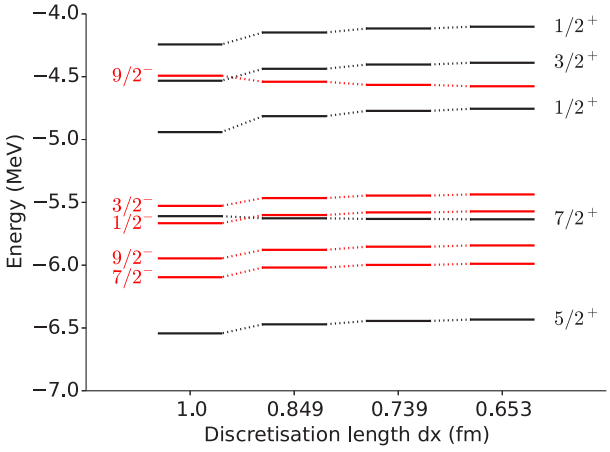

FIG. 16. (Color online) Eigenvalues of the single-particle Hamiltonian for the ground state of ^{240}Pu as a function of the mesh discretization dx. Only neutron single-particle levels within 1.5 MeV of the Fermi energy are shown.

can be significantly improved upon by recalculating the EDF at convergence with LM derivatives. Again, this procedure provides us with an upper bound of the energy, thus restoring the variational character of the calculation. Using Lagrange derivatives during the iterations allows us to improve the accuracy in energies further, but at the cost of at least doubling the computing time.

The second element on which mesh calculations depend is the size of the box in which the nucleus is confined. The examples of doubly magic nuclei and neutron-rich ^{34}Ne illustrate that results for energies and densities are already stable at small box sizes.

The third element is that the quality of the results depends on the mesh size, with errors in energies that are almost independent of the number of neutrons and protons and of the shape of the nucleus. A mesh size $dx = 0.8$ fm guarantees an accuracy that is, in general, better than 100 keV, which corresponds to a relative accuracy of less than 0.1%, even for lighter nuclei. Decreasing the mesh size to 0.7 fm permits one to gain nearly an order of magnitude and to reach an accuracy that is well below all the uncertainties of the mean-field model.

One can summarize these results by concluding that a mesh technique as implemented in our codes is flexible (it can accommodate any kind of symmetry breaking), is robust (the accuracy can be controlled by an adequate choice of the three elements mentioned above), and can be very accurate if necessary. The positive aspect of our numerical scheme is that using a mesh size of 0.8 fm, as used in most of our past applications, ensures an accuracy of better than 100 keV in energies and reliable shape properties for nuclei of any mass.

Our study has focused on the solution of mean-field equations and we have not touched on the description of pairing correlations. There has already been a study of this problem by Terasaki *et al.* [57]. It should be revisited to take into account new developments. However, the problem is not related exclusively to the way the mean-field equations are solved. The description of single-particle states well above the Fermi energy is probably very different when using a discretization on a mesh or an expansion on an oscillator basis.

ACKNOWLEDGMENTS

The authors are grateful to many collaborators who have contributed to the codes used in this work, both with their constructive criticism and, sometimes, with their involvement in coding, in particular, P. Bonche, H. Flocard, J. Meyer, J. Dobaczewski, B. Gall, N. Tajima, J. Terasaki, B. Avez, B. Bally, and V. Hellemans. Special thanks go to K. Bennaceur for providing us with LENTEUR, B. Bally for critically reading the manuscript, and G. Scamps for pointing out a typographical error in the corrigendum to our Ref. [19]. This work was supported in part by the IAP Belgian Science Policy BriX network P7/12, by the European Commission within the 7th Framework Programme through I3-ENSAR (Contract No. RII3-CT-2010-262010).

APPENDIX A: PARAMETRIZATIONS USED

We make some remarks here on the interactions used throughout the text.

TABLE VI. Value of the isoscalar effective mass in units of the nucleon mass m^*/m of the interactions used throughout this paper.

Parametrization	Ref. No.	m^*/m
SLy4 & SLy5	[58]	0.68
T22 & T65	[59]	0.7
SkI3	[60]	0.577
SV-min	[61]	0.95
unedf0	[62]	0.9

(i) SLy4 and SLy5 [58]: These parametrizations were used as intended.
(ii) T22 and T65 [59]: These parametrizations were used as intended.
(iii) unedf0 [62]: While this parametrization was adjusted with a nonzero pairing interaction, we used it without any pairing.
(iv) SV-min [61]: This parametrization was adjusted with unequal nucleon masses $m_n \neq m_p$. LENTEUR does not handle this option, so we used instead the average value $\frac{m_n+m_p}{2}$ as the nucleon mass.
(v) SkI3 [60]: This parameteriation was adjusted with the inclusion of a perturbative two-body c.m. correction, an option not included in LENTEUR.

The values of their isoscalar effective masses are listed in Table VI.

APPENDIX B: PAIRING INTERACTION

The density-dependent pairing interaction we used for the isotope chains and the fission path of ^{240}Pu is defined by [45]

$$\hat{v}^{\text{pair}}(\mathbf{r},\mathbf{r}') = -\frac{V_0}{2}(1-\hat{P}_\sigma)\left[1-\alpha\,\frac{\rho_0(\mathbf{R})}{\rho_s}\right]\delta(\mathbf{r}-\mathbf{r}'), \quad \text{(B1)}$$

where $\rho_0(\boldsymbol{R})$ is the isoscalar density at $\mathbf{R} = \frac{1}{2}(\mathbf{r}+\mathbf{r}')$. The parameters take the values $\alpha = 1$, $\rho_s = 0.16$ fm^{-3}, and $V_0 = 1250$ MeV fm^{-3}. In addition, this interaction was supplemented by two cutoffs, one above and the other below the Fermi energy, in order to eliminate the basis-size dependence of the total energy. They are defined by two Fermi functions,

$$f_k = [1+e^{(\epsilon_k-\lambda_q-\Delta\epsilon_q)/\mu_q}]^{-1/2}[1+e^{(\epsilon_k-\lambda_q+\Delta\epsilon_q)/\mu_q}]^{-1/2}, \quad \text{(B2)}$$

where λ_q is the Fermi energy, ϵ_k is the single-particle energy of the single-particle state k, and we chose $\mu_q = 0.5$ MeV and $\Delta\epsilon_q = 5.0$ MeV for protons and neutrons.

APPENDIX C: ROLE OF THE PHYSICAL CONSTANT WHEN USING SKYRME EDFS

By default, the physical constants used in our calculations are the following [38]:

$$e^2 = 1.43996446 \text{ MeV fm}, \quad \text{(C1)}$$

$$m = \frac{m_n+m_p}{2} = 938.9187125 \text{ MeV } c^{-2}, \quad \text{(C2)}$$

$$\hbar^2/(2m) = 20.735519104 \text{ MeV fm}^2. \quad \text{(C3)}$$

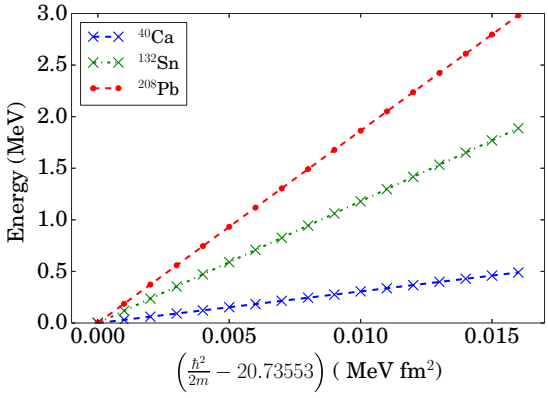

FIG. 17. (Color online) Energy difference for the spherical nuclei ^{40}Ca, ^{132}Sn, and ^{208}Pb for calculations with LENTEUR using SLy4 with a modified value of $\hbar^2/(2m)$. The reference calculation is that obtained using the value used during the adjustment of SLy4.

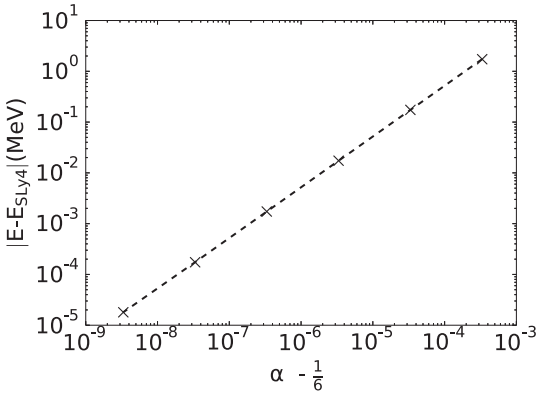

FIG. 18. Difference in the total energy obtained with LENTEUR for ^{40}Ca using a rounded value for the density dependence parameter α in Eq. (2) vs using the full double-precision value $\alpha = 1/6$ of the SLy4 parametrization.

Whenever possible, we have used the value of $\hbar^2/(2m)$ that was used during the adjustment of the parametrization. It might seem superfluous to completely specify the physical constant used, but the results of our calculations depend on the precise values of these constants. In particular, the level of agreement between EV8 and LENTEUR described in Sec. V A is only attainable when these codes use exactly the same numerical values for the physical constants.

In fact, significant errors can be introduced when the values of the physical constants are changed slightly. The seemingly innocuous value of $\hbar^2/(2m)$ in fact plays a very important role. Figure 17 shows LENTEUR calculations for the spherical nuclei ^{40}Ca, ^{132}Sn, and ^{208}Pb with SLy4. Every point was calculated by slightly changing the value of $\hbar^2/(2m)$ from 20.73553 MeV fm^2, the SLy4 value. We see that using a value for $\hbar^2/(2m)$ that is not consistent with the value used during the fit of the EDF can lead to an error of several MeV in the total energy. $\hbar^2/(2m)$ is, after all, the proportionality constant of the kinetic energy in Eq. (1). Typical values that have been used over the years vary at least between 20.73 and 20.7363 MeV fm^2. If the exact values of the physical constants used during the adjustment of a given parametrization are not available, then one cannot reliably compare the results with experimental data. In this case, one cannot judge the predictive power of this parametrization.

Similar concerns arise for the parameters of the Skyrme interactions. The energy obtained in our calculations is more sensitive to some Skyrme parameters than to others, but the close agreement observed in Sec. V A is not obtainable without carefully checking that the Skyrme parameters are completely consistent across codes. That this is not trivial can be concluded from examination of Fig. 18. There we plot the relative difference in energy found by LENTEUR between modified versions of the SLy4 functional and the correct SLy4. The interaction parameters are the same for every point, save for the density dependence parameter α in Eq. (2). There are very few parametrizations for which the value of α corresponds to a terminating decimal, for example, SV-min, for which $\alpha = 0.255368$. For the large majority of parametrizations the value of α is either $1/3$ or, as in the case of SLy4, $1/6$. Both of these correspond to a repeating decimal number, whose numerical representation might differ from code to code. Using $\alpha = 0.1667$ in a calculation with SLy4 corresponds to a rounding error of $\alpha - 1/6 \simeq 3.33 \times 10^{-5}$, which introduces an error in the total binding energy of ^{40}Ca of a few tens of keV.

It is clearly shown that a limited representation of α implies a roundoff error that has a visible effect on the energy. This kind of error shows up when comparing LENTEUR and EV8 results, and for this reason we conclude that relative errors of less than 10^{-5} become meaningless. Similar analyses can be made for the other interaction parameters, including the values of physical constants used to fit the interaction.

[1] M. Bender, P.-H. Heenen, and P.-G. Reinhard, Self-consistent mean-field models for nuclear structure, Rev. Mod. Phys. **75**, 121 (2003).

[2] Y. Gao, J. Dobaczewski, M. Kortelainen, J. Toivanen, and D. Tarpanov, Propagation of uncertainties in the Skyrme energy-density-functional model, Phys. Rev. C **87**, 034324 (2013).

[3] J. Dobaczewski, W. Nazarewicz, and P.-G. Reinhard, Error estimates of theoretical models: A guide, J. Phys. G **41**, 074001 (2014).

[4] D. G. Ireland and W. Nazarewicz, Enhancing the interaction between nuclear experiment and theory through information and statistics (Focus Issue), J. Phys. G **42** (2015).

[5] P. Bonche, H. Flocard, P.-H. Heenen, S. J. Krieger, and M. S. Weiss, Self-consistent study of triaxial deformations: Application to the isotopes of Kr, Sr, Zr and Mo, Nucl. Phys. A **443**, 39 (1985).

[6] J. A. Maruhn, P.-G. Reinhard, P. D. Stevenson, and A. S. Umar, The TDHF code Sky3D, Comp. Phys. Comm. **185**, 2195 (2014).

[7] A. S. Umar and M. R. Strayer, Basis-spline collocation method for the lattice solution of boundary value problems, Comput. Phys. Commun. **63**, 179 (1991).

[8] J. C. Pei, M. V. Stoitsov, G. I. Fann, W. Nazarewicz, N. Schunck, and F. R. Xu, Deformed coordinate-space Hartree-Fock-Bogoliubov approach to weakly bound nuclei and large deformations, Phys. Rev. C **78**, 064306 (2008).

[9] J. C. Pei, G. I. Fann, R. J. Harrison, W. Nazarewicz, Y. Shi, and S. Thornton, Adaptive multi-resolution 3 D Hartree-Fock-Bogoliubov solver for nuclear structure, Phys. Rev. C **90**, 024317 (2014).

[10] D. Baye and P.-H. Heenen, Generalised meshes for quantum mechanical problems, J. Phys. A **19**, 2041 (1986).

[11] H. Imagawa and Y. Hashimoto, Accurate random-phase approximation calculation of low-lying states on a three-dimensional Cartesian mesh, Phys. Rev. C **67**, 037302 (2003).

[12] Y. Hashimoto, Time-dependent Hartree-Fock-Bogoliubov calculations using a Lagrange mesh with the Gogny interaction, Phys. Rev. C **88**, 034307 (2013).

[13] B.-N. Lu, J. Zhao, E.-G. Zhao, and S.-G. Zhou, Multidimensionally-constrained relativistic mean field models and potential energy surfaces of actinide nuclei, Phys. Rev. C **89**, 014323 (2014).

[14] M. V. Stoitsov, J. Dobaczewski, W. Nazarewicz, and P. Ring, Axially deformed solution of the Skyrme-Hartree-Fock-Bogoliubov equations using the transformed harmonic oscillator basis (II) `HFBTHO` v2.00d: A. new version of the program, Comput. Phys. Commun. **167**, 43 (2005).

[15] T. R. Rodríguez, A. Arzhanov, and G. Martínez-Pinedo, Mean-field and beyond-mean-field global calculations with Gogny interactions, Phys. Rev. C **91**, 044315 (2015).

[16] N. Schunck, J. D. McDonnell, J. Sarich, S. M. Wild, and D. Higdom, Error analysis in nuclear density functional theory, J. Phys. G, Nucl. Part. Phys. **42**, 034024 (2015).

[17] R. Rodríguez-Guzmán, J. L. Egido, and L. M. Robledo, Correlations beyond the mean field in magnesium isotopes: Angular momentum projection and configuration mixing, Nucl. Phys. A **709**, 201 (2002).

[18] P. Bonche, H. Flocard, and P.-H. Heenen, Solution of the Skyrme HF + BCS equation on a 3D mesh, Comput. Phys. Commun. **171**, 49 (2005).

[19] W. Ryssens, V. Hellemans, M. Bender, and P.-H. Heenen, Solution of the Skyrme-HF+BCS equation on a 3D mesh. II. A new version of the `Ev8` code, Comput. Phys. Commun. **187**, 175 (2015); **190**, 231(E) (2015).

[20] P. J. Olver, *Introduction to Partial Differential Equations* (Springer, Heidelberg, 2014).

[21] K. Bennaceur, LENTEUR HFB code (unpublished).

[22] A. Bulgac and M. McNeil Forbes, Use of the discrete variable representation basis in nuclear physics, Phys. Rev. C **87**, 051301(R) (2013).

[23] V. Blum, G. Lauritsch, J. A. Maruhn, and P.-G. Reinhard, Comparison of coordinate-space techniques in nuclear mean-field calculations, J. Comput. Phys. **100**, 364 (1992).

[24] K. Rutz, *Struktur von Atomkernen im Relativistic-Mean-Field-Modell*, Doctoral thesis, J. W. Goethe-Universität Frankfurt am Main (Ibidem-Verlag, Stuttgart, 1999).

[25] V. Szalay, Discrete variable representations of differential operators, J. Chem. Phys. **99**, 1978 (1993).

[26] V. Szalay, T. Szidarovszky, G. Czakó, and A. G. Császár, A paradox of grid-based representation techniques: Accurate eigenvalues from inaccurate matrix elements, J. Math. Chem. **50**, 636 (2012).

[27] R. G. Littlejohn, M. Cargo, T. Carrington, K. A. Mitchell, and B. Poirier, A general framework for discrete variable representation basis sets, J. Chem. Phys. **116**, 8691 (2002).

[28] D. Baye, Lagrange-mesh method for quantum mechanical problems, Phys. Status Solidi B **243**, 1095 (2006).

[29] D. Baye, The Lagrange-mesh method, Phys. Rep. **565**, 1 (2015).

[30] R. J. Furnstahl, G. Hagen, and T. Papenbrock, Corrections to nuclear energies and radii in finite oscillator spaces, Phys. Rev. C **86**, 031301(R) (2012).

[31] S. A. Coon, M. I. Avetian, M. K. G. Kruse, U. van Kolck, P. Maris, and J. P. Vary, Convergence properties of *ab initio* calculations of light nuclei in a harmonic oscillator basis, Phys. Rev. C **86**, 054002 (2012).

[32] R. J. Furnstahl, G. Hagen, T. Papenbrock, and K. A. Wendt, Infrared extrapolations for atomic nuclei, J. Phys. G **42**, 034032 (2015).

[33] D. Baye, M. Hesse, and M. Vincke, The unexplained accuracy of the Lagrange-mesh method, Phys. Rev. E **65**, 026701 (2002).

[34] P.-H. Heenen, P. Bonche, J. Dobaczewski, H. Flocard, S. J. Krieger, J. Meyer, J. Skalski, N. Tajima, and M. S. Weiss, in *Proceedings of the International Workshop on 'Nuclear Structure Models', Oak Ridge, Tennessee (U.S.A.), March 1992* (World Scientific, Singapore, 1993), p. 3.

[35] P.-H. Heenen, P. Bonche, J. Dobaczewski, and H. Flocard, Generator-coordinate method for triaxial quadrupole dynamics in Sr isotopes. II. Results for particle-number projected states, Nucl. Phys. A **561**, 367 (1993).

[36] K. T. R. Davies, H. Flocard, S. Krieger, and M. S. Weiss, Application of the imaginary time step method to the solution of the static Hartree-Fock problem, Nucl. Phys. A **342**, 111 (1980).

[37] P.-G. Reinhard and R. Y. Cusson, A comparative study of Hartree-Fock iteration techniques, Nucl. Phys. A **378**, 418 (1982).

[38] P. J. Mohr, B. N. Taylor, and D. B. Newe, CODATA recommended values of the fundamental physical constants: 2010, Rev. Mod. Phys. **84**, 1527 (2012).

[39] H. Flocard, P. Quentin, D. Vautherin, M. Véneroni, and A. K. Kerman, Self-consistent calculation of the fission barrier of ^{240}Pu, Nucl. Phys. A **231**, 176 (1974).

[40] J. F. Berger, M. Girod, and D. Gogny, Microscopic analysis of collective dynamics in low energy fission, Nucl. Phys. A **428**, 23 (1984).

[41] V. Blum, J. A. Maruhn, P.-G. Reinhard, and W. Greiner, The fission barrier of ^{240}Pu in the relativistic mean field theory, Phys. Lett. B **323**, 262 (1994).

[42] K. Rutz, J. A. Maruhn, P.-G. Reinhard, and W. Greiner, Fission barriers and asymmetric ground states in the relativistic mean-field theory, Nucl. Phys. A **590**, 680 (1995).

[43] N. Schunck, D. Duke, H. Carr and, A. Knoll, Description of induced nuclear fission with Skyrme energy functionals: Static potential energy surfaces and fission fragment properties, Phys. Rev. C **90**, 054305 (2014).

[44] W. Younes and D. Gogny, Microscopic calculation of ^{240}Pu scission with a finite-range effective force, Phys. Rev. C **80**, 054313 (2009).

[45] C. Rigollet, P. Bonche, H. Flocard, and P.-H. Heenen, Microscopic study of the properties of identical bands in the $A = 150$ mass region, Phys. Rev. C **59**, 3120 (1999).

[46] T. Nikšić, D. Vretenar, and P. Ring, Beyond the relativistic mean-field approximation: Configuration mixing of angular-momentum-projected wave functions, Phys. Rev. C **73**, 034308 (2006).

[47] M. Warda, J. L. Egido, L. M. Robledo, and K. Pomorski, Self-consistent calculations of fission barriers in the Fm region, Phys. Rev. C **66**, 014310 (2002).

[48] J. Libert, M. Girod, and J.-P. Delaroche, Microscopic descriptions of superdeformed bands with the Gogny force: Configuration mixing calculations in the $A \sim 190$ mass region, Phys. Rev. C **60**, 054301 (1999).

[49] M. Kortelainen, J. McDonnell, W. Nazarewicz, P.-G. Reinhard, J. Sarich, N. Schunck, M. V. Stoitsov, and S. M. Wild, Nuclear energy density optimization: Large deformations, Phys. Rev. C **85**, 024304 (2012).

[50] S. Bjørnholm and J. E. Lynn, The double-humped fission barrier, Rev. Mod. Phys. **52**, 725 (1980).

[51] B. Singh, R. Zywina, and R. Firestone, Table of superdeformed nuclear bands and fission isomers (third edition), Nucl. Data Sheets **97**, 241 (2002).

[52] M. Hunyadi, D. Gassmann, A. Krasznahorkay, D. Habs, P. G. Thirolf, M. Csatlós, Y. Eisermann, T. Faestermann, G. Graw, J. Gulyás, R. Hertenberger, H. J. Maier, Z. Máté, A. Metz, and M. J. Chromik, Excited superdeformed $K = 0^+$ rotational bands in β-vibrational fission resonances of ^{240}Pu, Phys. Lett. B **505**, 27 (2001).

[53] J. Zhao, B.-N. Lu, D. Vretenar, E.-G. Zhao, and S.-G. Zhou, Multidimensionally constrained relativistic mean-field study of triple-humped barriers in actinides, Phys. Rev. C **91**, 014321 (2015).

[54] A. Blazkiewicz, V. E. Oberacker, A. S. Umar, and M. Stoitsov, Coordinate space Hartree-Fock-Bogoliubov calculations for the zirconium isotope chain up to the two-neutron drip line, Phys. Rev. C **71**, 054321 (2005).

[55] I. Angeli, A consistent set of nuclear rms charge radii: Properties of the radius surface $R(N,Z)$, At. Data Nucl. Data Tables **87**, 185 (2004).

[56] S. Goriely, N. Chamel, and J. M. Pearson, HFB mass models for nucleosynthesis applications, J. Korean Phys. Soc. **59**, 2100 (2011).

[57] J. Terasaki, P.-H. Heenen, H. Flocard, and P. Bonche, 3D solution of Hartree-Fock-Bogoliubov equations for drip-line nuclei, Nucl. Phys. A **600**, 371 (1996).

[58] E. Chabanat, P. Bonche, P. Haensel, J. Meyer, and R. Schaeffer, A Skyrme parametrization from subnuclear to neutron star densities. II. Nuclei far from stabilities, Nucl. Phys. A **635**, 231 (1998); **643**, 441(E) (1998).

[59] T. Lesinski, M. Bender, K. Bennaceur, T. Duguet, and J. Meyer, Tensor part of the Skyrme energy density functional: Spherical nuclei, Phys. Rev. C **76**, 014312 (2007).

[60] P.-G. Reinhard and H. Flocard, Nuclear effective forces and isotope shifts, Nucl. Phys. A **584**, 467 (1995).

[61] P. Klüpfel, P.-G. Reinhard, T. J. Bürvenich, and J. A. Maruhn, Variations on a theme by Skyrme: A systematic study of adjustments of model parameters, Phys. Rev. C **79**, 034310 (2009).

[62] M. Kortelainen, T. Lesinski, J. More, W. Nazarewicz, J. Sarich, N. Schunck, M. V. Stoitsov and S. Wild, Nuclear energy density optimization, Phys. Rev. C **82**, 024313 (2010).

Part III

Applications

Chapter 9

Shape transitions of the Radium isotopes

It has been known for a long time [45] that the mean-field minimum of several neutron-rich Radium ($A \geq 220$) isotopes exhibit octupole deformation on the mean-field level. They (and the neighboring even-even nuclei) have garnered considerable theoretical attention, both historically [45, 122] and more recently [43, 123, 44], and can be considered a testing ground for (beyond-)mean-field models featuring octupole degrees of freedom. Experimentally the E3 transition moments of ^{220}Rn and ^{224}Rn were recently measured [6], confirming a stable octupole deformation for the latter. This information is to be joined to the measured E3 transition moments of ^{226}Ra that were measured earlier [124]. A major motivation to experimentally understand octupole deformation in the region is the detection of atomic electric dipole moments to test the Standard Model. Stable octupole deformation would give rise to enhanced nuclear Schiff moments [57, 59], which in turn would enhance any CP-violating effect as discussed in chapter 2.
For all of these reasons, the region is very well suited to perform some proof-of-concept calculations with `MOCCa`, focusing especially on calculations that are not accessible with the ensemble of `ev8`, `cr8` and `ev4`. In particular, this concerns calculations with full HFB pairing when parity is not a self-consistent symmetry, to be compared with either `ev4` which is able to perform HF+BCS calculations with the same symmetries or `cr8` which allows the user to perform HFB calculations but only when conserving parity. The major interest of the HFB pairing ansatz for these nuclei is the extension to time-reversal-broken calculations, such as for rotational bands and odd nuclei in the region. Although for time-reversal conserving calculations of not-too exotic nuclei the difference between HF+BCS and HFB results is not important, even along the entire length of a fission barrier [125, 50], we will consistently use HFB+LN pairing for all the calculations of this chapter. Section 9.1 deals with the details of the calculations, specifically focusing on the choice of the pairing strength. In section 9.3 we will look at the appearance of octupole deformation for the neutron-rich radium isotopes. We will investigate the fission barrier of ^{226}Ra and ^{227}Ra in section 9.4. Finally, we will briefly describe rotational bands in ^{224}Ra and ^{226}Ra in section 9.5.

9.1 Details of the calculations

In order to reduce the CPU time demanded by these calculations, especially for the ones combining parity- and time-reversal breaking, we have opted to use a rather modest mesh with $(N_x, N_y, N_z) = (30, 30, 50)$ using a mesh discretisation of $dx = 1.0$ fm. The large asymmetry in the z-direction was chosen in order to accommodate large deformations in that direction, in order to be able to accurately describe fission paths. All multipole moments up to $\ell = 8$ were added to the boundary conditions of the Poisson problem so no extra points were added to the Coulomb box. This choice of mesh configuration is somewhat more modest than the mesh used to describe the fission of ^{240}Pu in [72] (see chapter 8) and is therefore less accurate. The overall picture however, such as multipole moments and the fission paths are not expected to deviate significantly from a more accurate result. As such this mesh size presents a suitable compromise for a proof-of-concept calculations with `MOCCa`. Any further study however, would probably benefit by taking somewhat larger box sizes and smaller mesh discretisations, comparable to the ones used for ^{240}Pu in [10].
As Skyrme parameterization of choice we have used mainly SLy5s1 [118] (and to lesser extent Sly5S2-7). This choice was mainly motivated by the surface properties of these interactions and the possibility of investigating their influence on the fission path of nuclei in this region.
Pairing was treated on the full HFB+LN level, using the pairing interaction from chapter 3 with $\alpha = 1.0$. This interaction was supplemented by a symmetric Fermi cutoff at a distance of 5 MeV around the Fermi energy. It is important to note that all of the calculations for the odd nuclei were performed using the Thouless method[1].

[1] This proved to be an invaluable tool in the region to converge the calculations. Direct diagonalisation often had problems to converge specific choices of quasiparticle excitations when parity was broken due to the sheer number of quasiparticle levels with identical quantum numbers.

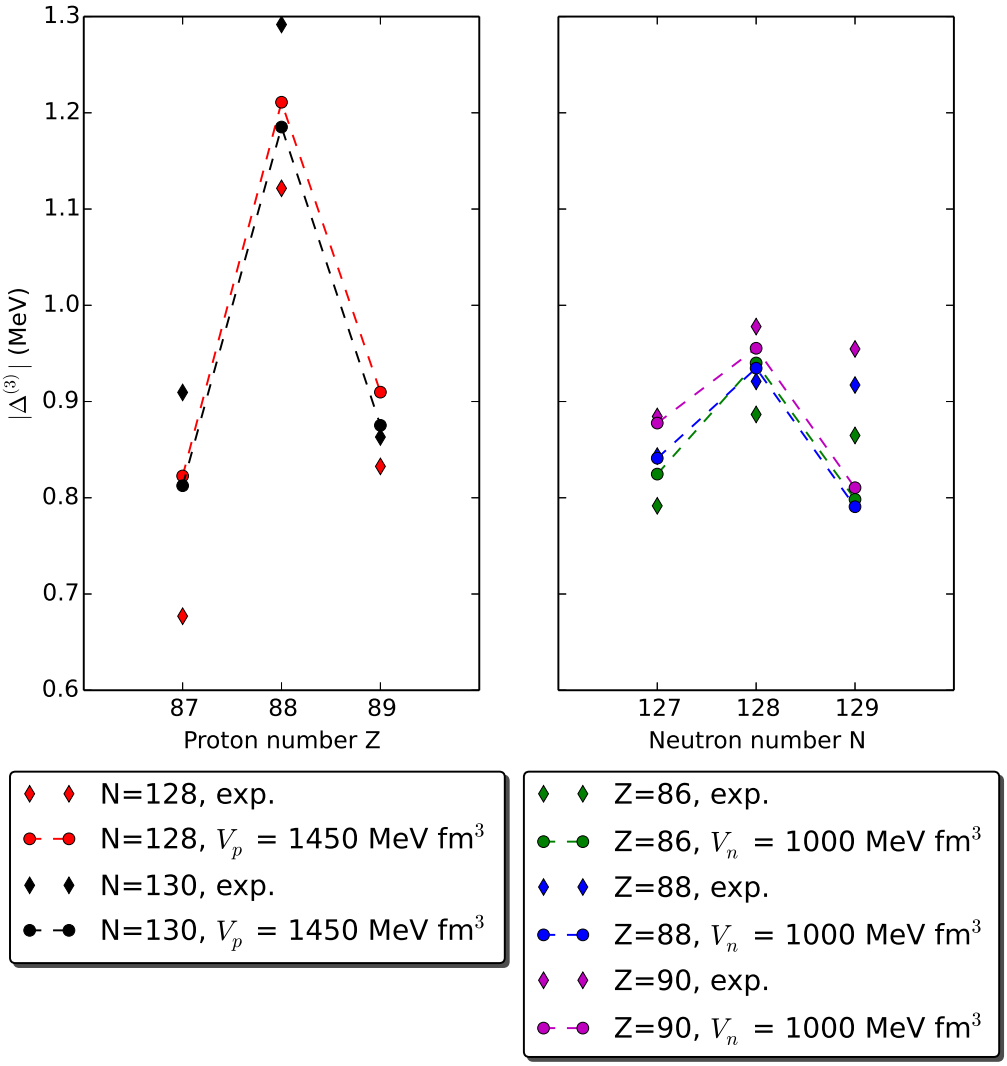

Figure 9.1: Absolute values of the three-point proton and neutron gaps around ^{216}Ra, using the SLy5s1 parameterization with full HFB+LN pairing with $V_n = 1000$ MeV fm^3 and $V_p = 1450$ MeV fm^3. Nuclei included in the calculation are ^{214,215,216,217,218}Ra, ^{213,215,217}Fr, ^{212,213,214,215,216}Rn , ^{215,217,219}Ac and ^{216,217,218,219,220}Th. Circles indicate calculated values, diamonds experimental values taken from [126].

Since the SLy5sX parameterizations were not adjusted with the inclusion of pairing, the pairing strengths V_n, V_p are in principle free parameters. They were fixed by adjusting the pairing strength to the three-point gaps in the region around ^{216}Ra. We used the following definitions for the proton and neutron three-point gaps [127, 128]

$$\begin{aligned} \Delta_n^{(3)}(N,Z) &= \frac{(-1)^N}{2}\left[E(N-1,Z)+E(N+1,Z)-2E(N,Z)\right] , \\ \Delta_p^{(3)}(N,Z) &= \frac{(-1)^Z}{2}\left[E(N,Z-1)+E(N,Z+1)-2E(N,Z)\right] . \end{aligned} \tag{9.1}$$

where $E(N,Z)$ is the binding energy of the nucleus with N neutrons and Z protons. The quasiparticles blocked in the calculations for the even-odd isotopes were chosen to match as well as possible the experimental ground state.[2].

The choice of the vicinity of ^{216}Ra was made for mainly practical reasons. The first is that the nuclei are close to the magic number for neutrons $N = 126$, and are thus (close to) spherical. This avoids any ambiguity in making a choice among different mean-field minima. Secondly, the even-odd nuclei in the region, exhibit

[2]Although, using the Thouless method for blocking them guarantees nothing about the nature of the blocked quasiparticles after convergence except for conserved quantum numbers, in this case parity and z-signature only.

$J = \frac{9}{2}$ ground states. For the neutron-odd nuclei ^{215,217}Ra and ^{213,215,217}Rn, this is a $\frac{9}{2}^+$ ground state while for the proton-odd nuclei ^{213,215,217}Fr, ^{215,217,219}Ac this is a $\frac{9}{2}^-$ ground state. These states are more easily identified than states of lower J in MOCCa, as they will stay significantly more pure than states of lower J. Thirdly, octupole correlations are not expected to be important (on a mean-field level) in these lighter isotopes, meaning that the calculations could conserve parity. This again significantly helps with the identification of the quasiparticles for the odd nuclei, as we can use the parity quantum number to identify quasiparticles.
These considerations are especially valid when doing calculations with the direct diagonalisation method. For the Thouless method as used here, the situation is more subtle. While these arguments help to identify the initial quasiparticle to be blocked, they do not tell us anything about the nature of the quasiparticle after self-consistency has been achieved. To this end the parity conservation for these calculations is valuable: it guarantees correct parity at convergence. No such guarantee is possible for the angular momentum however. Nevertheless, we checked that the odd configurations calculated by MOCCa are all consistent with $\frac{9}{2}$ ground states.
The adjusted values (to a precision of 50 MeV fm^3) used for V_n and V_p were

$$(V_n, V_p) = (1000, 1450) \text{ MeV fm}^3 . \tag{9.2}$$

The three-point proton gaps for these values for $N = 128$ and $N = 130$ are shown on the left side of Fig. 9.1 while the three-point neutron gaps for $Z = 86$ and $Z = 88$ and $Z = 90$ are shown on the right side. Experimental data were taken from the NNDC compilation [126].
For the proton gaps, the agreement is good, though not spectacular. The value $V_p = 1450$ MeV fm^3 corresponds to a compromise between the gap of ^{216}Ra and ^{218}Ra. Increasing the proton pairing strength might lead to a better agreement for ^{218}Ra but a worse agreement for ^{216}Ra, and vice versa with a smaller pairing strength. The value of the neutron pairing strength corresponds to the three-point gap of ^{216}Ra and slightly overshoots the gap in ^{214}Rn while undershooting the gap of ^{218}Th. The agreement with experiment for $N = 128$ is stunningly good, while for $N = 129$ the gaps are all significantly less in agreement with experiment, especially for ^{220}Th. It is not clear what the source of the mismatch between theory and experiment is here, as the pairing gaps are an intricate interplay of the Skyrme parameterization and our specific choice of pairing interaction.
The neutron and proton pairing strengths are somewhat small compared to the ones recently used to study nuclei in the Nobelium region [79]. The difference can likely be attributed to the absence of Lipkin-Nogami treatment in [79]. The proton pairing strength however, is significantly larger than the one used to describe very heavy nuclei in past publications [3], while the neutron strength is rather smaller. In a perfect world, the proton pairing strength should be less strong than the neutron pairing strength, since the pairing effect of the Coulomb force is not included in our calculations. This asymmetry is due to the form of the pairing interaction in Eq. 3.43 as discussed in [129]. When $\alpha = 1.0$, the pairing has a surface character, but the proton density at the surface of the nucleus is significantly smaller compared to the neutron density, simply because of the neutron number is larger than the proton number. A term in the pairing interaction dependent on isovector density ρ_1 would alleviate this problem [129].

9.2 Quadrupole deformation

A first quantity that is accessible to MOCCa, without breaking any symmetries of the $\mathcal{D}_{2h}^T$ group, is the deformation energy surface as a function of quadrupole deformation. Fig. 9.2 shows the energy surface of the isotopes ^{216}Ra,^{218}Ra,^{220}Ra,^{222}Ra,^{224}Ra and ^{226}Ra using the SLy5s1 parameterization. Note that the configurations are all axial and no triaxial degrees of freedom were taken into account.
The development from spherical configuration is the first phase transition of these isotopes: ^{216}Ra is clearly spherical, with a very flat energy surface directly surrounding the minimum. From ^{218}Ra onwards an increasingly pronounce prolate minimum develops at ever increasing values of β_2. A similar oblate minimum at comparable absolute values of β_{20} develops, but remains shallow for all isotopes. Several other minima develop with increasing mass. On the oblate side a shallow minimum forms that can be found at systematically higher absolute values of β_{20} and from ^{222}Ra is joined by a second shallow oblate minimum. The situation is different on the prolate side, where for all of the isotopes considered a shallow second prolate minimum at $\beta_{20} \approx 0.6$ can be seen. Beyond the barrier, the energy surface is very flat, in particular for ^{226}Ra.

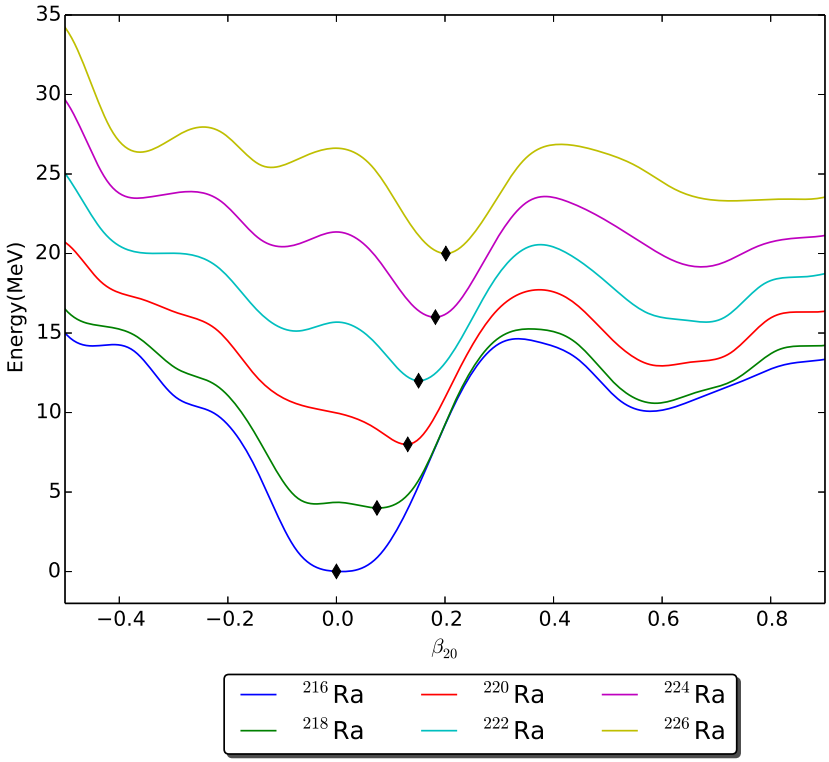

Figure 9.2: Energy surface of the even isotopes ^{216}Ra,^{218}Ra,^{220}Ra,^{222}Ra,^{224}Ra and ^{226}Ra with the SLy5s1 parameterization as a function of quadrupole deformation β_{20}, where positive values of β_{20} correspond to prolate configurations and negative values to oblate configurations with the same absolute value of β_{20}. The minima are indicated by black diamonds.

9.3 Octupole deformation

As was indicated before, octupole degrees of freedom are very relevant in the region. Fig. 9.3 shows the energy surface as a function of quadrupole deformation parameter β_{20} and the octupole deformation parameter β_{30} for the even-even Radium isotopes from $A = 216$ to $A = 226$. Every surface is symmetric about $\beta_{30} = 0$, as changing the direction of the z-axis for a given nuclear density changes the sign of β_{30}. Note that this type of plot is outside of the range of both `ev4` and `cr8`, as the calculation combines the HFB+LN pairing treatment with parity breaking.

This is the second shape transition in the region: ^{216}Ra is spherical, while the minimum of ^{218}Ra develops a lightly octupole deformed ground state. As the mass increases, the minimum becomes more and more octupole deformed at $\beta_{30} \approx 0.14$. The features of the parity-conserving calculation from the previous section are also clearly visible for all isotopes: the axial prolate minimum from the previous section becomes a saddle-point. It is interesting to see that on the oblate side octupole degrees of freedom do not lower the energy and the minimum does not become a saddle-point. The densities of the prolate saddle point and the global minimum for ^{226}Ra are shown in Fig. 9.4.

The deformation energy surfaces compare very well with the energy surface of ^{228}Th (two protons more) in [44]. The calculations therein were performed using the relativistic energy density functional DD-PC1 with HFB pairing. The prolate minimum is located at very comparable quadrupole and octupole deformation. No oblate axial minimum is visible for their figure of ^{228}Th, but it might simply be located at β_{20} values that are located beyond the limits of the figure. The surface of ^{222}Ra is also in good qualitative agreement with the original result of [45], which was calculated on a comparable Lagrange mesh with $dx = 1.0$ fm, although in the HF+BCS approximation with a constant gap pairing interaction and the SIII Skyrme parameterization.

The non-axial quadrupole deformation parameter β_{22} is not explored in Fig. 9.3 and was found not to lower the energy of the minimum: the prolate, octupole deformed minimum is still the global minimum. It can however play a role in lowering the axial barrier in the lower right of each every surface, as we will see in the next section for ^{226}Ra. The non-axial octupole deformation degree of freedom β_{32} was free to take non-zero values but did not lower the energy on any point of the energy surface.

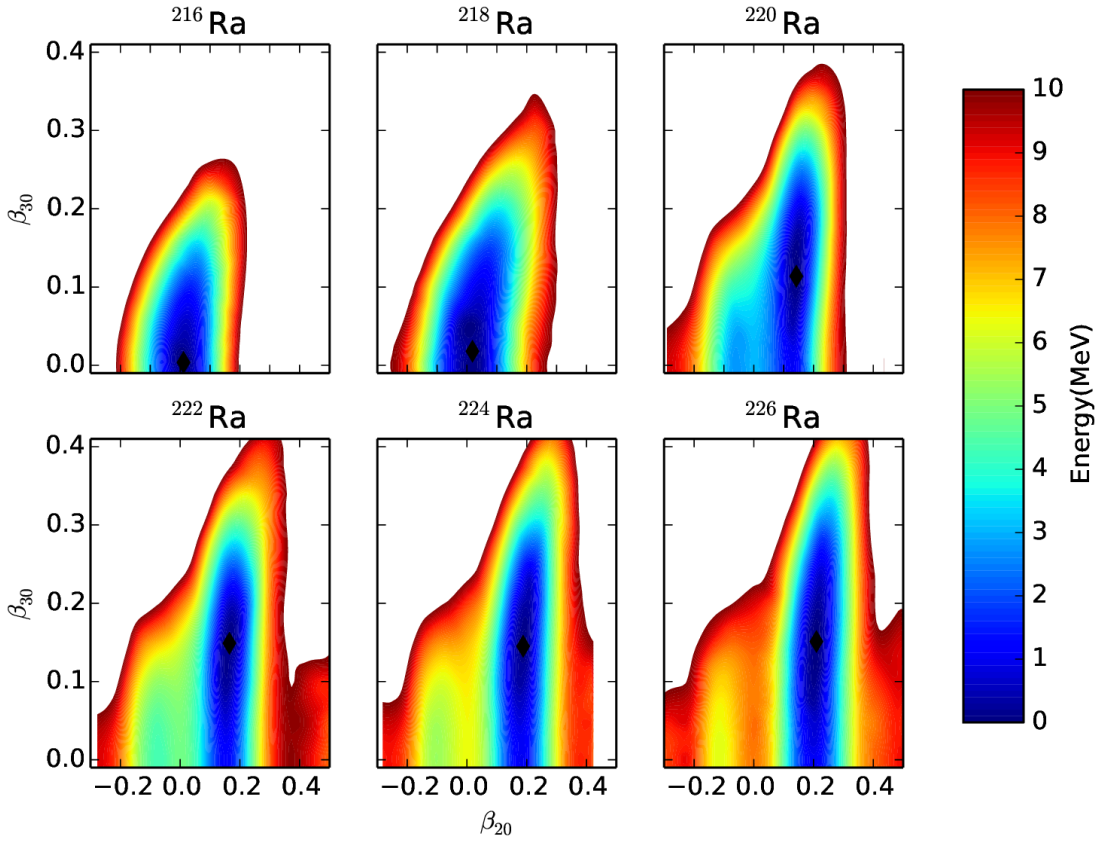

Figure 9.3: Energy of axial mean-field configurations as a function of β_{20} and β_{30} for ^{216}Ra, ^{218}Ra, ^{220}Ra, ^{222}Ra, ^{224} and ^{226}Ra calculated using the SLy5s1 Skyrme parameterization. The global minimum is marked with a black diamond. The energies are all with respect to this minimum.

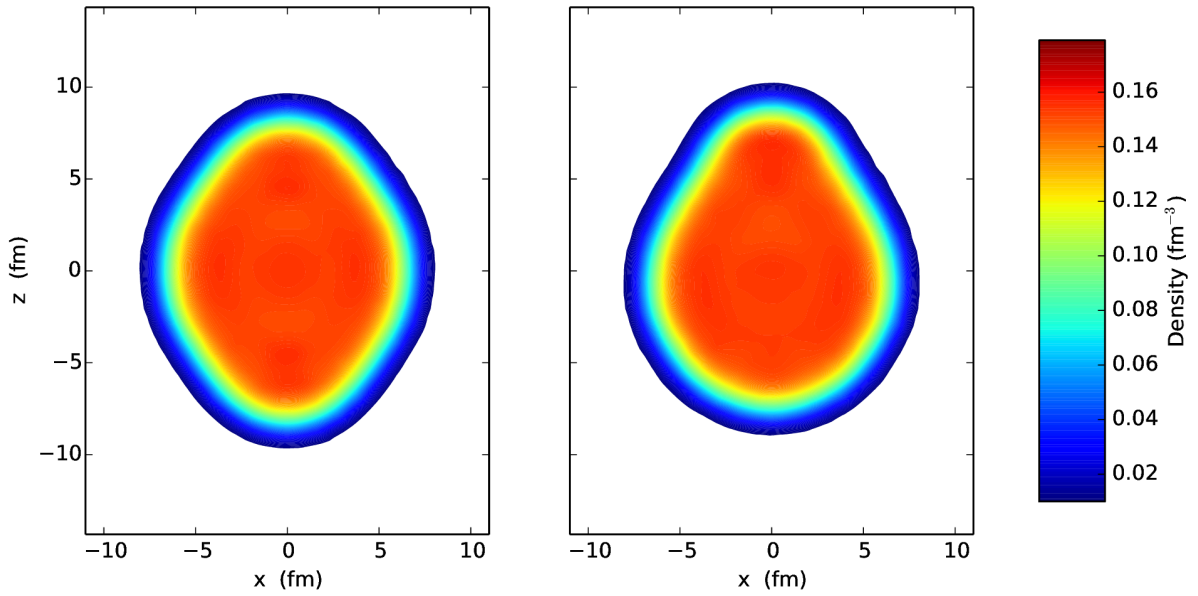

Figure 9.4: Density contours along the x- and z-axes for the respectively the axial prolate saddle-point and the octupole deformed minimum of ^{226}Ra.

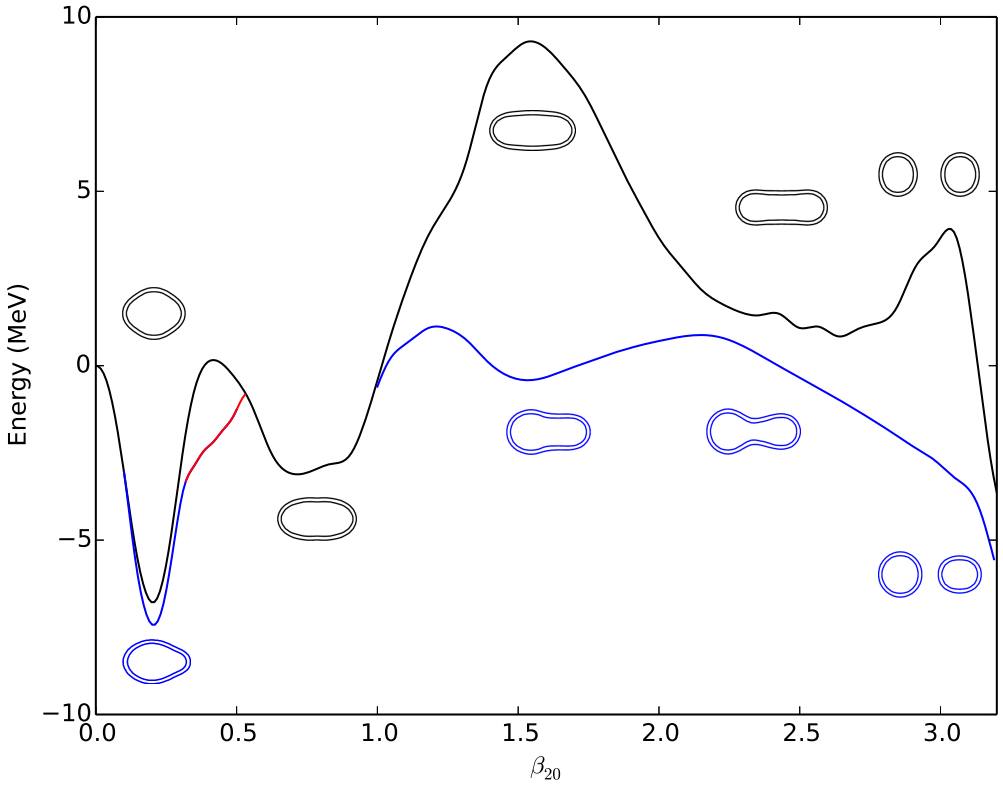

Figure 9.5: Fission barrier of ^{226}Ra as a function of β_{20} for axial, parity conserving (black), triaxial, parity conserving (red) and axial, parity breaking (blue) configurations for the SLy5s1 parameterization. Energy is relative to the spherical configuration. Density contour plots (along the y-axis) indicate the type of deformation at particular points on the curve.

9.4 Fission

Energy density functionals theory offers a fully microscopic model for the study of fission properties over the entire range of the nuclear chart [50]. Using constraints on collective parameters such as the multipole moments, one can generate fission barriers as a function of these collective parameters. The main quantity to be extracted from the calculations is the height of the fission barrier, which can be related to fission half-lives through a variety of models chief among which is the WKB approximation for transmission probabilities [130, 50]. We will not endeavour to compare in detail with experiment, as we are mainly interested in demonstrating the possibilities of `MOCCa`. In particular, we will use $\langle \hat{Q}_{20} \rangle$ as a collective coordinate[3] to study the fission barriers of ^{226}Ra and ^{227}Ra using the SLy5s1 parameterization. We will only briefly compare barrier heights to the RIPL-3 [131] recommended values.

9.4.1 Fission of ^{226}Ra

The fission path, as a function of the deformation parameter β_{20}, is shown in Fig. 9.5 for the SLy5s1 parameterization with HFB+LN pairing as described before. The different colors represent calculations with a different set of imposed symmetries: the black curve is calculated while imposing both axial and reflection (parity) symmetry. The red curve corresponds to lower solutions that are found around the first barrier when relaxing the constraint on axial symmetry. All of these conserve parity. The blue curve indicates lower solutions that are found when relaxing parity. Density contours in the x-z plane are included along the barrier to give the reader a visual representation of the type of shapes encountered.
The absolute minimum found at $\beta_{20} \approx 0.2$ is octupole deformed, a particularity of nuclei in this mass region, while the parity-conserving minimum of the black curve is actually a saddle point. These minima are the configurations for which Fig. 9.4 shows the density distribution in the x-z plane. However, the energy surface

[3] This is the most traditional choice, but certainly not the only possible one as both the octupole and hexadecupole multipole moments as well as so called neck-operators can be used [50].

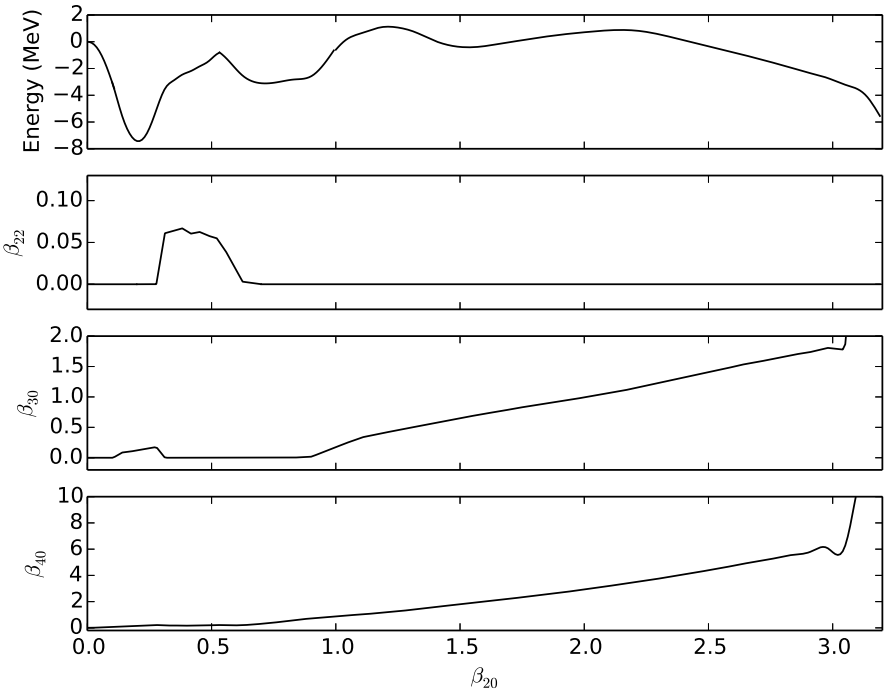

Figure 9.6: Energy, β_{22}, β_{30} and β_{40} along the fission barrier of ^{226}Ra as a function of β_{20}. The SLy5s1 parameterization was used together with HFB+LN pairing. Energy is relative to the spherical configuration.

is rather flat in this region and octupole deformation lowers the energy by slightly more than one MeV. At the first barrier at $\beta_{20} \approx 0.4$ ^{226}Ra, gradually loses its octupole deformation. Nevertheless, as mentioned before, triaxial degrees of freedom significantly lower the barrier height. The configuration corresponding to the broad second minimum at $\beta_{20} \approx 0.7$ takes an axial and parity conserving shape. If octupole deformations are not allowed at larger deformations, one finds a broad and very high second barrier around $\beta_{20} \approx 1.5$ that is followed by a third barrier at about $\beta_{20} \approx 3.0$ before the calculation jumps to a solution with two separate identical fragments. The two outer barriers are substantially lowered when allowing reflection asymmetric shapes as indicated by the blue path in Fig. 9.5 . The resulting height of the asymmetric barrier of 8.55 MeV agrees well with the experimental value of 8.5 MeV as reported in the RIPL-3 database [131]. This fission path leads to an asymmetric split-up, with the larger fragment being near-spherical and the smaller one remaining deformed. We have not found any solution that is non-axial with finite octupole moments, as was recently reported for actinide nuclei in [49, 132, 133]. All calculations initialized with such shapes converged to states for which one or the other of these symmetries is reestablished.

It is interesting to compare to previous results of [104], obtained within the framework of relativistic mean-field theory and incorporating HF+BCS pairing. Note that the older calculation does not include triaxial degrees of freedom. Both calculations are in rather good qualitative agreement obtaining minima at comparable quadrupole and octupole deformations. One notable difference is the alternative branch along the symmetric fission path reported in [104], differing mainly in hexadecapole deformations, that we have not found. A second difference concerns the relative energy of the symmetric and asymmetric fission paths at large deformations ($\beta_{20} \approx 2.5$): while the asymmetric path is preferred by the calculation shown here, the symmetric path is favoured in [104] in a small deformation region before the onset of the third barrier. These differences between the energy landscapes can be attributed to slight differences in the properties of the effective interactions used in both cases, in particular concerning shell structure and its change with deformation. There is however no fundamental difference between both approaches.

Note that it cannot be assumed that the symmetry restricted energy curve (the black line in Fig. 9.5) corresponds to a physical fission path with higher symmetries, i.e. that it is a local minimum in all non-constrained multipole degrees of freedom. In general, only the much more time-consuming calculation of a multi-dimensional energy surface can answer this question. Similarly, multi-dimensional calculations are sometimes needed to find the correct height of saddle points when the calculated fission path jumps from one valley to another, which is signaled by discontinuities in the non-constrained multipole moments. The calculation of deformation energy curves as presented here, however, is sufficient to analyze the overall

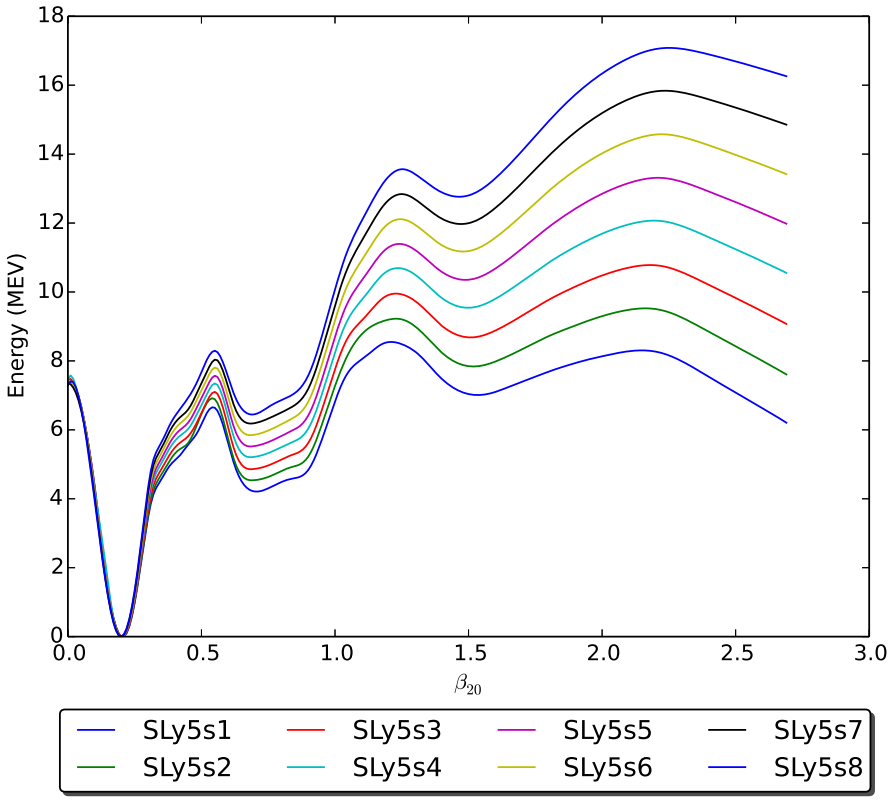

Figure 9.7: Fission barrier of ^{226}Ra as a function of β_{20} for the SLy5sX functionals with $X = 1, \ldots, 8$ with HFB+LN pairing. Energy is relative to minimum of the deformation surface.

structure of a fission barrier and to identify the relevant shape degrees of freedom for such more detailed studies. Such multi-dimensional studies are planned for the near future, and `MOCCa` is already capable carry them out.

9.4.2 Influence of the surface properties of the SLy5sX functionals

For the excellent reproduction of the barrier height of ^{226}Ra reported above it is not sufficient to have numerical codes that cover all relevant degrees of freedom. First and foremost it requires a properly fine-tuned parameterization of the energy density functional. As already mentioned, the SLy5s1 parameterization is one out of a series of eight fits that differ in the value of their surface energy coefficient a_{surf} [118]. This quantity provides a measure of the surface tension of symmetric nuclear matter. While the complex topography of an energy surface such as the one displayed in Fig. 9.5 is determined by changes of shell structure with deformation, the surface tension provides the smooth backdrop on which these shell effects generate valleys and ridges. In a simple liquid-drop picture of the nucleus, deforming a spherical nucleus leads to an energy loss that equals a_{surf} times the change of the nucleus' surface. The balance of this effect with the gain in energy from reducing the Coulomb repulsion by deforming the nucleus then leads to a broad singly-humped macroscopic barrier. The systematic variation of a_{surf} in steps of 0.2 MeV provided by the SLy5sX family of fits can be used to illustrate the interplay of these microscopic and macroscopic effects.
Figure 9.7 shows the deformation energy curve of ^{226}Ra for all eight parameterizations from the SLy5sX series. Pairing correlations are treated as before for all of them. Strikingly, all curves have the same overall shape, which indicates that the shell effects do not significantly change when going from one parameterization to another. This is also corroborated by the fission path being the same for all parameterizations: all multipole deformations of degree $\ell = 2$, 3, and 4 are virtually identical along the entire energy curve. What does dramatically change is the overall slope of the energy curves. Indeed, with increasing deformation the contribution of the surface energy grows quickly, such that, when going from the energy curve obtained for SLy5s1 to the one for SLy5s8, each is systematically higher than the previous one. Comparing the two extremes, SLy5s1 and SLy5s8, the height of the first barrier is already affected at a level of 1.5 MeV, while the excitation energy of the second minimum increases by about 3 MeV. Even more dramatically, the height

Functional	Barrier height(MeV)	Barrier location β_{20}
SLy5s1	8.552	1.21
SLy5s2	9.527	2.16
SLy5s3	10.771	2.18
SLy5s4	12.300	2.20
SLy5s5	13.288	2.21
SLy5s6	14.553	2.22
SLy5s7	15.805	2.24
SLy5s8	17.052	2.25

Table 9.1: Highest energy and its location along the fission barrier for the SLy5sX functionals. These were obtained by a cubic spline interpolation starting from the calculated points.

of the second barrier grows by about 6 MeV, and the third barrier by even more than 9 MeV. Most strikingly, the third barrier, relatively unpronounced for SLy5s1, becomes the dominant one for the other fits as its height increases much more quickly with a_{surf} than the one of the second barrier, see Table 9.1.
The same qualitative and quantitative variation of barrier heights and excitation energies of shape isomers is also found in similar calculations for other nuclei [118], indicating that the surface tension of SLy5s1 is more realistic than the one of the other fits from the same series when, as done here, one aims at mean-field calculations of energy surfaces without any quantum corrections related to deformation degrees of freedom. The most relevant one of these for the present discussion is projection of angular momentum, either exactly in a multi-reference framework [134], or in an approximate way through a rotational correction. Its effect tends to increase with deformation [3]. In order to reproduce data, calculations with such correction require parameterizations with larger surface tension than calculations without it. Thus, the possibility of achieving a parameter fit of an EDF that describes fission barriers at any level of modeling is very unlikely. Still, with the protocol suggested in [118] it is possible to construct parameterizations with controlled surface properties that can be adapted to the context of their use without any difficulty.

9.4.3 Fission of ^{227}Ra

MOCCa now opens the way to a complete new realm of describing fission processes: the application to even-odd systems such as ^{227}Ra. To the best of my knowledge there is currently no published result available on the mean-field fission barriers of systems that break time-reversal invariance, especially in combination with the breaking of reflection and axial symmetry. Ref. [135] reported axially-symmetric, reflection-asymmetric calculations for ^{235}U, but employed the equal-filling approximation, effectively approximating the even-odd nucleus by a time-reversal invariant mean-field state, similar in concept to a false vacuum. Ref. [136] reported calculations for several actinide nuclei in the region, also employing the equal-filling approximation and assuming axial symmetry.
The fission barrier of ^{227}Ra is shown in Fig. 9.8. The red and blue lines correspond to axial configurations with conserved parity, with a blocked quasiparticle with respectively positive and negative parity. The black line corresponds to configuration that are no longer limited by axial symmetry and parity. The overall structure of the fission barrier is identical to the one of ^{226}Ra. Octupole deformation is important for the minimum, as well at the onset of the second barrier. Triaxiality is important in lowering the first barrier significantly. Note that the barrier height when breaking parity is 8.1 MeV, in rather good agreement with the RIPL-3 recommended value [131] of 8.2 MeV.
It is interesting to look at the projection of the angular momentum along the symmetry axis for the axial calculation. For most of the curve, the positive parity quasiparticle has $K^\pi = \frac{1}{2}^+$ while the negative parity quasiparticle has $K^\pi = \frac{1}{2}^-$. This is however not true for the entirety of the curve: the Thouless method in principle conserves the quantum numbers of the quasiparticle and we should be able to follow one particular value of K along the entirety of the curve. This is difficult in practice however, as no representation on a 3D mesh is ever truly axial and mixing of K values can build up during the iterations, especially when using predictor-corrector constraints, since their use implies solving the pairing equations twice per mean-field iteration. More experience with the Thouless method is needed to better control this numerical problem.[4]. While we therefore refrain from making any strong statement on the K of the blocked quasiparticles, it is

[4]Note that the direct diagonalisation suffers less from this defect since this method selects a quasiparticle at every mean-field iteration thereby inhibiting mixing between different K, while the Thouless method only selects a quasiparticle at the start of the iterations and small triaxial contributions to the mean-field potentials can slowly mix different K values.

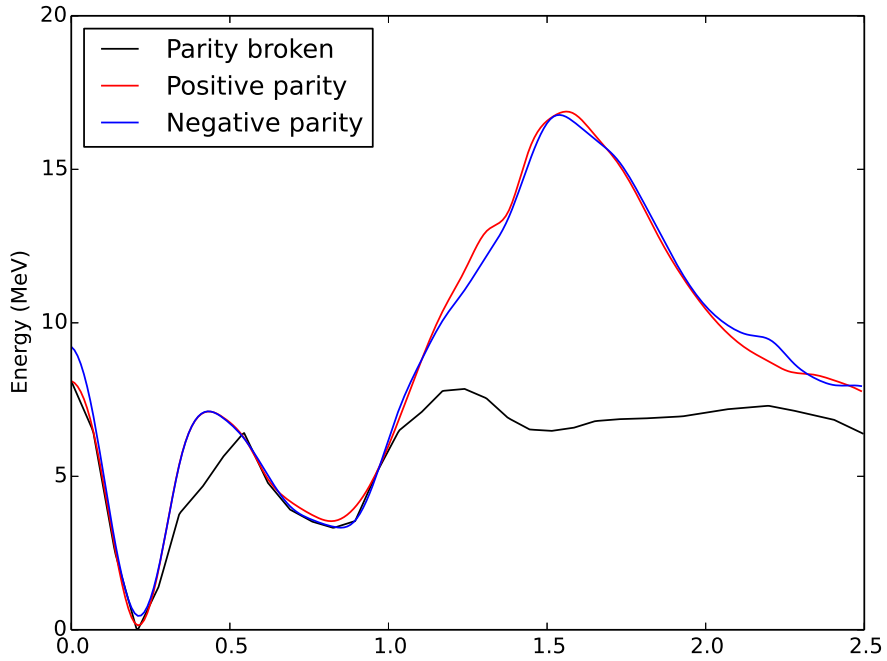

Figure 9.8: Fission barrier of ^{227}Ra calculated using the SLy5s1 parameterization either by conserving parity and blocking a quasiparticle of positive or negative parity and conserving axial symmetry, or by breaking parity and axial symmetry.

nevertheless interesting to notice that the positive parity quasiparticle is lower in energy than the negative quasiparticle at the minimum, while the situation is reversed after the first barrier.

9.5 Rotational bands

Breaking time-reversal invariance allows us not only to study odd nuclei in the region, but also rotational bands constructed by constraining one projection of the angular momentum $\langle \mathcal{J} \rangle$. We will conserve both z-signature and y-time-simplex, so $\langle \hat{\mathcal{J}}_z \rangle$ is the only projection that can take non-zero values.
While a deformed mean-field calculation cannot generate many-body wavefunctions with an angular momentum quantum number, we can associate a phenomenological value J to a mean-field state with a given z-projection of the angular momentum through [11]

$$\langle \hat{\mathcal{J}}_z \rangle^2 = J(J+1)\,. \tag{9.3}$$

Solving this equation for J, and calculating the mean-field states constrained to a range of values of $\langle \hat{\mathcal{J}}_z \rangle$ by using cranking constraints we obtain a function $E(J)$. Since $\langle \hat{\mathcal{J}}_z \rangle$ is not restricted to (half-)integer values, J will be in general a real number and our function $E(J)$ is thus continuous. We can then simply calculate γ energies as

$$E_\gamma(J) = E(J) - E(J-2)\,, \tag{9.4}$$

which is again a continuous function.
Note that, in order to be able to constrain $\langle \hat{\mathcal{J}}_z \rangle$ to non-zero values, the z-axis cannot be a rotational symmetry axis. One thus has to take care on how to orient the nuclear density on the Lagrange mesh, and put the axial symmetry axis in the y- or x-direction, see Appendix C.

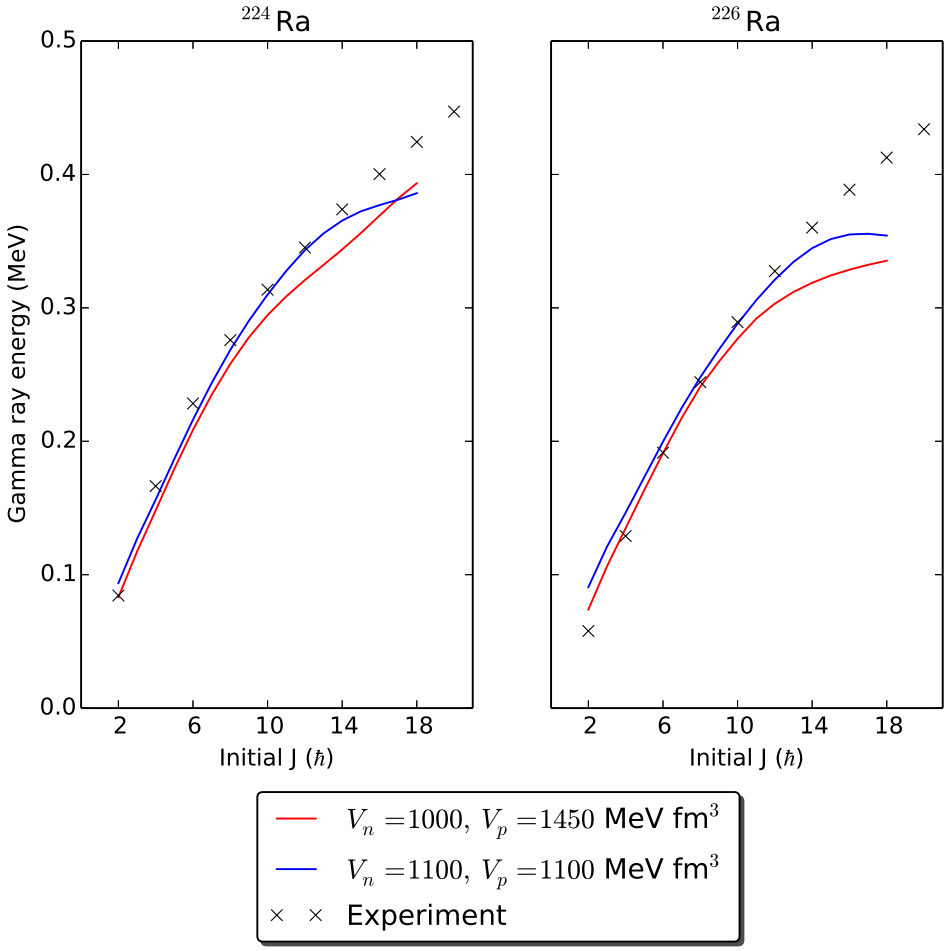

Figure 9.9: Gamma transition energy of the rotational bands constructed on the prolate saddle-point for ^{224}Ra and ^{226}Ra, for the adjusted pairing strengths $(V_n, V_p) = (1000, 1450)$ MeV fm^3 and alternative adjustment $V_n = V_p = 1100$ MeV fm^3. Experimental data correspond to the positive-parity rotational band based on the groundstate and is taken from [126].

Parity conserved calculations Orienting the nuclear density along the x-axis is no problem when parity is conserved. The function $E_\gamma(J)$ for the rotational band constructed on top of the prolate saddle-point for ^{224}Ra and ^{226}Ra is plotted in Fig. 9.9 for two sets of pairing strengths. The agreement with experiment is rather good for the adjusted pairing strength $(V_n, V_p) = (1000, 1450)$ MeV fm^3, up to $J \approx 10\hbar$ for both nuclei, after which the calculated curve underestimates the experimental values.
The pairing strengths were readjusted to the three-point gaps of ^{216}Ra and its neighbours. It interesting to see the effect when the pairing strengths get adjusted to the rotational band itself. The pairing strengths $(V_n, V_p) = (1100, 1100)$ MeV fm^3 result from a limited readjustment of the pairing, restricted to $V_n = V_p$, on the rotational band of ^{226}Ra. While these values are very different compared to the ones readjusted on the three-point gaps, the agreement with experiment is very comparable.

Parity-broken calculations In principle, we could improve the description of the rotational bands by constraining $\langle \hat{J}_z \rangle$ starting from the octupole deformed minimum. There are however two problems at this point in time that prevent us from presenting results here. The first, purely practical problem is related to signature symmetry. The octupole deformed minimum is still axial. If we want to orient the symmetry along the x-axis, the axial octupole deformation breaks the reflection symmetry through the y-z plane. In short, in addition to parity and time-reversal, a calculation that takes into account octupole deformation and non-zero values of $\langle \hat{J}_z \rangle$ needs to break signature symmetry[5]. This leaves only the y-time-simplex as conserved symmetry. While `MOCCa` is able to do this calculation, it adds another factor two to the computational effort required, and

[5]One could of course also do the opposite: orient the symmetry axis in the z-direction, and constrain the x-projection of the angular momentum instead of the z-projection.

we were unable to perform this calculation in time for this dissertation. Note that this is partly due to the design of MOCCa: one could do the calculation when conserving z-simplex $\hat{\mathcal{S}}_x$ and y-time-simplex $\check{\mathcal{S}}_y^T$. This combination of symmetries allows for orienting the axial symmetry axis along the x-axis, while not restricting the octupole deformations. Unfortunately, this option is not included in the possibilities of MOCCa and we are forced to do the calculation without the simplification that conserved x-simplex could bring.
A second problem is more related to the interpretation of the results. If parity is broken, the HFB wavefunctions obtained by cranking will mix positive and negative parity many-body states and it is not a priori clear how to compare the experimental data that is split into a positive-parity and a negative-parity band with transitions between both. Projection on parity solves this problem, but adds another layer of complexity.
It is worth noting that the literature on octupole deformed rotational bands is very limited: [137] is the only published self-consistent calculation we have been able to find and the presentation of results is lacking in many ways. Calculations using Wood-Saxon potentials exist [138, 139], and show a shape transition to octupole deformed shapes for increasing $\langle \hat{\mathcal{J}}_z \rangle$ for the spherical minima in the Radium region. Investigating how the inclusion of octupole deformation would change the results from Fig. 9.9 is thus definitely needed.

Chapter 10

Charge radii of Hg isotopes

This chapter will detail some calculations performed using the mean-field framework described in parts 1 and 2 of this dissertation. In particular, we will focus on the charge radii of the mercury isotopes, as a direct extension to the beyond-mean-field study from [140] that used the SLy6[17] functional to study even-even nuclei in the neutron-deficient lead region. Due to the presence of a two-body centre-of-mass contribution (see section 1.4.5) these calculations were carried out using `cr8` instead of `MOCCa`, which cannot handle this type of contribution to the energy density functional[1].
In particular, we are interested to look with more detail into the charge radii of the neutron-deficient mercury isotopes, a quantity that has a long history of experimental interest [141, 142]. The odd-even staggering in the charge radii of the mercury isotopes with mass numbers $A = 181$ through $A = 186$ specifically has been a subject of considerable interest, also on the theoretical side. Currently data is available from $A = 180$ up to $A = 206$, mainly through the application of optical pumping techniques [143]. In the near future, the measurements at ISOLDE using laser spectroscopy are planned to extend the available data on charge radii to more neutron deficient isotopes down to ^{177}Hg. The main motivation is to determine whether the odd-even staggering continues for nuclei lighter than ^{181}Hg.
For reasons of presentation we will divide the isotopic chain of the mercury isotopes into two: the isotopes ranging from $A = 192$ up to $A = 208$ on one hand and the isotopes from $A = 176$ up to $A = 190$ on the other. We will first look at the trends of the rms radii in both parts of the region (sections 10.2 and 10.3.), after which we will focus in more detail on the odd-even staggering in section 10.5.

10.1 Details of the calculations

The calculations were performed on a mesh of $(N_X, N_Y, N_Z) = (40, 40, 40)$ and $dx = 1.0$ fm. The box size has been shown to be large enough to accommodate ^{208}Pb and this mesh discretization length has been shown in chapter 8 to be accurate to a few percent of a fm on absolute rms-radii, an accuracy that is comparable to the error on the rms radius of ^{208}Pb of the original SLy6 fit [17]. The isotopic shifts, as differences of rms radii, are even significantly more accurate than the rms radii themselves, see Fig. 11 in [10].
As already discussed above, the SLy6 functional was employed in the calculations in order to be able to compare with the original beyond-mean-field results, and was originally selected for its ability to describe the low-lying level structure in neutron-deficient lead isotopes [144, 145]. We used the pairing interaction from chapter 3 using $V_n = V_p = 1250$ MeV fm^3 with $\alpha = 1.0$ and a symmetric Fermi cutoff at 5 MeV around the Fermi energy as described in section 3.9, as used in [140]. Note that the original study used HF+BCS pairing while we will use HFB+LN pairing in order to be able to treat odd-A nuclei on the same footing as the even-even ones. For most of the even-even nuclei the difference between HF+BCS and HFB is expected to be rather small, since the nuclei considered here are sufficiently far away from the dripline in order for the BCS approximation to hold [3].
As we are interested in the charge radii of even-even and odd-A nuclei in the region alike, we have to be able to break time-reversal symmetry. Both this prerequisite and the HFB pairing can be delivered by the `cr8` code, also because we will not be breaking any additional point symmetries. Unfortunately the breaking of time-reversal symmetry precludes any possibility[2] of restoring rotational symmetry and mixing mean-field configurations as done in [140]. We will thus limit ourselves to interpret mean-field results, which will unfortunately limit our ability to compare to experiment.
The mean-square (ms) charge radius is a simple one-body operator and can thus be easily evaluated for

[1] Though this is mainly a consequence of time constraints and the implementation of this contribution into `MOCCa` would be straightforward, though time-consuming.

[2] At least at the moment. Beyond-mean-field studies of odd nuclei have recently been demonstrated to be feasible for light nuclei as ^{25}Mg [32], but at tremendous computational cost.

mean-field states. For a mean-field state characterized by a density $\rho(\mathbf{r})$ it can be calculated as

$$r_p^2 = \frac{\int d\mathbf{r}\, \rho_p(\mathbf{r})\mathbf{r}^2}{\int d\mathbf{r}\, \rho_p(\mathbf{r})}\,, \tag{10.1}$$

and the root-mean-square (rms) radius is simply the square root of the ms radius. The isotopic shift with respect to a reference isotope in the chain with $N_0 = A - Z$ neutrons is

$$\delta r_A^2(N,Z) = r_p^2(N,Z) - r_p^2(N_0,Z)\,. \tag{10.2}$$

The results shown naively apply these formulas to calculate the isotopic shifts. These definitions assume however that the proton in the nuclear medium is point-like. Taking into account a charge distribution of a proton that is distributed over a finite region is possible but not employed here. In any case, this effect will cancel to first order when dealing with isotopic shifts [3].
A major problem of dealing with mean-field results without any symmetry restoration and/or configuration mixing procedures is the difficulty of interpreting results. This is especially true for this region on the nuclear chart, as shape coexistence plays a significant role and the beyond-mean-field results are often superpositions of different mean-field configurations of very different deformations [140, 145, 144, 146]. The isotopic shifts present an additional difficulty on the mean-field level, as it is not immediately clear what the reference value $r_p^2(N_0,Z)$ should be. Given different minima that one is interested on a given energy surface, what should be the reference value for every minimum? Given a beyond-mean-field calculation there is a clear answer: the rms charge radius of the ground-state obtained for an arbitrary nucleus. On the mean-field level however, no such clear-cut definition is possible and we are faced with a choice. In what follows we will (where possible) refer to isotopic shifts with respect to the mean-square charge radius as obtained by theory ^{206}Hg, but rescaled to match the experimental isotopic shift of this nucleus with respect to ^{198}Hg. The quantity we will be plotting is

$$\delta r^2_{p,\text{Theory}}(N,80) = r^2_{p,\text{Th.}}(N,80) - r^2_{p,\text{Th.}}(118,80) + \delta r^2_{p,\text{Exp.}}(118,80)\,. \tag{10.3}$$

The experimental shift of ^{206}Hg with respect ^{198}Hg needed in this formula was taken from [142]. The main motivation of choosing ^{206}Hg as a reference nucleus is that the nucleus is neutron-magic and exhibits a clear spherical minimum on the mean-field level, leaving no doubt as to the correct interpretation of the structure of the nucleus.

10.2 The less neutron-deficient Hg isotopes: from $A = 192$ up to $A = 208$

We have limited ourselves to the even-even mercury isotopes between A=192 and A=208. The deformation energy surfaces as a function of β_{20} are shown in Fig. 10.1. No triaxial degrees of freedom were considered, and consequently $\beta_{22} = 0$ along the curves. The location of the local minima for prolate and oblate minima are explicitly shown by respectively red and blue diamonds. The overall structure of the energy surface is rather comparable for all of these isotopes. A profound oblate minimum is found for all of the isotopes up to ^{204}Hg with a less pronounced prolate minimum to accompany it. As the neutron number increases, both minima get less pronounced and move to smaller absolute values of β_{20}, culminating in a single spherical minimum at the neutron magic number $N = 126$ for ^{206}Hg and $N = 208$ for ^{208}Hg.
The isotopic shift with respect to ^{206}Hg for these isotopes is shown in Fig. 10.2, either calculated from the prolate or oblate minima shown in Fig. 10.1, as well as the experimental values. The linear trend is rather well reproduced with more or less correct slope by both the prolate and oblate minima, although both get the offset quite wrong. Nevertheless the prolate minima show a closer agreement with experiment than the oblate minima. It is interesting to note that choosing a difference reference point (e.g. ^{194}Hg as in [140]) that includes a different reference value for the oblate and prolate minima can change the offset quite significantly, either improving or deteriorating the agreement with experiment.
The fact that the prolate minimum is the best candidate to reproduce the rms radii, but is not the mean-field minimum in ^{192}Hg to ^{206}Hg is clearly a deficiency of the model. The exact balance between the different mean-field minima is often very precarious in the sense that it depends sensitively on many details of the interaction, both in the particle-particle and particle-hole channel. Consequently, it is hard to point out any single element that is lacking in the model.

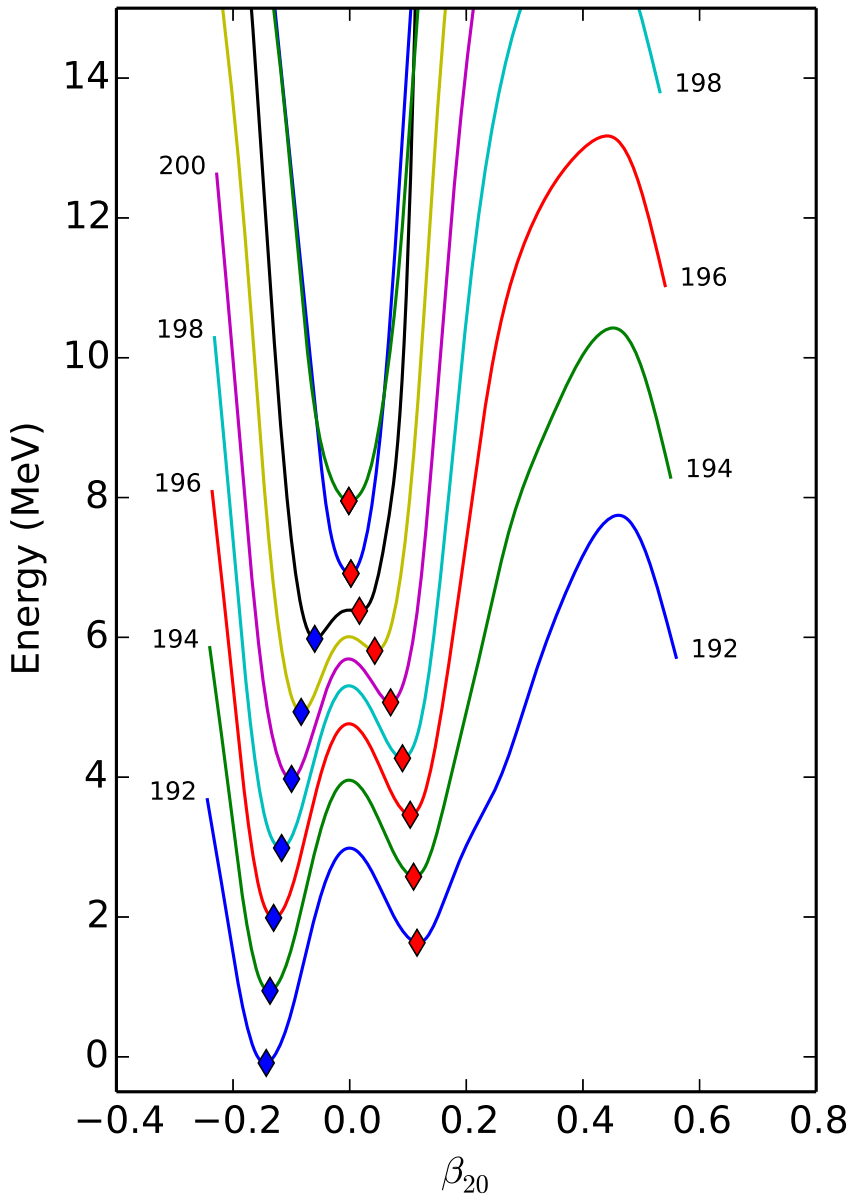

Figure 10.1: Deformation energy surface of the even $^{192-208}$Hg isotopes for SLy6 with HFB+LN pairing with $V_n = V_p = 1250$ MeV fm^3. All energies are with respect to the minimum of the deformation energy surface, but with an additional shift of 1 MeV between neighbouring isotopes for demonstration purposes. Blue diamonds denote oblate minima and red diamonds prolate minima. The numbers indicate the mass number of the even-even isotopes.

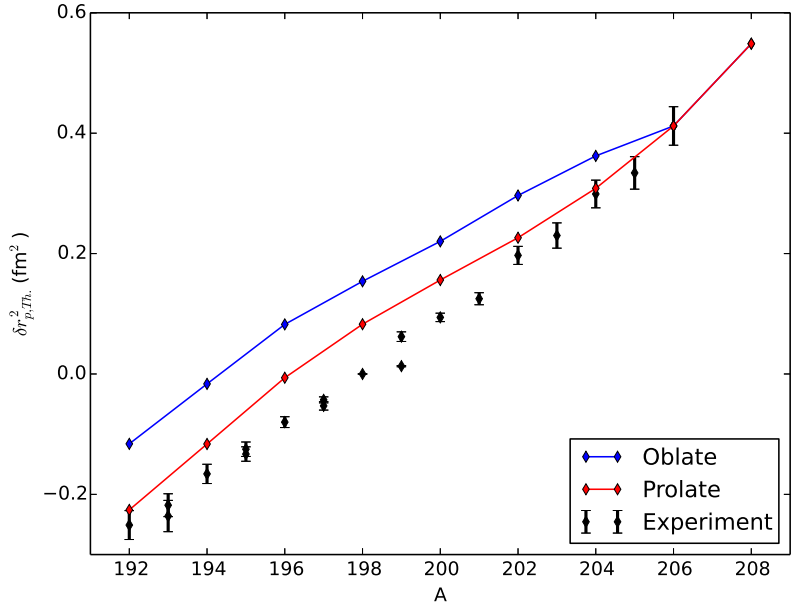

Figure 10.2: Isotopic shifts of the even neutron rich mercury isotopes $^{192-208}$Hg with respect to ^{206}Hg, calculated with the SLy6 parametrization complemented by HFB+LN pairing with $V_p = V_n = 1250$ MeV fm^3. Experimental data was taken from [142].

10.3 The more neutron-deficient Hg isotopes: from $A = 176$ up to $A = 191$

The deformation energy surfaces of the more neutron-deficient Hg isotopes are shown in Fig. 10.3. Again, the configurations considered are all axial, such that $\beta_{22} = 0$ along the entire curve. Note that the energy surfaces for the odd isotopes are false HFB vacua, meaning that they represent many-body states that are strictly even in nature (and conserve time-reversal) but the expectation value of $\hat{\mathcal{N}}$ is odd. The three heaviest isotopes $^{189-190-191}$Hg exhibit essentially the same structure as the heavier isotopes with a pronounced oblate minimum and a prolate minimum at slightly higher energy at roughly the same absolute value of β_{20}. From ^{188}Hg and downwards in mass number a more deformed minimum develops that is lower in energy than the oblate minimum for ^{179}Hg, ^{180}Hg, ^{181}Hg and ^{182}Hg. The balance between for these four isotopes is rather precarious as the energy difference between minima is about 100 keV for ^{180}Hg and ^{181}Hg while it is only roughly 10 keV for ^{179}Hg and ^{183}Hg. ^{178}Hg reverts back to the previous configuration of two prolate minima and a deeper oblate one, while ^{177}Hg and ^{176}Hg exhibit again the same structure as the heavier isotopes.

The corresponding isotopic shifts are shown in Fig. 10.4, calculated from either the prolate or oblate minima and compared with experimental data. For the heaviest isotopes, ^{191}Hg, ^{190}Hg and ^{189}Hg the prolate minimum agrees rather well with experiment, even though these values are based on false vacuum many-body states. Starting at ^{188}Hg, the second more deformed prolate minimum develops around $\beta_{20} \approx 0.3$ and the rms radii of the prolate minimum skyrockets. For even masses lower than $A = 188$ the oblate minimum in general is the best candidate to explain the experimental data. The available experimental data stops beneath ^{181}Hg, but our calculations continue in the same trend. The main feature is of the disappearance of the second prolate minimum for ^{177}Hg and ^{176}Hg, what induces the rms radii of the prolate minima to revert to the original trend at $A = 177$.

The masses between A=180 and A=186 exhibit the odd-even staggering already mentioned in the introduction of this chapter. While the even masses ^{180}Hg, ^{182}Hg, ^{184}Hg and ^{186}Hg are qualitatively explained by the oblate minimum, the odd masses in between exhibit significantly larger charge radii that correspond better to the second prolate minimum. The agreement is qualitative at best however for these isotopes and it is clear that the false vacuum does not correctly describe the charge radii for these odd nuclei. Note that this is not the case for ^{187}Hg where the experimental data for both the ground state and isomeric state agree rather well with the oblate minimum of the false vacuum. A special mention goes out to the isomeric state of ^{185}Hg which does not participate in the odd-even staggering and coincides rather well with the theoretical value of the oblate minimum.

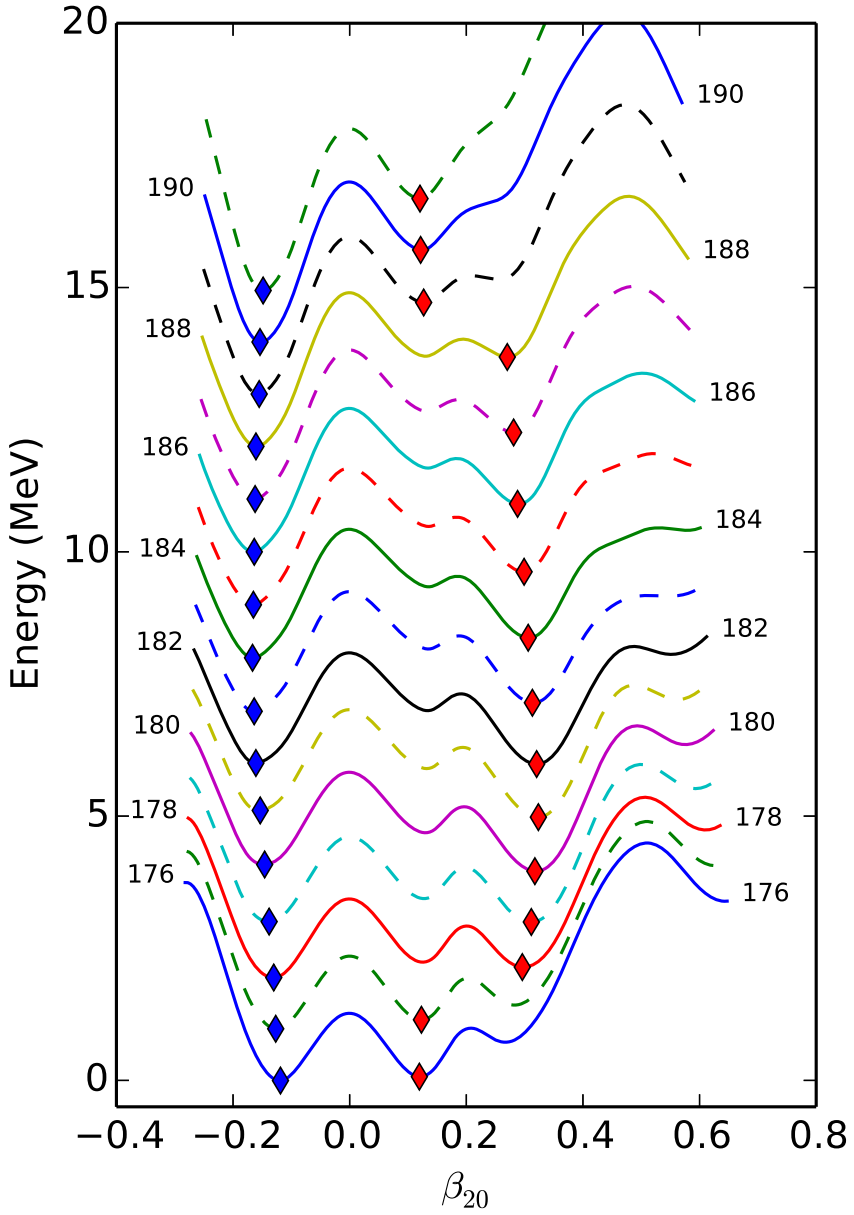

Figure 10.3: Energy surfaces of the neutron deficient mercury isotopes from A=176 up to and including A=191,using the SLy6 parameterization with HFB+LN pairing with $V_n = V_p = 1250$ MeV fm^{-3}. All energies are with respect to the minimum of the deformation surface, but with an additional shift of 1 MeV between neighbouring isotopes for demonstration purposes. Full lines denote even isotopes, dashed lines denote false vacua for odd isotopes. Blue diamonds denote oblate minima and red diamonds prolate minima. The numbers indicate the mass number of the even-even isotopes.

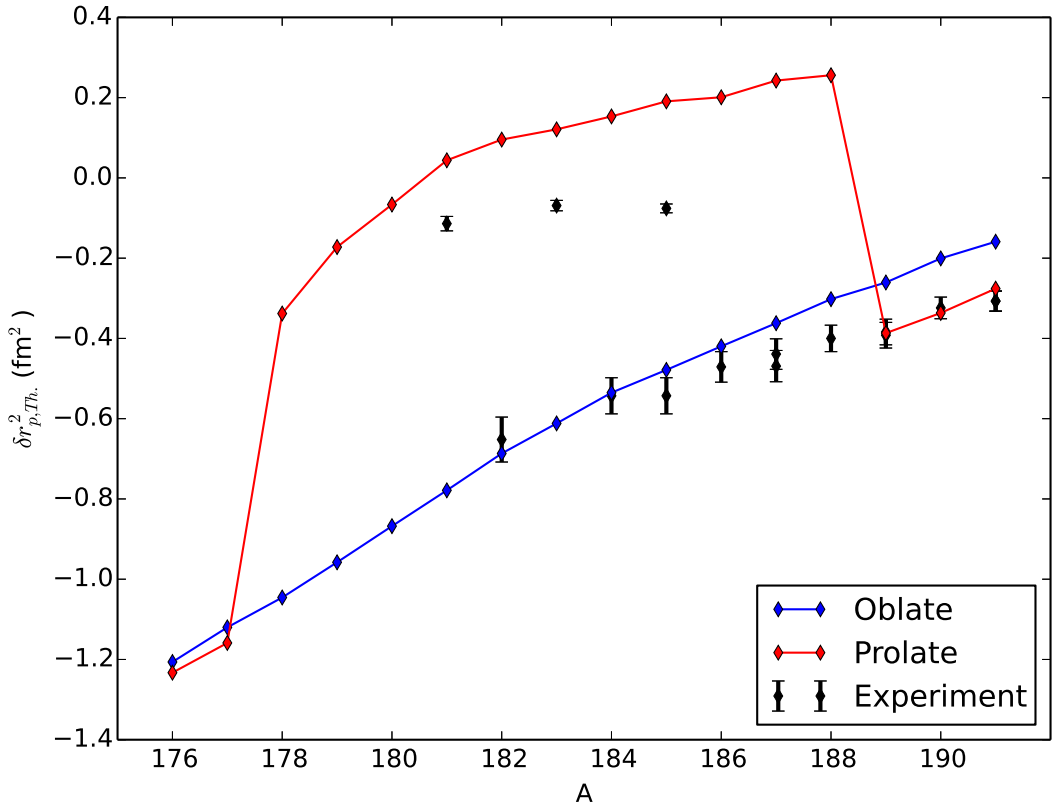

Figure 10.4: Isotopic shifts of the even neutron rich mercury isotopes $^{176-191}$Hg with respect to ^{194}Hg, calculated with the SLy6 parametrization complemented by HFB+LN pairing with $V_p = V_n = 1250$ MeV fm^{-3}. Note that the values shown for the odd-A nuclei are based on time-reversal invariant false-vacuum many-body states. Experimental data was taken from [142].

From these results one can naively expect the odd-even staggering to stop for ^{177}Hg, as there the first prolate minimum is lower in energy than the second one by almost 200 keV, giving rise to a reduced value of the charge rms radius for that nucleus. This is however not more than a naive expectation, as the energy difference between the two prolate minima of ^{179}Hg is only on the order of 10 keV. Any tiny change in the calculation (either in the functional, pairing interaction or other parameters) could upset this balance and change this prediction. In addition, we must not forget that we are dealing with false-vacuum states and the effects of including a quasiparticle excitation will surely have an effect significantly larger than 10 keV.

10.4 Comparing to the beyond-mean-field results

It is instructive to compare to the beyond-mean-field results from [140] for the even-even isotopes. These were unfortunately only available up to $A = 194$ and so we cannot present the isotopic shift with respect to ^{206}Hg. For the mean-field calculations, we have instead picked as reference the charge rms radius of the prolate minimum of ^{194}Hg. The experimental results were rescaled to the same nucleus and the error bars were removed. The combination of mean-field results obtained here, beyond-mean-field results and experimental data are shown in Fig. 10.5.
It was already noted in [140] that the isotopic shifts are rather well described for isotopes with $A > 184$, as the ground state isotopic shift is in rather good agreement with the data, only slightly underestimating the shifts of ^{188}Hg, ^{190}Hg and ^{192}Hg. The beyond-mean-field ground state for these $A > 184$ are dominated by prolate mean-field configurations while the 0^+_2 is dominated by oblate mean-field configurations. At ^{184}Hg however, an inversion takes place and 0^+_1 is dominated by oblate configurations. This is reflected in the isotopic shifts of the 0^+_1 state in ^{184}Hg, ^{182}Hg and ^{180}Hg: isotopic shift exhibits a jump to higher values while it is rather

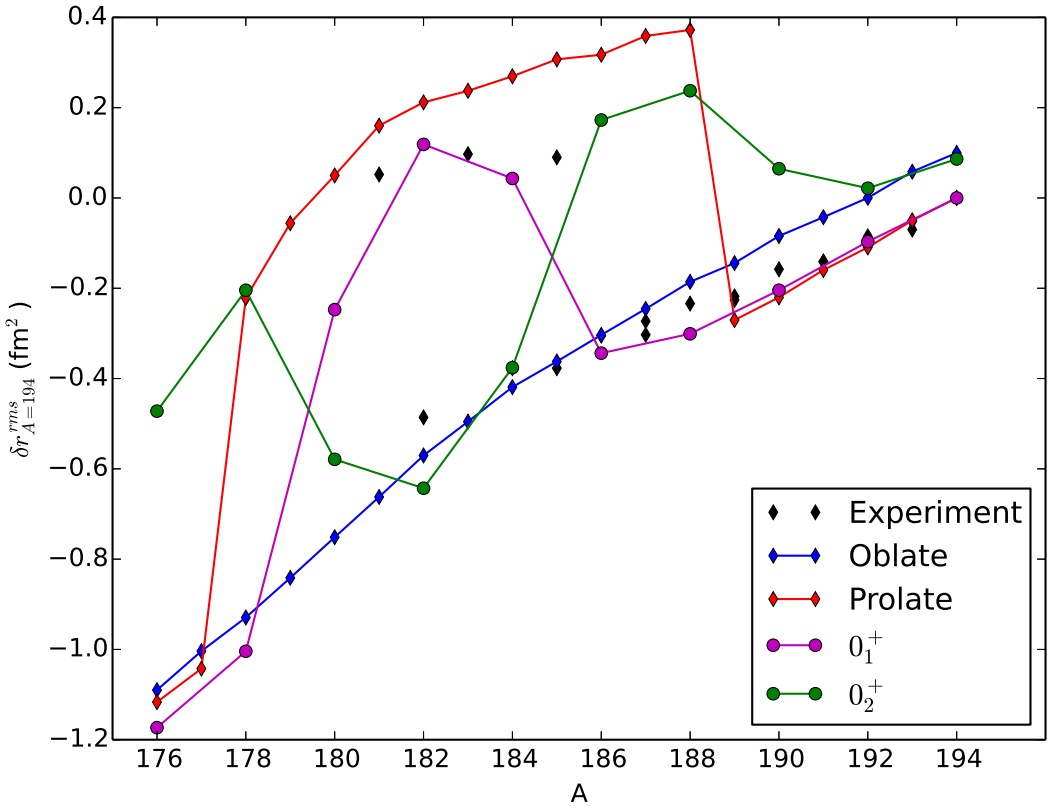

Figure 10.5: Mean-field, beyond-mean-field and experimental results for the isotopic shifts of ^{176}Hg up to ^{194}Hg. The beyond-mean-field results are plotted for the ground state, 0_1^+ and the first excited 0^+ state, 0_2^+. Note that the mean-field results take as a reference rms radius the rms radius of the prolate minimum of ^{194}Hg, while the beyond-mean-field results refer to the rms radius of the calculated ground state of ^{194}Hg. Beyond-mean-field results were taken from [140], while experimental data was taken from [142].

0_2^+ that describes the data. This inversion seems to mimic the behavior of the odd-A nuclei in the region. [140] takes this as indication that both 0_1^+ and 0_2^+ are indeed predominantly based on relative prolate and oblate mean-field configurations, but that the method gets the ordering of both levels wrong.
Interestingly, the beyond-mean-field results go back to ordinary ordering for ^{176}Hg and ^{178}Hg. Both ground states are superpositions of both prolate and oblate mean-field states [140] while the 0_2^+ states are based on prolate configurations. Note that the isotopic shift of the 0_2^+ state in both nuclei is still large compared to the experimental trend, while the mean-field results of the prolate minimum revert to the smaller values. This can be explained by the fact that the beyond-mean-field mixes several configurations that are even more deformed than the prolate mean-field minimum.
Unfortunately, no beyond-mean-field results are available for the odd-A mercury isotopes. It is thus very difficult to make meaningful statements about the odd-even staggering of ^{181}Hg, ^{183}Hg and ^{185}Hg starting from these results. Making a prediction on the possible staggering of the isotopic shift of more neutron deficient isotopes such as ^{179}Hg is likely also stretching the method beyond its limits.

10.5 Odd-even staggering: a more in-depth look at ^{181}Hg, ^{183}Hg and ^{185}Hg

In the previous section we considered only time-reversal invariant mean-field states. We can do better by creating quasiparticle excitations on top of the false vacuum, breaking time-reversal symmetry and changing the particle-number parity of the HFB vacuum to -1 as described in chapter 3. It is worth noting that the blocking procedure used was direct diagonalisation as described in chapter 6 as this is the only option available in `cr8`.

Experimentally, these three nuclei all have ground states with $J^\pi = \frac{1}{2}^-$ with low-lying $\frac{13}{2}^+$ excited states[3]. We are thus looking for quasiparticle excitations with these particular J^π quantum numbers. However, calculations presented in the previous sections had non-zero quadrupole deformations and thus break rotational invariance. The many-body state and the single-particle states therefore have no longer good angular momentum J, and a straightforward identification of quasiparticles is impossible. The projection of angular momentum on the axis of symmetry is still conserved, but will be of limited practical use. Parity however, is conserved and the parity quantum number can directly be used to identify quasiparticles.
Identifying the $\frac{13}{2}^+$ states is comparatively easy: since their J value is rather high, these states tend to stay relatively pure. Consequently, for these single-particle states

$$\langle J^2 \rangle \approx \left(\frac{13}{2}\right)^2 . \tag{10.4}$$

Note that this equality never exactly holds in practice and these kinds of arguments are only approximative as these single-particle states are in general superpositions of states with many different values of angular momenta. Adding the parity quantum number to the mix, we identified fourteen (seven in each mean-field minimum[4]) in every nucleus, close to the Fermi energy, that we used for blocking purposes. The case for the $\frac{1}{2}^-$ is less clear-cut since their low value of J implies that they will in general mix quite strongly with other levels, and the value of $\langle J^2 \rangle$ will be polluted. As such, we have simply selected four(two in every mean-field minimum) K $= \frac{1}{2}$ quasiparticles with negative parity to block that were located close to the Fermi energy.
The positive and negative parity states with lowest energy in every mean-field minimum obtained by blocking are plotted in Fig. 10.6. Note that the labels $\frac{1}{2}$ and $\frac{13}{2}$ do not directly denote the angular momentum of the mean-field state, but rather the identification of the blocked quasiparticle and thus should be taken as tentative assignments.
For ^{185}Hg the oblate minimum delivers a spectrum that can be considered in rather good agreement with experiment: blocking a quasiparticle with negative parity gives us the lowest energy and the relative energy of the closest positive parity candidate is comparable to the excitation energy of the experimental $\frac{13}{2}^+$ state. Purely based on the quasiparticle spectrum, the oblate well is a better match to explain experiment than the prolate well for ^{185}Hg. The situation is less clear for ^{183}Hg: the overall lowest quasiparticle is located in the prolate well, but has positive parity. The oblate well again gets the states in correct order and with an energy difference that is in the right ballpark. For ^{181}Hg the prolate well gives rise to the wrong ordering of states, but this time with an almost perfect energy difference. The oblate well gets the order correct again, with an energy difference between the states that is again in the right ballpark.
The isotopic shifts of these blocked HFB states, together with the values of the false vacuum states are shown together in Table 10.1. For ^{181}Hg the prolate well produces isotopic shifts that are significantly closer to the experimental result than the oblate well. Creating a quasiparticle excitation also brings theory closer to the experimental result for the $\frac{1}{2}^-$ state. The same is observed for ^{183}Hg, the prolate well produces isotopic shifts in the right ballpark while the oblate well is far off. Creating a quasiparticle excitation on top of the false vacuum also brings the theoretical value closer to the experimental value for the $\frac{1}{2}^-$ state. For ^{185}Hg the experimental isotopic shift of both the ground state and the isomeric state is available. The isotopic shift $\frac{1}{2}^-$ state matches most closely the negative parity quasiparticle in the prolate well, while the $\frac{13}{2}^+$ matches most closely the positive-parity quasiparticle in the oblate well. The blocked HFB wavefunctions in the prolate well provide an improvement of the agreement with experiment compared to the false vacuum, but this is not the case for the oblate well.
We are now faced with a rather interesting dichotomy: on one hand the spectrum generated by the oblate well is in rather better agreement with the experimental data, but on the other hand the isotopic shifts of the ground state configurations are in better agreement with the prolate minimum. The correct answer is of course that limiting ourselves to either one or the other of the different mean-field minima is not a sufficient description for these nuclei. Beyond-mean-field results for even-even nuclei in the region [140] clearly indicate that the beyond-mean-field wavefunctions are complicated superpositions of both prolate and oblate mean-field states. The same can be expected of these odd-A nuclei, only with an added degree of complexity: while we only have shown the lowest lying states obtained by blocking, several different choices for blocking of quasiparticles are possible. In principle, all of these should be mixed in a beyond-mean-field procedure.

[3]Note that this excitation is rather long-lived in ^{185}Hg and its rms radius was also measured.
[4]Note that for $J = \frac{13}{2}$ K can take 14 values, but K and $-K$ are degenerate in this case.

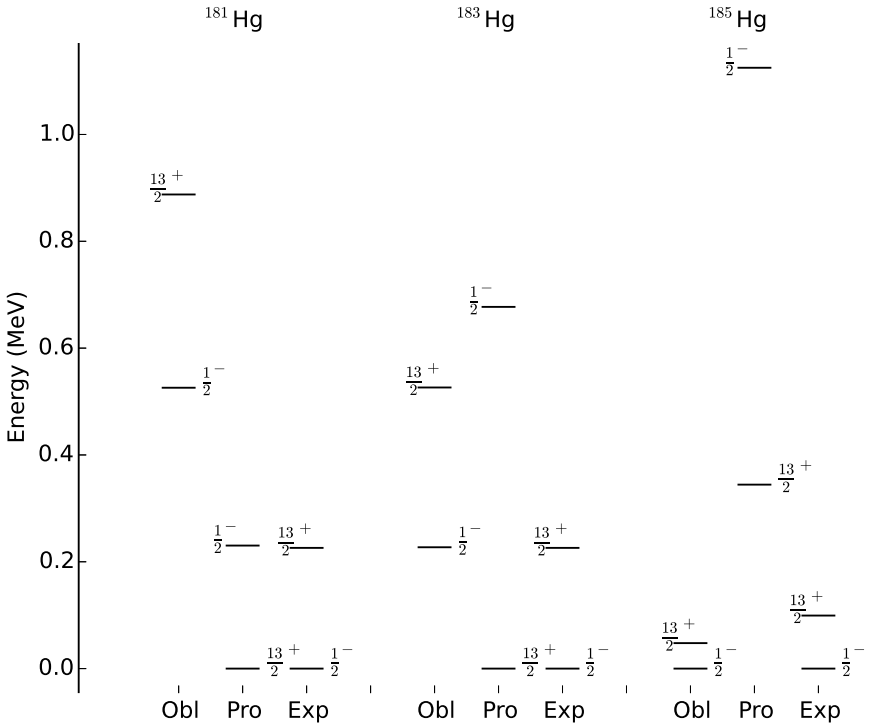

Figure 10.6: Spectrum of ^{181}Hg, ^{183}Hg and ^{185}Hg as obtained by blocking quasiparticles as described in the text. Note that the indices $\frac{13}{2}$ and $\frac{1}{2}$ for the theoretical results indicate the identification of the blocked quasiparticle as described in the text, and is not equal to the angular momentum of the HFB state. Only parity is a good quantum number. Energies are with respect to the overall lowest blocked HFB state studied. Experimental data was taken from [126].

		Oblate	Prolate	Experiment
^{181}Hg	False vacuum	-1.191	-0.368	
	$\frac{1}{2}^-$	-1.121	-0.471	-0.526 ± 0.018
	$\frac{13}{2}^+$	-1.120	-0.397	
^{183}Hg	False vacuum	-1.024	-0.291	
	$\frac{1}{2}^-$	-0.939	-0.424	-0.481 ± 0.013
	$\frac{13}{2}^+$	-0.958	-0.357	
^{185}Hg	False vacuum	-0.891	-0.221	
	$\frac{1}{2}^-$	-0.828	-0.328	-0.488 ± 0.011
	$\frac{13}{2}^+$	-0.820	-0.349	-0.955 ± 0.045

Table 10.1: Comparison between isotopic shifts relative to ^{206}Hg calculated with either false vacua and by creating quasiparticle excitations. Note that the angular momentum values for the theoretical results in this table are only tentative and indicate in fact the identification of the blocked quasiparticle as explained in the text. Experimental data was taken from [142].

10.6 Conclusion

We have extended the mean-field calculations of [140] to mercury isotopes with higher neutron number, as well as the odd-A isotopes between $A = 176$ and $A = 192$. Isotopic shifts of the even-even isotopes are in general in good qualitative agreement with the data. One has however to take into account that we have made the choice to consider both the isotopic shifts of the oblate and prolate minima, without consideration which one was lower in energy. Taking only the lowest-energy minimum would have resulted in less good agreement with the experimental data.
For the ^{187}Hg, ^{189}Hg, ^{191}Hg the isotopic shifts of the time-reversal invariant false vacuum wavefunctions already provides agreement with the data on the same quantitative level of the even-even isotopes. The shifts of the isotopes that exhibit the odd-even staggering, ^{181}Hg, ^{183}Hg and ^{185}Hg, can also be more or less understood in the spirit of the second prolate minimum that becomes important for these nuclei.
Quasiparticle excitations on top of the quasiparticle vacua of ^{181}Hg, ^{183}Hg and ^{185}Hg were created. The resulting spectrum was compared to experiment, through a tentative identification of the quasiparticles. The isotopic shifts of the blocked wavefunctions in general agreed better with the data compared to the shifts obtained from the false vacua.
It remains very difficult to make definite statements about the neutron-deficient mercury isotopes on a mean-field level. The beyond-mean-field wavefunctions of the even-even isotopes indicate that strong mixing between prolate and oblate configurations is relevant across the entire isotopic chain, rendering an interpretation on the basis of single mean-field configurations rather dubious. The possible odd-even staggering of the isotopic shifts of the nuclei that are yet to be measured (^{179}Hg and ^{177}Hg mainly) in particular is hard to predict. Naively one could argue that the second prolate minimum (almost) disappears for the false vacuum of ^{177}Hg, which makes the isotopic shifts in Fig. 10.4 of the prolate minimum come down. The disappearance of this minimum would then make the a staggering unlikely as very deformed prolate configurations rise in energy.

Part IV

A cup of MOCCa

Chapter 11

A cup of MOCCa: a users manual

MOCCa is a rather complex program with many input parameters. This chapter has as aim to teach the users how to use MOCCa in practice and how to utilize the options described in the rest of this thesis. Where possible in previous chapters we explicitly mentioned the relevant keywords in the hope to make interacting with the program intuitive. The code was designed in a what is hopefully a clear way and extensive documentation is present in the source code. Nevertheless, as always with large software projects, there are still many possible improvements: I hope the reader will forgive me the occasional irrational choice or bit of spaghetti code.
The chapter details how to compile the code in section 11.1. The requirements for a run are explained in section 11.2, followed by an example and an explicit list of all the input keywords. The chapter concludes with a list of the source code files in section 11.3 and a short description of their function with a reference to the rest of the dissertation for quick indexing. For a general overview of the structure of the code, the reader is referred to appendix H, where a schematic diagram of the workflow of the program is drawn.

11.1 Compilation

Most of MOCCa is written in FORTRAN-90, but it uses some features of the FORTRAN-03 and FORTRAN-08 standards. Specifically, it uses procedure pointers throughout the whole code, and should be compiled with compilers that support this FORTRAN-03 feature. A list of tested compiler versions is given in Table 11.1. A special mention goes out to gfortran v4.9, which refuses to compile the code correctly, even though both v4.8 and v5.3 do.
The code is completely independent of any compile-time parameters, meaning that a single compilation suffices to treat all nuclei, light or heavy, in all possible symmetry combinations with any of the other runtime options. This 'one compilation to end them all' can easily be achieved by issuing the make command in the MOCCa directory, using the accompanying Makefile. By default, this will compile with the currently installed version of gfortran, with maximum optimization. Users wishing to change compiler and/or compilation options can easily do so using the Makefile. Note however that the makefile is configured to use directories /mod/ and /obj/ in the MOCCa directory.
If the GNU Make tool is not available on your platform[1], one can compile MOCCa using the following command

```
gfortran -O3 -o MOCCa.exe
CompilationInfo.f90 GenInfo.f90 Force.f90 OptimizedDerivatives.f90 Derivatives.f90
CoulombDerivatives.f90 Mesh.f90 Spinor.f90 Spwf.f90 SpwfStorage.f90 Damping.f90
Densities.f90  Moments.f90 SpecialMoments.f90 Coulomb.f90 PairingInteraction.f90
HartreeFock.f90 HFB.f90 GradientHFB.f90 BCS.f90 Pairing.f90 Cranking.f90
MeanFields.f90 ImaginaryTime.f90 Energy.f90  DensityMixing.f90 Transform.f90
Interfaces.f90 InOut.f90 Main.f90 -llapack -lblas
```

The order of files in the command is strict and cannot be changed. The line breaks should be omitted, and the linking to the LAPACK library should be adapted to your system. MOCCa uses the LAPACK library to solve the linear system involved in the DIIS procedure for density mixing, see section 4.9.4). This is far from necessary however, and disabling the DIIS option would result in a completely self-sufficient code.

11.2 Running MOCCa

For a successful run, MOCCa needs three things: an input file containing a set of single-particle wavefunctions, another file named 'forces.param' containing a set parameters of Skyrme parameterizations and runtime input on STDIN. In turn, MOCCa will produce an output file containing the single-particle wavefunctions (and various

[1] A very rare occurrence indeed on a what I imagine would be a scientific computation platform.

Compiler	Version	Comments
gfortran	4.7.2	
gfortran	4.8.1	
gfortran	4.8.2	
gfortran	4.8.3	
gfortran	5.3.0	
ifort	13.1.3	Needs -assume realloc-lhs flag
ifort	14.02	Needs -assume realloc-lhs flag
ifort	15.01	Needs -assume realloc-lhs flag
ifort	15.03	Needs -assume realloc-lhs flag
ifort	16.01	Needs -assume realloc-lhs flag

Table 11.1: Tested compilers that compile MOCCa correctly.

details of the calculation) and print output to STDOUT. The most practical way to run the code is then, with the runtime input located in a file 'MOCCa.data',

```
./MOCCa.exe < MOCCa.data > MOCCa.out
```

where one has to take care that MOCCa can find the input file and the 'forces.param' file. The use of the wavefunction input and output files, the runtime input and the 'forces.param' file is detailed in the following subsections.

11.2.1 Wavefunction files

The gradient descent algorithm needs a starting guess. This starting point can be generated either by a previous run of MOCCa itself, or by the older mean-field codes ev8, cr8 or ev4. The output of NIL8, the code generating Nilsson model wavefunctions, can also be used as input [9].
The code needs the filename of the input wavefunction file as runtime input on STDIN, using the keyword InputFileName. In order to determine the format of the wavefunction file, meaning by which mean-field code it was generated, MOCCa looks at the starting letters of the InputFileName string. If these match either 'EV8', 'NIL8', 'CR8', 'EV4' or 'MOCCA'[2] the code will select the correct reading routines. If no match is found, MOCCa will assume it is a wavefunction file generated by MOCCa itself. Wrongly signalling the type of file to the code will result in severe errors, as the input information will be completely garbled.
When input from either ev8, cr8 or ev4 is used, one should not expect MOCCa to give identical results before the start of the iterations. Neither of these codes writes all of the data that is needed to completely replicate a calculation to file and MOCCa is thus obliged to recalculate some quantities at the start of the iterations. For a calculation that was well-converged, this effect will be on the level of a few keV, provided the user took extreme care to replicate the conditions of the run of the original mean-field code.
Breaking of symmetries is also handled completely automatically withing MOCCa. The code can read symmetry-conserved files and explicitly break the symmetry before the start of iterations[3]. Simply specifying the broken symmetries in the runtime input will make MOCCa apply the necessary transforms. Note however that this is only possible when starting from wavefunction files generated by MOCCa, input from the older mean-field codes cannot be used directly in symmetry-breaking calculations.

11.2.2 Runtime Input

The runtime options are organized in a number of FORTRAN namelists, which are a rather human-readable way of specifying input. A certain number of namelists needs to be present in every input datafile, while others are optional. The possible namelists are shown in Table 11.2. Note that the order is important and cannot be changed. The various keywords that MOCCa recognizes are grouped by namelist in Tables 11.3 through 11.16. Fig. 11.1 shows the minimal input MOCCa requires to function, corresponding to a Hartree-Fock calculation of ^{64}Ge for the parameters of chapter 7.
Most of the input parameters are fairly straightforward in usage, although it is useful to know that the input of

[2] This matching is not case-sensitive.
[3] For obvious reasons, MOCCa can not be expected to read symmetry-broken files and then try to re-conserve them.

Namelist	Comments	Concerns
/GenInfo/	Required	Mesh parameters, iteration scheme, nucleus
/SpwfStorage/	Required	Single-particle wavefunctions
/Densit/	Required	Mean-field densities
/Pairing/	Required	Type of pairing, pairing interaction
/HFConfig/	Optional	Hartree-Fock configuration
/Derivatives/	Required	Usage of derivatives
/MomentParam/	Required	General options for multipole constraints
/MomentConstraint/	Optional, repeatable	Specific input for single multipole constraints
/SpecialMoments/	Optional	For user-defined quantities to constrain
/InAndOutput/	Required	In- and output of wavefunction files
/Force/	Required	Skyrme parameterization options
/Coulomb/	Required	Coulomb solver options
/Cranking/	Required	General options for cranking constraints

Table 11.2: List of the namefiles of a MOCCa runtime input.

MOCCa is insensitive to case in all respects. Three namelists merit some additional attention: the /HFConfig/, /SpecialMoments/ and /MomentConstraint/.
The first, /HFConfig/ needs to be announced to the code by setting `HFConfig` to .true. in the /Pairing/ namelist. As it details the Hartree-Fock configuration desired (see sec 6.2) based on both parity and signature quantum numbers, it can presently only be used when both symmetries are conserved.
The second namelist /SpecialMoments/ deals with the addition of constraints on quantities that are not included by default in MOCCa. Its presence should be announced to the code by putting SpecialInput to .true.
The final namelist /MomentConstraint/ is not only optional, but repeatable, as for every time it is mentioned MOCCa adds a constraint on the corresponding multipole moment. The first presence of /MomentConstraint/ should be announced by setting `MoreConstraints` to .true. in the obligatory /MomentParam/ namelist. Further constraints can be added by including /MomentConstraint/ again, and setting `MoreConstraints` to .true. in the preceding namelist. As example, Fig. 11.2a shows the necessary input in order to impose constraints on $\langle\hat{\mathcal{Q}}_{20}\rangle$ and $\langle\mathrm{Re}\,\hat{\mathcal{Q}}_{22}\rangle$, when the user references the expected values of the multipole moments. A special case is the (q_1, q_2) representation of the quadrupole moments, see appendix C. Constraints on both quadrupole degrees of freedom need to be declare, but the reference to the (`iq1`, `iq2`) variables should only be made once. Fig 11.2a shows valid runtime input for this case.
Further examples of runtime input are provided with the MOCCa code itself in the folder `Examples/`.

```
&geninfo
protons=32, neutrons=32
nx=16,ny=16,nz=16,dx=1.0
MaxIter=1000, dt=0.02/

&SpwfStorage
nwt=64/

&Densit/
&Pairing/
&Derivatives/
&MomentParam/
&InAndOutput
OutputFileName="MOCCa.Ge64"
InputFileName="MOCCa.Ge64"/

&Force
afor="Sly4"/

&Coulomb/
&Cranking/
```

Figure 11.1: Minimal input for a calculation with MOCCa.

```
&MomentParam
MoreConstraints=.true./

&MomentConstraint
l=2,m=0,
Constraint=100,
MoreConstraints=.true./

&MomentConstraint
l=2,m=2,Constraint=0/
```

(a) Using the multipole values.

```
&MomentParam
MoreConstraints=.true./

&MomentConstraint
l=2,m=0,
iq1=100.0, iq2=0.0,
MoreConstraints=.true./

&MomentConstraint
l=2,m=2/
```

(b) Using iq1 and iq2.

Figure 11.2: Runtime input corresponding to constraints on $\langle\hat{\mathcal{Q}}_{20}\rangle$ and $\langle\hat{\mathcal{Q}}_{22}\rangle$.

/GenInfo/

Mesh options	nx, ny, nz, dx	Sec. 4.1
Nucleus	Neutrons, Protons	
Iteration	dt, MaxIter, PrintIter, KineticDamping, E0, TaylorOrder IterType, Restart	Sec. 4.1, 4.9
Symmetries	TimeReversal, Parity, Signature, TimeSimplex, Isospin	Sec. 4.2
Convergence	MomentPrec, EnergyPrec, PairingPrec, CrankPrec	Sec. 4.8
Error	ErrorFileName	
`nx, ny, nz`	integer Number of mesh points represented by MOCCa in every Cartesian direction.	Default: N.A.
`dx`	real Mesh discretisation size in Fermi.	Default: N.A.
`Neutrons, Protons`	real Number of neutrons, resp.protons for the many-body state to have on average. Needs to be integer in case of Hartree-Fock pairing.	Default: N.A.
`dt`	real Size of time-step of the iterative algorithm.	Default: 0.012
`MaxIter`	integer Maximum number of mean-field iterations to perform.	Default: 0
`PrintIter`	integer Number of iterations between printouts.	Default: 0.1×MaxIter
`KineticDamping`	logical If .true. precondition the gradient descent steps.	Default: .false.
`E0`	real E_0 parameter of the preconditioning operator $\hat{P}$.	Default: 100
`IterType`	character Use imaginary time-step algorithm ('ImTs') or Nesterov iterations ('Nest').	Default: 'ImTS'
`Restart`	integer Number of iterations after which to restart when using Nesterov Iterations.	Default: 25
`ErrorFileName`	character(len=256) File to write error messages to.	Default: 'MOCCa.error'
`MomentPrec`	real Convergence criterion for multipole moments.	Default: 10^{-4}
`EnergyPrec`	real Convergence criterion for the energy calculated from the functional.	Default: 10^{-9}
`PairingPrec`	real Convergence criterion for the quantities related to pairing.	Default: 10^{-6}
`CrankPrec`	real Convergence criterion on (projections of) angular momentum.	Default: 10^{-4}
`TimeReversal`	integer Conserve(1) or break(0) time-reversal symmetry.	Default: 1
`Parity`	integer Conserve(1) or break(0) parity symmetry.	Default: 1
`Signature`	integer Conserve(1) or break(0) signature symmetry.	Default: 1
`TimeSimplex`	integer Conserve(1) or break(0) y-time-simplex symmetry.	Default: 1
`Isospin`	integer Conserve(1) or break(0) isospin symmetry. Note that the second option is not implemented yet.	Default: 1

Table 11.3: Namelist `GenInfo`, its input parameters and the relevant sections in this dissertation.

/SpwfStorage/

General	nwt, PrintingWindow	Sec. 4.4
`nwt`	integer Total number of single-particle wavefunctions. Needs to match the number of wavefunctions on the input file.	Default: N.A.
`PrintingWindow`	real `MOCCa` prints only single-particle states within this distance from the Fermi energy, both in the Hartree-Fock and canonical basis.	Default: 10.0

Table 11.4: Namelist `SpwfStorage`, its input parameters and the relevant sections in this dissertation.

/Densit/

General	DampingParam, MixingScheme, PulayOrder, Recalc	Sec. 4.7.1
`DampingParam`	real Damping parameter for the linear density mixing.	Default: 0.85
`MixingScheme`	integer Use linear mixing(0) or DIIS mixing(1).	Default: 0
`PulayOrder`	integer Number of previous iterations to include in the DIIS mixing.	Default: 0
`Recalc`	logical Recalculate mean-field densities at the start of equations (.true.) or us the densities from file (.false.).	Default: .false.

Table 11.5: Namelist `densit`, its input parameters and the relevant sections in this dissertation.

/Pairing/		
General options	Type, SolvePairingStart, PairingIter	Sec .6.1
Pairing Interaction	PairingNeutron, PairingProton,AlphaProton, AlphaNeutron, Rhosat CutNeutron, CutProton, PairingMu, CutType	Sec. 3.9
Hartree-Fock	HFConfig, FreezeOccupation	Sec. 6.2
BCS	ConstantGap,NeutronGap, ProtonGap	Sec. 6.3, 6.5
`Type`	character(len=3) Do a Hartree-Fock ('HF'), HF+BCS ('BCS') or HFB ('HFB') calculation.	Default: 'HF '
`SolvePairingStart`	logical Solve the pairing equations at the start of the iterations (.true.) or not (.false.). Cannot be de-activated in the case of HFB.	Default: .true.
`PairingIter`	integer Maximum number of iterations for the pairing solver. Note that the default value is 1 when doing HFB calculations.	Default: 50
`PairingNeutron`, `PairingProton`	real Pairing strength V_n, V_p in MeV fm^3. Note that if the user specifies one, but not the other, `MOCCa` takes $V_n = V_p$.	Default: 0.0
`alphaneutron`, `alphaproton`	real Density dependence parameter α_q of the pairing interaction. Note that if the user specifies one, but not the other, `MOCCa` takes $\alpha_n = \alpha_p$.	Default: 0.0
`rhosat`	real Saturation value of the nuclear density to be used in the pairing interaction.	Default: 0.16
`CutNeutron`, `CutProton`	real Cutoff-lenght Δe_q for neutrons and protons. Note that if the user specifies one, but not the other, `MOCCa` takes $\Delta e_n = \Delta e_p$.	Default: 0.0
`PairingMu`	real Value of the pairing-cutoff dispersion μ.	Default: 0.5
`CutType`	integer Use a symmetric Fermi pairing cutoff (1) or a piece-wise cosine cutoff (2).	Default: 1
`HFConfig`	logical If .true. signals the presence of a `HFConfig` namelist in the input. Only to be activated for Hartree-Fock calculations.	Default: .false.
`FreezeOccupation`	logical If .true. `MOCCa` will not change the occupation numbers in the case of a Hartree-Fock calculation.	Default: .false.
`ConstantGap`	logical If .true., keep the pairing gaps constant when doing a BCS calculation.	Default: .false.
`NeutronGap`,`ProtonGap`	real When `ConstantGap` is .true., these are the values for Δ_p and Δ_n. Note that if the user specifies one, but not the other, `MOCCa` takes $\Delta_n = \Delta_p$.	Default: 0.0

Table 11.6: First part of the `Pairing` Namelist: general, pairing interaction, Hartree-Fock and BCS options.

/Pairing/

HFB	FermiSolver, HFBIter, QPPrintWindow, Lipkin, LNFraction, LNFixN, LNFixP	Sec. 6.4.3
	ConstrainDispersion, DN2P, DN2N	Sec. 6.5
	Block, GuessKappa	Sec. 6.8
	HFBgauge	App. G
`FermiSolver`	character(len=9) In the case of HFB pairing, use the bisection solver ('BISECTION'), the Broyden solver ('BROYDEN') or the Thouless method ('GRADIENT'). Note that the Thouless method can only be started from a `MOCCa` wavefunction file that contains a HFB state.	Default: 'BROYDEN'
`HFBIter`	integer Maximum number iterations for the Fermi solver in case of HFB pairing. Note the default value is clearly insufficient when using the Thouless method to solve the HFB equations, values of 100 500 are more appropriate in that case.	Default: 50
`GuessKappa`	logical Use the values of the anomalous density matrix κ from the wavefunction file(.false.) or reinitialize κ (.true.).	Default: .false.
`QPPrintWindow`	real Print only quasiparticles for which $\|E_{qp}\|$ is smaller than this value.	Default: 100.0
`Block`	integer Non-zero values signal the presence of a `Blocking` namelist further down the runtime input and the number of quasiparticle indices to block.	Default: 0
`HFBGauge`	real Gauge parameter α to use in the HFB Hamiltonian.	Default: 0.0
`Lipkin`	logical If .true. use the Lipkin-Nogami prescription for λ_2 when doing a HFB calculation.	Default: .false.
`LNFraction`	real Portion of the λ_2 contribution to the HFB Hamiltonian to be added to the single-particle Hamiltonian $\hat{h}$. (1 - LNFraction) will then be added to the pairing matrix Δ.	Default: 1.0
`LNFixN,LNFixP`	real Values of the λ_2 parameter constraining the dispersion for neutrons and protons.	Default: 0.0
`ConstrainDispersion`	logical If .true., constrain the values of the neutron and proton dispersion.	Default: .false.
`DN2N,DN2P`	real If ConstrainDispersion is .true. constrain the values of the neutron and proton dispersion to these values. Note that if the user specifies one, but not the other, `MOCCa` takes $\Delta N_p^2 = \Delta N_n^2$.	Default: 0.0

Table 11.7: Second part of the Pairing namelist: HFB options.

/HFConfig/

General	Npp,Npm,Nmp,Nmm,Ppp,Ppm,Pmp,Pmm	Sec. 6.2
Npp,Ppp	integer Number of positive signature, positive parity occupied neutron/proton states.	Default: 0
Nmp,Pmp	integer Number of negative signature, positive parity occupied neutron/proton states.	Default: 0
Npm,Ppm	integer Number of positive signature, negative parity occupied neutron/proton states.	Default: 0
Nmm,Pmm	integer Number of negative signature, negative parity occupied neutron/proton states.	Default: 0

Table 11.8: Namelist HFConfig, its input parameters and its relevant sections.

/Derivatives/

General	MaxFDOrder, MaxFDLapOrder, CoulombLapOrder, OptDer, BStack	Sec.4.1
MaxFDOrder	integer Order of finite difference formula for the first order derivative. Possible values: 1,2,3,4 or -1 for Lagrange derivatives.	Default: 3
MaxFDLapOrder	integer Order of finite difference formula for the second order derivative. Possible values: 1,2,3,4 or -1 for Lagrange derivatives.	Default: 4
CoulombLapOrder	integer Order of finite difference formula for the second order derivative in the Coulomb routines. Possible values: 1,2,3,4 or -1 for Lagrange derivatives.	Default: 2
OptDer	logical If .true., allow MOCCa to use optimized derivation routines for the derivatives, leading to significantly reduced CPU time. Note that the availability of these routines depend on the choices of symmetries and the parameters MaxFDOrder and MaxFDLapOrder.	Default: .true.
BStack	logical Calculate the action of the $\mathbf{B}$ mean-field potential through the chain-rule for derivatives (.false.) or by stacking derivatives (.true.).	Default: .true.

Table 11.9: Namelist Derivatives and its input parameters.

/MomentParam/

General	QuantisationAxis,SecondaryAxis	Sec. C.3.2
Constraints	ContinueMoment,MoreConstraints,SpecialInput	Chapter 5
Predictor-corrector	c0,d0,epsilon	Sec .5.4
Cut-off	CutoffType,radd, acut	Sec. 5.6
`QuantisationAxis`	integer Quantisation axis of the multipole moments: x(1), y(2) or z(3).	Default: 3
`SecondaryAxis`	integer Alphabetical order (1) of the two other axes or anti-alphabetical order(2).	Default: 1
`ContinueMoment`	logical If .true. take the values of the Lagrange multipliers of the constraints from the wavefunction file. If .false. initialize the Lagrange multipliers from the runtime input.	Default: .false.
`MoreConstraints`	logical Signals the presence of a namelist `MomentConstraint` after this one.	Default: .false.
`SpecialInput`	logical If .true. signals that a namelist `SpecialInput` will follow.	Default: .false.
`c0,d0,epsilon`	real C_0, d_0 and ϵ parameters for the predictor-corrector constraints.	Default: 0.2,0.01,7
`CutoffType`	integer Type of cutoff for the constraints. Spherical(1) or density-dependent(0).	Default: 0
`radd`	real Radius parameter for the cutoff.	Default: 4.0
`acut`	real Diffusion length parameter for the cutoff.	Default: 0.4

Table 11.10: Namelist `MomentParam` and its input parameters.

/MomentConstraint/

General	l,m,Impart,MoreConstraints	Sec. 5
Constraint values	Constraint, ConstraintNeutrons,ConstraintProtons,iq1,iq2	App. C
Constraint options	Isoswitch, Intensity,Total,ConstraintType,Intensity	Sec. 5.5
`l,m`	integer Values of (l,m) of the multipole moment to constrain. Must be smaller than MaxMoment. $\ell = -1$ corresponds to the rms radius.	Default: 0,0
`Impart`	logical Constrains the real(.false.) or the imaginary part(.true.) of the multipole moment.	Default: false
`MoreConstraints`	logical Signals the presence of another namelist `MomentConstraint` after this one.	Default: .false.
`Constraint`	real Desired value of the multipole moment, either isoscalar or isovector, depending on the value of isoswitch.	Default: 0.0
`ConstraintNeutrons/Protons`	real Desired value of the multipole for neutrons, respectively protons.	Default: 0.0
`iq1,iq2`	real Legacy option only valid for $\langle\hat{\mathcal{Q}}_{20}\rangle$ and $\langle\hat{\mathcal{Q}}_{22}\rangle$. Corresponds to the constraint options of `cr8`.	Default: 0.0
`Isoswitch`	integer Constraint on the total(isoscalar) multipole moment(1), neutrons and protons separately(2) or the difference of protons and neutrons(3).	Default: 1
`Total`	logical Constraint on $\langle\hat{\mathcal{Q}}_{\ell m}\rangle$ or on the total multipole moment Q_ℓ.	Default: .false.
`ConstraintType`	integer Type of constraint: no constraint(0), predictor-corrector(1) or augmented Lagrangian(2).	Default: 0
`Intensity`	real Intensity C_O of the constraint in the case of the augmented Lagrangian algorithm.	Default: 0.0

Table 11.11: Namelist `MomentConstraint` and its input parameters.

/SpecialMoments/

General	SchiffMoment,Constraint,ConstraintType	Sec. 5.5.4
SchiffMoment	integer When equal to 1, MOCCa calculates and prints the Schiff-moment.	Default: 0
ConstrainType	integer Type of constraint to place on the Schiff moment. No constraint(0), predictor-corrector constraints(1) or augmented Lagrangian (2).	Default: 0
Constraint	real Desired value of the Schiff moment.	Default: 0.0
Intensity	real Intensity C_O of the augmented Lagrangian constraint, if ConstraintType is equal to 2.	Default: 0.0

Table 11.12: Namelist SpecialMoments and its input parameters.

/InAndOutput/

Filenames	InputFileName,OutputFileName	
General	PromOutput,LegacyInput	
InputFileName	character(len=256) Name of the input wavefunction file. See the section on wavefunction files for the naming convention.	Default: 'fort.12'
OutputFileName	character(len=256) Name of the output wavefunction file.	Default: 'fort.13'
PromOutput	logical If .true. MOCCa writes an additional output file with the name of OutputFileName, but with extension .prom'. This can be used as input by the projection codes Promesse and Prom4.	Default: .false.
LegacyInput	logical When .true. MOCCa assumes the wavefunction file is in an older MOCCa format.	Default: .false.

Table 11.13: Namelist InAndOutput and its input parameters.

/Force/

General	afor, SkyrmeTreatment	App. A
afor	character(len=200) Name of Skyrme parameterisation to use, must be located of 'forces.param'.	Default: ''
SkyrmeTreatment	character(len=200) Print the contribution to the function either term by term ('DEFAULT') or grouped per coupling constant ('BTERMS').	Default: 'DEFAULT'

Table 11.14: Namelist Force and its input parameters.

/Coulomb/

General	CoulombMax,CoulombSolver, CEX/Y/Z, MaxLCoul	Sec. 4.7.2, App F
`CoulombMax`	integer Maximum number of iterations for the Coulomb solver.	Default: 500
`CoulombSolver`	integer Choice of the algorithm for solving the Poisson equation. No contribution from Coulomb(0), Conjugate Gradient(1), Red-black Gauss-Seidel(2) or Symmetric overrelaxation (3).	Default: 1
`CEX/Y/Z`	integer Number of points to add to boundary of the Cartesian mesh for the solution of the Coulomb problem. Note that this is the number of points on every side, and physical number of extra points is double this number.	Default: 0
`MaxLCoul`	integer Value of the highest order ℓ multipole moment to include in the boundary conditions of the Coulomb problem.	Default: 0

Table 11.15: Namelist `Coulomb` and its input parameters.

/Cranking/

Cranking values	OmegaX/Y/Z,CrankX/Y/Z,ContinueCrank	Sec. 5.5.3
Algorithm options	CrankDamp,CrankReadj,CrankTypeX/Y/Z,CrankC0	Chapter 5
`OmegaX/Y/Z`	real Value of the cranking frequency ω in the three Cartesian directions at the start of the iterations.	Default: 0.0
`CrankX/Y/Z`	real Desired value of the (projections) of the angular momentum.	Default: 0.0
`ContinueCrank`	logical Use the values of $\omega_{x/y/z}$ read from file to start the iterations.	Default: .false.
`CrankDamp`	real Slowdown factor for the contribution of the cranking contribution to the mean-field potentials.	Default: 0.95
`CrankReadj`	real Readjustment speed of the cranking constraint, takes the role of ϵ when using predictor-corrector constraints.	Default: 1.0
`CrankTypeX/Y/Z`	integer Type of constraint to use for the three Cartesian directions: no constraint (0), predictor-corrector(1) or augmented Lagrangian(2). Linear constraint can be used by using the predictor-corrector constraints with CrankReadj=0.	Default: 0
`CrankC0`	real Value of the C_0 parameter of predictor-corrector constraints for the cranking constraints.	Default: 0.8

Table 11.16: Namelist `Cranking` and its input parameters.

11.2.3 The 'forces.param' file

The forces.param file contains the details of parameterizations and is based on the design of the file of same name of the LENTEUR code. It is a practical way of maintaining a database of parameterizations for use in MOCCa. The disadvantage is that this file should be present in the current directory whenever MOCCa is run. The file itself is a list of namelists, al of the same type named /skf/. MOCCa will scan this file for a parameterization whose name matches the input parameter 'afor' from the /Force/ namelist. If found, the parameters of the corresponding parameterization are then used in the calculation. The details of the namelist /skf/ can be found in Table 11.17 and can be crossreferenced with Appendix A, which also contains a representative list of Skyrme parameterizations already defined.

/skf/

Coupling constants	t0,x0,t1,x1,t2,x2,x3a,x3b,t3a,t3b te,to,wso,wsoq	App. A
Natural constants	hbm,e2,hbar,nucleonmass,averagemass	App. A
Other options	COM1Body,J2Terms	Sec. 1.4.5
`t0,t1,t2,t3a,t3b`	real The $t_0, t_1, t_2, t_{3a}, t3b$ coupling constants of the Skyrme force.	Default: 0.0
`x0,x1,x2,x3a,x3b`	real The $x_0, x_1, x_2, x_{3a}, x_{3b}$ coupling constants of the Skyrme force.	Default: 0.0
`yt3a,yt3b`	real The α_a, α_b density dependence parameters of the Skyrme force.	Default: 0.0
`te,to,wso,wsoq`	real The t_e, t_o and W, W_q coupling constants of the Skyrme force.	Default: 0.0
`hbm`	real(x2) The value of $\frac{\hbar^2}{2m_q}$ in units of MeV fm^2. By default $\frac{\hbar^2}{2m_n} = \frac{\hbar^2}{2m_p} = 20.73551910$ MeV fm^2.	Default:
e2	real The value of the proton electric charge squared, e^2, in units of MeV fm. By default $e^2 = 1.43996446$ MeV fm.	Default:
`nucleonmass`	real(x2) The value of the nucleon masses in MeV c^{-2}, by default $(m_n, m_p) = (939.565379, 938.272046)$	Default:
`averagemass`	logical If .true. set the nucleon masses m_q to the average of the values in the array nucleonmass.	Default: .true.
`COM1Body`	integer(x2) Usage of the one-body centre-of-mass correction: no correction (0), perturbatively(1) or self-consistently(2).	Default: (2,0)
`J2Terms`	logical If .true., calculate the coupling constants B_{14}, B_{15}, B_{18} and B_{19} and use the corresponding terms in the functional. If .false., set them to zero.	Default: .false.

Table 11.17: Namelist `skf` and its input parameters that forms the 'forces.param' file.

11.3 List of source code files

Included here is also a list of files included in the present MOCCa distribution with a brief description of its functions, in order to give readers a first idea. Where possible a reference point is given to the relevant definitions and equations in this dissertation.

`BCS.f90` *Section 6.3*
All specific code for solving the BCS pairing equations.

`CompilationInfo.f90`
Contains the definition of the precision of real nubers used in MOCCa.

`Coulomb.f90` *Section 4.7.2, Appendix F*
Contains all of the routines to solve the Coulomb problem, with the exception of derivation routines to represent the Laplacian in the Poisson equation.

`CoulombDerivatives.f90` *Section 4.7.2, Appendix F*
Contains the routines to represent the Laplacian of the Poisson equation in the enlarged Coulomb box.

`Cranking.f90`, *Chapter 5*
Contains the variables related to constraining the components of the angular momentum and calculates the contribution of these constraints to the mean-fields.

`Damping.f90` *Section 4.9.2*
Contains the routines to apply the preconditioning operator from Eq. (4.40), in practice applying Eq. (4.43).

`Densities.f90`, *Sections 1.4.1, 3.2 and 4.7*
Contains the routines that calculate the mean-field densities, Eqs. (1.16), either using the Hartree-Fock basis or from the canonical basis.

`DensityMixing.f90`, *Section 4.9.4*
Contains the routines to perform the DIIS mixing of the mean-field densities.

`Derivatives.f90`, *Section 4.1 and chapter 8*
Routines that perform finite difference and lagrange derivatives on the Lagrange mesh. These are general versions that work for all symmetry combinations and are rather slow.

`Energy.f90`, *Section 1.4 and Appendix A*
Contains routines to calculate (and print) all the terms of the Skyrme functional.

`Force.f90` *Section 1.4 and A*
Manages all of the coupling constants of the Skyrme functional.

`GenInfo.f90` *Chapter 4*
Manages the parameters of the Lagrange mesh and other general parameters.

`GradientHFB.f90` *Section 6.7 and Appendix E*
Contains all of the routines to solve the HFB using the gradient HFB algorithm.

`HartreeFock.f90` *Section 6.2*
Contains the routines to pick the desired Hartree-Fock configuration.

`HFB.f90` *Section 6.4*
Contains all of the routines to solve the HFB pairing equations. Delegates the solving to `GradientHFB.f90` if the user requests the gradient algorithm to solve the HFB equations.

`ImaginaryTime.f90` *Sections 4.4, 4.9.2 and 4.9.3*
Contains the routines that execute the gradient descent algorithm, as well as the preconditioned gradient descent and the Nesterov iterations.

`InOut.f90` *Section 11.2*
Routines that regulate the input (both runtime and wavefunction files) and the output.

`Interfaces.f90`
Contains routines that allow `MOCCa` to read wavefunction files generated by `ev8`, `cr8` and `ev4`. Also contains an (experimental) routine that writes output that can be read by the projection codes.

`Main.f90` *Chapter 4*
Definition of the main program and iterative loop and judges convergence. Calls routines from the various modules.

`MeanFields.f90` *Section 1.4 and Appendix A*
Contains the routines to calculate the mean-field potentials from the mean-field densities. Also contains the routines to calculate the actions of the potentials on the single-particle wavefunctions.

`Mesh.f90` *Section 1.4 and Appendix A*
Determines the coordinates of the mesh points of the Lagrange mesh for the different symmetry combinations.

`Moments.f90` *Chapter 5 and Appendix C*
Regulates the expressions, calculation and constraints on multipole moments (including the rms-radius).

`OptimizedDerivatives.f90` *Section 4.1*
Contains optimized derivation routines for specific spatial symmetry combinations, that are generally significantly faster than the routines in `Derivatives.f90`.

`Pairing.f90` *Chapter 6*
General module that delegates between `PairingInteraction.f90`, `BCS.f90` and `HFB.f90` to solve the pairing equations.

`PairingInteraction.f90` *Chapter 6*
Module able to calculate the contribution of the pairing interaction to the pairing field in Eqs. 6.4 and 6.17.

`SpecialMoments.f90` *Section 2.9.1 and chapter 5*
Contains the definition of the Schiff nuclear moment and the routines to calculate its contribution to the Routhian when constrained. New constraints on other operators that are not yet implemented can easily be included here.

`Spinor.f90` *Section 4.3*
Contains the definition of the `Spinor` derived type, representing a spinor on the Lagrange mesh.

`Spwf.f90` *Section 4.3*
Contains the definition of the `Spwf` derived type, representing a single-particle wavefunction with isospin, parity, z-signature and y-time-simplex quantum numbers. It consists of five `Spinor` derived types representing the single-particle wavefunction itself, three first order derivatives of it and one being the laplacian of the wavefunction.

`SpwfStorage.f90` *Chapters 3and Chapter 4*
Contains the Hartree-Fock and canonical basis and the routines to perform the Gram-Schmidt orthogonalization.

`Transform.f90` *Chapter 11.2*
Contains all of the routines to transform the input from one combination of symmetries to a different set.

Chapter 12

Conclusion

In this dissertation we have presented a new framework to study nuclei in a mean-field model using Skyrme functionals. This framework, called MOCCa, is a direct generalisation of the methods pioneered by the Brussels-Saclay-Orsay collaboration, that have proven their worth in numerous applications [9, 72, 22]. By representing the single-particle wavefunctions on a Lagrange mesh [86, 87], this framework offers the user simple and complete control over the numerical accuracy of the solution and a large degree of flexibility to impose or relax symmetry constraints on the many-body wavefunction.
Part I of this thesis introduced the theoretical background of self-consistent calculations employing Skyrme functionals, paying special attention to the consequences of conserved symmetries as well as the opportunities of symmetry breaking. The more practical aspects of solving the equations were introduced in part II. Since a piece of software on the scale of MOCCa rapidly becomes very complex, we attempted to describe the algorithms behind the solving process in the most complete way possible. The description of the algorithm(s) for solving the mean-field equations, the treatment of constraints and the solution methods for the pairing equations should (in principle) put the reader in the position of constructing a functionally equivalent code. In addition, an extensive study was made of the factors that govern the numerical accuracy of the framework. Two new numerical additions compared to the predecessors ev8, cr8 and ev4 merit extra attention: the predictor-corrector constraints and the Thouless method for solving the HFB equations. Predictor-corrector constraints allow for a more automatic constraint handling, especially in the context of symmetry-broken calculations. The Thouless method allows for solving the HFB equations when one no longer imposes a signature symmetry, which turned out to be impossible in practice using the direct diagonalisation method. Part III of this dissertation focused on two applications: a proof-of-concept study of shape transitions in a series of Radium isotopes, notably describing the fission barriers of ^{226}Ra and ^{227}Ra using the recent SLy5sX family of functionals [118]. A second application concerned the rms charge radii of the Hg isotopes, specifically focusing on the more neutron-deficient ones $A = 176 - 190$ and the experimentally observed odd-even staggering between $A = 180$ and $A = 186$. A complete manual of MOCCa forms the final part of this text. While a manual is not part of a traditional dissertation (or research article), it is a too often neglected part of scientific software packages. It is my personal hope that this manual will help users that want to employ MOCCa on a day-to-day basis.
Some further comments on subjects that did not make into this dissertation are in order. Firstly, the number of applications of MOCCa in this document is not large. The unfortunate reality is that the development (and debugging) of the code took a very long time. In addition, the number of use-cases of the code is enormous, with more than 100 different input parameters, all of which need to be tested and cross-checked where possible with the older codes. In particular calculations of the type dubbed 'tilted axis cranking' (see chapter 2) turned out to be significantly more challenging than first thought. While tilted-axis cranking is by now often performed in Nilson-Strutinsky calculations and similar models [98], the literature on the subject in mean-field calculations is basically limited to [53, 147]. Other signature breaking calculations have been reported in [60], though not related to tilted-axis-cranking. While we attempted many times to recreate the results from [53] in particular, it is not clear how one can reliably occupy the correct Hartree-Fock configuration in our framework. Calculations with pairing included as in [60, 147] turned out to be even more problematic, as one needs a way to discern between HFB quasiparticles, as detailed in chapter 6. While [60] briefly comments on this issue no practical solution is presented and [147] does not mention any problems at all[1]. With the development of the Thouless method however, applying the machinery of MOCCa to a tilted axis calculation is within the possibilities, as was demonstrated for ^{64}Ge in chapter 7.

[1] This might be explained by the different representation schemes (both are based on a representation in a spherical oscillator basis) and/or a difference in the solution algorithms, but this is to be investigated further.

Looking to the future, the existence of MOCCa opens up an enormous amount of possibilities. Direct comparisons to experiment are now feasible in a significantly larger amount of cases. Examples that will be first choices in the future include tilted-axis cranking, scissor modes and octupole deformation in the Ra region. In particular for odd-A nuclei, the reach of framework is now significantly larger, mostly by virtue of the breaking of parity and signature symmetries. The description of fission of odd-A nuclei, as well as applications to the Schiff moment can be performed in the near future. Note that not only the reach of the mean-field framework of the Brussels-Lyon collaboration has been enriched, as already now MOCCa has been interfaced with the existing beyond-mean-field codes.
Beyond what is already possible now, the modular aspect of the code opens a window on even more applications. With moderate effort, several extensions can be envisioned. First is the inclusion of the new type of functionals that correspond to a many-body Hamiltonian [16], to bring the code up to par with the latest developments of cr8. The development of projection techniques for both signature and parity restoration to complement the current suite of beyond-mean-field techniques is a second very promising avenue. A third extension would be the breaking of z-isospin symmetry, allowing MOCCa to really probe virtually every combination of symmetries ever explored in the literature.

Part V

Appendices

Appendix A

The Skyrme Functional in MOCCa

A.1 The Skyrme part of the functional

The most general Skyrme energy density [22, 21, 23, 19, 10] that MOCCa can handle is given by

$$
\begin{aligned}
\mathcal{E}_{Skyrme} &= \mathcal{E}^t_{Skyrme} + \mathcal{E}^p_{Skyrme} + \mathcal{E}^n_{Skyrme}\,, \\
\mathcal{E}^t_{Skyrme}(\mathbf{r}) &= B_1\rho_t^2 + B_3\left(\rho_t\tau_t - \mathbf{j}_t^2\right) + B_5\rho_t\Delta\rho_t + B_{7a}\rho_t^{2+\alpha_a} + B_{7b}\rho_t^{2+\alpha_b} + B_9\left(\rho_t\nabla\cdot\mathbf{J}_t + \mathbf{j}_t\cdot\nabla\times\mathbf{s}_t\right) \\
&\quad + B_{10}\mathbf{s}_t^2 + B_{12a}\rho_t^{\alpha_a}\mathbf{s}_t^2 + B_{12b}\rho_t^{\alpha_b}\mathbf{s}_t^2 + B_{14}\left(\sum_{\mu,\nu=x,y,z} J_{t,\mu\nu}J_{t,\mu\nu} - \mathbf{s}_t\cdot\mathbf{T}_t\right) \\
&\quad + B_{16}\left[\left(\sum_{\mu=x,y,z} J_{t,\mu\mu}\right)^2 + \sum_{\mu,\nu} J_{t,\mu\nu}J_{t,\nu\mu} - 2\mathbf{s}_t\cdot\mathbf{F}_t\right] + B_{18}\mathbf{s}_t\cdot\Delta\mathbf{s}_t + B_{20}\left(\boldsymbol{\nabla}\cdot\mathbf{s}_t\right)^2\,, \\
\mathcal{E}^q_{Skyrme}(\mathbf{r}) &= B_2\rho_q^2 + B_4\left(\rho_q\tau_q - \mathbf{j}_q^2\right) + B_6\rho_q\Delta\rho_q + B_{8a}\rho_t^{\alpha_a}\rho_q^2 + B_{8b}\rho_t^{\alpha_b}\rho_q^2 + B_{9q}\left(\rho_q\nabla\cdot\mathbf{J}_q + \mathbf{j}_q\cdot\nabla\times\mathbf{s}_q\right) \\
&\quad + B_{11}\mathbf{s}_q^2 + B_{13a}\rho_t^{\alpha_a}\mathbf{s}_q^2 + B_{13b}\rho_t^{\alpha_b}\mathbf{s}_q^2 + B_{15}\left(\sum_{\mu,\nu=x,y,z} J_{q,\mu\nu}J_{q,\mu\nu} - \mathbf{s}_q\cdot\mathbf{T}_q\right) \\
&\quad + B_{17}\left[\left(\sum_{\mu=x,y,z} J_{q,\mu\mu}\right)^2 + \sum_{\mu,\nu} J_{q,\mu\nu}J_{q,\nu\mu} - 2\mathbf{s}_q\cdot\mathbf{F}_q\right] + B_{19}\mathbf{s}_q\cdot\Delta\mathbf{s}_q + B_{21}\left(\boldsymbol{\nabla}\cdot\mathbf{s}_q\right)^2\,.
\end{aligned}
\tag{A.1}
$$

A.2 Isospin representation of the Skyrme energy density

Instead of the representation in proton-neutron densities, the Skyrme energy density can also be written down as a function of isoscalar and isovector densities. We define

$$
\begin{aligned}
\rho_0(\mathbf{r}) &= \rho_n(\mathbf{r}) + \rho_p(\mathbf{r})\,, \\
\rho_1(\mathbf{r}) &= \rho_n(\mathbf{r}) - \rho_p(\mathbf{r})\,,
\end{aligned}
\tag{A.2}
$$

and similar for the other mean-field densities. In isospin representation the Skyrme energy density becomes

$$
\mathcal{E}_{Skyrme} = \sum_{t=0,1}\mathcal{E}^t_{Sk} \tag{A.3a}
$$

$$
\begin{aligned}
\mathcal{E}^t_{Skyrme} &= C_t^{\rho}\left[\rho_0\right]\rho_t^2 + C_t^{\Delta\rho}\rho_t\Delta\rho_t + C_t^{\tau}\rho_t\tau_t + C^{\nabla\cdot J}\rho_t\boldsymbol{\nabla}\cdot\boldsymbol{J}_t^{(1)} - C_t^T\sum_{\mu,\nu=x,y,z} J_{t,\mu\nu}J_{t,\mu\nu} \\
&\quad + C_t^s[\rho_0]\mathbf{s}_t^2 + C_t^{\nabla\cdot s}\left(\boldsymbol{\nabla}\cdot\mathbf{s}_t\right)^2 + C_t^{\Delta s}\mathbf{s}_t\cdot\Delta\mathbf{s}_t - C_t^{\tau}\mathbf{j}_t^2 + C_t^T\mathbf{s}_t\cdot\mathbf{T}_t + C_t^{\nabla\cdot J}\mathbf{s}_t\cdot\boldsymbol{\nabla}\times\mathbf{j}_t \\
&\quad + C_t^F\mathbf{s}_t\cdot\mathbf{F}_t - \frac{1}{2}C_t^F\left[\left(\sum_{\mu=x,y,z} J_{t,\mu\mu}\right)^2 + \sum_{\mu,\nu=x,y,z} J_{t,\mu\nu}J_{t,\nu\mu}\right]\,,
\end{aligned}
\tag{A.3b}
$$

and the coefficients C_t^ρ and C_t^s are defined as

$$C_t^\rho\left[\rho_0\right] = C_t^\rho[0] + \left(C_t^\rho\left[\rho_{\text{sat}}\right] - C_t^\rho[0]\right)\left[\left(\frac{\rho_0}{\rho_{\text{sat}}}\right)^{\alpha_a} + \left(\frac{\rho_0}{\rho_{\text{sat}}}\right)^{\alpha_b}\right], \tag{A.4a}$$

$$C_t^s\left[\rho_0\right] = C_t^s[0] + \left(C_t^s\left[\rho_{\text{sat}}\right] - C_t^s[0]\right)\left[\left(\frac{\rho_0}{\rho_{\text{sat}}}\right)^{\alpha_a} + \left(\frac{\rho_0}{\rho_{\text{sat}}}\right)^{\alpha_b}\right], \tag{A.4b}$$

and ρ_{sat} is the value of the isoscalar density ρ_0 in saturated infinite nuclear matter.

A.3 Coupling constants

The coupling constants B_1 through B_{21} are determined in MOCCa by input from the `forces.param` file. The relevant keywords are described in section 11.2.3, and in general refer to the following variables

$$t_0, t_1, t_2, t_{3a}, t_{3b}, x_0, x_1, x_2, x_{3a}, x_{3b}, t_e, t_o, W, W_q, \alpha_a, \alpha_b\,. \tag{A.5}$$

These relate to the B coupling constants as follows

$$B_1 = \frac{t_0}{2}\left(1 + \frac{1}{2}x_0\right), \qquad B_2 = -\frac{t_0}{2}\left(\frac{1}{2} + x_0\right), \tag{A.6a}$$

$$B_3 = \frac{1}{4}\left[t_1\left(1 + \frac{1}{2}x_1\right) + t_2\left(1 + \frac{1}{2}x_2\right)\right], \qquad B_4 = -\frac{1}{4}\left[t_1\left(\frac{1}{2} + x_1\right) - t_2\left(\frac{1}{2} + x_2\right)\right], \tag{A.6b}$$

$$B_5 = -\frac{3}{16}\left[t_1\left(1 + \frac{1}{2}x_1\right) - t_2\left(1 + \frac{1}{2}x_2\right)\right], \qquad B_6 = \frac{3}{16}\left[t_1\left(\frac{1}{2} + x_1\right) + t_2\left(\frac{1}{2} + x_2\right)\right], \tag{A.6c}$$

$$B_{7a} = \frac{t_{3a}}{12}\left(1 + \frac{1}{2}x_{3a}\right), \qquad B_{8a} = -\frac{t_{3a}}{12}\left(x_{3a} + \frac{1}{2}\right), \tag{A.6d}$$

$$B_{7b} = \frac{t_{3b}}{12}\left(1 + \frac{1}{2}x_{3b}\right), \qquad B_{8b} = -\frac{t_{3b}}{12}\left(x_{3b} + \frac{1}{2}\right), \tag{A.6e}$$

$$B_9 = -\frac{W}{2}, \qquad B_{9q} = -\frac{W_q}{2}, \tag{A.6f}$$

$$B_{10} = \frac{1}{4}t_0x_0, \qquad B_{11} = -\frac{t_0}{4}, \tag{A.6g}$$

$$B_{12a} = \frac{t_{3a}x_{3a}}{24}, \qquad B_{13a} = -\frac{x_{3a}}{24}, \tag{A.6h}$$

$$B_{12b} = \frac{t_{3b}x_{3b}}{24}, \qquad B_{13b} = -\frac{x_{3b}}{24}, \tag{A.6i}$$

$$B_{14} = -\frac{1}{8}(t_1x_1 + t_2x_2) + \frac{1}{4}(t_e + t_o), \qquad B_{15} = \frac{1}{8}(t_1 - t_2) - \frac{1}{4}(t_e - t_o), \tag{A.6j}$$

$$B_{16} = -\frac{3}{8}(t_e + t_o), \qquad B_{17} = \frac{3}{8}(t_e - t_o), \tag{A.6k}$$

$$B_{18} = -\frac{1}{32}(3t_1x_1 - t_2x_2) + \frac{1}{16}(3t_e - t_o), \qquad B_{19} = \frac{1}{32}(3t_1 + t_2) - \frac{1}{16}(3t_e + t_o), \tag{A.6l}$$

$$B_{20} = \frac{3}{16}(3t_e - t_o), \qquad B_{21} = -\frac{3}{16}(3t_e + t_o). \tag{A.6m}$$

The coupling constants of the isospin representation of the functional can be obtained as linear combinations of the B coupling constants, see e.g. [19]. MOCCa does print the values of these, but does not use them internally to compute the energy.

A.4 The single-particle Hamiltonian $\hat{h}$

The single-particle Hamiltonian $\hat{h}_q$ due to the complete functional can be split into three contributions

$$\hat{h}^q = \hat{h}^q_{\text{Skyrme}} + \hat{h}^q_{\text{Coul}} + \hat{h}^q_{\text{Corr}}\,. \tag{A.7}$$

The Skyrme contribution is given by

$$\begin{aligned}\hat{h}^q_{\text{Skyrme}} = &-\boldsymbol{\nabla}\cdot B_q\boldsymbol{\nabla} + U_q + \mathbf{S}_q\cdot\hat{\boldsymbol{\sigma}} + \frac{1}{2i}\sum_{\mu,\nu=x,y,z}\left[W_{q,\mu\nu}\nabla_\mu\hat{\sigma}_\nu + \nabla_\mu\hat{\sigma}_\nu W_{q,\mu\nu}\right] \\ &+ \frac{1}{2i}\left[\boldsymbol{A}_q\cdot\boldsymbol{\nabla} + \boldsymbol{\nabla}\cdot\boldsymbol{A}_q\right] - \boldsymbol{\nabla}\cdot\left[\hat{\boldsymbol{\sigma}}\cdot\mathbf{C}_q\right]\boldsymbol{\nabla} - \frac{1}{2}\boldsymbol{\nabla}\cdot\mathbf{D}_q\hat{\boldsymbol{\sigma}}\cdot\boldsymbol{\nabla} \\ &- \frac{1}{2}\sum_{\mu,\nu=x,y,z}\left(\nabla_\nu D_\mu\sigma_\nu\nabla_\mu + D_\mu\sigma_\nu\nabla_\mu\nabla_\nu\right)\,,\end{aligned} \tag{A.8}$$

where the mean-field potentials $B, U, W_{\mu\nu}, \mathbf{A}, \mathbf{S}, \mathbf{C}$ and $\mathbf{D}$ are given by

$$B_q = \frac{\hbar^2}{2m_q} + B_3\rho_t + B_4\rho_q\,, \tag{A.9}$$

$$\begin{aligned}U_q = &\,2B_1\rho_t + 2B_2\rho_q + B_3\left(\tau_t + i\boldsymbol{\nabla}\cdot\mathbf{j}_t\right) + B_4\left(\tau_q + i\boldsymbol{\nabla}\cdot\mathbf{j}_q\right) + 2B_5\Delta\rho_t + 2B_6\Delta\rho_q \\ &+ B_{7a}\left(2+\alpha_a\right)\rho_t^{1+\alpha_a} + B_{7b}\left(2+\alpha_b\right)\rho_t^{1+\alpha_b} + B_8\left(\alpha\rho_t^{\alpha-1}\left[\rho_q^2+\rho_{q'}^2\right] + 2\rho^\alpha\rho_q\right) \\ &+ B_9\boldsymbol{\nabla}\cdot\mathbf{J}_t + B_{9q}\boldsymbol{\nabla}\cdot\boldsymbol{J}_q + \alpha_a\rho_t^{\alpha_a-1}\left(B_{12a}\mathbf{s}_t^2 + B_{13a}\left(\mathbf{s}_q^2+\mathbf{s}_{q'}^2\right)\right) \\ &+ \alpha_b\rho_t^{\alpha_b-1}\left(B_{12b}\mathbf{s}_t^2 + B_{13b}\left(\mathbf{s}_q^2+\mathbf{s}_{q'}^2\right)\right)\,,\end{aligned} \tag{A.10}$$

$$\begin{aligned}W_{\mu\nu,q} = &\sum_{j=x,y,z}\epsilon_{j\mu\nu}\left(B_9\nabla_j\rho_t + B_{9q}\nabla_j\rho_q\right) + 2B_{15}J_{q,\mu\nu} + 2B_{16}\left(J_{t,\nu\mu} + \sum_{j=x,y,z}J_{t,jj}\delta_{\mu\nu}\right) \\ &+ 2B_{17}\left(J_{q,\nu\mu} + \sum_{j=x,y,z}J_{q,jj}\delta_{\mu\nu}\right),\end{aligned} \tag{A.11}$$

$$\mathbf{A}_q = -2B_3\,\mathbf{j}_t - 2B_4\mathbf{j}_q + B_9\boldsymbol{\nabla}\times\mathbf{s}_t + B_{9q}\boldsymbol{\nabla}\times\mathbf{s}_q\,, \tag{A.12}$$

$$\begin{aligned}\mathbf{S}_q = &\,B_9\boldsymbol{\nabla}\times\mathbf{j}_t + B_{9q}\boldsymbol{\nabla}\times\mathbf{j}_q + 2B_{10}\mathbf{s}_t + 2B_{11}\mathbf{s}_q + 2B_{12a}\rho^{\alpha_a}\mathbf{s}_t + 2B_{13a}\rho_t^{\alpha_a}\mathbf{s}_q \\ &+ 2B_{12b}\rho^{\alpha_b}\mathbf{s}_t + 2B_{13b}\rho_t^{\alpha_b}\mathbf{s}_q - B_{14}\mathbf{T}_t - B_{15}\mathbf{T}_q - 2B_{16}\mathbf{F}_t - 2B_{17}\mathbf{F}_q \\ &+ 2B_{18}\Delta\mathbf{s}_t + 2B_{19}\Delta\mathbf{s}_q - 2B_{20}\boldsymbol{\nabla}\left(\boldsymbol{\nabla}\cdot\mathbf{s}_t\right) - 2B_{21}\boldsymbol{\nabla}\left(\boldsymbol{\nabla}\cdot\mathbf{s}_q\right)\,,\end{aligned} \tag{A.13}$$

$$\mathbf{C}_q = -B_{14}\mathbf{s}_t - B_{15}\mathbf{s}_q\,, \tag{A.14}$$

$$\mathbf{D}_q = -2B_{16}\mathbf{s}_t - 2B_{17}\mathbf{s}_q\,. \tag{A.15}$$

Note that the contribution of the kinetic energy to the single-particle Hamiltonian is contained in the action of the B_q potential, which is why we did not split $\hat{h}_q$ into four parts.
Compared to [22] and `cr8` some conventions have changed, the potential $\mathbf{C}$ corresponds to $-\mathbf{A}$ and our $\mathbf{S}$ potential corresponds to $\mathbf{V}$ from the same paper. Note also that the formula given in Eq. (25) of [19] contains two errors. First, the sign of the B_9 and B_{9q} terms in the $W_{\mu\nu}$ potential is opposite the correct sign used in the mean-field codes. A second more insidious error is that the action of the D-potential is not hermitian [148], as it does not contain the final term involving the $\mathbf{D}$ potential of Eq. A.8. While this was wrongly implemented at the time of [19] this error has meanwhile been corrected in `cr8` and `MOCCa`[1].
A third error is (at the time of writing) still affecting `cr8` and `ev8`: the B_{16} and B_{17} terms in the energy density and the single-particle Hamiltonian erroneously did not include the contribution of $J^{(0)}$, although they are included in Eq. (25) of [19]. These terms are correctly included in `MOCCa`.
The Coulomb contribution for protons is simply

$$\hat{h}^p_{\text{Coul}} = V(\mathbf{r}) - \left(\frac{3}{\pi}\right)^{\frac{1}{3}}e^2\rho_p^{\frac{1}{3}}(\mathbf{r})\,, \tag{A.16}$$

where $V(\mathbf{r})$ is the Coulomb potential of the proton charge density. The neutron contribution is of course zero. Depending on what is incorporated in E_{Corr}, $\hat{h}_{\text{Corr}^q}$ can take many different forms. In `MOCCa` only the one-body centre-of-mass correction can be included. The corresponding contribution to the single-particle Hamiltonian becomes

$$\hat{h}^q_{\text{Corr}} = \frac{\hbar^2}{2(Nm_n + Zm_p)}\Delta\,. \tag{A.17}$$

[1] Since the $\mathbf{D}$-potential is time-odd this error did not affect `ev8` and `ev4`.

A.5 Details of the numerical implementation

We will here list some specifics of the implementation in MOCCa, since not all terms are of the single-particle Hamiltonian are trivial to implement.

A.5.1 The effective mass term

The term proportional to $B_q(\mathbf{r})$ in the single-particle Hamiltonian needs some care. Indeed, we can write the action on a single-particle wavefunction of isospin q as

$$[\boldsymbol{\nabla} \cdot (B_q(\mathbf{r})\boldsymbol{\nabla}\phi_q)](\mathbf{r},\sigma) = B_q(\mathbf{r})\,[\Delta\Psi_q](\mathbf{r},\sigma) + [\boldsymbol{\nabla}\Psi_q](\mathbf{r},\sigma)\,[\boldsymbol{\nabla}B_q](\mathbf{r})\,. \tag{A.18}$$

Mathematically the left-hand side and the right-hand side are equivalent. When the derivatives are implemented numerically with finite difference formulas, this is no longer the case.
One can easily check that

$$\Delta_{FD} \neq \boldsymbol{\nabla}_{FD} \cdot \boldsymbol{\nabla}_{FD}\,. \tag{A.19}$$

The default derivatives in MOCCa and the older codes all employ the left-hand side of Eq. (A.18). In addition, the FD formula is of the fourth order for the second order derivative, while the first order derivative only has a third order FD formula. This further increases the inconsistency between calculations using the left- or right-hand side of Eq. (A.18). Note that MOCCa can use either side of Eq. (A.18), depending on the keyword `BStack`. If it is set to '.true.' the left-hand side of Eq. (A.19) is used, while if it '.false.' the right-hand side is used.
The typical difference is not that big however, for a HF-calculation for ^{20}Ne with a mesh discretisation of $dx = 1$ fm the difference is typically about 50 keV. Since this difference is quite consistent across calculations it is usually of no importance. This inconsistency of course disappears when using Lagrange derivatives self-consistently, as Eq. (A.19) is a strict equality for that implementation of derivatives.
Similar concerns affect also the actions of the $\mathbf{C}$ and $\mathbf{D}$ potentials: the only option currently implemented is by using the equivalent of the left-hand side of Eq. (A.19).

A.5.2 The action of mean-field potentials A and W

The action of the mean-field potential $\mathbf{A}_q$ can be rewritten as

$$\frac{1}{2i}\left[\boldsymbol{A}_q \cdot \boldsymbol{\nabla} + \boldsymbol{\nabla} \cdot \boldsymbol{A}_q\right] = -i\boldsymbol{A}_q \cdot \boldsymbol{\nabla}\,, \tag{A.20}$$

because the curl of the divergence of $\mathbf{s}$ is zero and the divergence of the current $\mathbf{j}$ current can be related to the time-derivative of the density

$$\boldsymbol{\nabla} \cdot \mathbf{j} = -\frac{\partial \rho}{\partial t}\,, \tag{A.21}$$

under the condition of local gauge invariance of the functional [149]. This is the case for all of the functionals described in this dissertation and we can thus safely drop this term for the static calculations of MOCCa.
The action of the mean-field potential $W_{\mu\nu}$ is also simplified as

$$\frac{1}{2i}\sum_{\mu,\nu=x,y,z}\left[W_{q,\mu\nu}\nabla_\mu\hat{\sigma}_\nu + \nabla_\mu\hat{\sigma}_\nu W_{q,\mu\nu}\right] = -i\sum_{\mu,\nu=x,y,z} W_{q,\mu\nu}\nabla_\mu\hat{\sigma}_\nu\,. \tag{A.22}$$

The contribution of the B_9 term to $W_{\mu\nu}$ in Eq. (A.12) allows for this simplification, as the divergence of the curl of $\mathbf{j}$ is zero. It is unclear if this holds for the other contributions to $W_{\mu\nu}$. Nevertheless, both MOCCa and `cr8` implement the right-hand side of Eq.(A.22)[19].

A.5.3 The Coulomb contribution

As detailed in chapter 4, the direct Coulomb energy term is calculated by solving the Poisson equation and the exchange term is calculated using the Slater approximation. They also contribute to the proton single-particle Hamiltonian as described above. Since $\hat{h}^p_{\text{Coul}}$ is local in coordinate space, these terms are in MOCCa simply incorporated into the U mean-field potential.

SLy4,SLy5	[17]
SLy4T	[150]
SLy5s1/2/3/4/5/6/7/8	[118]
Skm*	[151]
T44, T46, T66	[21]
UNEDF0	[76]
UNEDF1	[18]
UNEDF2	[78]

Table A.1: Predefined functionals on the `forces.param` file shipped with `MOCCa`.

A.5.4 The contribution of the centre-of-mass correction

The contribution of E_{corr} to the single-particle Hamiltonian takes the same form as the action of the B_q potential. In `MOCCa`, it is taken into account by modifying this potential as follows

$$B_q = \frac{\hbar^2}{2m_q} + B_3\rho_t + B_4\rho_q \rightarrow \frac{\hbar^2}{2m_q}\left(1 - m_q\frac{1}{Nm_n + Zm_p}\right) + B_3\rho_t + B_4\rho_q\,. \tag{A.23}$$

A.5.5 Contribution from constraints

Constraints on multipole moments or on projections of the angular momentum also contribute to the single-particle Hamiltonian, as described in chapter 5. For the multipole moments (whose operators are local in coordinate space) this contribution is incorporated in the U mean-field potential. They always take the following simple form

$$U \rightarrow U - \sum_{\ell,m}\lambda^{(i)}_{\ell m}Q_{\ell m}(r,\theta,\phi)f(\mathbf{r})\,, \tag{A.24}$$

where the multipliers $\lambda^{(i)}$ are determined by the various recipes described in chapter 5. The factor $f(\mathbf{r})$ is a cutoff function, as described in section 5.6.
The case is not that simple for cranking constraints, as the operators $\hat{\mathcal{J}}$ involve derivatives and are thus not local in coordinate space. The contribution to the single-particle Hamiltonian is always of the following form

$$\hat{h}^{Sk}_q \rightarrow \hat{h}^{Sk}_q - \omega^{(i)}_\mu\hat{J}_\mu\,, \tag{A.25}$$

where again the $\omega^{(i)}_\mu$ are determined on the basis of the type of constraint. `MOCCa` takes this contribution into account in the same way as the original paper on `cr8` [22]: by modifying the potentials $\mathbf{A}$ and $\mathbf{S}$ as follows

$$\mathbf{A}(\mathbf{r}) \rightarrow \mathbf{A}(\mathbf{r}) - f(\mathbf{r})\,(\boldsymbol{\omega}\times\mathbf{r})\,, \tag{A.26a}$$

$$\mathbf{S}(\mathbf{r}) \rightarrow \mathbf{S}(\mathbf{r}) - f(\mathbf{r})\frac{1}{2}\boldsymbol{\omega}\,, \tag{A.26b}$$

where the vector $\boldsymbol{\omega}$ is simply the vector $(\omega_x,\omega_y,\omega_z)$ and the cutoff function $f(\mathbf{r})$ is identical to the one used for the multipole constraints.
In addition, the reader should not forget that the contribution of these constraints to the $U, \mathbf{S}$ and $\mathbf{A}$ potentials are subject to a damping procedure from one mean-field iteration to the next, see Eq. (5.30).

A.6 Functionals included with the code

The current version of `MOCCa` is completed by a `forces.param` file with a set of predefined functionals, ready to use. This set is summarized in Table A.1. A special remark is in order for the UNEDF0/1/2 parameterizations: the fits were performed with a finite pairing strength using a code that represents the single-particle wavefunctions in a harmonic-oscillator basis [76, 18, 78]. The pairing properties of this type of basis are unfortunately impossible to reproduce on a Lagrange mesh because of the differences between the bases. The recommended values of the pairing strength are thus not implemented and an exact replication of the features of these functionals is impossible.

Appendix B

Symmetry Operators

This appendix is dedicated to the classification and some not-so-trivial results on symmetry operator. Antilinear operators can be severely counterintuitive and are in many cases not standard fare in quantum mechanics textbooks. While we will be using the notation of single-particle operators and states, these considerations are perfectly applicable to many-body states and in fact to general Hilbert spaces.

B.1 Classification

Consider a symmetry operator $\hat{A}$. All of the symmetry operators we will encounter conserve probability amplitudes, that is to say

$$|\langle\psi|\phi\rangle|^2 = |\langle\hat{A}\psi|\hat{A}\phi\rangle|^2 \,. \tag{B.1}$$

Following Wigners arguments [152, 153], one can conclude that $\hat{A}$ should be either unitary or antiunitary

$$\langle\psi|\phi\rangle = \langle\hat{A}\psi|\hat{A}\phi\rangle \text{ or } \langle\psi|\phi\rangle^* = \langle\hat{A}\psi|\hat{A}\phi\rangle \,. \tag{B.2}$$

Unitary operators $\hat{A}$, denoted with a hat, are linear, meaning that for states $|\psi\rangle, |\phi\rangle$ and complex numbers a, b the following holds

$$\hat{A}\,(a\psi + b\phi) = a\hat{A}\psi + b\hat{A}\phi \,. \tag{B.3}$$

An antiunitary operator $\check{B}$, denoted with an inverted hat, is antilinear, meaning that for states $|\psi\rangle, |\phi\rangle$ and complex numbers a, b we have the following

$$\check{B}\,(a\psi + b\phi) = a^*\check{B}\psi + b^*\check{B}\phi \,. \tag{B.4}$$

The inverse of both unitary and antiunitary operators are given by their hermitian conjugates, meaning that for $\hat{A}$ and $\check{B}$ we have

$$\hat{A}^\dagger\hat{A} = \hat{A}\hat{A}^\dagger = \hat{\mathbb{1}} \,, \tag{B.5a}$$

$$\check{B}^\dagger\check{B} = \check{B}\check{B}^\dagger = \hat{\mathbb{1}} \,. \tag{B.5b}$$

One can further separate both the unitary and antiunitary operators into hermitian and antihermitian operators, respectively obeying

$$\hat{A}^\dagger = +\hat{A} \,, \text{ (hermitian)} \tag{B.6a}$$

$$\hat{A}^\dagger = -\hat{A} \,. \text{ (antihermitian)} \tag{B.6b}$$

B.2 Eigenstates, invariants and normal pairs

An eigenstate of a linear, unitary operator $\hat{A}$ is a state $|\phi\rangle$ so that

$$\hat{A}|\phi\rangle = a|\phi\rangle \,. \tag{B.7}$$

for some value a. Because of unitarity, we have $|a| = 1$. It is also well known that hermitian operators have real eigenvalues while antihermitian operators have purely imaginary eigenvalues. In both cases, the

eigenstates of linear operators form a complete basis of the Hilbert space.
The concept of eigenstate does not trivially generalize to antiunitary operators. Let us first limit ourselves to a hermitian, antiunitary operator $\check{B}$. Suppose we can find some state $|\phi\rangle$ so that

$$\check{B}|\phi\rangle = b|\phi\rangle\,. \tag{B.8}$$

Multiplying by a complex phase a produces a state that is still an eigenstate of $\check{B}$ but with a different eigenvalue, $\frac{a^*b}{a}$.

$$\check{B}a|\phi\rangle = a^*b|\phi\rangle = \frac{a^*b}{a}a|\phi\rangle. \tag{B.9}$$

If we hold on to the notion of a Hilbert space as a vector space, where the overall phase of a wavefunction does not matter, this means we are free to actually choose eigenvalues of $\check{B}$ by multiplying the states with a well chosen complex phase a.
The notion of eigenvalue for an antilinear hermitian operator is thus not very well defined in a physical sense[1]. We will refrain from using the terminology. Instead, we introduce an invariant state $|\Phi\rangle$ for an antilinear, hermitian operators as

$$\check{B}|\phi\rangle = |\phi\rangle\,, \tag{B.10}$$

which automatically fixes the phase of the state[2].
The situation for antiunitary, antihermitian operators is even more counterintuitive: an antilinear, antihermitian operator $\check{C}$ does not admit either eigenstates or invariants. Suppose that we have an eigenstate $|\phi\rangle$ with some eigenvalue c which is necessarily purely imaginary. Then we have immediately

$$c^*c|\Phi\rangle = \check{C}c|\Phi\rangle = \check{C}\check{C}|\Phi\rangle = -|\Phi\rangle\,, \tag{B.11}$$

which is strictly impossible. Wigner showed however that every antiunitary operator [152] could be brought into what he called 'normal form'. We will repeat here a slightly less general argument that is heavily inspired by Wigners argument, although slightly modernized. Since $\check{C}$ is antihermitian and antilinear, $\check{C}^2$ is necessarily hermitian and linear. We can diagonalize this operator to obtain eigenstates $|\phi_i\rangle$. We have thus

$$\check{C}^2|\phi_i\rangle = -|\phi_i\rangle\,. \tag{B.12}$$

Notice that $\check{C}|\phi_i\rangle$ is also an eigenvector of $\check{C}^2$ with eigenvalue -1, since

$$\check{C}^2\check{C}|\phi_i\rangle = \check{C}\check{C}^2|\phi_i\rangle = -\check{C}|\phi_i\rangle\,. \tag{B.13}$$

In addition $\check{C}|\phi_i\rangle$ is orthogonal to $|\phi_i\rangle$ since

$$\langle\phi_i|\check{C}|\phi_i\rangle = \langle\phi_i|\check{C}^\dagger\check{C}\check{C}|\phi_i\rangle = -\langle\phi_i|\check{C}|\phi_i\rangle\,. \tag{B.14}$$

This means that the set of $|\phi_i\rangle$ is a complete orthonormal set of states in the Hilbert space that consists of pairs of vectors that are linked by the action of $\check{C}$. In direct analog of Wigners 'normal form' we will call two conjugate states $(|\phi_i\rangle, \check{C}|\phi_i\rangle)$ a normal pair.
An often used notation (also in this dissertation) for a normal pair is $(|\phi_i\rangle, |\phi_i\rangle)$. Note that this notation hides a counterintuitive feature of a normal pair, as we have the following equations

$$\check{C}|\phi_i\rangle = \quad |\phi_{\bar{i}}\rangle\,, \tag{B.15}$$

$$\check{C}|\phi_{\bar{i}}\rangle = -|\phi_i\rangle\,. \tag{B.16}$$

B.3 Simultaneous eigenstates

Let us look at the possibilities of having wavefunctions that are simultaneous eigenstates of two operators $\hat{A}$ and $\hat{B}$. There are different relevant cases: when $\hat{A}$ and $\hat{B}$ are both linear operators, when $\hat{A}$ and $\check{B}$ are respectively hermitian linear and hermitian antilinear and when $\hat{A}$ and $\check{B}$ are respectively hermitian linear and antihermitian antilinear. Note that we do not have to treat the cases where either operator is antihermitian, antilinear, as these operators do not have eigenstates.

[1] Mathematically speaking, $|\phi\rangle$ and $a|\phi\rangle$ are different vectors in the Hilbert space and there is no problem at all. It is the physical requirement that what we observe are actually rays of vectors in Hilbert spaces rather than vectors in Hilbert space.
[2] In the language of Wigner [152, 153]: we have selected a particular element of the ray of $|\phi\rangle$

B.3.1 $\hat{A}$ and $\hat{B}$ are both linear

This is the classic textbook case. Consider an eigenstate $|\Psi\rangle$ of both $\hat{A}$ and $\hat{B}$ with eigenvalues a and b respectively. In that case we have

$$\hat{A}\hat{B}|\Psi\rangle = b\hat{A}|\Psi\rangle = ba|\Psi\rangle = \hat{B}a|\Psi\rangle = \hat{B}\hat{A}|\Psi\rangle\,, \tag{B.17}$$

from which it follows that

$$\left[\hat{A},\hat{B}\right] = 0\,. \tag{B.18}$$

The condition for the existence of simultaneous eigenstates of $\hat{A}$ and $\hat{B}$ is thus that $\hat{A}$ and $\hat{B}$ commute.

B.3.2 $\hat{A}$ is hermitian linear and $\check{B}$ is hermitian antilinear

Consider again an eigenstate $|\Psi\rangle$ of both $\hat{A}$ and $\check{B}$ with eigenvalues a and b respectively. Note that both a and b are necessarily real. We have again

$$\hat{A}\check{B}|\Psi\rangle = b\hat{A}|\Psi\rangle = ba|\Psi\rangle = \hat{B}a^*|\Psi\rangle = \hat{B}a|\Psi\rangle = \hat{B}\hat{A}|\Psi\rangle\,, \tag{B.19}$$

from which it follows that

$$\left[\hat{A},\hat{B}\right] = 0\,. \tag{B.20}$$

The condition for the existence of simultaneous eigenstates of $\hat{A}$ and $\hat{B}$ is thus that $\hat{A}$ and $\check{B}$ commute.

B.3.3 $\hat{A}$ is antihermitian linear and $\check{B}$ is hermitian antilinear

Consider again an eigenstate $|\Psi\rangle$ of both $\hat{A}$ and $\check{B}$ with eigenvalues a and b respectively. Note that both a is purely imaginary and that b is real. We have again

$$\hat{A}\check{B}|\Psi\rangle = \hat{A}b|\Psi\rangle = b\hat{A}|\Psi\rangle = ba|\Psi\rangle = ab|\Psi\rangle = a\check{B}|\Psi\rangle = \check{B}a^*|\Psi\rangle = -\check{B}a|\Psi\rangle = -\check{B}\hat{A}|\Psi\rangle\,, \tag{B.21}$$

and we conclude that if we want $\hat{A}$ and $\check{B}$ to have simultaneous eigenstates, they need to anticommute, i.e.

$$\left\{\hat{A},\check{B}\right\} = 0\,. \tag{B.22}$$

Appendix C

Multipole moments

The expectation values of multipole operators $\hat{\mathcal{Q}}_{\ell m}$, or multipole moments for short, characterize the shape of the nuclear density. They are primarily used to study the dependence of the energy (or other observables) as a function of nuclear shape, and can easily serve as good candidates for a GCM generator coordinate. In addition, they are intrinsically linked to the breaking of self-consistent symmetries, as many of them can be considered as order parameters of various spatial symmetries.

C.1 Definition

The single-particle multipole operators as used in this dissertation and as implemented in `MOCCa` are defined in spherical coordinates (r, θ, ϕ) as

$$\hat{Q}_{\ell m}(r, \theta, \phi) = \hat{r}^{\ell} \hat{Y}_{\ell m}(\theta, \phi) \qquad \text{with } \ell > 0 \text{ and } -\ell \leq m \leq \ell \tag{C.1}$$

where ℓ is a positive integer and m is an integer between $-\ell$ and ℓ. We take the following convention [154] for the spherical harmonics $\hat{Y}_{\ell m}(\theta, \phi)$

$$\hat{Y}_{\ell m}(\theta, \phi) = (-1)^m \sqrt{\frac{(2\ell+1)}{4\pi} \frac{(\ell-m)!}{(\ell+m)!}} P_{\ell}^{m}(\cos(\theta)) e^{im\phi} \,. \tag{C.2}$$

In this equation P_l^m is an associated Legendre polynomial. It is interesting to note that the $\hat{Q}_{\ell m}$ are sometimes called regular solid harmonics and form half of the solid harmonics [155]. The irregular solid harmonics are obtained by scaling the $\hat{Y}_{\ell m}$ with negative powers of r, but since they are singular at the origin they are not relevant for nuclear wavefunctions.
This definition makes the matrix elements of the multipole operators complex. The real and imaginary parts of the multipole operators of positive and negative m are related by the following equation

$$\hat{Q}_{\ell -m}^{\dagger} = (-1)^m \hat{Q}_{\ell m} \,. \tag{C.3}$$

It is thus possible for the implementation and printouts of `MOCCa` to forget about the multipole moments of negative m but rather refer to the real and imaginary parts of the $\hat{Q}_{\ell m}$ with $m \geq 0$.
The one-particle operators $\hat{Q}_{\ell m}$ have straightforward many-body counterparts

$$\hat{\mathcal{Q}}_{\ell m} = \sum_{i=1}^{A} \hat{Q}_{\ell m}(\mathbf{r}_i, \theta_i, \phi_i) \,. \tag{C.4}$$

For the expectation value in a many-body state of the many-body operator we have

$$\langle \hat{\mathcal{Q}}_{\ell m} \rangle = \sum_{i,j} \rho_{ij} \langle \phi_j | \hat{Q}_{\ell m, i} | \phi_i \rangle = \sum_{ij} \rho_{ij} \int d\mathbf{r}\, \phi_j^*(\mathbf{r}) \hat{Q}_{\ell m}(\mathbf{r}) \phi_i(\mathbf{r}) = \int d\mathbf{r}\, Q_{\ell m}(\mathbf{r}) \rho(\mathbf{r}) \,, \tag{C.5}$$

where we have dropped the hat on the $Q_{\ell m}$ in the last equality to emphasize that this is now simply a function of $\mathbf{r}$ and no longer an operator. Using this equality we can easily see that the expectation values of the $\hat{\mathcal{Q}}_{\ell m}$

are the in fact the coefficients of the expansion of $\rho(\mathbf{r})$ in solid harmonics.[1]
One can also look separately at the multipole expansion of the proton and neutron, or isoscalar and isovector densities

$$\langle \hat{\mathcal{Q}}_{\ell m,n} \rangle = \int d\mathbf{r}\, Q_{\ell m}(\mathbf{r}) \rho_n(\mathbf{r})\,, \tag{C.6a}$$

$$\langle \hat{\mathcal{Q}}_{\ell m,p} \rangle = \int d\mathbf{r}\, Q_{\ell m}(\mathbf{r}) \rho_p(\mathbf{r})\,, \tag{C.6b}$$

$$\langle \hat{\mathcal{Q}}_{\ell m,0} \rangle = \int d\mathbf{r}\, Q_{\ell m}(\mathbf{r}) \rho_0(\mathbf{r})\,, \tag{C.6c}$$

$$\langle \hat{\mathcal{Q}}_{\ell m,1} \rangle = \int d\mathbf{r}\, Q_{\ell m}(\mathbf{r}) \rho_1(\mathbf{r})\,. \tag{C.6d}$$

When a subscript is not explicitly indicated, the implied reference is to the multipole moment of the total density ρ_t, which coincides with ρ_0.
In order to meaningfully compare multipole moments of nuclei with different mass numbers A we define the dimensionless quantities $\beta_{\ell m}$ as

$$\beta_{\ell m} = \frac{4\pi}{3R_0^\ell A} \langle \hat{\mathcal{Q}}_{\ell m} \rangle\,, \tag{C.7}$$

where we take $R_0 = 1.2A^{1/3}$ fm.
Another derived quantity is the total multipole moment of degree ℓ, defined as

$$Q_\ell = \sqrt{\frac{16\pi}{2\ell+1} \sum_{m=-\ell,..,\ell} |\langle \hat{\mathcal{Q}}_{\ell m} \rangle|^2} = \sqrt{\frac{16\pi}{2\ell+1} \langle \hat{\mathcal{Q}}_{\ell 0} \rangle^2 + \frac{32\pi}{2\ell+1} \sum_{m=1,..,\ell} \langle \mathrm{Re}\, \hat{\mathcal{Q}}_{\ell m} \rangle^2 + \langle \mathrm{Im}\, \hat{\mathcal{Q}}_{\ell m} \rangle^2}\,, \tag{C.8}$$

which is a real quantity. This can also be transformed to a dimensionless quantity

$$\beta_\ell = \frac{4\pi}{3R_0^\ell A} Q_\ell\,, \tag{C.9}$$

where R_0 is taken as before. The interest of the total multipole moments $\hat{\mathcal{Q}}_\ell$ is the simplified picture they represent: it is the quantity that determines the total deformation of the nuclear density combined across the multipole moments of given ℓ but different values of m. For $\ell = 2$ this corresponds to the total 'size' of the quadrupole moment, and the degree of freedom not considered is the triaxiality angle γ, see section C.2. For $\ell = 3$, this again measures the total deformation, but this time leaving 6 relevant angles free [157, 158].
Figures C.1 and C.2 give the reader an idea of the deformation non-zero values of these multipole moments imply up to $\ell = 4$. What is plotted is either of the following surfaces

$$R(\theta,\phi) = (1 + \epsilon\ \mathrm{Re}\, Q_{\ell m}(\theta,\phi))\,, \tag{C.10a}$$

$$R(\theta,\phi) = (1 + \epsilon\ \mathrm{Im}\, Q_{\ell m}(\theta,\phi))\,, \tag{C.10b}$$

parametrized in spherical coordinates.

C.2 Quadrupole deformation

The quadrupole deformation parameters merit some extra attention, as they are by far the most widely used shape parameters of nuclear densities. Other parametrizations, specific to the quadrupole moments $\ell = 2$ are widely spread [10]. One of these is the Cartesian representation $(\hat{\mathcal{Q}}_x, \hat{\mathcal{Q}}_y, \hat{\mathcal{Q}}_z)$, which are related to the multipole operators by the following relations

$$\hat{\mathcal{Q}}_x = -\sqrt{\frac{4\pi}{5}} \left(\hat{\mathcal{Q}}_{20} - \sqrt{6} \hat{\mathcal{Q}}_{22} \right) = 2\hat{x}^2 - \hat{y}^2 - \hat{z}^2\,, \tag{C.11}$$

$$\hat{\mathcal{Q}}_y = -\sqrt{\frac{4\pi}{5}} \left(\hat{\mathcal{Q}}_{20} + \sqrt{6} \hat{\mathcal{Q}}_{22} \right) = 2\hat{y}^2 - \hat{x}^2 - \hat{z}^2\,, \tag{C.12}$$

$$\hat{\mathcal{Q}}_z = \sqrt{\frac{16\pi}{5}} \hat{\mathcal{Q}}_{20} \qquad\qquad = 2\hat{z}^2 - \hat{x}^2 - \hat{y}^2\,. \tag{C.13}$$

[1] Note that the calculation of magnetic multipole moments [156] is significantly more involved, as they depend on derivatives of the single-particle wavefunctions. They are currently not implemented in MOCCa and do not figure in this dissertation.

(a) $\hat{Q}_{20}$ (b) $\mathrm{Re}\,\hat{Q}_{21}$ (c) $\mathrm{Re}\,\hat{Q}_{22}$

(d) $\hat{Q}_{30}$ (e) $\mathrm{Re}\,\hat{Q}_{31}$ (f) $\mathrm{Re}\,\hat{Q}_{32}$ (g) $\mathrm{Re}\,\hat{Q}_{33}$

(h) $\mathrm{Re}\,\hat{Q}_{40}$ (i) $\mathrm{Re}\,\hat{Q}_{41}$ (j) $\mathrm{Re}\,\hat{Q}_{42}$ (k) $\mathrm{Re}\,\hat{Q}_{43}$ (l) $\mathrm{Re}\,\hat{Q}_{44}$

Figure C.1: Impression of deformation linked to the real parts of the multipole moments $\mathrm{Re}\,Q_{\ell m}$ for $\epsilon = 0.2$. The surfaces plotted are given by Eq. (C.10) with $\epsilon = 0.2$.

(a) $\mathrm{Im}\,\hat{Q}_{21}$ (b) $\mathrm{Im}\,\hat{Q}_{22}$ (c) $\mathrm{Im}\,\hat{Q}_{31}$ (d) $\mathrm{Im}\,\hat{Q}_{32}$ (e) $\mathrm{Im}\,\hat{Q}_{33}$ (f) $\mathrm{Im}\,\hat{Q}_{41}$ (g) $\mathrm{Im}\,\hat{Q}_{42}$ (h) $\mathrm{Im}\,\hat{Q}_{43}$ (i) $\mathrm{Im}\,\hat{Q}_{44}$

Figure C.2: Impression of deformation linked to the imaginary parts of the multipole moments $\mathrm{Im}\,Q_{\ell m}$. The surfaces plotted are given by Eq. (C.10) with $\epsilon = 0.2$.

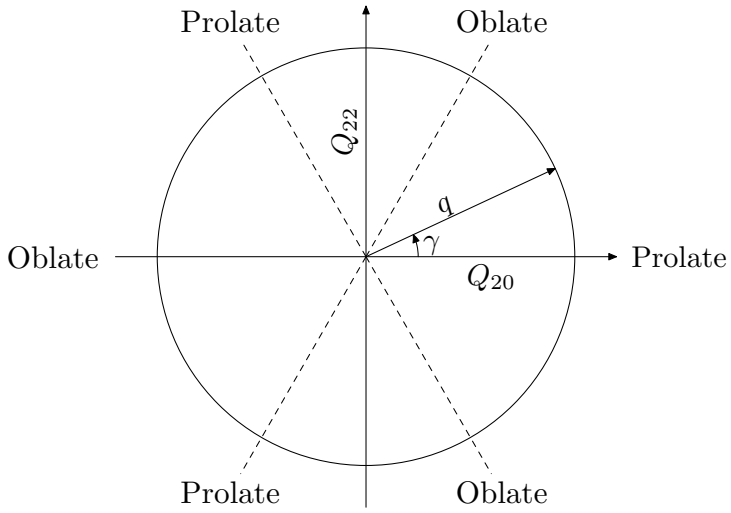

Figure C.3: Depiction of the (q, γ) and $(\langle\hat{\mathcal{Q}}_{20}\rangle, \langle\hat{\mathcal{Q}}_{22}\rangle)$ parameterization for the quadrupole moments. The Q_{20} and Q_{22} axes are drawn as full lines. Axial configurations lie either on the Q_{20} axis or on the drawn dotted lines. All other configurations are triaxial.

A third parametrization can be given in terms of the numbers (q, γ) which are related to the spherical harmonics and Cartesian representation by the following identities. Note the error in Eq. (68) in [10].

$$q = \sqrt{\frac{16\pi}{5}\left(\left\langle\hat{\mathcal{Q}}_{20}\right\rangle^2 + 2\left\langle\hat{\mathcal{Q}}_{22}\right\rangle^2\right)} = \sqrt{\frac{2}{3}\left(\left\langle\hat{\mathcal{Q}}_x\right\rangle^2 + \left\langle\hat{\mathcal{Q}}_y\right\rangle^2 + \left\langle\hat{\mathcal{Q}}_z\right\rangle^2\right)}\,, \tag{C.14}$$

$$\gamma = \mathrm{atan2}\left(\sqrt{2}\,\langle\hat{\mathcal{Q}}_{22}\rangle, \langle\hat{\mathcal{Q}}_{20}\rangle\right) \qquad = \mathrm{atan2}\left(\langle\hat{\mathcal{Q}}_x - \hat{\mathcal{Q}}_y\rangle, \sqrt{3}\langle\hat{\mathcal{Q}}_z\rangle\right)\,, \tag{C.15}$$

Note that this definition of q matches exactly the one for the total quadrupole moment β_2. This parameterization and its relation to the quadrupole moments $(\langle\hat{\mathcal{Q}}_{20}\rangle, \langle\hat{\mathcal{Q}}_{22}\rangle)$ are depicted in Fig. C.3.
We can again create a dimensionless parameter β_q for this parameterization,

$$\beta_q = \frac{4\pi}{3R_0^2 A} q\,. \tag{C.16}$$

A final parametrization of the quadrupole moments is defined in terms of (q, γ)

$$q_1 = q\cos(\gamma) - \frac{1}{\sqrt{3}} q\sin(\gamma)\,, \tag{C.17}$$

$$q_2 = \frac{2}{\sqrt{3}} q\sin(\gamma)\,. \tag{C.18}$$

This parameterization is the one used in the old codes `ev8`, `cr8` and `ev4` and can be used in `MOCCa` using the keywords `iq1` and `iq2`.
Let us finally remark on the words 'prolate', 'oblate' and 'triaxial' which are in extremely common usage in nuclear physics. Both 'prolate' and 'oblate' indicate axial configurations, meaning that the nucleus still has one rotational axis of symmetry. A configuration is prolate if the deformation along the symmetry axis is larger than the deformation along the two other axes and oblate if it is shorter. Any quadrupole configuration is triaxial if there is no longer a rotational symmetry axis present. A practical parameterization of prolate and oblate configurations is simply given by the sign of $\langle\hat{\mathcal{Q}}_{20}\rangle$: if it is positive the configuration is 'prolate', otherwise it is 'oblate'.[2] Other combinations of multipole moments can characterize the axial configurations, but they are related to this parameterization by a permutation of axes, see subsection C.3. The location of the prolate and oblate configurations in the (q, γ) plane is also depicted in Fig. C.3.

[2]This only works if all of the non-axial multipole moments $(m \neq 0)$ vanish, as otherwise we have no symmetry axis and the configuration is triaxial.

C.3 Redundant multipole moments

A certain nuclear density $\rho(\mathbf{r})$ is uniquely determined by the complete set of values of $\langle\hat{\mathcal{Q}}_{\ell m}\rangle$ for all ℓ and m. The reverse statement is also true: given all of the values of$\langle\hat{\mathcal{Q}}_{\ell m}\rangle$ one can reconstruct $\rho(\mathbf{r})$ at every point in space. There is a high degree of redundancy in the solid harmonics as a basis though: consider a density ρ and a rotated and displaced density ρ'. They are physically equivalent, but the multipole expansion of ρ' will be different from the one for ρ.
These redundant degrees of freedom are related to the choice of a Cartesian system of three axes (x,y,z). The three coordinates of the origin and three Euler angles of the orientation of the axes together constitute six continuous degrees of freedom. Even after choosing a Cartesian system of axes, there is still the degree of freedom related to the labeling of axes. We will investigate the consequences for both here.

C.3.1 The choice of Cartesian axes

The continuous degrees of freedom of the origin of the axes and their orientation in space all give rise to a corresponding degree of freedom for the multipole moments. The coordinates of the origin of the axes system are the most straightforward. Note that the multipole moments of degree one are proportional to the position operators $\hat{x}, \hat{y}$ and $\hat{z}$[3].

$$\hat{Q}_{10} \sim \hat{z}\,, \mathrm{Re}\,\hat{Q}_{11} \sim \hat{x}\,, \mathrm{Im}\,\hat{Q}_{11} \sim \hat{y}\,. \tag{C.19}$$

We will make the choice of origin in such a way that

$$\langle\hat{\mathcal{Q}}_{10}\rangle = \langle\hat{\mathcal{Q}}_{11}\rangle = 0\,. \tag{C.20}$$

In other words, we put the origin of the axes in the centre-of-mass of the nucleus. Different choices of the other origin are of course possible, but it is clear that this simply changes the localization of the nucleus in space. Differing values of the multipole moments of degree one are not linked to different shapes of $\rho(\mathbf{r})$.
There is another, more practical, reason to fix this particular choice of origin. If the nucleus would not have its centre-of-mass at the origin, the single-particle wavefunctions might have appreciable values near the boundary of the box, and thus deteriorating the accuracy of a calculation.
After fixing the origin, we are still left with the freedom of orienting our axes. We need two free parameters to fix a unit vector $\mathbf{e}_x$ that indicates the x-direction and one free parameter to choose a unit vector $\mathbf{e}_y$, orthogonal to $\mathbf{e}_x$. The z-direction is then fixed by requiring a right-handed Cartesian axis system. The convention used in this text and in `MOCCa` is to use these three degrees of freedom to eliminate the following three quadrupole moments.

$$\langle\mathrm{Im}\,\hat{\mathcal{Q}}_{22}\rangle = \langle\hat{\mathcal{Q}}_{21}\rangle = 0\,. \tag{C.21}$$

This is equivalent to requiring that

$$\langle\hat{x}\hat{y}\rangle = \langle\hat{x}\hat{z}\rangle = \langle\hat{y}\hat{z}\rangle = 0\,, \tag{C.22}$$

or requiring that the following tensor (often called the inertia tensor $\mathcal{I}$) is diagonal

$$\mathcal{I} = \begin{pmatrix} \hat{x}^2 & \hat{x}\hat{y} & \hat{x}\hat{z} \\ \hat{x}\hat{y} & \hat{y}^2 & \hat{y}\hat{z} \\ \hat{x}\hat{z} & \hat{y}\hat{z} & \hat{z}^2 \end{pmatrix}\,, \tag{C.23}$$

which can always be enforced by rotating the axes. As such, non-zero values of $\langle\mathrm{Im}\,\hat{\mathcal{Q}}_{22}\rangle$ or $\langle\hat{\mathcal{Q}}_{21}\rangle$ represent a rotation of the nucleus in space and as such do not indicate a physically different shape of $\rho(\mathbf{r})$.
While this choice is the one used in this dissertation and in `MOCCa`, one can use the six inherent degrees of freedom to eliminate other (combinations of) multipole moments as redundant degrees of freedom. See for instance [159], where specific combinations of octupole moments are eliminated.
As a concluding remark, note that the centre-of-mass coordinates and the three rotational degrees of freedom are only redundant when they pertain to the total mass distribution. The degrees of freedom regarding the isovector multipole moments $\langle\hat{\mathcal{Q}}_{10,1}\rangle, \langle\hat{\mathcal{Q}}_{11,1}\rangle, \langle\hat{\mathcal{Q}}_{21,1}\rangle$ and $\langle\mathrm{Im}\,\hat{\mathcal{Q}}_{22,1}\rangle$ are real physical degrees of freedom and represent respectively relative displacements and rotations of the proton and neutron density.

[3] Note that this specific matching in fact already implies a choice of axes: nevertheless for every choice the vector $(\hat{Q}_{10}, \mathrm{Re}\,\hat{Q}_{11}, \mathrm{Im}\,\hat{Q}_{11})$ corresponds to a permutation of $(\hat{x}, \hat{y}, \hat{z})$.

C.3.2 Labelling Cartesian axes

A second degeneracy arises due to the labelling of axes. The traditional way to associate (r, θ, ϕ) to (x, y, z) is

$$x = r \sin\theta \cos\phi \,, \tag{C.24a}$$
$$y = r \sin\theta \sin\phi \,, \tag{C.24b}$$
$$z = r \cos\theta \,. \tag{C.24c}$$

However, in a Cartesian coordinate system we have the freedom to interchange axes. In abusive notation, we have six possibilities of axis system

$$(x, y, z), \quad (y, x, z),$$
$$(z, x, y), \quad (x, z, y),$$
$$(y, z, x), \quad (z, y, x).$$

This translates to a freedom of choice in the definition of θ and ϕ. For each of these six combinations (x_1, x_2, x_3) the corresponding transform to spherical coordinates is given by

$$x_1 = r \sin\theta \cos\phi \,, \tag{C.25a}$$
$$x_2 = r \sin\theta \sin\phi \,, \tag{C.25b}$$
$$x_3 = r \cos\theta \,. \tag{C.25c}$$

While a nuclear density obviously is invariant under the specific choice of axes we choose to describe it, the multipole expansion of the nuclear density clearly is not. A given density $\rho(\mathbf{r})$ will give rise to different values of $\langle \hat{\mathcal{Q}}_{\ell m} \rangle$ in different choices for the axes.
When all of the symmetries in MOCCa[4] are conserved all of these six choices are indeed completely equivalent. The six possible permutations of (x,y,z) imply that we can describe the same density $\rho(\mathbf{r})$ with six different sets of values of the $\langle \hat{\mathcal{Q}}_{\ell m} \rangle$. Thus, when investigating different shapes of the nuclear densities, we need not investigate all of the possibilities: every shape can be represented in six different ways. This degeneracy can be seen on Fig. C.3 for the quadrupole moments, indicated by the dashed lines. Every sextant contains all of the possible shapes and corresponding shapes in different sextants are related by a permutation of the axes. The sextants are best categorized in terms of the angle γ, taking values in either $[0°, 60°]$, $[60°, 120°]$, $[120°, 180°]$, $[180°, 240°]$, $[240°, 300°]$ or $[300°, 360°]$.
However, it is very important to realize that this degeneracy breaks down whenever one introduces a preferred direction in space. With a preferred direction in space, the different sextants are no longer all equivalent as reorienting the nucleus in space will not result in the same configuration. When such a preferred direction is present, the six-fold degeneracy is lifted and a two-fold degeneracy takes its place, related to the labelling of the two non-preferred directions in space. Of course, when one adds another preferential direction (different from the first) this degeneracy is again lifted and all six sextants describe different physical configurations. This is of great practical importance for MOCCa, as cranking constraints introduce such preferred directions. Once one cranking frequency ω_{x_i} is non-zero, a given triaxial shape with a long, medium and short axis will have a different energy depending on the orientation of the shape with respect to the preferred direction x_i.

C.4 Consequences of the symmetries of MOCCa

The conservation of parity, z-signature and y-time-simplex introduce symmetries into the nuclear density ρ, see section 2.8, which in turn are reflected by the multipole moments of this density. Some $\beta_{\ell m}$ are restricted to be zero when these symmetries are conserved and consequently form natural order parameters for these symmetries.
Since the radial coordinate r is not affected by either $\hat{P}$, $\hat{R}_z$ or $\check{S}_y^T$, it is sufficient to look at the effect of those operators on $\cos\theta, \sin\phi$ and $\cos\phi$. This effect depends of course on the choice of axes we have made. The signs that $\cos\theta, \sin\phi$ and $\cos\phi$ receive under the action of the symmetries are summarized in Table C.1. The signs can be straightforwardly derived from Eqs. (C.25). Given the signs in Table C.1 and the fact that $P_\ell^m(-x) = (-1)^{\ell+m} P_\ell^m(x)$ one can deduce for every choice of axes (x_1, x_2, x_3) the multipole moments that are restricted by symmetries. As example, we detail up to $\ell = 3$ the multipole moments that are constrained by symmetry for the traditional choice $(x_1, x_2, x_3) = (x, y, z)$ in Table C.2.

[4] The same considerations are valid for ev8, ev4 and cr8.

	Symmetry	(x,y,z)	(y,x,z)	(z,x,y)	(x,z,y)	(y,z,x)	(z,y,x)
$\cos\theta$	$\hat{P}$	-	-	-	-	-	-
	$\hat{R}_z$	+	+	-	-	-	-
	$\check{S}_y^T$	+	+	-	-	+	+
$\cos[(2n+1)\phi]$	$\hat{P}$	-	-	-	-	-	-
	$\hat{R}_z$	+	-	+	-	-	+
	$\check{S}_y^T$	+	-	+	+	-	+
$\sin[(2n+1)\phi]$	$\hat{P}$	-	-	-	-	-	-
	$\hat{R}_z$	-	-	-	+	+	-
	$\check{S}_y^T$	-	+	+	+	+	-
$\cos[(2n)\phi]$	$\hat{P}$	+	+	+	-	+	+
	$\hat{R}_z$	+	+	+	-	+	+
	$\check{S}_y^T$	+	+	+	+	+	+
$\sin[(2n)\phi]$	$\hat{P}$	+	+	+	+	+	+
	$\hat{R}_z$	+	+	-	-	-	-
	$\check{S}_y^T$	-	-	+	+	-	-

Table C.1: Behavior of $\cos\hat{\theta}, \sin m\hat{\phi}$ and $\cos m\hat{\phi}$ $(m \neq 0)$ under the symmetry operators for odd and even m.

	$\ell=1$	$\ell=2$	$\ell=3$
$\hat{P}$	$\langle\hat{\mathcal{Q}}_{10}\rangle$, $\langle\hat{\mathcal{Q}}_{11}\rangle$		$\langle\hat{\mathcal{Q}}_{30}\rangle$,$\langle\hat{\mathcal{Q}}_{31}\rangle$, $\langle\hat{\mathcal{Q}}_{32}\rangle$,$\langle\hat{\mathcal{Q}}_{33}\rangle$
$\hat{R}_z$	$\langle\hat{\mathcal{Q}}_{11}\rangle$	$\langle\hat{\mathcal{Q}}_{21}\rangle$	$\langle\hat{\mathcal{Q}}_{31}\rangle$,$\langle\hat{\mathcal{Q}}_{33}\rangle$
$\check{S}_y^T$	$\mathrm{Im}\langle\hat{\mathcal{Q}}_{11}\rangle$	$\mathrm{Im}\langle\hat{\mathcal{Q}}_{21}\rangle$, $\mathrm{Im}\langle\hat{\mathcal{Q}}_{22}\rangle$	$\mathrm{Im}\langle\hat{\mathcal{Q}}_{31}\rangle$,$\mathrm{Im}\langle\hat{\mathcal{Q}}_{32}\rangle$,$\mathrm{Im}\langle\hat{\mathcal{Q}}_{33}\rangle$

Table C.2: Multipole moments up to $\ell = 3$ constrained by symmetries of MOCCa for the choice of axes $(x_1, x_2, x_3) = (x, y, z)$.

C.5 Redundant degrees of freedom in MOCCa

The redundant degrees of freedom have practical consequences when representing $\rho(\mathbf{r})$ on a Lagrange mesh in MOCCa, particularly when symmetries are broken.
The freedom of permutation of axes implies that we need only calculate one sextant of the entire $(\langle\hat{\mathcal{Q}}_{20}\rangle, \langle\hat{\mathcal{Q}}_{22}\rangle)$ plane when calculating energy surfaces. A user of MOCCa can either use directly the values of $(\langle\hat{\mathcal{Q}}_{20}\rangle, \langle\hat{\mathcal{Q}}_{22}\rangle)$ to constrain the code to particular orientations of the nuclear density or use the keyword `Quantisationaxis` to choose the permutation of the axes used and thus the sextant.[5]
Enforcing the redundant degrees of freedom in $\langle\hat{\mathcal{Q}}_{21}\rangle, \langle\mathrm{Im}\,\hat{\mathcal{Q}}_{22}\rangle$ and the centre-of mass coordinates to be zero in a mean-field procedure is another matter. The only feasible way to control these degrees of freedom is by introducing constraints on them. If one would leave these degrees of freedom unconstrained, the imaginary time-step would in general have troubles converging, as there would be infinitely many competing configurations would be either displaced or rotated compared to our convention.
Conserved symmetries do however limit the number of redundant degrees of freedom severely. Table C.4 shows the redundant degrees of freedom that MOCCa constrains automatically when breaking certain combinations of spatial symmetries. Note that these depend on the permutation of axes that was chosen, as the symmetries in MOCCa carry explicit references to the axis names.
As a side-remark: breaking symmetries is not only costly in terms of number of represented points on the mesh but also indirectly costly due to the added number of constraints. This severely impacts the effort needed to find the mean-field solution as simultaneously satisfying several constraints is rather difficult. When all of the spatial symmetries are broken MOCCa needs to satisfy six constraints on redundant degrees of freedom, in addition to any constraints imposed by the user.

[5] This might seem of academic interest, as the physics is generally independent of the choice of axes but this is not always the case. When introducing a cranking constraint on $\mathcal{J}_z$ for example, this creates a preferred direction in space and thus destroys the six-fold symmetry. In that case, a user might need MOCCa to generate shapes in a certain sextant.

Broken	Cartesian	Multipole					
		(x,y,z)	(x,z,y)	(y,x,z)	(y,z,x)	(z,x,y)	(z,y,x)
$\hat{\mathcal{P}}$	$\langle\hat{z}\rangle$	$\langle\hat{\mathcal{Q}}_{10}\rangle$	$\langle\mathrm{Im}\,\hat{\mathcal{Q}}_{11}\rangle$	$\langle\hat{\mathcal{Q}}_{10}\rangle$	$\langle\mathrm{Re}\,\hat{\mathcal{Q}}_{11}\rangle$	$\langle\mathrm{Im}\,\hat{\mathcal{Q}}_{11}\rangle$	$\langle\mathrm{Re}\,\hat{\mathcal{Q}}_{11}\rangle$
$\hat{\mathcal{R}}_z$	$\langle\hat{x}\hat{z}\rangle$	$\langle\mathrm{Re}\,\hat{\mathcal{Q}}_{21}\rangle$	$\langle\mathrm{Im}\,\hat{\mathcal{Q}}_{22}\rangle$	$\langle\mathrm{Im}\,\hat{\mathcal{Q}}_{21}\rangle$	$\langle\mathrm{Im}\,\hat{\mathcal{Q}}_{21}\rangle$	$\langle\mathrm{Im}\,\hat{\mathcal{Q}}_{22}\rangle$	$\langle\mathrm{Re}\,\hat{\mathcal{Q}}_{21}\rangle$
$\check{\mathcal{S}}_y^T$	$\langle\hat{x}\hat{y}\rangle$	$\langle\mathrm{Im}\,\hat{\mathcal{Q}}_{22}\rangle$	$\langle\mathrm{Re}\,\hat{\mathcal{Q}}_{21}\rangle$	$\langle\mathrm{Im}\,\hat{\mathcal{Q}}_{22}\rangle$	$\langle\mathrm{Re}\,\hat{\mathcal{Q}}_{21}\rangle$	$\langle\mathrm{Im}\,\hat{\mathcal{Q}}_{21}\rangle$	$\langle\mathrm{Im}\,\hat{\mathcal{Q}}_{21}\rangle$
$\hat{\mathcal{P}},\hat{\mathcal{R}}_z$	$\langle\hat{x}\rangle$	$\langle\mathrm{Re}\,\hat{\mathcal{Q}}_{11}\rangle$	$\langle\mathrm{Re}\,\hat{\mathcal{Q}}_{11}\rangle$	$\langle\mathrm{Im}\,\hat{\mathcal{Q}}_{11}\rangle$	$\langle\hat{\mathcal{Q}}_{10}\rangle$	$\langle\mathrm{Im}\,\hat{\mathcal{Q}}_{11}\rangle$	$\langle\hat{\mathcal{Q}}_{10}\rangle$
$\hat{\mathcal{P}},\check{\mathcal{S}}_y^T$	$\langle\hat{y}\rangle$	$\langle\mathrm{Im}\,\hat{\mathcal{Q}}_{11}\rangle$	$\langle\hat{\mathcal{Q}}_{10}\rangle$	$\langle\mathrm{Re}\,\hat{\mathcal{Q}}_{11}\rangle$	$\langle\mathrm{Re}\,\hat{\mathcal{Q}}_{11}\rangle$	$\langle\hat{\mathcal{Q}}_{10}\rangle$	$\langle\mathrm{Im}\,\hat{\mathcal{Q}}_{11}\rangle$
$\check{\mathcal{S}}_y^T,\hat{\mathcal{R}}_z$	$\langle\hat{y}\hat{z}\rangle$	$\langle\mathrm{Im}\,\hat{\mathcal{Q}}_{21}\rangle$	$\langle\mathrm{Im}\,\hat{\mathcal{Q}}_{21}\rangle$	$\langle\mathrm{Re}\,\hat{\mathcal{Q}}_{21}\rangle$	$\langle\mathrm{Im}\,\hat{\mathcal{Q}}_{22}\rangle$	$\langle\mathrm{Re}\,\hat{\mathcal{Q}}_{21}\rangle$	$\langle\mathrm{Im}\,\hat{\mathcal{Q}}_{22}\rangle$

Table C.3: Redundant degrees of freedom constrained in MOCCa, depending on the choice of broken symmetries and permutation of axes. The corresponding operators in Cartesian operators are also given (up to constant factors).

Appendix D

An introduction to the conjugate gradients numerical algorithm

The conjugate gradient algorithm is a very well-known iterative method to solve linear equations. Since it figures quite often in the entirety of MOCCa, we add this short appendix detailing where and how it is used in the code. This will be a small introduction on a rather intuitive level and we refer to the reader to some of the many excellent texts on the subject.

D.1 Conjugate gradients for linear problems

Consider a linear equation of the form

$$Ax - b = 0\,, \tag{D.1}$$

where x and b are vectors in a certain vector space and A is a symmetric matrix. Consider the following quadratic form on the vector space of interest

$$f(x) = \frac{1}{2}x^T Ax - b^T x\,. \tag{D.2}$$

Note that the solution of Eq. D.1 is a minimum(or maximum) of this quadratic form since

$$\left[\nabla f\right](x) = Ax - b\,. \tag{D.3}$$

One could simply use a gradient descent scheme (see chapter 4) to solve the linear equation: starting from a vector $x^{(i)}$ at iteration i, one can construct a new vector $x^{(i)}$ by stepping in the direction of steepest descent with some suitable step-size α.

$$\delta x^{(i+1)} = x^{(i+1)} - x^{(i)} = -\alpha\left[\nabla f\right](x^{(i)})\,. \tag{D.4}$$

The conjugate gradient however improves on this step by making sure the update $\delta x^{(i+1)}$ is conjugate to the previous update $\delta x^{(i)}$, meaning that if $i \neq j$ then

$$\delta x^{(i)T} A \delta x^{(j)} = 0\,, \tag{D.5}$$

which is equivalent to the update directions being orthogonal with respect to the inproduct induced by A. In practical applications, one introduces a second vector sequence $y^{(i)}$ (with $y^{(0)} = x^{(0)}$) and updates the pair (x,y) at every iteration

$$x^{(i+1)} = x^{(i)} - \alpha^{(i)} A y^{(i)} \tag{D.6a}$$

$$y^{(i+1)} = x^{(i+1)} + \gamma^{(i)} A y^{(i)} \tag{D.6b}$$

where the coefficients (α_i, γ_i) are given by

$$\alpha^{(i)} = \frac{x^{(i)T} x_i}{y^{(i)T} A y^{(i)}}\,, \qquad \gamma^{(i)} = \frac{x^{(i+1)T} x^{(i+1)}}{x^{(i)T} x^{(i)}}\,. \tag{D.7}$$

This scheme ensures that all the updates $\delta x^{(i+1)} = -\alpha_i A y^{(i)}$ are conjugate to the other updates $\delta x^{(j)}$. It really is quite practical that the step-sizes $\alpha^{(i)}$ are in fact dictated by the scheme, instead of relying on the

user to supply a suitable value, as is the case for the gradient descent method. Note that we recover ordinary gradient descent with stepsize $\alpha^{(i)}$ if one puts the $\gamma^{(i)}$ to zero.
There are many nice results that (in provable way) detail how exactly conjugate gradient has better convergence properties than simple gradient descent. The intuition is however rather simple: the conjugate gradient method picks a direction to update $Ay^{(i)}$ and determines a step in that direction in an optimal way by calculating $\alpha^{(i)}$. Afterwards the method looks for another direction to optimize in: in order not to destroy the work of the previous step, this new direction needs to be conjugate to the previous one. Compared to this procedure, ordinary gradient descent simply picks a direction and advances with a certain step-size α in that direction. If this step is not optimal, further iterations will be needed to improve the solution in that direction. In summary, for a simple linear problem, it is really rather hard to conceive an algorithm that is better suited for practical applications. It is rather straightforward to implement and converges significantly faster than gradient descent [160]. This comes at only a very modest cost, that is simply the storage of one additional vector ($y^{(i)}$) and one additional matrix multiplication per iteration. The only often used improvement to the method is by incorporating a preconditioner for the problem, which in many ways can be seen as remedying the problems of the matrix A instead of the problems of the iterative algorithm.

D.2 Conjugate gradient for the optimization of non-linear problems

Consider (positive-definite) $f(x)$, that does no longer have to be linear. We can still calculate $\nabla f(x)$ and look for an optimum of the function, that is to say

$$[\nabla f](x) = 0\,. \tag{D.8}$$

One can still implement an analog of Eq.D.6 as an iterative solution to the problem with an auxiliary vector sequence $y^{(i)}$

$$\begin{aligned} x^{(i+1)} &= x^{(i)} - \alpha^{(i)} \nabla f(y^{(i)})\,, \\ y^{(i+1)} &= x^{(i+1)} + \gamma^{(i)} \nabla f(y^{(i)})\,. \end{aligned} \tag{D.9}$$

The catch is that there is no longer an 'optimal' choice for $\alpha^{(i)}$. Usually one resorts to a line-search at every iteration to search for a more or less optimal value, i.e. one picks a value of $\alpha^{(i)}$ that (approximatively) minimizes $f(x^{(i)} - \alpha^{(i)} \nabla f(y^{(i)}))$ through some one-dimensional optimization algorithm. If the evaluation of f is costly, one can however just take the $\alpha^{(i)}$ to be constants throughout the process. The user needs to supply a value for α in analogy to ordinary gradient descent.
The value of $\gamma^{(i)}$ is also rather hard to choose, but many choices have been studied in the literature. Two of them are

$$\gamma^{(i)}_{FR} = \frac{x^{(i+1)T} x^{(i+1)}}{x^{(i)T} x^{(i)}}\,, \tag{D.10}$$

$$\gamma^{(i)}_{PR} = \frac{x^{(i+1)T} [x^{(i+1)} - x^{(i)}]}{x^{(i+1)T} x^{(i+1)}}\,. \tag{D.11}$$

The first of these corresponds to the formula for the linear case and is usually called the 'Fletcher-Reeves' formula. The second one is usually called the 'Polak-Ribiere' formula. Note that they are equivalent when f is linear, but for non-linear problems the Polak-Ribiere formula is in many cases observed to be superior.

D.3 Conjugate gradients in `MOCCa`

The conjugate gradient technique is mainly used in three different parts of `MOCCa`. They are listed below. Note that the main mean-field iteration scheme could in principle also be a conjugate gradient solver, but I as it turns out the problem is too non-linear to gain any actual CPU time compared to simple gradient descent.

Coulomb solver

The Poisson equation 4.28 is a linear equation on the mesh, and so we can use the method here. The matrix A corresponds to the Laplacian Δ, the vector space is the space of functions on the mesh of which the Coulomb potential $V(\mathbf{r})$ is an element, and the proton density (with a factor $4\pi^2$) is the vector b.

Kinetic preconditioner

Eq. 4.43 constitutes again a linear equation on the Lagrange mesh. The vector space is this time the space of the single-particle spinors on the mesh, the matrix A is $\hat{P}^{-1}$ and the vector b is the single-particle wavefunction $|\psi_l\rangle$.

Thouless method for the HFB equations

The energy $E(Z, \lambda)$ from Eq. 6.50 is a quadratic form that can be optimized with the conjugate gradient method. The matrix A is in this case the HFB Hamiltonian $\hat{\mathcal{H}}$ and the vector space the space of the matrices $(U, V)^T$. A linear or quadratic constraint involving λ_2 do not change the character of the problem, but the Lipkin-Nogami system does: when it is added the problem is no longer linear. It is for this reason that MOCCa implements the non-linear version of conjugate gradients for this problem.

Appendix E

The conjugate gradient method to solve the Thouless-HFB equations

We will delve into the details of the optimization process discussed in section 6.7, using the Thouless theorem as a variational ansatz. The entire appendix is based on [112, 113].

E.1 The gradient method

Starting from a reference HFB state $|\Psi_0\rangle$, one introduces the ansatz $|\Psi(Z)\rangle$

$$|\Psi(Z)\rangle = \hat{\theta}(Z)|\Psi_0\rangle = \left[-\frac{1}{2}\sum_{ij} Z_{ij}\beta_i^\dagger\beta_j^\dagger\right]|\Psi_0\rangle\,. \tag{E.1}$$

which is a function of the matrix Z. The energy of this state is given by

$$E(Z,\Psi_0) = \frac{\langle\Psi(Z)|\hat{\mathcal{H}}_{\text{HFB}}|\Psi(Z)\rangle}{\langle\Psi(Z)|\Psi(Z)\rangle}\,. \tag{E.2}$$

We would now like to construct a numerical algorithm to minimize this energy as a function of Z. However, as before in ordinary HFB calculations, we need to introduce a Fermi energies λ to constrain the average particle number. The quantity we want to minimize is thus

$$E(Z,\Psi_0,\lambda) = \frac{\langle\Psi(Z)|\hat{\mathcal{H}}_{\text{HFB}} - \lambda_n\hat{\mathcal{N}}_n - \lambda_p\hat{\mathcal{N}}_p|\Psi(Z)\rangle}{\langle\Psi(Z)|\Psi(Z)\rangle}\,, \tag{E.3}$$

with subsidiary conditions

$$f_n(\lambda) = \langle\mathcal{N}_n\rangle - N = 0\,, \tag{E.4a}$$
$$f_p(\lambda) = \langle\mathcal{N}_p\rangle - Z = 0\,. \tag{E.4b}$$

In what follows, we drop the index Ψ_0 in the function of the energy as it is intricately linked to the variational space spanned by the expression in Eq. (E.1). It is important to note that the optimization of Eq. (E.3) is done against the background of the Hartree-Fock basis, that is to say at a specific mean-field iteration that delivers single-particle energies and pairing gaps to put into the HFB Hamiltonian. The matrices U and V are thus coordinates of the HFB state in the space of all possible HFB states that one can construct using the specific Hartree-Fock basis at this specific mean-field iteration. The natural variational quantities are thus the the entries in the matrices U and V.
Starting from the matrices U_0 and V_0 associated with $|\Psi_0\rangle$, we want to find the matrices U and V that characterize the minimal energy state $|\Psi(Z)\rangle$. In what follows we will drop the isospin q as subscript to lighten the notation and focus on one particle species. The variation of Eq. E.3 with respect to the elements of the matrix Z is

$$\frac{\partial E(Z,\lambda)}{\partial Z} = \mathcal{H}^{20}_{\text{HFB}} - \lambda\mathcal{N}^{20}\,, \tag{E.5}$$

where $\mathcal{H}^{20}$ and $\mathcal{N}^{20}$ are given by

$$\mathcal{H}^{20} = U^\dagger hV^* + U^\dagger\Delta U^* - V^\dagger h^T U^* - V^\dagger\Delta^* V^*\,, \tag{E.6a}$$
$$\mathcal{N}^{20} = U^\dagger V^* - V^\dagger U^*\,. \tag{E.6b}$$

Note that both these matrices are antisymmetric.
Starting from the initial matrices U_0 and V_0, we can now construct new matrices U_1 and V_1 by simply stepping in the direction of steepest descent, cf. section 4.4. The gradient step is

$$U_1 = U_0 - \epsilon V_0^* \left(\mathcal{H}^{20}_{\text{HFB}} - \lambda \mathcal{N}^{20}\right)^* , \tag{E.7a}$$

$$V_1 = V_0 - \epsilon U_0^* \left(\mathcal{H}^{20}_{\text{HFB}} - \lambda \mathcal{N}^{20}\right)^* , \tag{E.7b}$$

where ϵ is some small step parameter, currently fixed by experience in `MOCCa` as 0.02. Note that this transformation does not conserve the Fermionic anticommutation relations of the quasiparticle operators: in order to enforce them an additional Gram-Schmidt orthonormalisation of the columns of $(U_1, V_1)^T$ is performed.
From $(U_1, V_1)^T$ one can construct the gradient again and construct a new update $(U_2, V_2)^T$. This process will converge to a stationary point[1], and `MOCCa` judges convergence based on the norm of the gradient

$$\left|\frac{\partial E(Z,\lambda)}{\partial Z}\right| = \sqrt{\sum_{ij}\left(\frac{\partial E(Z,\lambda)}{\partial Z}^*\Big|_{ij} \frac{\partial E(Z,\lambda)}{\partial Z}\Big|_{ji}\right)} \leq \texttt{PairingPrec}\,, \tag{E.8}$$

where `PairingPrec` is an input parameter of `MOCCa` and typically on the order of 10^{-6}.
This process is not complete however, as minimizing the energy is not enough: we have to also fix the Fermi energy λ to have the correct particle number on average. From the initial $\lambda^{(0)}$ we construct $\lambda^{(1)}$ as follows

$$\lambda^{(1)} = \lambda^{(0)} + \frac{\left(N - N(\lambda^{(0)})\right)}{\left|\hat{\mathcal{N}}^{20}\right|}\,, \tag{E.9}$$

where $|\hat{\mathcal{N}}^{20}|$ is the norm of the $\hat{\mathcal{N}}^{20}$ matrix, defined similarly to Eq. (E.8). This corresponds to the setting $N(\lambda^{(1)}) = N$ and solving to first order in $(\lambda^{(1)} - \lambda^{(0)})$. This is also rather reminiscent of a an augmented Lagrangian constraint, see chapter 5. After some iterations, $\lambda^{(i)}$ will tend to the correct value, and `MOCCa` checks also the number of particles for convergence:

$$|N(\lambda) - N| \leq \texttt{PairingPrec}\,. \tag{E.10}$$

A similar addition to the scheme can be made in the case of a constraint on λ_2. We take the practical route and simply add the constraint term $-\lambda_2 \Delta N^2$ to the HFB Hamiltonian, resulting in a slightly different $\hat{\mathcal{H}}^{20}$. In the case of the Lipkin-Nogami method, the parameter $\lambda_2^{(i)}$ is also varied in a rather straightforward way

$$\lambda_2^{(i+1)} = \lambda_2^{(i)} + 0.1\left(\lambda_2^{(i)} - \lambda_2^{LN}\right)\,, \tag{E.11}$$

where λ_2^{LN} is calculated from the current HFB state via Eq. 6.33. When λ_2 is constrained to a user-defined value, the code could in principle use a similar update principle as for the Fermi energy, but this is at the moment not implemented[2].

E.2 The conjugate gradient method

The speed of this algorithm can be greatly improved by changing the update formula in Eq. (E.7) to a conjugate gradient scheme as described in Appendix D. For completeness' sake, we write down the update formula

$$U^{(i+1)} = U^{(i)} - \epsilon V^{(i),*} G^{(i),*} + \gamma^{(i)}\left[U^{(i)} - U^{(i-1)}\right]\,, \tag{E.12a}$$

$$V^{(i+1)} = V^{(i)} - \epsilon U^{(i),*} G^{(i),*} + \gamma^{(i)}\left[V^{(i)} - V^{(i-1)}\right]\,, \tag{E.12b}$$

with the following auxiliary definitions

$$G^{(i)} = \left(\mathcal{H}^{(i)20}_{\text{HFB}} - \lambda \mathcal{N}^{(i),20}\right)\,, \tag{E.13}$$

$$\gamma^{(i)} = \frac{|G^{(i)}|}{|G^{(i-1)}|} - \frac{\langle G^{(i)}|G^{(i-1)}\rangle}{|G^{(i-1)}|}\,, \tag{E.14}$$

$$\langle G^{(i)}|G^{(i-1)}\rangle = \sqrt{\sum_{kl}\left(G^{(i),*}_{lk} G^{(i-1)}_{kl}\right)}\,, \tag{E.15}$$

[1] Provided ϵ is not too large. An adaptive scheme for this parameter would be most welcome.
[2] Strictly because of time limitations, as the implementation would be straightforward.

where the formula employed for γ is the Polak-Ribière one. Note that we kept the stepsize in the algorithm, instead of taking the 'optimal' stepsize α as is possible for a linear problem. This is motivated by the fact that the problem becomes nonlinear the moment the Lipkin-Nogami approach is activate, and in this way the algorithm works in all cases.
It is worth mentioning that the entire algorithm is a rather recent addition to `MOCCa` and many optimizations and simplifications can still be envisioned, as we have not a lot of experience with it at the moment.

Appendix F

Coulomb Solvers

This appendix has as aim to document very briefly the various Coulomb solvers included with `MOCCa`. All of them are tested to give the same result. The user can choose between various options using the input parameter `CoulombSolver`:

0. No Coulomb contribution
1. Conjugate gradient
2. Red-black Gauss-Seidel
3. Symmetric overrelaxation

The first option simply disables all contribution from the electrostatic interaction to the functional. As discussed in chapter 4 the three other methods are iterative methods to solve Poisson's equation Eq. (4.28) with suitable boundary conditions Eq. (4.30). On the Lagrange mesh this differential equation is simply a system of linear equations. The conjugate gradient method we will not discuss separately, as it is a simple implementation of the scheme discussed in Appendix D. The Gauss-Seidel and Symmetric overrelaxation will be briefly discussed, but the interested reader can find a much more educative and exhaustive treatment in [88].
Three general remarks are in order: the system of linear equations is of course dependent on the chosen representation of the Laplacian Δ on the mesh. This can be controlled by the `CoulombLapOrder` input parameter. Its default value is 2, corresponding to a second order finite difference scheme, that has been shown to be accurate enough for all applications [72].
The Coulomb potential from previous mean-field iterations is saved and used as a starting point for the iterative solvers. While at the start of the iterations the Coulomb solver may take several iterations to converge, as convergence sets in on the mean-field level the proton density becomes stationary and the numerical effort needed to solve for the Coulomb potential is close to zero.
A final remark is on the imposed accuracy of the solver. `MOCCa` judges convergence on equal footing for all of the solvers using the following inequality

$$\int d\mathbf{r} \left(\left[\Delta + 4\pi e^2 \rho_p(\mathbf{r}) \right] V(\mathbf{r}) \right)^2 \leq V_{\text{box}}^{-1} \times \texttt{CoulombPrec}\,, \tag{F.1}$$

where `CoulombPrec` is an input parameter and defaults to 10^{-9} and V_{Box} is the volume of the Lagrange mesh, possibly extended with extra points compared to the standard mesh.

Finite Difference order	1	2	3	4
optimal ω	1.91	1.5	1.45	1.39

Table F.1: Optimal value of ω for the symmetric overrelaxation method as determined for a uniformly charged sphere with an equivalent charge of 82 protons.

F.1 Red-black Gauss-Seidel

A Gauss-Seidel scheme [88]solves the Poisson equation by applying the following update formula

$$V^{(i)}(\mathbf{r}) = V^{(i-1)}(\mathbf{r}) + \left[\Delta + 4\pi e^2 \rho_p(\mathbf{r})\right] V^{(i-1)}(\mathbf{r})\,. \tag{F.2}$$

Just applying Eq. (F.4) iteratively is a simple gradient-descent scheme, but the Gauss-Seidel method augments this by applying a special rule for computing Δ on the mesh. The discretisation of the Lagrange mesh makes that Δ becomes a linear operator

$$\left[\Delta V^{(i)}\right](\mathbf{r}_i) = \sum_j \Delta_{ij} V^{(i)}(\mathbf{r}_j)\,, \tag{F.3}$$

where the coefficients Δ_{ij} depends on our specific choice of representation. The naive update formula thus becomes, at every point $\mathbf{r}_i$,

$$V^{(i)}(\mathbf{r}_i) = \sum_j \Delta_{ij} V^{(i-1)}(\mathbf{r}_j) + 4\pi e^2 \rho_p(\mathbf{r}_i) V^{(i-1)}(\mathbf{r}_i)\,. \tag{F.4}$$

For the first point computed $\mathbf{r}_1$, we can do no better. But already for $\mathbf{r}_2$ we can use the updated value $V^{(i)}(\mathbf{r}_1)$ in the update formula, instead of the old value $V^{(i-1)}(\mathbf{r}_1)$. The actual update thus uses as much information as is available at the moment of update, so that we get

$$V^{(i)}(\mathbf{r}_i) = \sum_{j<i} \Delta_{ij} V^{(i)}(\mathbf{r}_j) + \sum_{j>i} \Delta_{ij} V^{(i-1)}(\mathbf{r}_j) + 4\pi e^2 \rho_p(\mathbf{r}_i) V^{(i-1)}(\mathbf{r}_i)\,. \tag{F.5}$$

where the notation $j < i$ means that $\mathbf{r}_j$ comes before $\mathbf{r}_i$ in our calculation.
The implementation becomes 'red-black' the moment we choose a specific ordering for the points on the Lagrange mesh, in order to optimize the inclusion of as much new information as possible. Recalling the coordinates on the Lagrange mesh of chapter 4, a point on the Lagrange mesh is determined by its Cartesian coordinates (x_i, y_j, z_k). The mesh points are then divided into two groups: those for who $i + j + k$ is even, and those that have odd $i + j + k$. The second group is first updated using Eq. (F.5), in lexicographical order of (i, j, k). The first group is then updated in lexicographical order afterwards, profiting from the new information that is already contained in the values of V on the first group of mesh points. This ordering is known as 'red-black' since the division of mesh in two submeshes in two-dimensions is exactly the division of a checkers-board into red and black tiles.

F.2 Symmetric Overrelaxation

A symmetric overrelaxation solver generalizes Eq. (F.4) by introducing a new constant ω to the update formula [88]

$$V^{(i)}(\mathbf{r}) = V^{(i-1)}(\mathbf{r}) + \omega \left[\Delta + 4\pi e^2 \rho_p(\mathbf{r})\right] V^{(i-1)}(\mathbf{r})\,. \tag{F.6}$$

When $\omega > 1$ this method updates strictly faster compared to the ordinary Gauss-Seidel method. The optimal value of ω is however heavily dependent on the problem under consideration. Table F.1 contains the optimal values of ω as determined for a uniformly charged sphere with a charge equivalent of 82 protons for different representations of the Laplacian with finite difference derivatives. When ω is not optimal however, the method performs very comparably to ordinary Gauss-Seidel. The cost in human time for searching for an optimal value of ω is however not worth it in general.

Appendix G

A peculiar feature of the HFB equations

Recall that the HFB Hamiltonian $\hat{\mathcal{H}}_{\text{HFB}}$ and the generalized density matrix $\hat{\mathcal{R}}$ commute, and thus share eigenvectors. This fact has been used in chapter 3 to construct the canonical basis. However, this means that one has an extra degree of freedom to work with. Consider the following matrix, for a real parameter α

$$\hat{\mathcal{H}}_{\text{HFB}} + \alpha\hat{\mathcal{R}} = \begin{pmatrix} h & \Delta \\ -\Delta & -h \end{pmatrix} + \alpha \begin{pmatrix} \rho & \kappa \\ -\kappa & \mathbb{1} - \rho \end{pmatrix} . \tag{G.1}$$

One can diagonalize this matrix instead of the HFB Hamiltonian in order to obtain the $(U_k, V_k)^T$ vectors. Only the eigenvalues, the quasiparticle energies, change. Since $\mathcal{R}$ has eigenvalues equal to one or zero, whether or not a quasiparticle is 'picked' (see the discussion in chapter 6 and [11]), this operation breaks the symmetry between a quasiparticle and its conjugate, as they will no longer have opposite energies E_k and $-E_k$ but rather E_k and $-E_k + \alpha$. Because this transformation leaves the HFB solution invariant, we will call the parameter α the HFB gauge parameter.

Fig. G.1 shows part of the quasiparticle spectrum of ^{64}Ge, for negative parity proton quasiparticles as a function of the gauge parameter α. The picked quasiparticle energies are unaffected, but the distance between canonical partners can be controlled by the gauge parameter. Depending on the choice of selected quasiparticles, non-zero values of α can either be chosen to enlarge or shrink the gap between selected and non-selected quasiparticles.

As example, let us look at the ground state of a time-reversal invariant system. All of the picked quasiparticles have positive quasiparticle energies $E_k > 0$ and the unselected ones have $E_k < 0$. For positive values of α the non-selected states rise in energy, closer to the selected quasiparticles. When they cross zero, naively selecting the positive energy quasiparticles leads to an invalid choice, since we will have too many quasiparticles. Even when carefully selecting along signature blocks, we encounter trouble when an originally unselected quasiparticle rises past an originally picked level, the picking algorithm will select the wrong quasiparticle. In a time-reversal case, this results in a two-quasiparticle excitation on the ground state. This will lead to numerical instability very quickly, as of course the quasiparticle spectrum will vary from one mean-field iteration to the next and `MOCCa` will start mixing different configurations and in general not converge.

The gauge parameter α can also be used to stabilize convergence. If α is taken to be negative, the unselected states go down in energy, which means that in a time-reversal conserved case the gap between selected and not selected quasiparticles enlarges. While not particularly helpful in this case, in a cranked calculation this might help stave off crossings of quasiparticles and their conjugates, greatly stabilizing convergence.

For blocked calculations, the situation is hard to analyze in general, as the quasiparticle spectrum can vary greatly depending on the blocked state under investigation. However, a clever choice of the gauge parameter α can help keep the blocked quasiparticle away from other quasiparticles, avoiding crossings and changes in the nature of the quasiparticle. This freedom has been in use for a long time in `cr8` (at least when the Lipkin-Nogami method was used) to promote convergence of quasiparticles [32], but was always used rather ad-hoc.

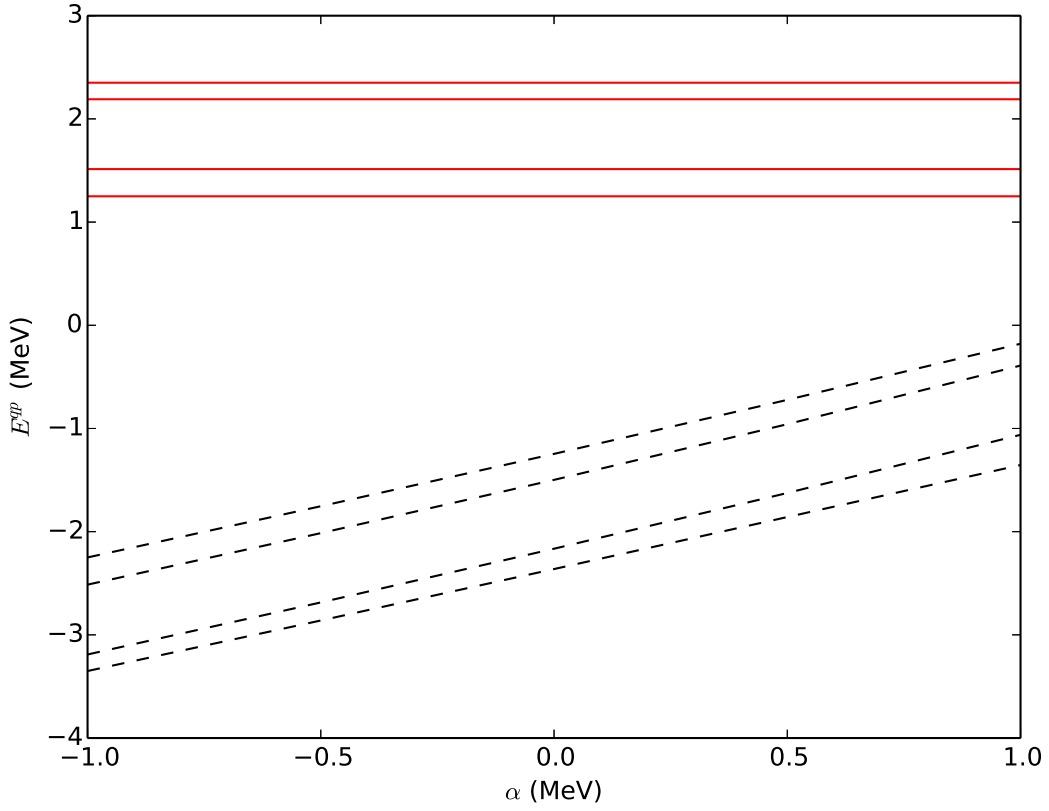

Figure G.1: Lowest negative parity proton quasiparticle energies and their conjugate partners of ^{64}Ge as a function of the HFBGauge parameter. Red lines are picked quasiparticles, black dashed lines are the conjugate partners that are not picked.

Appendix H

Structure of the code

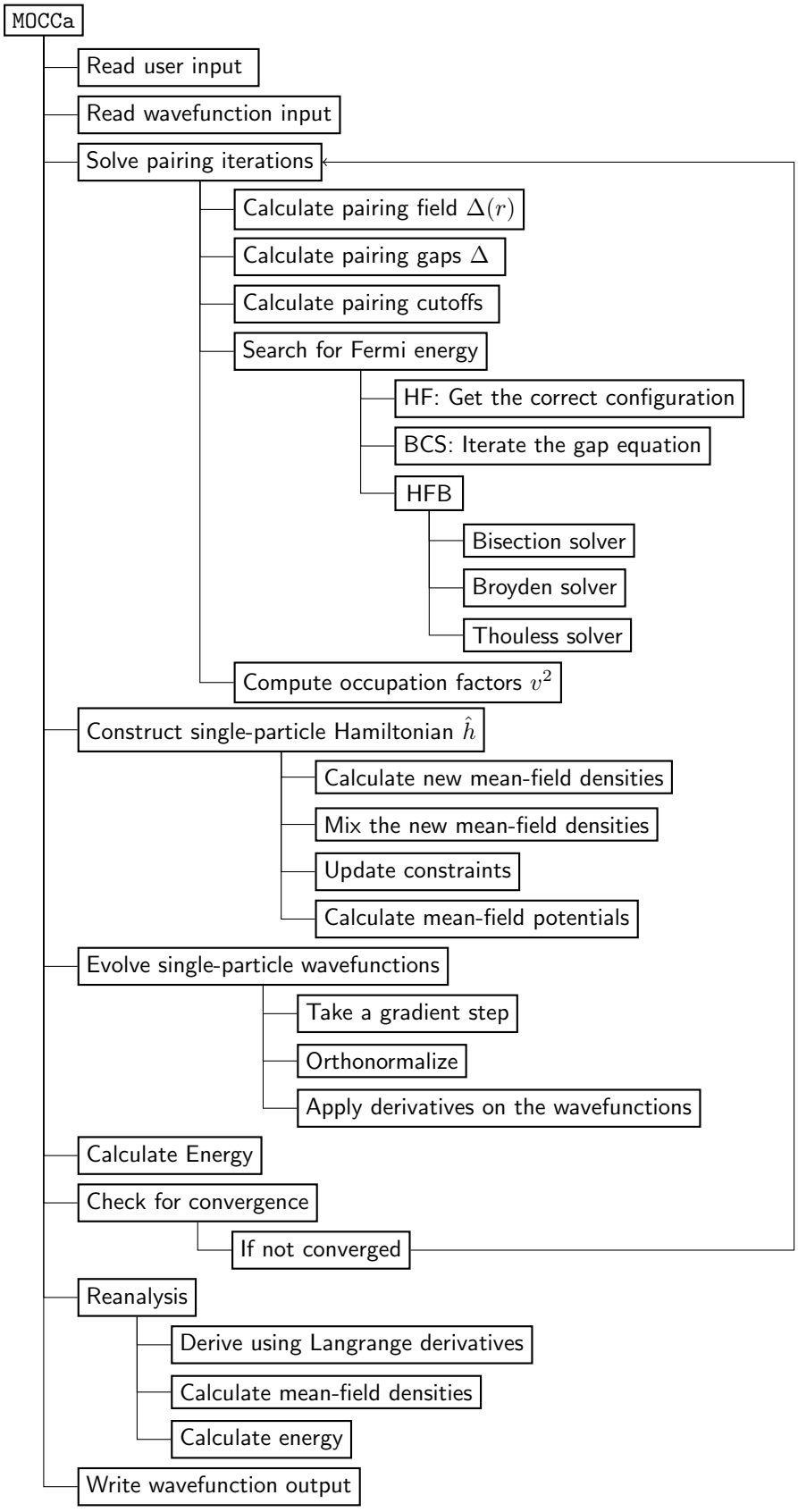
MOCCa
Read user input
Read wavefunction input
Solve pairing iterations
Calculate pairing field $\Delta(r)$
Calculate pairing gaps Δ
Calculate pairing cutoffs
Search for Fermi energy
HF: Get the correct configuration
BCS: Iterate the gap equation
HFB
Bisection solver
Broyden solver
Thouless solver
Compute occupation factors v^2
Construct single-particle Hamiltonian $\hat{h}$
Calculate new mean-field densities
Mix the new mean-field densities
Update constraints
Calculate mean-field potentials
Evolve single-particle wavefunctions
Take a gradient step
Orthonormalize
Apply derivatives on the wavefunctions
Calculate Energy
Check for convergence
If not converged
Reanalysis
Derive using Langrange derivatives
Calculate mean-field densities
Calculate energy
Write wavefunction output

Bibliography

[1] D. Vautherin and D. M. Brink, *Hartree-Fock calculations with Skyrme's interaction. I. Spherical nuclei*, Phys. Rev. C **5** (1972) 626–647.

[2] T. Skyrme, *The effective nuclear potential*, Nucl. Phys. **9** (1958) 615–634.

[3] M. Bender, P.-H. Heenen, and P.-G. Reinhard, *Self-consistent mean-field models for nuclear structure*, Rev. Mod. Phys. **75** (2003) 121–180.

[4] D. Auverlot, P. Bonche, H. Flocard, and P. Heenen, *On the deformation energy surface of* ^{16}O, Phys. Lett. B **149** (1984) 6–8.

[5] P. Bonche, H. Flocard, P. Heenen, S. Krieger, and M. Weiss, *Self-consistent study of triaxial deformations: Application to the isotopes of Kr, Sr, Zr and Mo*, Nucl. Phys. **A443** (1985) 39–63.

[6] L. P. Gaffney, P. A. Butler, M. Scheck, A. B. Hayes, F. Wenander, M. Albers, B. Bastin, C. Bauer, A. Blazhev, S. Bonig, N. Bree, J. Cederkall, T. Chupp, D. Cline, T. E. Cocolios, T. Davinson, H. De Witte, J. Diriken, T. Grahn, A. Herzan, M. Huyse, D. G. Jenkins, D. T. Joss, N. Kesteloot, J. Konki, M. Kowalczyk, T. Kroll, E. Kwan, R. Lutter, K. Moschner, P. Napiorkowski, J. Pakarinen, M. Pfeiffer, D. Radeck, P. Reiter, K. Reynders, S. V. Rigby, L. M. Robledo, M. Rudigier, S. Sambi, M. Seidlitz, B. Siebeck, T. Stora, P. Thoele, P. Van Duppen, M. J. Vermeulen, M. von Schmid, D. Voulot, N. Warr, K. Wimmer, K. Wrzosek-Lipska, C. Y. Wu, and M. Zielinska, *Studies of pear-shaped nuclei using accelerated radioactive beams*, Nature **497** 7448, (May, 2013) 199–204. Article.

[7] C. M. Petrache, S. Frauendorf, M. Matsuzaki, R. Leguillon, T. Zerrouki, S. Lunardi, D. Bazzacco, C. A. Ur, E. Farnea, C. Rossi Alvarez, R. Venturelli, and G. de Angelis, *Tilted axis rotation, candidates for chiral bands, and wobbling motion in* ^{138}Nd, Phys. Rev. C **86** (2012) 044321.

[8] D. Vautherin, *Hartree-Fock calculations with Skyrme's interaction. II. Axially deformed nuclei*, Phys. Rev. C **7** (1973) 296–316.

[9] P. Bonche, H. Flocard, and P. Heenen, *Solution of the Skyrme HF+BCS equation on a 3D mesh*, Comp. Phys. Comm. **171** (2005) 49–62.

[10] W. Ryssens, V. Hellemans, M. Bender, and P.-H. Heenen, *Solution of the Skyrme–HF+BCS equation on a 3D mesh, II: A new version of the Ev8 code*, Comp. Phys. Comm. **187** (2015) 175 – 194.

[11] P. Ring and P. Schuck, *The Nuclear Many-Body Problem*. Springer-Verlag Berlin, 1980.

[12] P.-H. Heenen and M. R. Godefroid, The Hartree-Fock method, `http://www.scholarpedia.org/article/The_Hartree-Fock_method`. Accessed: 05-04-2016.

[13] M. Baldo, P. Schuck, and X. Viñas, *Kohn–Sham density functional inspired approach to nuclear binding*, Phys. Lett. B **663** (2008) 390–394.

[14] D. Lacroix, T. Duguet, and M. Bender, *Configuration mixing within the energy density functional formalism: Removing spurious contributions from nondiagonal energy kernels*, Phys. Rev. C **79** (2009) 044318.

[15] T. Duguet, M. Bender, K. Bennaceur, D. Lacroix, and T. Lesinski, *Particle-number restoration within the energy density functional formalism: Nonviability of terms depending on noninteger powers of the density matrices*, Phys. Rev. C **79** (2009) 044320.

[16] J. Sadoudi, M. Bender, and K. Bennaceur, *Skyrme pseudo-potential-based EDF parametrization for spuriousity-free MR-EDF calculations*, Physica Scripta **T154** (2013) 014013.

[17] E. Chabanat, P. Bonche, P. Haensel, J. Meyer, and R. Schaeffer, *A Skyrme parametrization from subnuclear to neutron star densities Part II. Nuclei far from stabilities*, Nucl. Phys. **A635** (1998) 231–256.

[18] M. Kortelainen, J. McDonnell, W. Nazarewicz, P.-G. Reinhard, J. Sarich, N. Schunck, M. V. Stoitsov, and S. M. Wild, *Nuclear energy density optimization: Large deformations*, Phys. Rev. C **85** (2012) 024304.

[19] V. Hellemans, P.-H. Heenen, and M. Bender, *Tensor part of the Skyrme energy density functional. III. Time-odd terms at high spin*, Phys. Rev. C **85** (2012) 014326.

[20] S. G. Rohoziński, J. Dobaczewski, and W. Nazarewicz, *Self-consistent symmetries in the proton-neutron Hartree-Fock-Bogoliubov approach*, Phys. Rev. C **81** (2010) 014313.

[21] T. Lesinski, M. Bender, K. Bennaceur, T. Duguet, and J. Meyer, *Tensor part of the Skyrme energy density functional: Spherical nuclei*, Phys. Rev. C **76** (2007) 014312.

[22] P. Bonche, H. Flocard, and P. Heenen, *Self-consistent calculation of nuclear rotations: The complete yrast line of ^{24}Mg*, Nucl. Phys. **A467** (1987) 115 – 135.

[23] M. Bender, K. Bennaceur, T. Duguet, P. H. Heenen, T. Lesinski, and J. Meyer, *Tensor part of the Skyrme energy density functional. II. Deformation properties of magic and semi-magic nuclei*, Phys. Rev. C **80** (2009) 064302.

[24] J. Le Bloas, M. H. Koh, P. Quentin, L. Bonneau, and J. I. A. Ithnin, *Exact Coulomb exchange calculations in the Skyrme-Hartree-Fock-BCS framework and tests of the Slater approximation*, Phys. Rev. C **84** (2011) 1–11.

[25] M. Samyn, S. Goriely, P.-H. Heenen, J. Pearson, and F. Tondeur, *A Hartree–Fock–Bogoliubov mass formula*, Nucl. Phys. **A700** (2002) 142–156.

[26] S. Goriely, *Further explorations of Skyrme–Hartree–Fock–Bogoliubov mass formulas. XV: The spin–orbit coupling* , Nucl. Phys. **A933** (2015) 68 – 81.

[27] M. Bender, K. Rutz, P.-G. Reinhard, and J. Maruhn, *Consequences of the center–of–mass correction in nuclear mean–field models*, Eur. Phys. J **A7** 4, (1999) 467–478.

[28] L. Coraggio, A. Covello, A. Gargano, and N. Itaco, *Similarity of nuclear structure in the ^{132}Sn and ^{208}Pb regions: Proton-neutron multiplets*, Phys. Rev. C **80** 2, (2009) 021305.

[29] V. Somà, C. Barbieri, and T. Duguet, *Ab initio gorkov-green's function calculations of open-shell nuclei*, Phys. Rev. C **87** (2013) 011303.

[30] J. D. Holt, J. Menéndez, J. Simonis, and A. Schwenk, *Three-nucleon forces and spectroscopy of neutron-rich calcium isotopes*, Phys. Rev. C **90** (2014) 024312.

[31] S. Binder, J. Langhammer, A. Calci, and R. Roth, *Ab initio path to heavy nuclei*, Phys. Lett. B **736** (2014) 119–123.

[32] B. Bally, *Description des noyaux impairs à l'aide d'une méthode de fonctionelle énergie de la densité à plusieurs états de référence*. PhD thesis, Université de Bordeaux-Gradignan, 2014.

[33] B. Bally, B. Avez, M. Bender, and P.-H. Heenen, *Beyond Mean-Field Calculations for Odd-Mass Nuclei*, Phys. Rev. Lett. **113** (2014) 162501.

[34] H. Zduńczuk, W. Satuła, J. Dobaczewski, and M. Kosmulski, *Angular momentum projection of cranked Hartree-Fock states: Application to terminating bands in $A \sim 44$ nuclei*, Phys. Rev. C **76** (2007) 044304.

[35] B. G. Carlsson, J. Dobaczewski, and M. Kortelainen, *Local nuclear energy density functional at next-to-next-to-next-to-leading order*, Phys. Rev. C **78** (2008) 044326.

[36] J. Dobaczewski, J. Dudek, S. G. Rohoziński, and T. R. Werner, *Point symmetries in the Hartree-Fock approach.I. Densities, shapes, and currents*, Phys. Rev. C **62** (2000) 014310.

[37] W. Satula and W. Nazarewicz, *Isospin effects in N∼Z nuclei in extended Density Functional Theory*, Physica Scripta **023013** (2015) 023013.

[38] J. Dobaczewski, J. Dudek, S. G. Rohoziński, and T. R. Werner, *Point symmetries in the Hartree-Fock approach.II. Symmetry-breaking schemes*, Phys. Rev. C **62** (2000) 014311.

[39] S. Åberg, H. Flocard, and W. Nazarewicz, *Nuclear shapes in mean-field theory*, Annu. Rev. Nucl. Part. Sci. **40** (1990) 439.

[40] P. Bonche, H. Flocard, P. H. Heenen, S. J. Krieger, and M. S. Weiss, *Self-consistent study of triaxial deformations: Application to the isotopes of Kr, Sr, Zr and Mo*, Nucl. Phys. **A443** (1985) 39–63.

[41] T. Nikšić, P. Marević, and D. Vretenar, *Microscopic analysis of shape evolution and triaxiality in germanium isotopes*, Phys. Rev. C **89** (2014) 044325.

[42] S. W. Ødegård, G. B. Hagemann, D. R. Jensen, M. Bergström, B. Herskind, G. Sletten, S. Törmänen, J. N. Wilson, P. O. Tjøm, I. Hamamoto, K. Spohr, H. Hübel, A. Görgen, G. Schönwasser, A. Bracco, S. Leoni, A. Maj, C. M. Petrache, P. Bednarczyk, and D. Curien, *Evidence for the wobbling mode in nuclei*, Phys. Rev. Lett. **86** (2001) 5866–5869.

[43] J. M. Yao, E. F. Zhou, and Z. P. Li, *Beyond relativistic mean-field approach for nuclear octupole excitations*, Phys. Rev. C - Nuclear Physics **92** (2015) 1–5.

[44] K. Nomura, D. Vretenar, and B.-N. Lu, *Microscopic analysis of the octupole phase transition in Th isotopes*, Phys. Rev. C **88** (2013) 021303.

[45] P. Bonche, P. Heenen, H. Flocard, and D. Vautherin, *Self-consistent calculation of the quadrupole-octupole deformation energy surface of ^{222}Ra*, Phys. Lett. B **175** (1986) 387–391.

[46] K. Nomura, R. Rodríguez-Guzmán, and L. M. Robledo, *Spectroscopy of quadrupole and octupole states in rare-earth nuclei from a Gogny force*, Phys. Rev. C **92** (2015) 014312.

[47] T. Tanaka, R. G. Nazmitdinov, and K. Iwasawa, *Nonaxial octupole deformations in light $N = Z$ nuclei at high spins*, Phys. Rev. C **63** (2001) 034309.

[48] B. Bucher, S. Zhu, C. Y. Wu, R. V. F. Janssens, D. Cline, A. B. Hayes, M. Albers, A. D. Ayangeakaa, P. A. Butler, C. M. Campbell, M. P. Carpenter, C. J. Chiara, J. A. Clark, H. L. Crawford, M. Cromaz, H. M. David, C. Dickerson, E. T. Gregor, J. Harker, C. R. Hoffman, B. P. Kay, F. G. Kondev, A. Korichi, T. Lauritsen, A. O. Macchiavelli, R. C. Pardo, A. Richard, M. A. Riley, G. Savard, M. Scheck, D. Seweryniak, M. K. Smith, R. Vondrasek, and A. Wiens, *Direct evidence of octupole deformation in neutron-rich ^{144}Ba*, Phys. Rev. Lett. **116** (2016) 112503.

[49] B.-N. Lu, J. Zhao, E.-G. Zhao, and S.-G. Zhou, *Multi-dimensional potential energy surfaces and non-axial octupole correlations in actinide and transfermium nuclei from relativistic mean field models*, J. Phys.: Conf. Ser **492** (2013) 012014.

[50] N. Schunck and L. M. Robledo, *Microscopic Theory of Nuclear Fission: A Review*, Invited Review Article submitted to Reports on Progress in Physics., 2015.

[51] P. Bonche, H. Flocard, and P.-H. Heenen, *Cranked Hartree-Fock study of the yrast line of ^{80}Sr*, Nucl. Phys. **A523** (1991) 300 – 312.

[52] B. Gall, P. Bonche, J. Dobaczewski, H. Flocard, and P. H. Heenen, *Superdeformed rotational bands in the mercury region. A cranked Skyrme-Hartree-Fock-Bogoliubov study*, Z. Phys. A **348** (1994) 183–197.

[53] Y. Shi, J. Dobaczewski, S. Frauendorf, W. Nazarewicz, J. C. Pei, F. R. Xu, and N. Nikolov, *Self-consistent tilted-axis-cranking study of triaxial strongly deformed bands in ^{158}Er at ultrahigh spin*, Phys. Rev. Lett. **108** (2012) 092501.

[54] S. Frauendorf, *Spontaneous symmetry breaking in rotating nuclei*, Rev. Mod. Phys. **73** (2001) 463–514.

[55] M. Bender, J. Dobaczewski, J. Engel, and W. Nazarewicz, *Gamow-Teller strength and the spin-isospin coupling constants of the Skyrme energy functional*, Phys. Rev. C **65** (2002) 054322.

[56] V. V. Flambaum and J. S. M. Ginges, *Nuclear Schiff moment and time-invariance violation in atoms*, Physical Review A **65** (2002) 032113.

[57] L. I. Schiff, *Measurability of nuclear electric dipole moments*, Phys. Rev. **132** (1963) 2194–2200.

[58] J. Dobaczewski and J. Engel, *Nuclear Time-Reversal Violation and the Schiff Moment of ^{225}Ra*, Phys. Rev. Lett. **94** (2005) 232502.

[59] J. Engel, M. Bender, J. Dobaczewski, J. H. d. Jesus, and P. Olbratowski, *Time-reversal violating Schiff moment of ^{225}Ra*, Phys. Rev. C **68** (2003) 025501.

[60] H. Dancer, *Une symétrie brisée dans le formalisme de Hartree-Fock-Bogoliubov: la z-signature. Applications à la dynamique des noyaux déformés.* PhD thesis, Université Claude Bernard - Lyon 1, 2000.

[61] K. Heyde, P. von Neumann-Cosel, and A. Richter, *Magnetic dipole excitations in nuclei: Elementary modes of nucleonic motion*, Rev. Mod. Phys. **82** (2010) 2365–2419.

[62] M. Anguiano, J. Egido, and L. Robledo, *Mean-field based approaches to pairing correlations in atomic nuclei*, Phys. Lett. **B545** (2002) 62 – 72.

[63] J. A. Sheikh, P. Ring, E. Lopes, and R. Rossignoli, *Pairing correlations and particle-number projection methods*, Phys. Rev. C **66** (2002) 044318.

[64] M. V. Stoitsov, J. Dobaczewski, R. Kirchner, W. Nazarewicz, and J. Terasaki, *Variation after particle-number projection for the Hartree-Fock-Bogoliubov method with the Skyrme energy density functional*, Phys. Rev. C **76** (2007) 014308.

[65] T. R. Rodríguez and J. L. Egido, *New beyond-mean-field theories: Examination of the potential shell closures at $n = 32$ or 34*, Phys. Rev. Lett. **99** (2007) 062501.

[66] C. Bloch and A. Messiah, *The canonical form of an antisymmetric tensor and its application to the theory of superconductivity*, Nucl. Phys; **39** (1962) 95–106.

[67] J. Dobaczewski, *Generalization of the Bloch-Messiah-Zumino theorem*, Phys. Rev. C **62** (2000) 017301.

[68] G. Bertsch and J. Dobaczewski, *Hartree-Fock-Bogoliubov theory of polarized Fermi systems*, Phys. Rev A **79** (2009) 1–9.

[69] B. Banerjee, H. Mang, and P. Ring, *Variational calculation of energy spectra of rotational nuclei at high spins*, Nucl. Phys. **A215** (1973) 366–382.

[70] B. Banerjee, P. Ring, and H. Mang, *On the character of the Hartree-Fock-Bogoliubov solutions in a rotating frame*, Nucl. Phys. **A221** (1974) 564–572.

[71] A. Valor, J. L. Egido, and L. M. Robledo, *Approximate particle number projection for finite range density dependent forces*, Phys. Rev. C **53** (1996) 172–175.

[72] W. Ryssens, P.-H. Heenen, and M. Bender, *Numerical accuracy of mean-field calculations in coordinate space*, Phys. Rev. C **92** (2015) 064318.

[73] J. Dobaczewski, W. Satuła, B. Carlsson, J. Engel, P. Olbratowski, P. Powałowski, M. Sadziak, J. Sarich, N. Schunck, A. Staszczak, M. Stoitsov, M. Zalewski, and H. Zduńczuk, *Solution of the Skyrme–Hartree–Fock–Bogolyubov equations in the Cartesian deformed harmonic-oscillator basis.: (VI) HFODD (v2.40h): A new version of the program*, Comp. Phys. Comm. **180** (2009) 2361–2391.

[74] D. Thouless, *Stability conditions and nuclear rotations in the hartree-fock theory*, Nucl. Phys. **21** (1960) 225.

[75] S. Krieger, P. Bonche, H. Flocard, P. Quentin, and M. Weiss, *An improved pairing interaction for mean field calculations using Skyrme potentials*, Nucl. Phys. **A517** (1990) 275 – 284.

[76] M. Kortelainen, T. Lesinski, J. Moré, W. Nazarewicz, J. Sarich, N. Schunck, M. V. Stoitsov, and S. Wild, *Nuclear energy density optimization*, Phys. Rev. C **82** (2010) 024313.

[77] M. Kortelainen, J. McDonnell, W. Nazarewicz, P.-G. Reinhard, J. Sarich, N. Schunck, M. V. Stoitsov, and S. M. Wild, *Nuclear energy density optimization: Large deformations*, Phys. Rev. C **85** (2012) 024304.

[78] M. Kortelainen, J. McDonnell, W. Nazarewicz, E. Olsen, P. G. Reinhard, J. Sarich, N. Schunck, S. M. Wild, D. Davesne, J. Erler, and A. Pastore, *Nuclear energy density optimization: Shell structure*, Phys. Rev. C **89** 5, (2014) 1–18.

[79] J. Dobaczewski, A. Afanasjev, M. Bender, L. Robledo, and Y. Shi, *Properties of nuclei in the nobelium region studied within the covariant, Skyrme, and Gogny energy density functionals*, Nucl. Phys. **A944** (2015) 388–414.

[80] C. Rigollet, P. Bonche, H. Flocard, and P.-H. Heenen, *Microscopic study of the properties of identical bands in the $A = 150$ mass region*, Phys. Rev. C **59** (1999) 3120–3127.

[81] B. Avez. Private communications.

[82] B. Fornberg, M. Abramowitz, I. A. Stegun, B. Fornberg, H. B. Keller, V. Pereyra, and W. D. Lakin, *Generation of finite difference formulas on arbitrarily spaced grids*, Mathematics of Computation **51** (1988) 699–699.

[83] B. Carlsson, J. Dobaczewski, J. Toivanen, and P. Veselý, *Solution of self-consistent equations for the N3LO nuclear energy density functional in spherical symmetry. The program hosphe (v1.02)*, Comp. Phys. Comm. **181** 9, (2010) 1641–1657.

[84] J. Dobaczewski and J. Dudek, *Solution of the Skyrme-Hartree-Fock equations in the Cartesian deformed harmonic oscillator basis I. The method*, Comp. Phys. Comm. **102** (1997) 166–182.

[85] M. Stoitsov, N. Schunck, M. Kortelainen, N. Michel, H. Nam, E. Olsen, J. Sarich, and S. Wild, *Axially deformed solution of the Skyrme-Hartree–Fock–Bogoliubov equations using the transformed harmonic oscillator basis (II) hfbtho v2.00d: A new version of the program*, Comp. Phys. Comm. **184** 6, (2013) 1592–1604.

[86] D. Baye and P. H. Heenen, *Generalised meshes for quantum mechanical problems*, Journal of Physics A: Mathematical and General **19** 11, (1986) 2041.

[87] D. Baye, *The Lagrange-mesh method*, Physics Reports **565** (2015) 1 – 107.

[88] W. Press, S. Teukolsky, W. Vetterling, and B. Flannery, *Numerical recipes: the art of scientific computing*. Cambridge University Press, third ed., 2007.

[89] K. T. R. Davies, H. Flocard, S. Krieger, and M. S. Weiss, *Application of the imaginary time step method to the solution of the static Hartree-Fock problem*, Nuclear Physics **A342** (1980) 111–123.

[90] J. Dobaczewski and J. Dudek, *Solution of the Skyrme-Hartree-Fock equations in the Cartesian deformed harmonic oscillator basis II. The program HFODD*, Comp. Phys. Comm. **102** (1997) 183–209.

[91] A. Baran, A. Bulgac, M. M. Forbes, G. Hagen, W. Nazarewicz, N. Schunck, and M. V. Stoitsov, *Broyden's method in nuclear structure calculations*, Phys. Rev. C **78** (2008) 014318.

[92] P.-G. Reinhard and R. Cusson, *A comparative study of Hartree-Fock iteration techniques*, Nucl. Phys. **A378** (1982) 418–442.

[93] Y. Nesterov, *A method for unconstrained convex minimization problem with the rate of convergence $O(k^{-2})$*, Doklady ANSSSR (translated as Soviet.Math.Docl.) **269** (1983) 543– 547.

[94] N. Qian, *On the momentum term in gradient descent learning algorithms*, Neural Networks **12** (1999) 145–151.

[95] S. Bubeck, Y. T. Lee, and M. Singh, *A geometric alternative to Nesterov's accelerated gradient descent*, arXiv:1506.08187.

[96] E. Candès, C. B. by Felipe Cucker O, and E. Candès, *Adaptive Restart for Accelerated Gradient Schemes*, Found. Comput. Math. **15** (2015) 715–732.

[97] P. Pulay, *Convergence acceleration of iterative sequences. the case of scf iteration*, Chem. Phys. Lett. **73** (1980) 393–398.

[98] S. Frauendorf, *Spontaneous symmetry breaking in rotating nuclei*, Rev. Mod. Phys. **73** (2001) 463–514.

[99] J. A. Sheikh, N. Hinohara, J. Dobaczewski, T. Nakatsukasa, W. Nazarewicz, and K. Sato, *Isospin-invariant Skyrme energy-density-functional approach with axial symmetry*, Phys. Rev. C **89** (2014) 054317.

[100] A. Staszczak, M. Stoitsov, A. Baran, and W. Nazarewicz, *Augmented Lagrangian method for constrained nuclear density functional theory*, Eur. Phys. J. A **46** (2010) 85–90.

[101] M. R. Hestenes, *Multiplier and gradient methods*, Journal of Optimization Theory and Applications **4** (1969) 303–320.

[102] R. Y. Cusson, P. G. Reinhard, M. R. Strayer, J. A. Maruhn, and W. Greiner, *Density as a constraint and the separation of internal excitation energy in TDHF*, Z. Phys. A **320** (1985) 475–482.

[103] K. Rutz, *Struktur von Atomkernen im Relativistic-Mean-Field-Modell*. PhD thesis, Frankfurt am Main, 1998.

[104] K. Rutz, J. Maruhn, P.-G. Reinhard, and W. Greiner, *Fission barriers and asymmetric ground states in the relativistic mean-field theory*, Nucl. Phys. **A590** (1995) 680–702.

[105] J. Dobaczewski and J. Dudek, *Solution of the Skyrme-Hartree-Fock equations in the Cartesian deformed harmonic-oscillator basis. (III) HFODD (v1.75r): a new version of the program*, Comp. Phys. Comm. **131** (2000) 164–186.

[106] M. Bender and P.-H. Heenen, *Configuration mixing of angular-momentum and particle-number projected triaxial Hartree-Fock-Bogoliubov states using the Skyrme energy density functional*, Phys. Rev. C **78** (2008) 024309.

[107] H. J. Lipkin, *Collective motion in many-particle systems*, Annals of Physics **9** (1960) 272–291.

[108] M. Bender, K. Rutz, P. G. Reinhard, and J. A. Maruhn, *Pairing gaps from nuclear mean-field models*, Eur. Phys. J. **A8** (2000) 59–75.

[109] M. Bender. Private communications.

[110] W. Satuła, R. Wyss, and P. Magierski, *The Lipkin-Nogami formalism for the cranked mean field*, Nucl. Phys. **A578** (1994) 45–61.

[111] J. Egido, H.-J. Mang, and P. Ring, *Selfconsistent treatment of excited rotational bands in deformed nuclei*, Nucl. Phys. **A334** (1980) 1–20.

[112] J. Egido, J. Lessing, V. Martin, and L. Robledo, *On the solution of the Hartree-Fock-Bogoliubov equations by the conjugate gradient method*, Nucl. Phys. **A594** (1995) 70–86.

[113] L. M. Robledo and G. F. Bertsch, *Application of the gradient method to Hartree-Fock-Bogoliubov theory*, Phys. Rev. C **84** (2011) 014312.

[114] A. Coc, P. Bonche, H. Flocard, and P. Heenen, *Deformation of ^{121}Cs and of its neighbours calculated in the mean field approximation*, Phys. Lett. B **192** (1987) 263–267.

[115] P.-H. Heenen, P. Bonche, and H. Flocard, *Microscopic study of superdeformation in ^{193}Hg*, Nucl. Phys. **A588** (1995) 490–500.

[116] J. Terasaki, H. Flocard, P. H. Heenen, and P. Bonche, *Superdeformed bands of odd nuclei in a=190 region in the quasiparticle picture*, Phys. Rev. C **55** (1997) 1231–1235.

[117] P.-H. Heenen and R. V. F. Janssens, *Hartree-Fock-Bogoliubov description of quasiparticle excitations in the superdeformed wells of $^{191-192}$Hg and ^{192,193}Tl*, Phys. Rev. C **57** (1998) 159–165.

[118] R. Jodon, M. Bender, K. Bennaceur, and J. Meyer, *Constraining the surface properties of effective skyrme interactions*, Phys. Rev. C **94** (2016) 024335.

[119] P. Mohr, B. Taylor, and D. Newell, *CODATA recommended values of the fundamental physical constants: 2010*, Rev. Mod. Phys. **84** 4, (2012) 1527–1605.

[120] J. Dobaczewski, W. Nazarewicz, and P.-G. Reinhard, *Error estimates of theoretical models: a guide*, J. Phys. G **41** (2014) 074001.

[121] Y. Gao, J. Dobaczewski, M. Kortelainen, J. Toivanen, and D. Tarpanov, *Propagation of uncertainties in the Skyrme energy-density-functional model*, Phys. Rev. C **87** (2013) 034324.

[122] J. Egido and L. Robledo, *Microscopic study of the octupole degree of freedom in the radium and thorium isotopes with gogny forces*, Nucl. Phys. **A494** (1989) 85–101.

[123] Rodríguez-Guzmán, R. and Robledo, L. M., *Microscopic description of fission in neutron-rich radium isotopes with the Gogny energy density functional*, Eur. Phys. J. **A52** (2016) 12.

[124] H. Wollersheim, H. Emling, H. Grein, R. Kulessa, R. Simon, C. Fleischmann, J. de Boer, E. Hauber, C. Lauterbach, C. Schandera, P. Butler, and T. Czosnyka, *Coulomb excitation of ^{226}Ra*, Nucl. Phys. **A556** (1993) 261–280.

[125] M. Samyn, S. Goriely, and J. M. Pearson, *Further explorations of Skyrme-Hartree-Fock-Bogoliubov mass formulas. V. Extension to fission barriers*, Phys. Rev. C **72** (2005) 044316.

[126] National nuclear data center, information extracted from the chart of nuclides database, `http://www.nndc.bnl.gov/chart/`. Last accessed May 2016.

[127] T. Duguet, P. Bonche, P.-H. Heenen, and J. Meyer, *Pairing correlations. I. Description of odd nuclei in mean-field theories*, Phys. Rev. C **65** (2001) 014310.

[128] T. Duguet, P. Bonche, P.-H. Heenen, and J. Meyer, *Pairing correlations. II. Microscopic analysis of odd-even mass staggering in nuclei*, Phys. Rev. C **65** (2001) 014311.

[129] M. Yamagami, Y. R. Shimizu, and T. Nakatsukasa, *Optimal pair density functional for the description of nuclei with large neutron excess*, Phys. Rev. C **80** (2009) 064301.

[130] S. Bjørnholm and J. E. Lynn, *The double-humped fission barrier*, Rev. of Mod. Phys. **52** (1980) 725–931.

[131] R. Capote, M. Herman, P. Obložinský, P. Young, S. Goriely, T. Belgya, A. Ignatyuk, A. Koning, S. Hilaire, V. Plujko, M. Avrigeanu, O. Bersillon, M. Chadwick, T. Fukahori, Z. Ge, Y. Han, S. Kailas, J. Kopecky, V. Maslov, G. Reffo, M. Sin, E. Soukhovitskii, and P. Talou, *RIPL – Reference Input Parameter Library for Calculation of Nuclear Reactions and Nuclear Data Evaluations*, Nuclear Data Sheets **110** (2009) 3107–3214.

[132] J. Zhao, B.-N. Lu, E.-G. Zhao, and S.-G. Zhou, *Nonaxial-octupole Y_{32} correlations in $n = 150$ isotones from multidimensional constrained covariant density functional theories*, Phys. Rev. C **86** (2012) 057304.

[133] J. Zhao, B.-N. Lu, D. Vretenar, E.-G. Zhao, and S.-G. Zhou, *Multidimensionally constrained relativistic mean-field study of triple-humped barriers in actinides*, Phys. Rev. C **91** (2015) 014321.

[134] M. Bender, P. Bonche, T. Duguet, and P.-H. Heenen, *Configuration mixing of angular momentum projected self-consistent mean-field states for neutron-deficient Pb isotopes*, Phys. Rev. C **69** (2004) 064303.

[135] S. Perez-Martin and L. M. Robledo, *Fission properties of odd-A nuclei in a mean-field framework*, Int. J. Mod. Phys. E **18** (2009) 788–797.

[136] M. H. Koh, *Fission-barriers and energy spectra of odd-mass actinide nuclei in self- consistent mean-field calculations.* PhD thesis, Université de Bordeaux-Gradignan, 2015.

[137] A. Tsvetkov, J. Kvasil, and R. G. Nazmitdinov, *Octupole deformations in actinides at high spins within the cranking Skyrme-Hartree-Fock approach*, J. Phys. G **28** (2002) 305.

[138] W. Nazarewicz, G. Leander, and J. Dudek, *Octupole shapes and shape changes at high spins in Ra and Th nuclei*, Nucl. Phys. **A467** (1987) 437–460.

[139] W. Nazarewicz and S. L. Tabor, *Octupole shapes and shape changes at high spins in the $Z \sim 58$, $N \sim 88$ nuclei*, Phys. Rev. C **45** (1992) 2226–2237.

[140] J. M. Yao, M. Bender, and P.-H. Heenen, *Systematics of low-lying states of even-even nuclei in the neutron-deficient lead region from a beyond-mean-field calculation*, Phys. Rev. C **87** (2013) 034322.

[141] J. Bonn, G. Huber, H.-J. Kluge, L. Kugler, and E. Otten, *Sudden change in the nuclear charge distribution of very light mercury isotopes*, Phys. Lett. B **38** (1972) 308–311.

[142] G. Ulm, S. K. Bhattacherjee, P. Dabkiewicz, G. Huber, H. J. Kluge, T. Köhl, H. Lochmann, E. W. Otten, K. Wendt, S. A. Ahmad, W. Klempt, R. Neugart, and I. Collaboration, *Isotope shift of ^{182}Hg and an update of nuclear moments and charge radii in the isotope range ^{181}Hg-^{206}Hg*, Z. Phys. A **325** (1986) 247–259.

[143] G. Huber, J. Bonn, H. J. Kluge, and E. W. Otten, *Nuclear Radiation Detected Optical Pumping of neutron-deficient Hg isotopes*, Z. Phys. A **276** (1976) 187–202.

[144] T. Duguet, M. Bender, P. Bonche, and P. H. Heenen, *Shape coexistence in ^{186}Pb: Beyond-mean-field description by configuration mixing of symmetry restored wave functions*, Phys. Lett. B **559** (2003) 201–206.

[145] M. Bender, P. Bonche, T. Duguet, and P.-H. Heenen, *Configuration mixing of angular momentum projected self-consistent mean-field states for neutron-deficient Pb isotopes*, Phys. Rev. C **69** (2004) 064303.

[146] R. R. Rodríguez-Guzmán, J. L. Egido, and L. M. Robledo, *Beyond mean field description of shape coexistence in neutron-deficient Pb isotopes*, Phys. Rev. C **69** (2004) 054319.

[147] Y. Shi, C. L. Zhang, J. Dobaczewski, and W. Nazarewicz, *Kerman-Onishi conditions in self-consistent tilted-axis-cranking mean-field calculations*, Phys. Rev. C **88** (2013) 034311.

[148] P. D. Stevenson, E. B. Suckling, S. Fracasso, M. C. Barton, and A. S. Umar, *Skyrme tensor force in heavy ion collisions*, Phys. Rev. C **93** 5, (2016) 054617.

[149] F. Raimondi, B. G. Carlsson, J. Dobaczewski, and J. Toivanen, *Continuity equation and local gauge invariance for the N 3 LO nuclear energy density functionals*, Phys. Rev. C **84** (2011) 064303.

[150] M. Zalewski, J. Dobaczewski, W. Satuła, and T. R. Werner, *Spin-orbit and tensor mean-field effects on spin-orbit splitting including self-consistent core polarizations*, Phys. Rev. C **77** (2008) 024316.

[151] J. Bartel, P. Quentin, M. Brack, C. Guet, and H.-B. Håkansson, *Towards a better parametrisation of Skyrme-like effective forces: A critical study of the SkM force*, Nucl. Phys. **A386** (1982) 79–100.

[152] E. P. Wigner, *Normal Form of Antiunitary Operators*, J. Math. Phys **1** (1960) 409.

[153] E. P. Wigner, *Phenomenological Distinction between Unitary and Antiunitary Symmetry Operators*, J. Math. Phys. **1** (1960) 414.

[154] A. Messiah, *Quantum Mechanics, volume II*. Dunod, 1959.

[155] R. J. A. Tough and A. J. Stone, *Properties of the regular and irregular solid harmonics*, J. Phys. A **10** 8, (1977) 1261.

[156] J. Dobaczewski and P. Olbratowski, *Solution of the Skyrme-Hartree-Fock-Bogolyubov equations in the Cartesian deformed harmonic-oscillator basis. (IV) HFODD (v2.08i): A new version of the program*, Comp. Phys. Comm. **158** (2004) 158–191.

[157] P. A. Butler and W. Nazarewicz, *Intrinsic reflection asymmetry in atomic nuclei*, Rev. Mod. Phys. **68** 2, (1996) 349–421.

[158] S.G. Rohoziński, *A parametrisation of the octupole deformation*, J. Phys. G **16** 9, (1990) L173–L177.

[159] I. Hamamoto, X. Z. Zhang, and H.-X. Xie, *Parametrization of octupole deformation*, Phys. Lett. B **257** (1991) 1 – 4.

[160] J. R. Shewchuk, *An Introduction to the Conjugate Gradient Method Without the Agonizing Pain*, 1994. Technical report, School of Computer Science, Carnegie Mellon University.